Evaluating the Wear and Corrosion Resistance of Plasma-Sprayed Tungsten Carbide Coatings on Aluminium-6082 Alloy

MSc Research Dissertation

Prepared by

Oluwadamilola Solomon MacGregor

Submitted to the School of Chemical and Metallurgical Engineering, Faculty of Engineering and the Built Environment, University of the Witwatersrand, Johannesburg.

December, 2017

DECLARATION

I, Oluwadamilola Solomon MacGregor, declare that this dissertation is my own unaided work. It is being submitted for the degree of Master of Science to the University of the Witwatersrand, Johannesburg, South Africa. It has not been submitted before for any degree or examination to any other university.

……..

……..…….. day of ….…….…….……. 2017

[Day] [Month] [Year]

ABSTRACT

The benefits of Al alloys to industry are significant. For the truck loading application in this study, the use of Al can deliver a greater payload than most other metals, due to its low relative density. However, it has poor tribological properties. This study investigated ways to improve the wear resistance of AA6082, an Al alloy widely used in transport. This was done by studying WC-based coatings to improve the wear resistance of the AA6082 surface. To ensure a sufficient WC-substrate bond, Al powder was used as a binder for the coatings. Although these coatings improved the wear resistance of the AA6082, it was imperative to test and establish that their corrosion resistance was not inferior to that of the AA6082 itself.

Differences in hardness and tensile properties of the substrate were evaluated for varying ageing durations. The plasma spray technique was used to coat the AA6082 substrate. The heat input from this coating process on an Al alloys with high thermal conductivity could have lowered the hardness and mechanical properties of the AA6082 substrate. Therefore, hardness tests were carried out on the cross-section of each coated substrate. The hardnesses of all coated AA6082 samples were not lowered by the heat input from the plasma spray process.

The coatings were varied to contain 20%, 40%, 60%, 80% and 100% volume of WC admixed with Al-102 powder. The wear resistance of AA6082 was significantly improved as WC content increased. From the wear resistance results, both 60% and 80% WC showed the highest wear resistance. The 60% WC coating, which contained a lower quantity of WC than the 80% WC coating, was the preferred option for truck loading applications because of cost. The 60% WC coating had a lower hardness value than the 80% WC coating, giving the 60% WC coating a higher allowance for work-hardening in service as ductile Al-102 is present in higher quantity.

Al and its alloys, with no coating, are known to have good corrosion resistance. It was therefore imperative to evaluate and compare the corrosion resistance of the coated samples with AA6082. The lowest corrosion rate of all coated samples exposed to the neutral and acidic media was the 20% WC coating. Generally, all the coated samples had very low corrosion rates in the neutral solution, which is more applicable to typical truck loading conditions. Therefore, the 60% WC coating was most preferred for wear and hardness tests and also had acceptable corrosion behaviour for the proposed truck loading application.

DEDICATION

I dedicate this work, foremost, to God the creator of all things seen and unseen.

I also dedicate this endeavour to my late uncle, Mr Samuel Agbebi, for his relentless support; having wholeheartedly played a fatherly role to me from birth, until his passing. Also I dedicate this work to my mother, Ms Abiola Agbebi, for having nurtured me through every stage. Then, I dedicate this finally to my late biological father, Chief Adebisi MacGregor, for his substantial contributions to my life. I am forever grateful to all, for believing and investing in me.

ACKNOWLEDGMENTS

The **Carnegie Corporation of New York**, **Science Initiative Group (SIG)** and **Regional Initiative in Science and Education (RISE)**, for providing full financial support for my studies and research through the **African Materials Science and Engineering Network (AMSEN)**.

Dr. J. W. van der Merwe, for his kindness, patience, positivity, understanding, sacrificial heart and overall fantastic supervisory role. He has helped me become a better person.

Professor M. O. Daramola, for the very constructive outlook to all areas of the project, thanks to his versatility.

Dr. O. T. Johnson, for being sensitive, brilliant and available to guide me through my work, academic and otherwise. Physical distance was insignificant, thanks to constant communication.

Professor A. E. Paterson, for being a pillar of exceptional intellectual value and emotional intelligence in all his dealings with me. I found a father in him, far beyond a scholarly context.

School of Chemical and Metallurgical Engineering, Wits University, Staff (Prof J. H. Potgieter and Prof. N. Sacks) and postgraduate students (Mr. M. O. Bodunrin, Miss A. Fabuyide and Mr. A. O. Ladenika) for the friendship and support.

School of Mechanical, Industrial and Aeronautical Engineering, Wits University, Staff (Prof. C. Polese and Prof I. Botef) and postgraduate students (Mr. Terence Malama and Brett Freeman) for their support in the technical aspects of my work.

The Department of Science and Technology (DST) and National Research Foundation (NRF), South Africa; particularly the DST-NRF Centre of Excellence in Strong Materials (CoE-SM), Director (Prof L. A. Cornish) and Staff (Mrs C. Sparkes, M. Labuschagne and J. Jacobs) for all the assistance, advice and for delivering administrative and logistic excellence.

I appreciate **Major General Olatilewa Amusu**, as well as **Mr Olurotimi and Mrs Oluwaseyi Aju**, for all the great support. Ultimately, I give my deepest gratitude to all in continuous support of the **Green Tempers** brand. The journey to endless discoveries has just begun!

TABLE OF CONTENTS

LIST OF FIGURES

APPENDIX

LIST OF TABLES

APPENDIX

NOMENCLATURE & SYMBOLS

6XXX	6000-series aluminium alloys
AA6082	Aluminium-6082 alloy
Al-102	Aluminium-102 powder (containing 12% Si, as-received)
WC	Tungsten carbide
AMC	Aluminium matrix composite
MMC	Metal matrix composite
UFG	Ultra-fine grain
CoF	Coefficient of friction
DSA	Dynamic strain ageing
PLC	Portevin Le-Chatelier effect
SRS	Strain rate sensitivity
RCF	Rolling contact fatigue
CVD	Chemical vapour deposition
REACH	Registration, Evaluation, Authorization and Restriction of Chemicals
µm	micron / micrometer
CHMT	School of Chemical and Metallurgical Engineering
Wits	University of the Witwatersrand, Johannesburg, South Africa

Mg (Magnesium), Mn (Manganese), Sr (Strontium), Si (Silicon), Ru (Ruthenium)

CHAPTER 1: BACKGROUND AND MOTIVATION

Advanced technology has progressively influenced civilization and improved the quality of life. Among these solutions are transport means such as cars, trains, ships and aircrafts. When making vehicles, material selection is vital. Materials used to make vehicles have been susceptible to surface degradation due to wear and corrosion. Extensive research has been carried out to evaluate the properties of materials; in order to determine which material best fits a specific application for longevity in service life. The best suited material is thus carefully selected and fabricated, based on intrinsic properties such as corrosion resistance, toughness, wear resistance and properties for transport applications.

Minimized weight in vehicles, especially of truck bed surfaces for transportation of products, increases service life. Lightweight truck beds are the preferred choice, as their energy-saving advantage makes them eco-friendly. The use of heavier sacrificial materials to prevent corrosion or wear actually defeats the purpose of lightweight vehicles. This disadvantage confirms the need for both erosion-corrosion resistance and minimized tare (unloaded) weight. It is thus important to minimize additional weight of truck beds in order to combine effectiveness with efficiency. Wear and corrosion are detrimental phenomena that reduce the service life of materials and are to be significantly reduced or completely averted.

1.1 Wear

Friction is a force which resists the motion of solid surfaces in contact. Frictional force can be beneficial or detrimental. In cases where the resistance to movement of the solid surfaces is necessary for safety, as against free motion, friction is deemed beneficial. Examples of such cases include the clutches and brakes needed to control the speed of a vehicle and ultimately bring it to a complete stop. However, the wear associated with friction is undesirable.

During the transportation of heavy loads, friction mostly results in the progressive degradation or complete loss of material (Hutchings, 1992). This detrimental wear phenomenon can be prevented, as different surface enhancement techniques have evolved for engineering materials, e.g. to minimize material loss due to erosive wear. Erosive wear occurs when particles of a solid, liquid or slurry cause material removal from the target surface, as a result of repeated

deformation and break-off. The size, velocity and impact angle of the particles are factors that affect erosive wear.

Lubrication, for moving vehicle parts, can also be used to reduce friction. This is because lubricants minimize direct contact between bodies moving in close proximity, thereby lowering the likelihood and frequency of such surfaces rubbing against each other while in service. In this study, the wear resistance of an Al alloy substrate was improved by applying a surface coating.

1.2 Corrosion

Metals corrode in environments where they are thermodynamically unstable. This can be detrimental to many industrial applications. This results in loss of facilities and high maintenance costs for many industries and economies. Finished metallic products in which corrosion occurs include structural materials, automobiles and aircrafts parts, machine parts and other engineering applications where Al is used. There are several ways by which corrosion occurs. Peak-aged Al alloys inherently have excellent corrosion resistance, but they are susceptible to localized corrosion and stress-corrosion cracking in chloride environments (Trdan and Grum, 2012).

1.3 Surface Engineering

Wear and corrosion have been major causes of material failure in the transport sector. One of the ways through which both phenomena can be prevented is through surface engineering solutions. Surface protection techniques generally have much to do with creating new surfaces, modifying existing surfaces or a combination of both. The processes employed include the production of coatings that may be multi-component in nature and multi-layer in structure. Examples of materials used as surface protection are WC-based coatings (Houdková et al., 2011), due to their high levels of hardness and toughness. The lightweight advantage offered by Al alloys, particularly AA6082, is sufficient reason to use them in truck beds. However, due to the susceptibility to surface degradation in abrasive or corrosive environments, adequate surface protection becomes imperative.

The selected surface protection technique must be evaluated against parameters such as hardness, wear resistance and corrosion resistance of the new protective surface, in comparison to the substrate to be protected. Therefore, the selected material and coating procedure used to mitigate

wear should not lower the corrosion resistance or weaken mechanical properties. Surface engineering can promote lasting solutions for wear and corrosion protection (Burnell-Gray and Datta, 1996). The interaction between the coating and the surface of the substrate is to be evaluated, as poor adhesion could lead to failure. This means that the choice of materials will determine the effectiveness of the surface protection. Also, coating application procedures, such as thermal spray processes, need to be compared. Parameters such as adhesion, porosity, toughness, hardness and microstructure determine the effectiveness and longevity of the coating and the coating-substrate interface.

Characterising coated surfaces reveal the morphology and properties of the product as various tests are carried out. However, where new surfaces are developed and improved, additional advantages are found due to a constructive combination of two or more of the following; metallic, polymeric and ceramic materials to derive composites. A cermet, being a combination of ceramic and metal, combines the high temperature strength and hardness of a ceramic with the toughness and ductility of metallic materials. This is why cermets exhibit more reliable properties for specific industrial applications such as TiC, TiN and TiCN. In this study, the surface of AA6082 was protected using a plasma-sprayed WC coating.

1.4 Problem Statement

AA6082 is desirable for use in truck beds. Although AA6082 has excellent corrosion resistance, it is susceptible to localized corrosion and stress-corrosion cracking in chloride environments during its service life (Trdan and Grum, 2012). AA6082 also has poor tribological properties which lead to failure under extreme wear conditions in automobiles (Basavarajappa et al. 2007; Aruri et al. 2013). The corrosion resistance of the wear resistant coatings need to be evaluated.

1.5 Research Aim

The aim of this work is to evaluate plasma sprayed WC coatings to improve wear and corrosion resistance of AA6082 which serves as beds for trucks, without compromising the lightweight, mechanical and other intrinsic beneficial properties of AA6082. The addition of ceramic particles such as SiC, TiB_2 and Al_2O_3 to Al alloys produces aluminium matrix composites (AMCs) and results in improved specific strength and wear resistance, while lowering their thermal expansion (Palanivel et al., 2016). These advantages make AMCs useful in the aerospace

and automotive industries (Mazahery and Shabani, 2012; Vijayarangan et al., 2013). No significant weight is added to the material being protected from surface wear, because the lightweight Al is the bulk of the AMCs. It is imperative to evaluate the effect of the application of wear resistant coatings on the structural, mechanical and corrosion properties intrinsic to AA6082, to ensure that these properties are not compromised.

1.6 Research Questions

In applications where materials are susceptible to aggressive conditions, addition of wear liners (for instance, in skips) and sacrificial anodes (for corrosion) are sometimes used to prevent abrasion and corrosion respectively. This can result in a significantly increased tare mass and such should be avoided. This research project focuses on answering the following:

1) How do structural and mechanical properties, intrinsic to AA6082, change in response to the heat input of the coating process?

2) To what degree does the corrosion resistance of AA6082 improve by the varying concentrations of WC in the plasma sprayed coatings?

3) What minimum volume concentration of WC is sufficient to adequately protect the AA6082 surface from wear, without additional weight to the tare mass of the substrate?

1.7 Research Objectives

The aim of this project is to improve the wear and corrosion resistance of AA6082, using WC and Al-102 powder coatings. The tare mass should be kept low, despite the coatings used. Also, wear and corrosion resistance of the AA6082 substrate must be improved by using a thermal spray technique. Specific objectives to achieve this aim are:

a) To evaluate and establish the mechanical properties for various AA6082 heat treatment and ageing conditions.

b) To mix and plasma-spray various concentrations of WC and Al-102 powders onto the AA6082 substrate.

c) To evaluate the coating-substrate adherence of the various coatings, as well as compare their hardness with the uncoated AA6082.

d) To compare the corrosion resistance of the various coatings with the uncoated AA6082.

e) To establish the improvement of the wear resistance of the sprayed coatings, compared to the uncoated AA6082, and also to ascertain which coating is most effective with the least amount of WC.

1.8 Proposed Contribution to Knowledge

By employing the proposed methodology, it is expected that this research will:

a) Confirm that coating thickness of the various volume concentrations can be effective for wear resistance without a significant increase in the tare mass of the truck bed.

b) Establish which WC/Al-102 coating mixture adheres best to AA6082 while still exhibiting optimal hardness.

c) Evaluate how the corrosion resistance of the coatings compare with uncoated AA6082.

d) Ascertain which coating exhibits the most effective wear resistance, while remaining affordable for the truck bed applications.

In Chapter 2, a detailed literature review is given on the effect of heat treatment on the mechanical properties of AA6082, the wear resistance of cermets and cemented carbides, thermal spray techniques and the corrosion phenomenon.

Chapter 3 provides details of the AA6082 substrate, WC and Al-102 powders used for the study. The experimental procedures and all facilities used during the study are also described in this chapter.

Chapter 4 describes the results obtained from the experiments carried out during this study.

Chapter 5 shows the results of this study discussed in comparison with literature.

Chapter 6 contains the overall conclusions of this research and some recommendations for future research as an extension of this work.

CHAPTER 2: LITERATURE REVIEW

Aluminium is the second most abundant metal on earth, after iron; and it is fully recyclable (Paterson, 2007a). Because of high strength-to-mass ratio, corrosion resistance and ease of formability, Al alloys are used in transport (Miller et al., 2000; Gudić et al., 2010; Mikhaylovskaya et al., 2014). Al alloys are used in the fuselage and wings of aircraft, yachts and smaller boats, wheel-spacers in automobiles, cans for packaging food and beverages, bodies of trucks, helicopter rotors, ultra-high vacuum (UHV) chambers, sporting utilities and the construction industry. In addition to ductility and average strength, Al alloys have been attractive because they are available, affordable and recyclable.

As an alternative to incurring high energy costs producing Al from its ore, Al scrap can be fully recycled. The significantly low cost of recycling Al offers an immense economic benefit for the industry. The energy cost for recycling used Al is as low as 5% of the amount required to extract it from its ore (Paterson, 2007). Also, as much as 10% reduction in weight can improve fuel efficiency by 5% (Ma et al., 2015), so over a period of 10 years, structures of Al cost about 5% less than those of steel. Al alloys have almost completely replaced steel in automobile and aerospace industries, as their density is one-third that of steel (Sajjadi et al., 2012; El Mehtedi et al., 2014; Shi et al., 2014).

2.1 Advantages of Aluminium Alloys in Transport

The lightweight property of Al alloys is the reason fuel efficiency and weight balance in automobiles can be improved (Chang et al., 2009). Hirsch (2014) affirmed that the advantage of low tare mass justifies the use of 6xxx series Al alloys in automobiles parts. For this reason, AA6082 was used in this study as the selected material for use in truck beds.

The American Aluminium Association established a system by which the nomenclatures of Al alloys are known worldwide. The designation, “6082”, based on its internationally recognized chemical composition. Being a 6xxx series alloy, the first digit “6” means that Si and Mg are its major alloying elements. The digit “0” refers to the conventional state of the base alloy, as numbers other than “0” indicate an internationally recognized modification to known base alloy. The last two digits, “82”, are of no technical significance but rather represent the order in which the alloy was registered internationally.

The temper condition “T651” qualifies the state of the alloy used for this work. For this, the letter “T” means that the alloy is heat-treatable. “65” means it is slightly under-aged as a “T6x” temper; where “T6” would normally mean it is fully aged to its maximum strength. The last digit “1” behind “T65” indicates that subsequent strain-hardening (to about 1% of its original length) was performed to relieve internal stresses, consequently achieving the ultimate T6 strength.

Xu et al. (2017b) recently mentioned that strength and weldability are known beneficial properties which make 6xxx series Al alloys highly sought after in lightweight structural applications. Over a number of years, extruded Al alloy products have mostly been made from 6xxx series (Borrelly et al., 1989), and AA6082 is mostly used (Birol, 2008; Mohamed et al., 2012; Wan et al., 2014). The presence of Mg and Si in 6xxx Al alloys makes the formation of magnesium silicide (Mg_2Si) possible, essentially making the alloy heat treatable.

The use of Al alloys for structural and transport applications is extensive. AA6082 is the focus of this work and has shown valuable properties. These include reasonable strength, weldability, corrosion resistance and improved mechanical properties through heat treatment (Paterson, 2007a). By similarity in composition and function, it is the European equivalent of aluminium 6061 alloy (AA6061) which is used in the USA. From a strength-mass ratio viewpoint, excellent mechanical properties rank Al alloys highly useful in the automotive industry (Canales et al., 2012; Jayalakshmi et al., 2013; Król et al., 2017). The ease of casting, as well as the improved corrosion resistance of Al alloys containing Mg, make the 6xxx series particularly sought after (Kaygısız and Maraşlı, 2015; Yan and Li, 2014).

2.1.1 Payload means Profit

The essence of transport, be it road, rail, air or vertical as in mining, is payload. The lightweight advantage offered by aluminium alloys inherently promises delivery of greater payload than most other metals, as tare mass is low. This high strength-to-mass ratio (Gupta et al., 2015) makes Al alloys the basis of the aerospace sector. Al alloys are susceptible to wear and localized corrosion when used in vehicles which operate in chloride environments (Yu et al., 1997; Basavarajappa et al. 2007; Aruri et al. 2013; Trdan and Grum, 2012). Gross load is limited by operating conditions such as safe take-off in aircraft, mining hoist capacity or gross allowable

axle loads for commercial transport. The difference between gross mass and tare (un-laden) mass of the vehicle is the payload which ultimately determines profit (Hossain et al., 2014).

$$PL = GM - TM \qquad \text{Equation 2.1}$$

where: GM is gross mass, TM is the tare (unloaded) mass and PL is the payload.

2.1.2 Energy and the Green Initiative

The heavier a vehicle, the higher its environmental footprint as it consumes more fuel. The goal for commercial transport is to ensure that gross loads do not exceed legislated limits, based on energy supply and overall safety. The overloading of trucks and carrier vehicles constitutes risks to health, safety, the environment (Zhang et al., 2012; Karim et al., 2014) and the road infrastructure. Similarly, factors such as size, tare mass and stability (Eichelberger et al., 2015) of the vehicles themselves affect performance. Dwindling oil and gas reserves and greenhouse effects are reasons for which lightweight materials are highly sought after (Alam et al., 2013), for the purpose of lower gross loads.

Reducing the tare mass of a vehicle below its expected minimum weight can be detrimental, as it will lose its capacity to bear the load it is designed to carry. Therefore, the goal in fuel efficiency is to keep its tare mass low enough to have a minimum gross mass as payload is additional. The techniques used to improve material surface properties thus need to be evaluated to avoid any additional weight. Therefore, increasing the wear and corrosion resistance of AA6082 alloy by improved surface characteristics, without adding to its tare mass, is worth researching. The benefits of minimum tare mass and increased payload makes it imperative to use materials which are light, strong and adequately tough for transport (Glaeser, 2010). Aluminium, which has a density of ~2.70 g/cm^3, qualifies as a lightweight material strong enough to be used in vehicles.

2.1.3 Eco-friendly procedures

When a vehicle is loaded, reduced tare mass offers economic and environmental advantages as the payload is boosted and carbon footprint reduced respectively (Galos et al., 2015). Due to taxes, prosecution and potential loss of business, the depletion of natural resources as well as health and environmental degradation (Gehin et al., 2008), industries are increasingly becoming conscious of the carbon footprint and environmental matters (Serres et al., 2010). To achieve

eco-friendly manufacturing with the use of life cycle assessment (LCA), an environmental impact assessment (EIA) of each stage in the surface engineering procedure is to be taken into account. These processes consist of the extraction and preparation of raw materials, through their various industrial applications and perhaps recycling, until the materials are eventually deemed unfit for further use at the end of their service lives.

The deposition of electrolytic hard chromium (EHC) have been used for wear and corrosion reduction (Natishan et al., 2000; Bolelli et al., 2006; Picas et al., 2006). In transport applications, they are mostly used in landing gears which support the full weight of an aircraft during landing and ground operations (Gong et al., 2016). However, the formation of toxic hexavalent chromium compounds during the EHC deposition process has posed an immense threat to health and the environment (Sartwell et al. 1998; J.R. Davis & Associates and ASM International, 2004; Cho et al. 2008).

The European standard legislated limits, against the production and use of chemical products such as hexavalent Cr compounds and other toxic substances, have been imposed on manufacturers (Kimbrough et al., 1999; Directive, 2000; Parliament and Council, 2003; Registration, Evaluation, Authorization and Restriction of Chemicals 2017). The production of these potentially toxic Cr-based compounds became the reason to seek alternative hard materials which will be less harmful to health and the environment (Villalobos-Gutiérrez et al., 2008; Picas et al., 2011; Ward and Pilkington, 2014). For these reasons, more eco-friendly processing techniques have been researched (Rastegar and Richardson, 1997; Espallargas et al., 2008).

From an environmental impact point of view, several studies have been conducted on replacing EHC with WC-based materials. WC-Co coatings were found to be an alternative, with higher wear resistance than EHC. However, surface enhancement processes are generally required to meet a prescribed standard of effectiveness (Le Pochat et al., 2007), particularly for resistance to wear (Bolelli et al., 2006) and also for corrosion protection (Natishan et al., 2000). For this reason, the addition of Cr was made to improve the surface properties of WC-Co matrix used in the oil and gas industry and other engineering applications (Wesmann and Espallargas, 2016).

Both wear and corrosion resistance were achieved as Cr was added to WC-Co to yield surface coatings of WC-CoCr in a ductile matrix (Sartwell et al., 1998; Murthy and Venkataraman,

2006; Picas et al., 2006; Maiti et al., 2007; Kumari et al., 2010; Agüero et al., 2011; Bolelli et al., 2014; Ghabchi et al., 2014), without forming the environmentally toxic hexavalent Cr synthesized during EHC deposition (Legg et al., 1996). Other studies have shown that WC-CoCr coatings offer improved wear and corrosion resistance (Jacobs et al., 1999; Bolelli et al., 2006; Ghabchi et al., 2010; Wood, 2010). However, a major drawback is that HVOF spraying process is rather expensive. EHC deposition is gradually being outlawed in Europe and the United States.

2.2 Heat Treatment of alloys

Alloys can form single phase solid solutions under certain conditions. Such solid solution alloys usually exhibit properties similar to the pure parent metal, albeit with improved higher strength and hardness. When atoms of the parent metal are completely replaced by atoms of the second metal due to similar atom size, the resulting alloy is a substitutional solid solution. On the other hand, when the atoms of the second metal are significantly smaller than those of the parent metal, an interstitial solid solution is formed. These are illustrated in Figure 2.1.

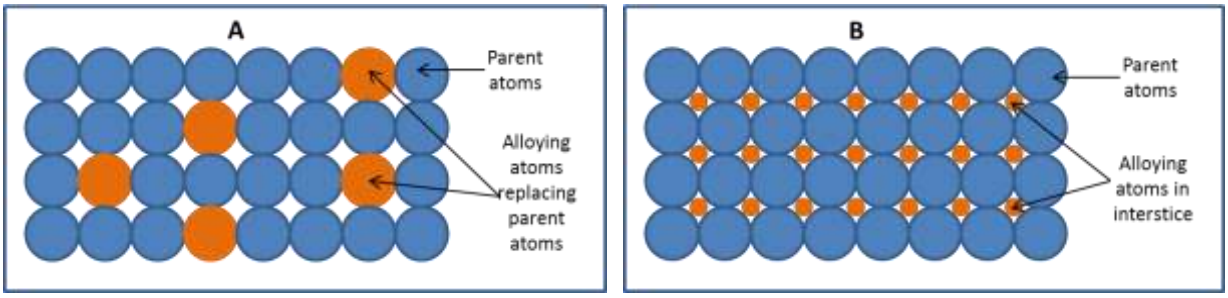

Figure 2.1: Schematic diagram showing (A) substitutional and (B) interstitial solid solution.

2.2.1 Alloys and phase diagrams

Temperature and time significantly affect an alloy, with respect to the constituent metals therein. Thermal equilibrium (phase) diagrams typically provide information about the changes in phases that occur, for different alloys, through processes of heating and cooling. Most metals are completely soluble in the liquid phase, but not soluble in the solid phase. The resulting alloys in such cases are called eutectic alloys, examples of which are the cadmium-bismuth alloys. The

eutectic point in a phase diagram is the point where a liquid alloy solidifies without undergoing the transient liquid/solid state. Therefore, both the liquidus and solidus lines meet at the eutectic point, as seen in Figure 2.2.

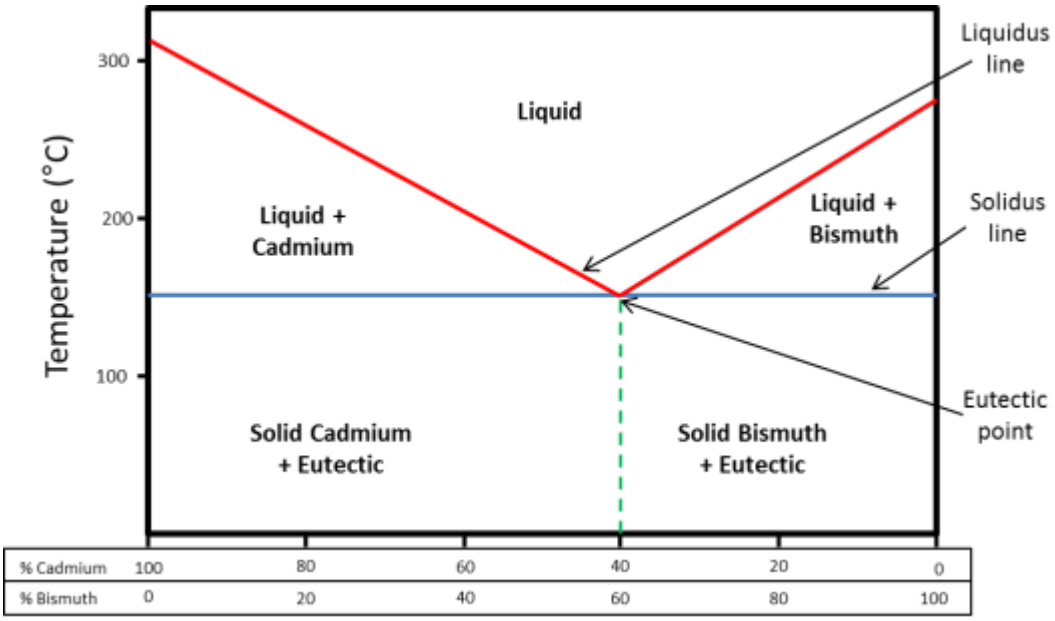

Figure 2.2: Schematic for a typical cadmium-bismuth phase diagram (Askeland and Pradeep, 2003).

Also, some alloys result from a mixture of metals which are partially soluble in each other. An example is the lead-tin phase diagram shown in Figure 2.3, where the solvus line shows the amount of Sn dissolved in Pb up to its eutectic temperature of 183°C, and vice-versa. The maximum solubility of Sn in Pb at 183°C is about 19.2% Sn. However, at the same eutectic temperature of 183°C, Pb is soluble in Sn only to the point where the Sn-rich part of the phase diagram is 97.5% Sn.

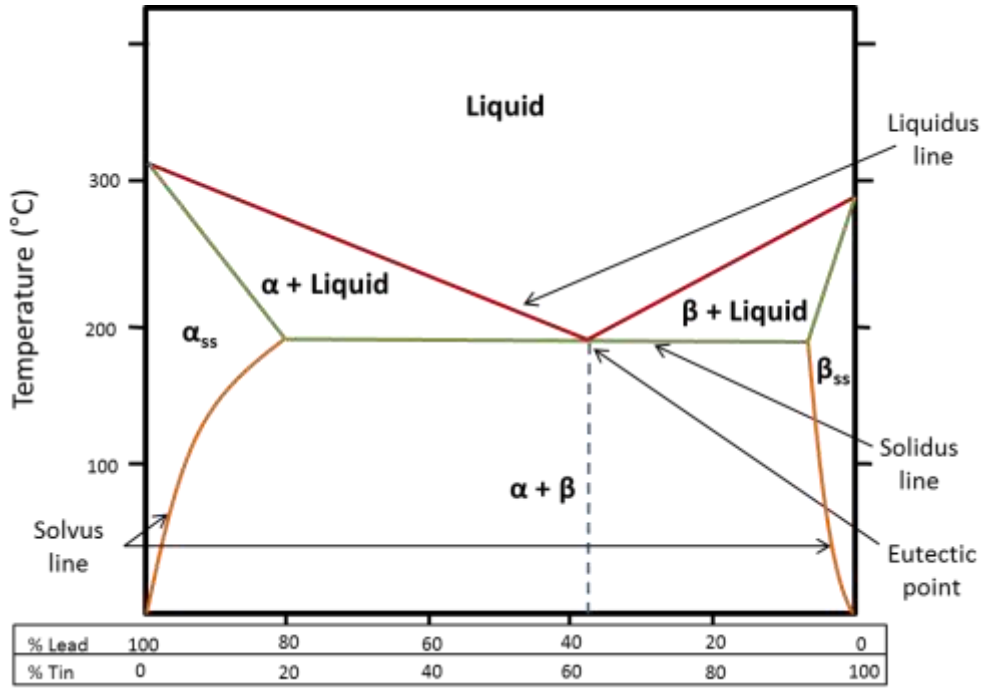

Figure 2.3: Schematic showing solvus lines for a lead-tin phase diagram (Askeland and Pradeep, 2003).

In Figure 2.3, α_{ss} and β_{ss} refer to solid solutions of α and β phases respectively.

Certain intermediate phases, which are formed when chemical compounds are created in binary alloys, are known as intermetallics. Intermetallics mostly have higher melting points and hardnesses than the principal elements that make up the main compound. They are also brittle. The two types of intermetallics are electron and interstitial compounds. Electron compounds are formed between metals which have similar electrochemical properties, an example of which is the CuZn intermetallic. On the other hand, interstitial compounds may result from metal/metal or metal/non-metal combinations. Similar to interstitial solid solutions shown in Figure 2.1B, smaller atom sizes of interstitial compounds infiltrate the interstices between larger surrounding atoms. For example, in Al-Cu alloys, $CuAl_2$ interstitial intermetallic compounds may be formed.

2.2.2 Ageing mechanisms

Generally, molten metal cools from high temperature to a point where solidification begins. Solidification occurs in a defined pattern wherein grains form. At this freezing point, small particles within the molten metal start to solidify first. These particles grow as the surrounding

particles solidify. Similar to the solidification of water particles into ice, metallic particles grow branches to form dendrites. Ideal crystalline structures of metals, in which there are no defects, are rare to find in reality. Most fully solidified metals have inherent crystal defects which are imperfections within their lattice structure. Line defects, which form as a result of atoms being out of linear alignment, are known as dislocations.

The presence of dislocations causes slip, due to shear stress. One apparent advantage of slip is that the metal exhibits ductility under such shear stress. However, an insufficient amount of independent slip systems within a polycrystalline material results in strains between incompatible grains in close proximity, and voids are formed (Ball and Smallman, 1966). Bowman et al. (1992) found that cross-slip and the inclusion of more slip systems make plasticity possible without cracks, though not under cryogenic conditions. To limit the movement of dislocations, the metal can be alloyed or cold worked. Alloying is typically used in the case of Al alloys, which differ in chemical composition, depending on the alloying elements within its matrix. For example, 6xxx Al alloys are solution heat-treated between 500°C and 530°C, to dissolve the precipitate-forming elements and derive a supersaturated α solid solution (Xu et al. 2017b). The solution treated alloy is then quenched to room temperature, and aged.

When changes in alloy properties occur slowly at room temperature, the phenomenon is known as natural ageing. On the other hand, during the artificial ageing process, Al alloys are held at above room temperature to cause a significant change in the alloy properties. Hossain and Kurny (2013) showed from their recent study that the artificial ageing of Al alloys, typically carried out between 100°C and 260°C, allows for controlled precipitation of its alloying elements to yield different mechanical properties. For example, the hardness value will increase as solutes impede the movement of dislocations within the lattice structure, during artificial ageing.

Precipitation hardening is a second phase precipitation process during which solute particles, which diffuse through an alloy, serve as obstacles to the movement of dislocations, thereby strengthening the alloy (Gladman, 1999). Generally, factors such as size, volume fraction and interactivity of the particles determine the extent to which the alloy is strengthened. Inter-particle spacing is a function of both size and volume fraction of the particles. The dislocation line exerts

a tension force (*T*) which is opposed by a resistant force (*F*) of a precipitated particle. The directions of these forces are shown in Figure 2.4.

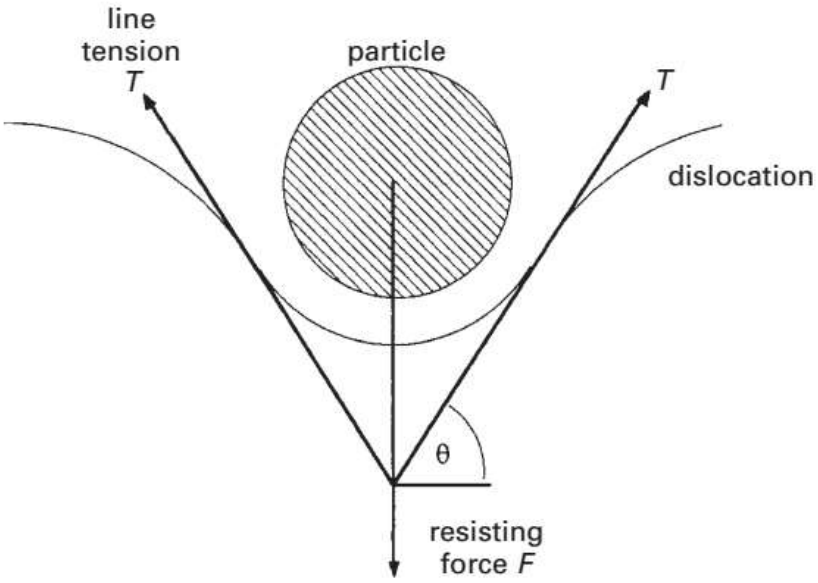

Figure 2.4: Schematic showing forces at play during dislocation movement (Gladman, 1999).

As *F* increases, the dislocation bends inwards and θ increases. *F* reaches maximum when sin θ equals 1. For a predetermined inter-particle spacing, softer particles shear and the dislocation will move through because *F* is less than *T*. However, for harder particles where *F* is greater than *T*, movement of dislocations is resisted and bypass such particles by means of Orowan looping or cross-slip (Gladman, 1999), thus making the alloy harder. The schematic diagram in Figure 2.5 represents the situation in which dislocation movement is resisted by, and it finally by-passes, the hard particle.

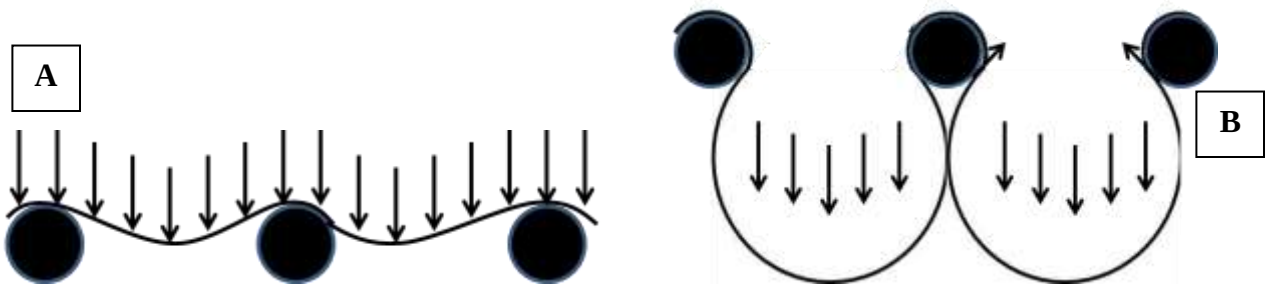

Figure 2.5: Dislocation (A) being resisted and (B) escaping hard particle (Gladman, 1999).

Being a precipitation-hardening phenomenon, the increase in material strength depends on the solubility of solid impurities within the principal matrix. Since the plasticity of materials is influenced by the movements of dislocations, the impedance of such dislocations reduces plasticity, thereby hardening the material. This procedure causes strengthening of the alloys, and maximum strength level is the T6 condition (Myhr et al., 2001). This explains why Al alloys are more ductile in the as-quenched T4 condition than when aged to the T6 condition. Depending on the intended use of the Al alloy, its formability in the T4 condition or the strengthened T6 condition may be advantageous (Engler et al., 2015).

Prabhukhot and Prasad (2015) reported that changes in hardness values, due to significant alterations in grain size and structure, are highly influenced by variations in the temperature and time used for both solution heat treatment and artificial ageing. They also found that ageing without prior solution heat treatment causes a percentage increase in the brittle β phase, thereby lowering hardness values. Additionally, they reported that insufficient soaking time nullifies the supposedly beneficial effect of the entire heat treatment process.

The structure and composition which the precipitation sequence follows has been under ongoing investigation (Smith, 1973; Lynch et al. 1982; Dumolt et al., 1984; Chakrabarti and; Dutta and Allen, 1991; Edwards et al. 1998; Miao and Laughlin, 1999; Murayama and Hono, 1999; Laughlin, 2004). The ageing sequence depends on alloy composition, quenching condition and ageing temperature. The precipitation sequence during the ageing of Al alloys is:

Supersaturated solid solution → Solute Clusters → GP Zones → β" → β' → β (Mg_2Si)

where the GP zones are spherical clusters, the β" phase consists of a monoclinic structure with semi-coherent needle-like $Mg_5Al_2Si_4$ zones, the β' phase contains a hexagonal crystal structure of semi-coherent rod-shaped precipitates of $Mg_{1.8}Si$ and the β phase has the regular over-aged FCC structure of Mg_2Si (Miao and Laughlin, 1999; Blommedal, 2013).

The supersaturated solid solution (SSS) contains high amounts of vacancies which allow solute elements to move through the ternary Al-Mg-Si alloys (Banhart et al. 2012). As the vacancies migrate within the matrix, solute particles diffuse to form clusters (GP zones) when Al alloys are quenched to room temperature after the solution treatment (Liu et al., 2015). The chemical

composition, melting procedure and cooling rate determine the eventual microstructure of an Al alloy (Król et al., 2015; Krupiński et al., 2016). The microstructure of Al alloys, which influences their mechanical behaviour, is significantly influenced by heat treatment (Leo et al., 2016) as well as the morphology, the inter-dendritic distance and the distribution of their secondary phases (Canales et al., 2012; Aguilera Luna et al., 2013; Shokuhfar and Nejadseyfi, 2014; Krupiński et al., 2016).

Precipitation hardening is generally achieved through the transformation of different phases by which coherent precipitates are uniformly dispersed within a softer alloy matrix (Fransson, 2009). Alloying elements within heat treatable Al alloys generally exceed the equilibrium solubility limit for solid solutions at room temperature. The quantity, solubility and diffusion rate of alloying elements influence their rates of dissolution or precipitation of the alloying elements within the Al alloy matrix.

In order for precipitation hardening to be effective, the solute particles which constitute the secondary phase needs to dissolve adequately in the matrix at the elevated solution treatment temperature, while also being less soluble at lower temperatures for artificial ageing (Gladman, 1999). Controlled precipitation, which is achieved at artificial ageing temperatures, helps to derive desirable properties for the Al alloys. For example, at an artificial ageing temperature of 175°C, the undissolved precipitates obstruct dislocation movements within the lattice structure of 6xxx Al alloys. This leads to reduced plasticity, which hardens the alloy.

Although beneficial properties are sought, the post-quench condition of the Al alloy, particularly the storage temperature, influences its response to ageing. Banhart et al. (2012) found that the intermediate storage of 6xxx Al alloys at room temperature, after being quenched from an elevated solution treatment temperature, results in natural ageing. This causes significant changes in the precipitation kinetics of alloying elements within the Al alloy, thereby rendering the artificial ageing process ineffective and resulting in low T6 peak hardness of the Al alloy (Pashley et al. 1967; Yamada et al. 2000; Kleiner et al. 2001; Ravi 2004).

A study by Kovaćs et al. (1972) showed that natural ageing results from Guinier-Preston (GP) zones, in which solute particles form clusters which make the hardening process rather slow. Such an effect arises because clusters formed by natural ageing at room temperature confine the

available vacancies, while disallowing the nucleation of the β" phase (Liu and Banhart, 2016). Within the GP zones, pre-β" and β" Mg_5Si_6 precipitates exhibit a range of shapes between near-spherical and needle-like structures (Chang et al., 2009). The different behaviours of these clusters have been widely studied (Edwards et al. 1998; Murayama and Hono, 1999; Esmaeili et al., 2003; De Geuser et al. 2006; Banhart et al. 2011; Rometsch et al. 2011). The effects of clusters on the subsequent artificial ageing process may be either beneficial (Chang et al., 2009) or detrimental (Gayler and Preston, 1929) to the alloy.

Pre-ageing (Zhen and Kang, 1997), pre-straining (Birol, 2005; Yassar et al., 2005) and a combination of both (Masuda et al., 2010; Yan et al., 2014) are ways by which the strength of Al alloys can be improved through artificial ageing (Liu and Banhart, 2016). Natural ageing has been reported to yield some positive effects (Røyset et al., 2006; Chang et al., 2009). However, other studies have also reported its negative impacts (Murayama and Hono, 1999; Esmaeili et al., 2007; Banhart et al. 2010), during which natural pre-ageing had an altered the mechanism of the artificial ageing process.

The beneficial type of cluster transforms into the β" phase during the artificial ageing process, thereby hardening and strengthening the alloy (Serizawa et al., 2008), while the detrimental one is incapable of acting as a nucleation site for hardening precipitates in the alloy matrix (Torsæter et al., 2011). Although a theoretical sequence of artificial ageing appears linear as the alloy approaches its peak strength, the reality is non-linear as the precipitation processes are affected by the clustering phenomenon (Chang and Banhart, 2011). The addition of Cu to 6xxx Al alloys has been found to reduce the negative effect of natural ageing (Wenner et al., 2012). Pashley et al. (1966) had earlier found that Cu controls the diffusion of solute atoms.

The effects of ageing on automobile parts are an example. Al alloys used for vehicle bodies are artificially aged to neutralize any possible detrimental effect of natural ageing on paint-baking procedures (Ding et al., 2015) at 180°C (Van Huis et al., 2007a; 2007b). This is to ensure that the solute atoms of alloying elements (precipitates) are hindered from clustering (Cao et al., 2013a), as artificial ageing depends on clusters for the nucleation of hardening precipitates (Serizawa et al., 2008). During the paint-bake hardening (artificial ageing) procedure at 180°C which lasts

about half an hour, the high density of $Mg_xSi_yAl_z$ precipitates causes an increase in strength of the Al alloy (Van Huis et al., 2007).

Grain size is influenced by the nucleation of dendrites, and the network of coherent dendrites restricts the smooth flow of liquid metal to inter-dendritic locations (Król et al., 2017). Grain refinement has been shown to improve the mechanical properties of Al alloys (Kumar et al., 2003; Khan et al., 2008). The formation of ultrafine grains (UFGs), by severe plastic deformation (Vorhauer and Pippan, 2004; Korchef et al., 2007; Li et al., 2008), has been reported to improve ductility, toughness, hardness and strength of Al alloys (Xu et al. 2017a).

Temperature and ageing time have an effect on the properties of the resulting Al alloy, causing an increase in strength until its peak T6 condition. Symbols based on β refer to precipitate phases in Mg/Si-containing 6xxx Al alloys, while those of θ refer to Cu-containing 2xxx Al alloys. In Al-Mg-Si alloys, GP zones develop first, followed by the ordered β' and β (Mg_2Si) phases. In Al-Cu-Mg alloys, GP zones develop first, followed by the ordered S' and then the S (Al_2CuMg) phases. Figure 2.6 illustrates the stages in the heat treatment procedure of Al alloys.

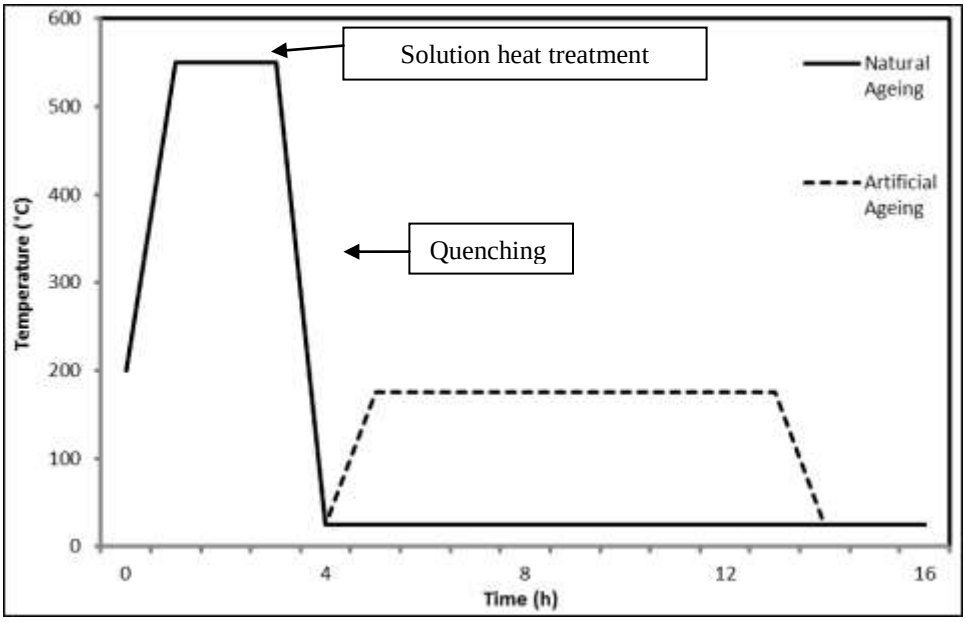

Figure 2.6: Schematic showing the stages of heat treatment of Al alloys (Paterson, 2007).

2.2.3 Solubility and Precipitation

The solubility of its alloying elements does determines the extent to which precipitation may occur in a peak-aged alloy (Gladman, 1999). In the Al-Cu system, 4 wt % of Cu dissolved in Al close to the eutectic temperature resulted in up to 5 vol. % of the θ phase that is formed ($CuAl_2$ precipitate) is formed. Figure 2.7 shows a partial phase diagram of Al-Cu alloys.

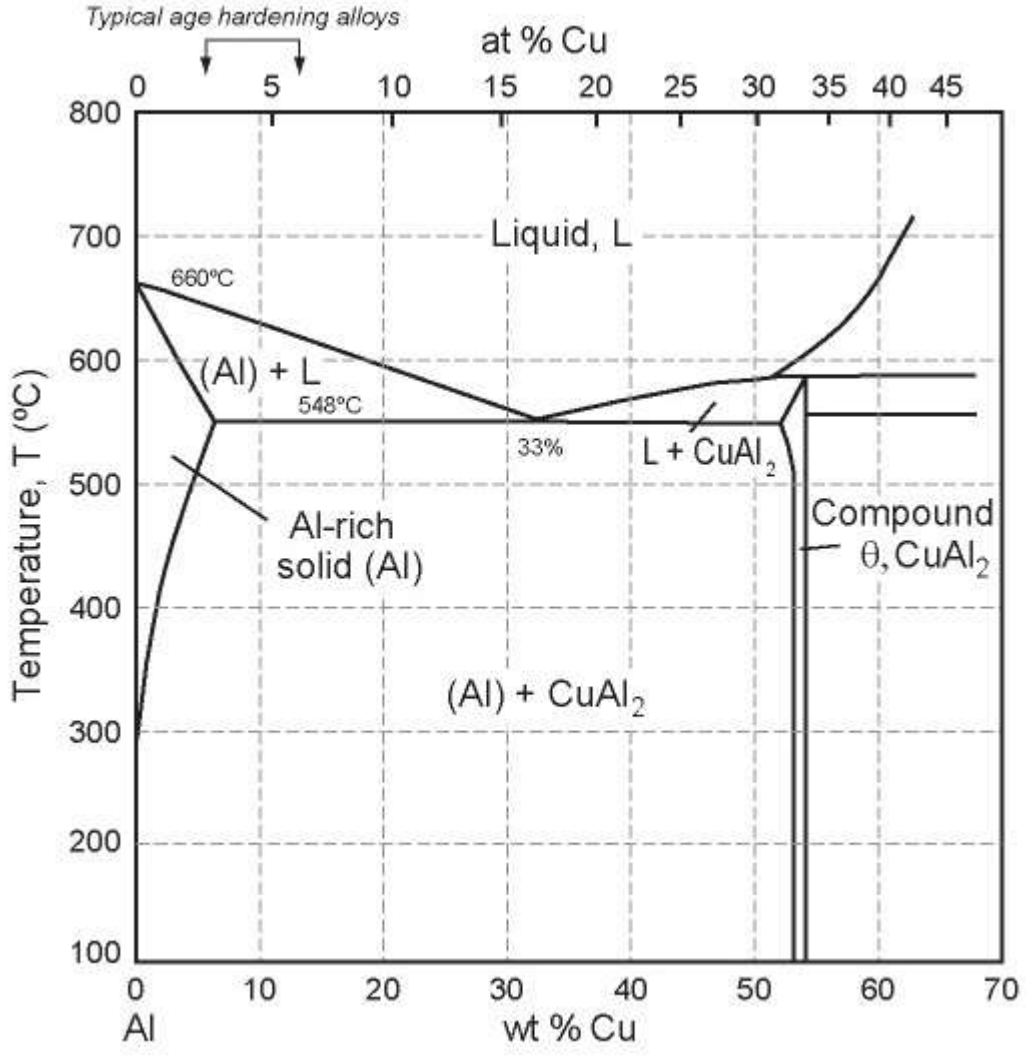

Figure 2.7: Partial phase diagram of 2xxx series wrought Al alloys with 2.5-7% Cu (Granta Material Intelligence, 2017).

In Al-Cu alloys, GP zones develop first, followed by θ", θ' and θ phases. Depending on ageing temperature used relative to the solvus temperature, the intermediate θ" and θ' phases may result

in single-stage or multi-stage hardening of the alloy. The rate of clustering, which depends on the solute diffusion rate, is directly influenced by the concentration of vacancies formed by quenching from the elevated solution treatment temperature. In other words, a lower vacancy concentration results in a lower rate of clustering.

The θ" region is the preferred nucleation site for the θ' phase, the region on which the θ phase preferentially nucleates (Guyot and Cottignies, 1996). When a 2xxx series Al alloy with 4 wt % Cu is solution treated between 500°C and 548°C, the alloy is super-saturated when quenched. This is because the stable θ precipitates are unable to form, due to the fast cooling rate which limits the diffusion of Cu through the Al matrix (Fransson, 2009). Rather, a non-equilibrium diffusion results in clusters of tiny precipitates known as the GP zones. GP1 precedes GP2, then the θ' phase is derived as the precipitates grow to a certain stage. Cu atoms are able to diffuse as ageing takes place, albeit through short distances, to produce the α + θ phase. Natural ageing is aided by the formation of GP zones, while artificial ageing is aided by incoherent precipitation (Miao and Laughlin, 1999). Figure 2.8 shows the phase diagram of Al-4Cu alloy.

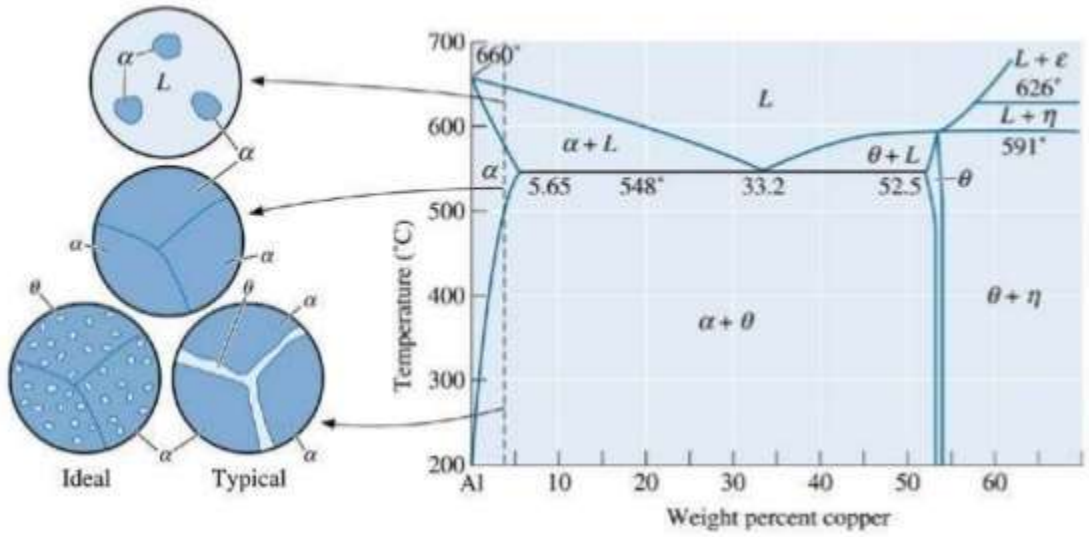

Figure 2.8: Al-4Cu alloy phase diagram (Khaira, 2013).

Hamana et al. (2004) observed a change in composition and lattice parameters of an Al matrix when the equilibrium phase is reached. This is because a supersaturated solid solution gradually becomes stable by ageing. A metastable phase may re-dissolve to grow with the stable phase or

may self-stabilize directly. The degree of particle coherency influences the type of precipitation, as illustrated in Figure 2.9.

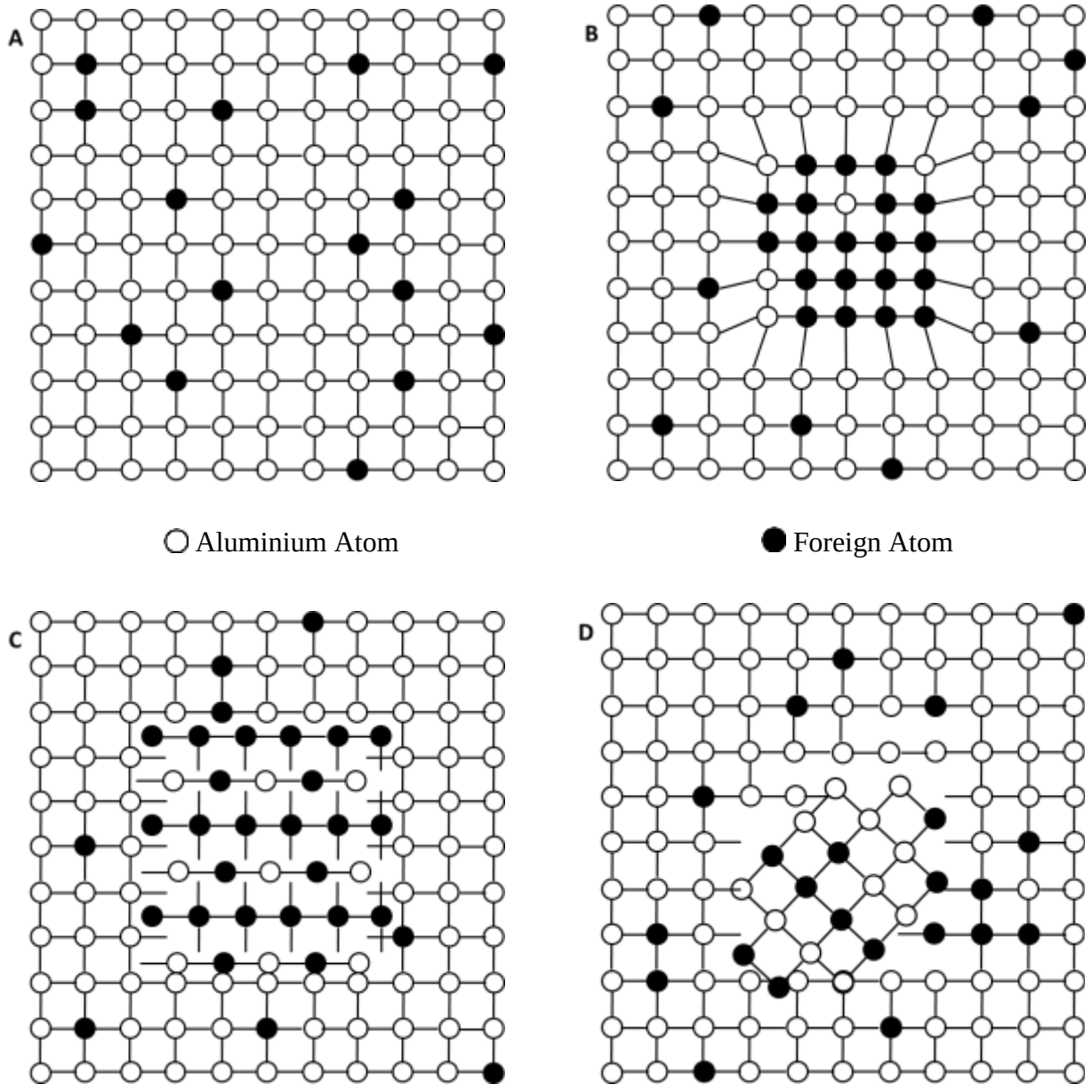

Figure 2.9: Effect of atom coherency on the precipitation of (A) solid solution (B) strained coherent precipitation (C) semi-coherent precipitation and (D) incoherent precipitation

The process of strengthening Al alloys through heat treatment depends on the fine precipitates formed from the supersaturated α matrix (Li et al., 1999; Peng et al., 2017). The α-supersaturated solid solution generally makes a transition through GP zones to a metastable η' phase and

stabilizes into an equilibrium η phase (Berg et al., 2001; Liu et al., 2010; Mazzer et al., 2013). Although precipitates formed at room temperature and at early stages of artificial ageing are suitable GP zones (Chen et al., 2009), the main hardening phase in the Al matrix is the semi-coherent metastable η' as seen in 2.10c (Stiller et al., 1999; Yang et al., 2014).

The super-saturated solution makes a transition into the GP zones, then onto β" phase being an $L1_2$ ordered phase composed of Al_3Mg (Sato et al., 1982), then to a semi-coherent hexagonal intermediate β' phase composed of Al_3Mg_2 and is the main hardening precipitate (Nebti et al., 1995). Finally, β is the equilibrium phase composed of Al_3Mg_2 but with a complex face-centered cubic structure (Bernole et al., 1973). Many studies have confirmed the precipitation sequence for Al-Mg alloys (Dauger et al., 1976; Nozato and Ishihara, 1980; Sato et al., 1982; Osamura and Ogura, 1984; Van et al., 1988). The amount of alloying elements within the alloy is the principal factor that determines its mechanical properties.

When an Al-Mg alloy having up to 18 wt % Mg is artificially aged between 100°C and 250°C, no $L1_2$ ordered phase or GP zone is formed. However, when Mg content is reduced to less than 18 wt %, the β' phase forms first, and then the β phase becomes more visible as the Mg content is almost fully depleted (Žagar and Grum, 2013). From a study on Al-Mg alloys having 8.8 wt % and 9.9 wt % Mg, β' was seen to nucleate on dislocation loops (Embury and Nicholson, 1963; Bouchear et al., 1996). This was, however, found to conflict with Eikum and Thomas (1964) who had earlier found that dislocation loops did not influence the nucleation of β'. This may be debatable, as old microscopes in those years were not as powerful as recent ones.

It has long been established by (Russell and Aaronson (1975) that, due to the minimal interfacial free energy required, the interphase boundary of one precipitate serve as the preferred nucleation site for the next, with subsequent precipitates following the same trend. Although Yukawa et al. (1995) reported that the precipitates in an Al-Mg alloy having 9 wt % Mg were equilibrium β phase, Hamana et al. (2001) suggested that such precipitates were the β' phase. The volume concentration of alloying elements thus makes a difference in precipitation mechanisms.

Itoh et al. (1990) reported that β' nucleation occurred in structural defects such as tetrahedral-shaped vacancies, and precipitation at the interface of β' and β phases occurred after five years of natural ageing (Nebti et al. 1995). Although β' and β phases were thought by Nozato and Ishihara

(1980) to precipitate independently at the same time, while β' transformed into the β phase in as high as 12.5 wt % Mg, particles in the β' phase were shown to be needle-like in structure and stretched in more than one direction (Hamana et al., 2001). The precipitation of GP-zones causes 6xxx series Al alloys to age naturally (Murayama and Hono, 1999; Esmaeili et al., 2003; Wang et al., 2003; Birol and Karlik, 2006; Pogatscher et al., 2011; Banhart et al., 2012; Cao et al., 2013b; Aruga et al., 2014). Naga Krishna et al. (2010) showed that in peak aged alloys, being T6 in this case, precipitates pin the dislocations and suppress dynamic recovery. Figure 2.10 shows a schematic section of an Al-Mg-Si ternary system.

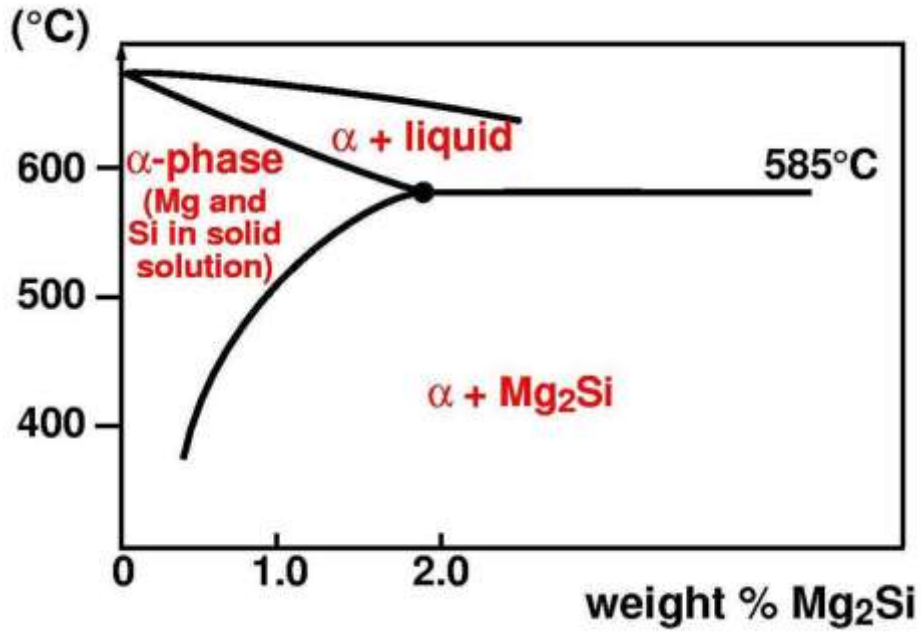

Figure 2.10: Schematic section of an Al-Mg-Si ternary system (Ostermann, 1995).

The strength and hardness of 6xxx series Al alloys strongly depend on the duration of artificial ageing, as well as the Mg_2Si phase which precipitates on dispersoids of Al(MnFeCr)Si and at grain boundaries when the extruded alloy is being slowly cooled (Lohne and Dons, 1983). Medium to high strength 6xxx series Al alloys with a significant amount of Mg and Si have high quench sensitivity, which is the loss of its beneficial properties due to quench rate (Milkereit et al., 2010; Strobel et al., 2011) as well as the density of heterogeneous sites (Strobel et al. 2016).

The process of precipitation hardening is significantly influenced by temperature and time. When heat treated and artificially aged, AA6082 matrix goes through a number of stages. The Al solid

solution matrix is supersaturated with regions rich in Mg and Si. The atoms of Mg dissolve and form a GP1 zone. The GP2 zone, containing homogeneously distributed needle-like particles of the β" phase, is then formed as ageing approaches the peak-aged T6 condition (Fransson, 2009). The precipitation of the β' rod then evolves into a stable β phase, which is mostly Mg_2Si.

The hardness and strength of AA6082 are higher when GP1 and GP2 zones are more finely dispersed within the matrix, because the mechanisms by which the Mg_2Si nucleates and grows ultimately influences the eventual properties of the alloy. Fransson (2009) discussed that its microstructure mostly consists of dendrites in the semi-solid state, but the eutectic phase is significantly reduced as the α-Al phase becomes spheroidized. An over-ageing phenomenon occurs in AA6082 when the stable Mg_2Si precipitates become coarse. Although ageing time is a major factor, temperature change is also very crucial. For instance, the orientation of fibres within an alloy, relative to the direction of the applied notch, may cause an increase in hardness when temperature is increased even while the ageing time is kept constant.

In dilute alloys, the dynamic interaction between dislocations and the interstitial solid solutes results in dynamic strain ageing (DSA) (Cui et al., 2011; Ekaputra et al., 2016). Dislocations in a solid solution generally move in a discontinuous manner. The motion of these dislocations may be inhibited for a while once they are obstructed by atoms. When interstitial atoms diffuse to impede these dislocations, sufficient energy is generated to either knock down a soft particle by shearing, or otherwise bypass a hard particle, as seen in Figure 2.5. Afterwards, the dislocation proceeds to another particle where the same process occurs. Supersaturation of Al alloys by solid solute particles is the principal cause of DSA (Kolar et al., 2012). When DSA proliferates, the discontinuous yielding phenomenon results in a microscopic mechanism called the Portevin Le-Chatelier (PLC) effect (Ekaputra et al., 2016).

DSA and PLC may sometimes occur simultaneously (Jiang et al., 2007). A combination of these may yield an undesirable results (Ozturk et al., 2011), as DSA is generally known to reduce the strain-hardening capacity of alloys (Zhong et al., 2017). When the strain rate sensitivity (SRS) of flow stress required for stretch formability is below the minimum threshold required, PLC becomes almost inevitable as DSA is dominant within the alloy (Jiang et al., 2007). Heat

treatment is then required to alleviate such stresses. The tensile strength of Al alloys, relating to temperature and ageing time, is given in figure 2.11:

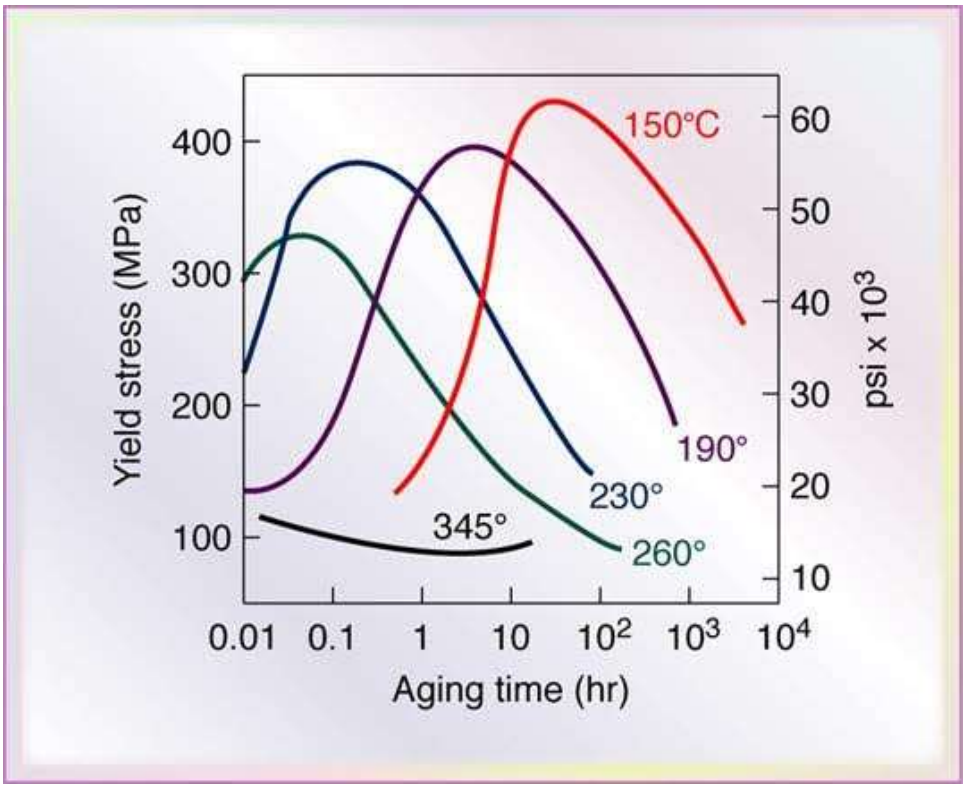

Figure 2.11: Tensile strength of Al alloy based on aging time and temperature (Paterson, 2007a)

The orientation of grains influences the occurrence of slip bands, as confirmed in a model on the de-cohesion mechanism of slip bands of Al-Li alloys (Roven, 1992). Kramer et al. (2005) found that, at room temperature, dislocations occur mostly on slip planes but propagate through cross slip. Also, as opposed to deformation at low temperature, coarse voids and cracks are formed around particles at room temperature. In a study on the tensile behaviour of peak aged AA6082, Xu et al. (2017) found that higher stress levels were experienced at -196°C (77 K) than at 22°C (295 K) which is comparable with room temperature. This is shown in Figure 2.12.

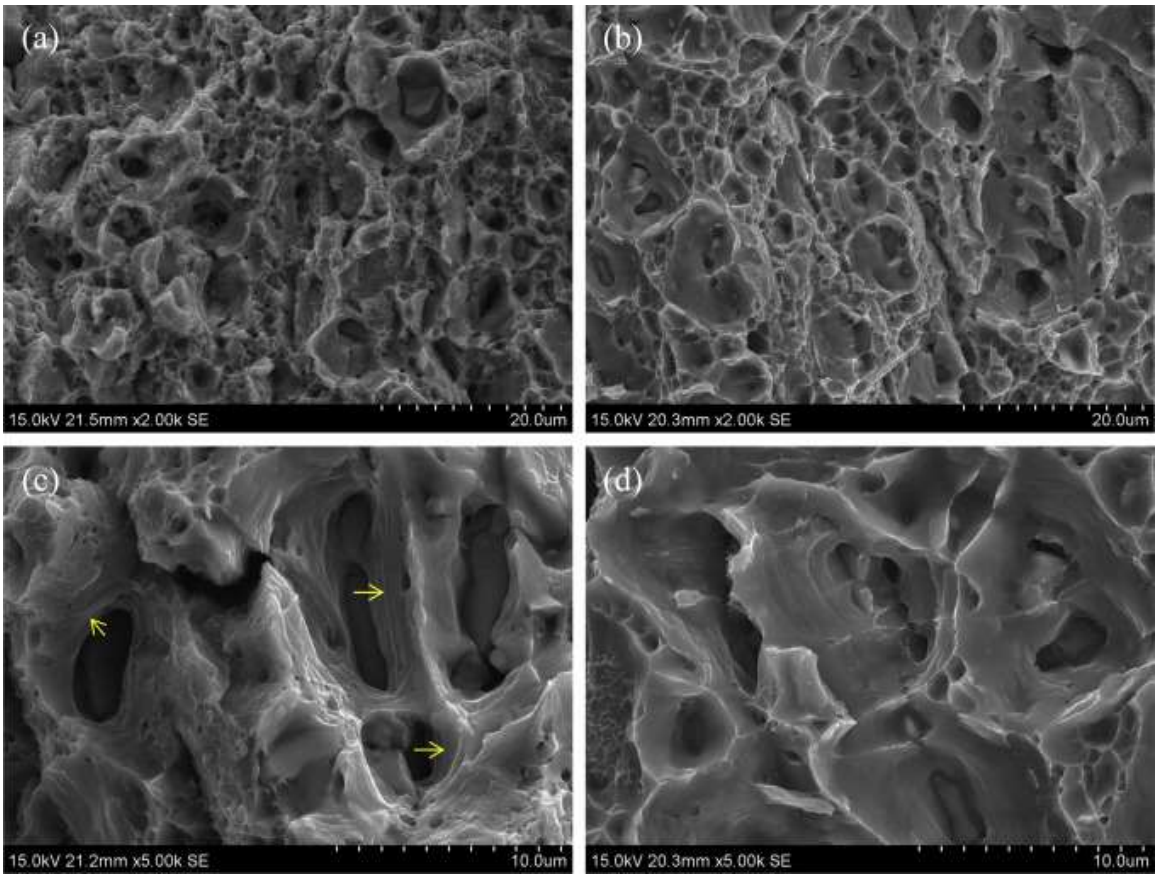

Figure 2.12: SEM images (SE mode) showing the micrographic phenomena of tensile fracture in AA6082 at (a) and (c) –196°C and (b) and (d) 22°C (Xu et al., 2017)

Xu et al. (2017b) discussed that a dislocation glide spreads in three dimensions throughout the volume of the AA6082 specimen as the higher stress level at –196°C resulted in high lattice friction known as Peierls stress. There was some difficulty in the movement of dislocations which were densely packed at 22°C (Xu et al., 2017b), as the arrows in Figure 2.12c show that the grain boundaries delaminated along the tensile stress direction. A similar phenomenon has been reported by Venkateswara Rao et al. (1988) to occur along the grain boundaries of AA2090. Figure 2.13 shows tensile properties in relation to hardness measurements for different Al alloys.

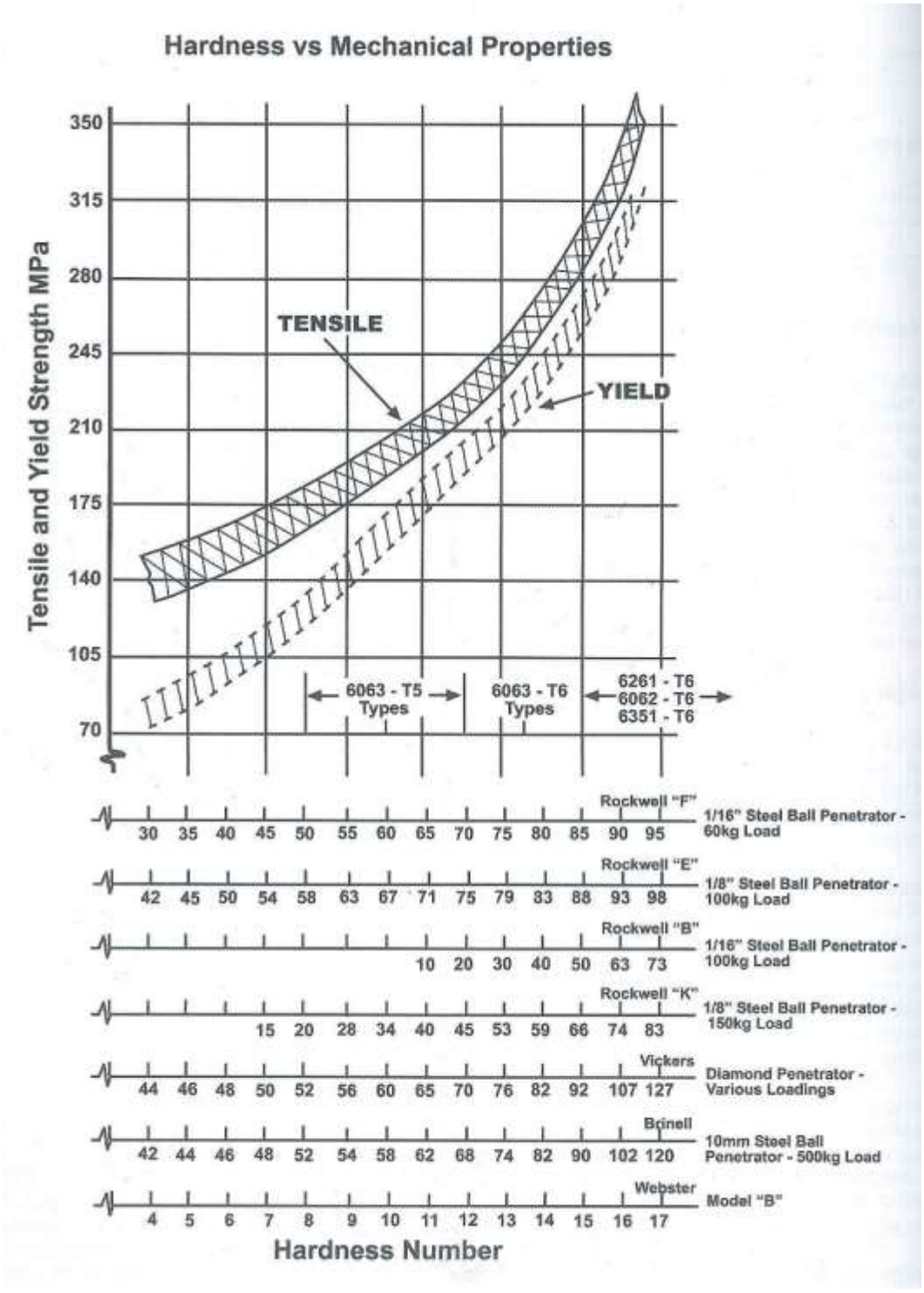

Figure 2.13: Relationship between hardness numbers from standard tests and the tensile and yield strengths of particular extrusion alloys (Paterson, 2007).

2.3 Wear Behaviour

Wear is inversely related to the ductility of a material. A study done by Vlok et al. (2007) on AA5083, AA5182 and AA6061, to be used in the manufacture of tipper trailers, showed that soft materials were ploughed away and showed material loss due to high ductility. Harder samples would resist wear for longer, but can experience brittle fracture which could also lead to material loss. Medium strength materials can strain harden due to plastic deformation, delaying material failure and prolonging life. However, wear resistance should not be the only factor by which materials for tipper trucks are chosen (Vlok et al., 2007).

Bist et al. (2016) discussed the potential suitability of structural materials in military, aerospace and other forms of transport where Al matrix composites are reinforced with particles. There has been ongoing research to continuously develop materials to improve strength, as well as wear and corrosion resistance (Song, 2009; Kumar and Rajadurai, 2016). The strength to mass advantage of lightweight materials can be further improved upon with the addition of reinforcements (Lloyd, 1994; Gupta and Sharon, 2010).

Al matrix composites (AMCs) are widely useful due to combined properties such as damping capacity, thermal expansion, wear and creep resistance, specific strength and stiffness (Han et al., 2006; Yadav and Bauri, 2011). These advantages are important in the automobile and aircraft manufacturing industries (Clyne and Withers, 1995; Li et al., 2009). Due to poor tribological performance of Al alloys, efforts have been made to develop aluminium matrix composites with improved wear resistance (Basavarajappa et al., 2007a).

2.3.1 Reinforcements for wear resistance

Metal matrix composites reinforced with ceramic particles exhibit higher wear resistance than unreinforced alloys (Alpas and Zhang, 1994; Satyanarayana et al., 2002; Gul and Acilar, 2004). The mechanical properties of Al alloys are enhanced by the ductile Al matrix reinforced with borides, carbides, nitrides and oxides which are hard and brittle (Prabhu et al., 2006). Reinforcing an Al matrix with SiC particles gives excellent tribological properties against abrasive wear (Sahin, 2007).

Asgari et al. (2017) discussed how parameters like design, composition and fabrication of engineering materials have been varied to improve the wear resistance. Variances in these factors resulted in improved service life, significantly increasing productivity (Subrahmanyam et al., 1986; Mateen et al., 2011; Mahmud et al., 2014; Bolelli et al., 2015). Also, to increase tribo-corrosion resistance, the mechanical properties of Al alloys have been improved by reinforcing them with SiC whiskers and particles (Kumar et al. 2012).

When ceramic particles are dispersed within an Al alloy, the resulting material is an AMC with superior wear resistance (Palanivel et al., 2016). AMCs have replaced Al alloys in nuclear and transport applications; particularly in the structural parts of automobiles and aircrafts (Mazahery and Shabani, 2012; Vijayarangan et al., 2013). The use of TiB_2 ceramic particles in AMCs results in highly enhanced properties such as increased melting point, elastic modulus, overall thermodynamic stability, hardness and wear resistance (Wang et al., 2014; Gao et al., 2016).

Some common procedures by which TiB_2-based AMCs are produced include powder metallurgy (Suresh et al., 2014b), squeeze casting (Chi et al., 2015), stir and *in situ* casting (Suresh et al., 2014a). However, these fabrication techniques result can cause segregation (Yadav and Bauri, 2015), agglomeration (Chen et al., 2015a), porosity (Suresh et al., 2014b) and slag inclusions (Xue et al., 2011). These fabrication techniques can also cause the TiB_2-based AMCs to become inhomogeneous (Palanivel et al., 2016). Even when K_2TiF_6 and KBF_4 reacted with molten Al to derive more homogeneous TiB_2-based AMCs, the resulting matrix had a TiB_2 content above 10 vol % (Pramod et al., 2015). Having produced higher concentrations of TiB_2 in AMCs using stir casting, Ramesh et al. (2011) found that TiB_2 particles settled at the bottom of the cast due to the weight and poor wettability of the TiB_2 particles.

There are also issues with the effectiveness of the AMCs themselves. Although TiB_2 reinforced AMCs have improved wear resistance, they initiate excessive wear of the counterface which causes a wide clearance between parts and results in early failure (Chen et al., 2015b; Pramod et al., 2015). To manage this problem, additives such as BN, MoS_2 and graphite serve as lubricants for the TiB_2-based AMCs and further improve the wear resistance of the AMC while causing less degradation on the counterface material (Suresh et al., 2014b; Chi et al., 2015). These,

however, may result in a rather expensive procedure to effectively and efficiently tackle wear problems. More efficient materials and procedures should be investigated.

While manufacturing AA2124 matrix material, Karamis et al. (2012) showed that both particle size and volume fraction of reinforcement inclusions substantially influenced the wear rate of the resulting composites. In their study, B_4C, SiC and Al_2O_3 were used as particle reinforcements with varying volume fractions. B_4C yielded the optimal wear resistance at only 10 vol. %, while SiC showed the optimal wear resistance at 30 vol. % with an average particle size of 20 µm size (Karamış et al., 2012). Some wear inhibitors clearly require less volume concentration than others, for optimal effectiveness. The cost-benefit analysis therefore becomes the important factor for determining which material to deploy in such a case.

Matrices having SiC exhibit some known advantages. Whether in the form of particles, whiskers or fibers, a combination of SiC and Al_2O_3 reduced wear by either a load-supporting mechanism or the restriction of surface deformation (Basavarajappa et al., 2007b; Ureña et al., 2009). The coefficient of friction is higher in Al-SiC composites than in Al alloys, as an increase in the wear rate of Al alloys is inhibited in the presence of about 10 vol. % of SiC (Venkataraman and Sundararajan, 1996). Increasing the volume concentration of SiC keeps wear resistance effective at room temperature, but makes no difference above room temperature (Wang and Song, 2010).

2.3.2 Cermets as reinforcements

Coefficient of friction defines the relationship between the frictional force between two bodies and the normal reaction of their surfaces to that force. When both bodies are motionless, the coefficient of static friction exists between the bodies. However, when one or both bodies move, the coefficient of kinetic friction exists between the bodies. The progressive loss of material, due to the relative motion of their surfaces, is defined as wear. The dimensions of components reduce due to the material loss, thus creating increased clearance between the moving surfaces. This may result in catastrophic failure of the component, due to fatigue.

Wear occurs by one or a combination of mechanisms. These include abrasion, adhesion, oxidation and fatigue. Abrasion and adhesion are the two severe types of wear. Once abrasion is initiated between two bodies, certain factors influence the severity of wear. Lekatou et al. (2015)

summarized that the major factors by which wear occurs are adhesive wear, delamination wear and mechanically mixed layer by which oxidation products form and plastic deformation occurs. The debris undergoes a continuous cycle of fragmentation and re-consolidation, ultimately resulting in a protective layer hard enough to avert further wear. Various phenomena of mild wear are common in erosive wear situations, while wear transition states are driven by delamination and adhesive wear mechanisms, causing the most severe form of wear conditions (Al-Qutub et al., 2006).

In most cases, cermets can also serve as wear inhibitors. Cermets are MMCs consisting of ceramic materials with a metallic binder (Ettmayer et al., 1995; Ahn and Kang, 2001; Zhao et al., 2014; Acharya et al., 2016). They combine the hardness and wear resistance of ceramics with the ductility, thermal stability and toughness of metals (Chen et al., 2017). Also, the oxidation resistance and friction coefficient of cermets are generally superior to those of metals (Zheng et al., 2005). The type and composition of cermets determine their coefficient of friction, as well as wear resistance (Pirso et al., 2006). For example, Liu et al., (2014) found that the reciprocating sliding wear resistance of WC-10Ni_3Al paired with Ti-6Al-4V is superior to that of WC–8Co.

Tungsten carbide (WC) was discovered in 1923 and has been used in cemented form for metal cutting and as drill bits for rocks (Spriggs, 1995). WC coatings have been extensively used to reduce manufacturing costs of materials for aerospace applications (Geng et al., 2015). They are also used in engineering applications which require high levels of toughness and resistance to surface wear, as WC-based materials have very strong and hard surfaces (Houdková et al., 2011). The automotive and space shuttle industries use WC powder to coat the surfaces of the substrates, due to its high resistance to abrasion (Schwartzkopf and Keiffer, 1953).

For the WC-Co matrix, certain additives can produce better results. For example, the ability of Cr_3C_2 to effectively inhibit grain growth makes cermets more efficient as their hardnesses increase with smaller grain size (Zheng et al., 2005; Lei et al., 2007; Huang et al., 2008; Kellner et al., 2009). Ti(C,N) cermets are the preferred option for sliding bearings because they possess higher wear resistance than metals and are less expensive than cemented carbides (Zheng et al., 2003; Zhou et al., 2009; Yi et al., 2013), of which the WC-Co matrix is an example. Also, an additive such as TaC increases the fracture toughness of a WC-Co matrix (Upadhyaya, 2001;

Mahmoodan et al., 2009), while also serving as an effective grain growth inhibitor (Pirso et al., 2006). In the presence of the Co binder, addition of less than 1 wt % TaC improved wear resistance of the WC-Co coating matrix (van der Merwe and Sacks, 2013).

Due to the strong interfacial bond combined with improved hardness and ductility, Co is mostly used as a binder for WC (Pan et al., 2011). Wear in industry has been substantially managed by thermally sprayed coatings of hard materials which are resistant to erosion and abrasion, as well as corrosion and high temperature environments (Liao et al., 2000). Although WC-Co coatings have been found reliable when applied using thermal spray procedures, their porosity and poor bonding with the substrate have been a concern (Jin et al., 2007). Therefore, to ensure a good bond with an AA6082 substrate, an Al-based binder may be preferred to Co, to mix with WC.

2.3.3 Particle Sizes and Binder Content

The addition of micro-particles to Al alloys is another technique used to obtain fine-grained structures which improve their mechanical properties (Hamana et al., 2004; Venkatachalam et al., 2010). The effectiveness of a reinforcement material depends on its particle size as well as the volume concentration of the binder. Carbides of V and Cr have proven to be effective as grain growth inhibitors for the WC-Co system, lowering the coefficient of friction as resistance to micro-abrasion occurs, thus improving its wear resistance (Bonny et al., 2009; Espinosa et al., 2011; Poetschke et al., 2012). Shatov et al. (2009) found that TiC increases both hardness and strength of WC by changing its shape into flatter orientations of triangular prisms, thereby reducing its shape equiaxiality. Such flatter shapes improve wear resistance (Shatov et al., 2008), by ensuring less detrimental inter-crystalline interaction and fracture along carbide-carbide interfaces (Shatov et al. (2009).

Hardness, strength and toughness of WC are not necessarily improved by the same factors that increase its wear resistance (Sevim and Eryurek, 2006; Konyashin et al., 2010, 2015). Within a WC-Co matrix, added ZrC was seen on the grain boundaries of WC to refine and inhibit grain growth (Weidow and Andrén, 2011). The addition of ZrO_2 results in the grain refinement of WC, by reducing its triangular prism shape (Detournay et al., 2008; Hussainova et al., 2011). Overall, fracture toughness was improved without compromising the hardness of the matrix (Kimmari et al., 2009). By inhibiting crack propagation of WC, the addition of ZrO_2 increases wear resistance

as decreased brittleness reduced the likelihood of carbide fracture and removal (Hussainova et al., 2011).

Nano-structured carbides have been found useful in metallurgical applications. Some advantages of nano-WC are increased fracture toughness, hardness, compressive strength, as well as oxidation and corrosion resistance (Koc and Kodambaka, 2000). WC nano-particles have a larger surface area than the micron-sized particles. Hong et al. (2014) also found improved hardness, wear resistance and toughness with nano-structured WC-Co coatings, compared to micro-sized particles of the same matrix. Particle size thus plays a crucial role in WC properties.

Additionally, binder content also influences both wear and corrosion resistance of carbides. Although cemented carbides offer a combination of hardness and toughness, the extent to which a WC-Co matrix resists wear during its service life remains a function of its grain size, bulk hardness and WC/binder ratio (Bonny et al., 2010). For example, low volume concentrations of the binder material with sub-micron WC has been reported to yield very high wear resistance (Larsen-Basse, 1985; Jia and Fischer, 1997; Engqvist et al., 2000b; Pirso et al., 2006; Saito et al., 2006, Bonny et al., 2009).

In determining the optimal WC level for friction and wear resistance, Fernández et al. (2015) found that wear rates decreased significantly with only 30 vol. % WC in a coating, despite the inhomogeneous distribution of the WC content. Jia and Fischer (1997) also showed that, with equal amounts of Co binder, nanostructured WC exhibited only 60% of the wear rate of conventional micron-sized WC. However, they concluded that reducing Co binder volume concentration while increasing WC grain size to the micron scale was even more effective for the improvement of wear resistance. This shows that binder content and particle size can influence coating performance separately or in combination.

2.4 Thermal Spray Process

Thermal spray coatings had been used effectively since the 1980s. During thermal spraying procedures, both kinetic and thermal energy are used to deposit powder feedstock on a substrate (Asgari et al., 2017). Most studies of thermal spray coatings have examined wear resistance and microstructure of WC-Co coatings (Sampath, 1992; Stewart et al., 2000; Stokes and Looney,

2001; Wayne and Yang et al., 2003; Picas et al., 2009), WC-CoCr coatings (Karimi et al., 1993; Murthy and Venkataraman, 2006; Stack and Abd El-Badia, 2008; Picas et al., 2011; Thakur et al., 2011; Ghabchi et al., 2014; Wesmann and Espallargas, 2016) and WC-Ni matrix coatings (Guilemany et al., 1995; Sobolev et al., 1996a, 1996b). These provide a variety of choices from which to select coatings to suit specific applications.

In order to reduce manufacturing cost and extend service life of components, coatings deposited by thermal spray have been found useful in environments where erosion-abrasion take place. Air plasma spray, high velocity air fuel (HVAF), high velocity oxy-fuel (HVOF) and low pressure plasma spray (LPPS) are common thermal spray methods by which WC-Co coatings have been applied to surfaces (Chen et al., 2005; Geng et al., 2016a). These techniques produce coatings that function at operating temperatures around 600°C (Rhys-Jones, 1990; Chen et al., 2010). The performance of coatings in high temperature operations has been investigated based on thermal processes such as air plasma spray (Zhao et al., 2006; Chen et al., 2010; Balamurugan et al., 2012) and HVOF (Yang et al., 2006; Yin et al., 2010). Oxidation at such an elevated temperature decreases the wear resistance of such coatings (Geng et al., 2015, 2016a).

The effect of microstructure on the tribological performance of WC-Co coatings has been widely studied (Naerheim et al., 1995; Lovelock, 1998; Qiao et al., 2001; Di Girolamo et al., 2009). Microstructures of thermally sprayed coatings exhibit different tribological behaviours (Geng et al., 2016b). At the initial stage of edge wear, using fine SiC abrasive, submicrometric WC-Co shows homogeneous plowing, while coarse WC-Co shows inhomogeneous pull-out of grains (Krakhmalev et al., 2007). Coarse SiC abrasive causes flaking also at the beginning. At the final stages, however, plowing is evident, regardless of microstructure of both SiC and WC-Co.

2.4.1 HVOF Spray Coatings

Generally, thermally sprayed carbide coatings are useful in protecting surfaces against high temperature wear and corrosion (Pawlowski, 2008; Matthews and James, 2010; Vernhes et al., 2013; Szymański et al., 2015). The flame temperature for HVOF ranges between 2300°C and 3000°C, with spray velocity between 550 and 850 ms^{-1} (Stokes and Looney, 2001). HVOF produces high density coatings and excellent bond strength, with minimal oxidation (Kamali and Binesh, 2009; Matthews and James, 2010; Guo et al., 2014). In the HVOF spray technique,

oxygen mixed with fuel in a combustion chamber is ignited to generate a high temperature flame which partially or fully melts the feedstock and projects it towards the substrate (Yang et al., 2003; Morks et al., 2005; Liu et al., 2008; Picas et al., 2009; Wesmann and Espallargas, 2016).

The HVOF thermal spray technique has been optimized and used for WC-based coatings due to desirable characteristics such as low porosity, hardness (Stewart et al., 1999) and wear resistance due to the low flame temperature and high particle velocity (Morks et al., 2006; Geng et al., 2015). HVOF spraying of composite coatings is generally proven to produce high strength as well as wear and corrosion resistant coatings (Wood, 2010). High spray velocities result in minimal evolution of thermal energy, as the travel time of the molten or semi-molten feedstock towards the target surface is reduced (Asgari et al., 2017). Therefore, minimal oxidation occurs on in-flight particles and the coating density is improved. In the case of WC-based particles, the heat is mostly too low to cause degradation of its particles and result in brittle hemi-carbides (Wayne and Sampath, 1992; Stewart et al., 2000). However, the work of Dent et al. (2002) has shown results to the contrary.

The preheating requirement of the HVOF method causes thermal dissociation of WC, making it less effective for wear resistance (Kear et al., 2001; Jin et al., 2007). For this reason, post improvement techniques such as densification, phase change of coating, surface-coating interface modification and deep cryogenic treatment (DCT) have recently been recommended by Wang et al. (2016). When compared with HVOF, the HVAF method is a closely related alternative which achieves superior WC-Co coatings using much lower flame temperature and operational cost, while being more efficient with oxygen and heat (Jacobs et al., 1999).

The HVOF method can be effectively used to spray nanostructured WC-Co powders that bond well with the substrate (Hong et al., 2014). This is due to high spray velocities and the relatively lower spray temperature, rather than the volume concentration of the WC-based powder (Souza & Neville 2007; Wu et al. 2012). Besides spray distance and angle, the flow of oxygen, kerosene and overall fuel chemistry influence the microstructure and wear behaviour of the coated surface (He and Schoenung, 2002; Qiao et al., 2003; Marple and Lima, 2005; Houdková et al., 2010).

Nieminen et al. (1997) found that rolling contact fatigue (RCF) failure is mostly influenced by high surface roughness for coatings deposited using both HVOF and plasma spray. RCF reduces

the service life of uncoated materials, thus rendering them unreliable (Nicholson and Davis, 2012; Beghini and Santus, 2013; Upadhyay et al., 2013). The amount of stress in contact with surfaces, shear stress distribution, microstructure and bond strength have also been found to influence RCF damage and failure in plasma sprayed CrC–NiCr coatings (Zhang et al., 2008, 2011). However, plasma spraying has been reported to prevent failure due to wear and RCF in industries where rolling and sliding operations are common (Hashimoto et al., 2011; Qin et al., 2014; Reis et al., 2014; Xu et al., 2014; Zeng et al., 2014).

2.4.2 Plasma Spray Coatings

The plasma spray procedure is used for coating substrates with material feedstock, especially in powder form. During the process, metallic powder particles are injected into a hot plasma jet in which they are melted, and thereafter projected towards a target substrate (Kumar et al., 2006). On hitting the substrate, the molten feedstock flattens out into deposits and solidifies to form coatings. Depending on the thickness and target application of such coatings, the coatings may be separated from the substrate to stand alone as whole parts.

The plasma spray procedure achieves low particle velocity and high deposition rates, using high spraying temperatures (Zhang et al., 2015). Low pressure plasma spray is found to achieve high particle velocity and low particle oxidation, also using high temperature, as the substrate-coating adhesion is significantly strengthened by transferred-arc surface cleaning (Geng et al., 2016b). Plasma spraying technology improves surface properties of components in operation, preventing the occurrence of surface wear in industry (Liu et al., 2010; Balamurugan et al., 2012; Song et al., 2012; An et al., 2014; Di Girolamo et al., 2014).

2.5 Corrosion

Metals naturally exist alongside minerals, within ores in which they are chemically stable as oxides, silicates or sulphides. For example, magnetite (Fe_3O_4) is an oxide containing 72.4% Fe, while hematite and goethite contain 69.9% and 62.9% Fe respectively. The ore of Al is bauxite. After a metal has been processed from its ore, it may be susceptible to corrosion. This is because corrosion is a process by which the metal is converted to its thermodynamically stable state, due to exposure to particular types of environment where chemical or electrochemical reactions can occur. This makes corrosion a destructive process, as its physical properties are compromised.

Some of the degradation mechanisms include material loss and even cracking. Therefore, corrosion control and mitigation are paramount in industry.

Hihara and Latanision (1992) established that, when reinforced with SiC and TiB_2, the corrosion rate of AA6061 is reduced by at least a factor of 30. The same reinforcements of SiC and TiB_2 also improved wear resistance. However, not all materials or coatings that have excellent wear resistance demonstrate optimal corrosion resistance in aggressive media (Engqvist et al., 2000a). The chemical composition of a material generally influences its corrosion resistance. Similar to SiC and TiB_2, WC with a Co binder demonstrate improved corrosion resistance. Many studies have been carried out to show the effect of WC grain size, as well as binder content (Hochstrasser-Kurz et al., 2007; Kellner et al., 2009).

Tomlinson and Linzell (1988) found that smaller grain size of WC reduced the passive current densities in acidic solutions. However, Human and Exner (1996) showed that the grain size of WC had no effect on its corrosion resistance. Rather, the Co binder plays a major role in the corrosion behaviour of the WC-Co matrix (Hochstrasser-Kurz et al., 2007). In an alkaline solution, W dissolves readily as the Co binder passivates in a stable manner (Ghandehari, 1980).

The dissolution of W and C during the sintering process was found to change the composition of the Co binder (Exner, 1979). This results in improved corrosion resistance (Human et al., 1998; Sutthiruangwong and Mori, 2003). Certain additives to the WC-Co matrix have also been found to influence its corrosion resistance. For example, adding carbides of Ti and Ta, in small amounts, improved the corrosion resistance of the sintered WC-Co samples (Mori et al., 2001; Sutthiruangwong et al., 2005; Kellner et al., 2009). Also, Cr_3C_2 and Ni, added into the binder phase, improved the corrosion resistance of the WC-Co matrix (Mori et al., 2001; Bozzini et al., 2002; Kellner et al., 2009).

Corrosion behaviour of thermally sprayed WC-Co coatings are not easily predictable due to their complex microstructures (Myalska et al., 2017). This complexity is as a result of inclusions, pores, splat interfaces, inhomogeneous distribution of carbides within the matrix and boundaries between layers and phases (Verdon et al., 1998; Stewart et al., 2000; Lekatou et al., 2015). The corrosion resistance of HVOF-sprayed WC-Co matrix coatings have been widely investigated (Guilemany et al., 2006; Lekatou et al., 2008; Bolelli et al., 2012). At the initial stage of WC-Co

corrosion in an acidic medium, the Co binder dissolves. Subsequently, the oxidized W in the Co binder extends to the surface of the carbide particles and forms a pseudo-passive WO_3 layer (Lekatou et al., 2015). In a 3.5% NaCl solution, WC-Co coatings passivate as the outward diffusion of Co is limited to the interface, forming hydrated oxide films (Lekatou et al., 2008).

The wear and corrosion performance of composite materials depend on the binder composition and the environment to which it is exposed. The addition of VC has no effect on the corrosion resistance of WC (Human et al., 1998). However, replacing some WC to accommodate about 10 wt % VC significantly protects the entire WC matrix in a sulphuric acid environment (Konadu et al., 2010). Adding carbides of Cr to the WC-Co matrix generally improves its corrosion resistance (Perry et al., 2001, 2002).

Although Ni based binders such as Ni-Cr and Ni-Cr-Mo may cause WC grains to corrode preferentially, they generally improve the corrosion resistance of the binder matrix itself (Scholl et al., 1992; Bozzini et al., 2002). As consistent with the study done by Gant et al. (2013), WC with a Co-Ni binder matrix showed very high resistance to surface degradation in both air and acidic media, although pure Ni binder did not improve the wear resistance in an acidic environment (Gant et al., 2013).

Monticelli et al. (2004) found that Co binder concentration and overall coating thickness influence corrosion resistance. The corrosion resistance of an HVOF-sprayed WC-Co coating on a carbon steel substrate improved when the Co binder was increased from 12% to 17% Co. Also, thicker coating layers improved pitting corrosion resistance (Monticelli et al., 2004). Generally, the corrosion resistance of WC hard metals have been investigated by Human and Exner (1996). Also, the corrosion behaviour and Al-based materials are being studied (Donatus et al. (2017).

Due to its excellent corrosion resistance, Al films have been widely applied as coatings (Mraied et al., 2016), especially as an alternative to Cd which is toxic (Bielawski, 2004). Some substrates on which Al films have been coated include steel (Caporali et al., 2008; Cheng and Wang, 2009), Mg alloys (Wu et al., 2008; Pardo et al., 2009) and NdFeB magnets (Mao et al., 2011). Various methods by which Al coatings can be deposited include hot-dipping (Cheng and Wang, 2009), electroplating (Caporali et al., 2008) as well as physical and chemical vapour deposition (Yun and Rhee, 1998; Wu et al., 2008).

In a solution with pH ranging from 4 to 9, the substrate is protected by an amorphous passive film formed on the surface of Al (Creus et al., 1999). However, the same protective film has been found to be susceptible to pitting and crevice corrosion, due to halide ions in saline environments (Mraied et al., 2016). The weak mechanical and wear properties of a passive Al film makes it unreliable for industrial applications (Vargel, 2004). However, alloying increases the strength of Al-based materials (Lepper et al., 1997).

As long as the alloying elements remain in solid solution, the corrosion resistance is also improved by an increase in pitting potential (Sanchette et al., 2009; Kim et al., 2010). The addition of transition metals such as Mn and W also increases the resistance of Al to pitting corrosion in chloride solutions (Szklarska-Smialowska, 1999). This is achieved as over-potential for the anodic dissolution is increased, while metastable pit initiation and growth rates are decreased (Kim and Buchheit, 2007).

In this study, AA6082 was used as the substrate for truck bed application. The effect of solution heat treatment on the mechanical properties of AA6082 was first evaluated, and the effects of natural and artificial ageing were investigated. Unlike the conventional binders such as Co, Ni and CoCr used with WC, Al-102 powder which has 12 wt % Si (Al12Si) was used as the binder to keep the coating density low. A matrix of WC and Al-102 powder, in varying concentrations, was used as the coating. The mixed powder was applied to the surface by the plasma spray procedure. The effect of the heat input from the plasma-spray process was evaluated. Both wear and corrosion resistance of the coating were evaluated.

CHAPTER 3: MATERIALS AND METHODS

The AA6082 alloy used as the substrate for this research study was purchased from NK Cutting South Africa, in the T651 condition. The chemical analysis, carried out by spark test at Scrooby's Laboratory South Africa for the as-received AA6082 T651 is given in Table 3.1:

Table 3.1: Composition of aluminium-6082 used for this study (wt %)

Si	Fe	Cu	Mn	Mg	Cr	Ni	Zn	Ti	Sn	Pb	Sr	Al
1.10	0.24	0.03	0.57	0.66	0.11	0.01	0.027	0.039	0.005	0.005	0.0005	Bal.

3.1 Heat Treatment

To establish a base line to examine further material improvement, the effect of artificial ageing on hardness and tensile strength of AA6082 was investigated.

3.1.1 Material Preparation

All the AA6082 samples were cut from one 6 m strip for homogeneity. Figure 3.1 shows a schematic diagram of the specimen used for the tensile test, with a 42 mm gauge length and 7×7 mm cross section. Flat samples were machined to 18×18×12 mm for the hardness evaluation.

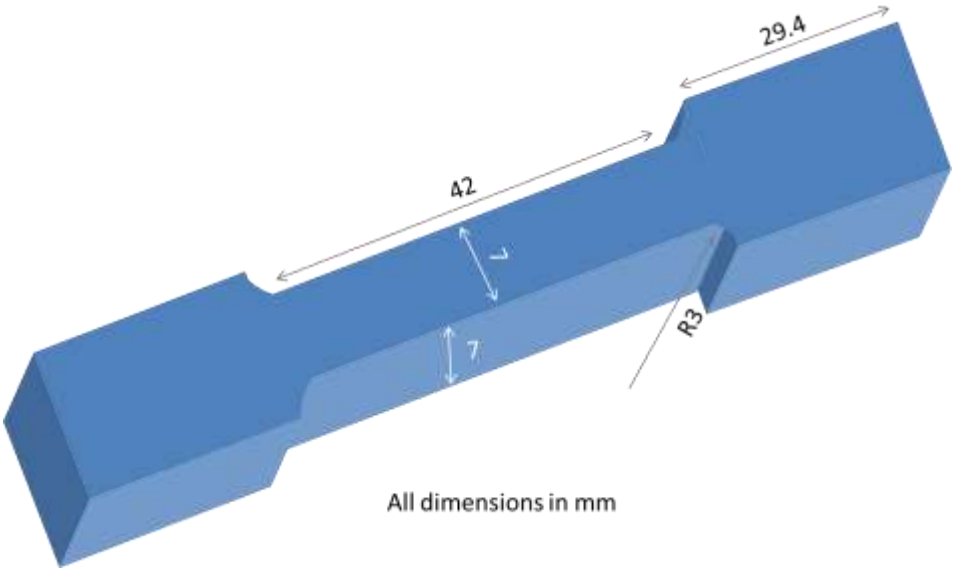

Figure 3.1: Sample for tensile tests.

3.1.2 Methods

Two heat treatment experiments A and B were carried out, and both tensile strength and hardness tests were performed on these samples. In Experiment A, twenty samples were solution heat-treated at 520°C for two hours. They were quenched in water to room temperature and were kept at 0°C for 48 hours, to study natural ageing characteristics (Banhart et al. 2010). Afterwards, the samples were aged at 175±2°C for 2, 4, 8, 16 and 32 hours.

Experiment B was carried out on another set of twenty samples with similar dimensions to those used in experiment A. This time, all samples were solution heat treated for 6 hours at 520°C before quenching. As opposed to experiment A, all samples were cooled to –17°C for 48 hours to prevent the occurrence of natural aging (Banhart et al. 2010). Artificial aging was performed at 175±2°C for 2.5, 5, 10, 20 and 40 hours, and four samples were used per condition.

A Tinius Olsen machine was used for the tensile tests, both in the as-received condition and after the heat treatment. The tensile behaviour of the as-received AA6082 was evaluated for four samples. Four flat 18×18×12 mm samples were used for the hardness tests. Six hardness measurements, at a 3 kg load, were taken on each sample. These mechanical properties of the as-received AA6082, compared with those of the heat treated samples, established the base line for

this study. To evaluate the precipitate growth in the heat treated samples, the microstructures of the heat treatment samples were compared with those of the as-received samples. Weck's reagent was used to etch the samples to reveal the microstructures (Gao et al., 2015).

3.2 Plasma Spray Coating

The primary purpose of the plasma spraying procedure was to apply the metal matrix coating on the surface of the AA6082 substrate.

3.2.1 Materials

The WC powder, purchased from Weartech (Pty) Ltd South Africa, had a particle size range between 15 and 45 µm as provided by the supplier. The particle size analysis for the Al-102 powder, also purchased from Weartech (Pty) Ltd, was carried out with a Malvern Particle Size Analyzer (Model: Master-sizer 2000).

3.2.2 Methods

The density of WC powder is 15.63 g/cm^3. The density of Al-102 powder (having 12 vol. % Si) is 2.7 g/cm^3. The powder composites were prepared by mixing Al-102 and WC powders in varying proportions, using an ultrasonic vibratory sieve shaker. The mass required to derive the target volume concentration of each coating is shown in Equation 3.1.

Mass = Density × Volume *Equation 3.1*

For instance, in the first mixture having 20 vol. % WC and 80 vol. % Al-102, the mass of WC (M_{WC}) and Al-102 ($M_{Al\text{-}102}$) required to derive 48cm^3 is shown in Equations 3.1a and 3.1b.

$$M_{WC} = 15.63 \times (\frac{20}{100} \times 48) = 150.048\,\text{g}$$

Equation 3.1a

The mass concentration of for the target volume of 48cm^3 is:

$$M_{Al-102} = 2.7 \times (\frac{80}{100} \times 48) = 103.68\,\text{g}$$

Equation 3.1b

The same formula was followed to calculate the mass concentrations required for the other matrix composite mixtures having 40, 60, 80 and 100 vol. % WC. Table 3.2 shows the volume and mass concentration of each composite powder mixture, for an overall volume of 48 cm^3. The mixtures weighed significantly more with increasing WC content.

Table 3.2: Powder matrix composites for coating mixtures.

Micro Al-102 + **Micro** WC						
	Mixtures	Volume of WC (cm^3)	Volume of Al (cm^3)	Mass of WC (g)	Mass of Al (g)	TOTAL (g)
1	20 vol. % WC 80 vol. % Al	9.60	38.40	150.05	103.68	253.73
2	40 vol. % WC 60 vol. % Al	19.20	28.80	300.10	77.76	377.86
3	60 vol. % WC 40 vol. % Al	28.80	19.20	450.14	51.84	501.98
4	80 vol. % WC 20 vol. % Al	38.40	9.60	600.19	25.92	626.11
5	100 vol. % WC 0 vol. % Al	48.00	0.00	750.24	0.00	750.24
	TOTAL			**2250.70**	**259.20**	**2509.92**

The AA6082 was machined, in preparation for coating. Figure 3.2 shows the sand-blasted samples which were prepared for plasma spraying. They were 240×20×12 mm in dimension.

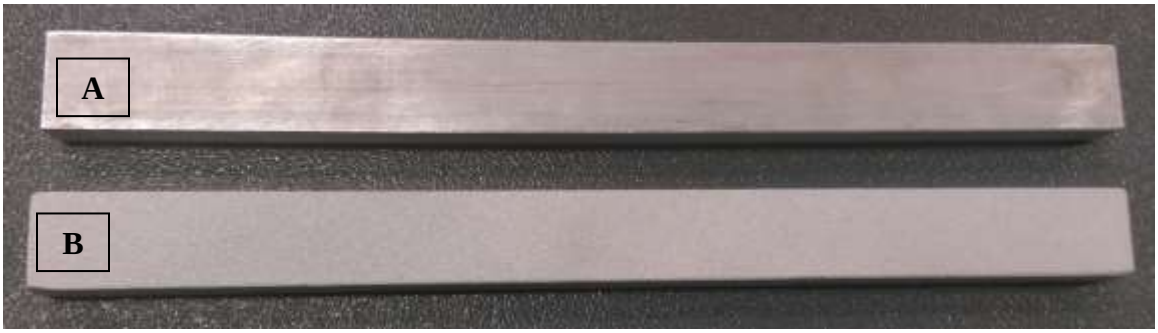

Figure 3.2: AA6082 strips of 240 mm length being prepared for plasma spraying.

In Figure 3.2, the as-received sample is labelled “A”, while the other labelled “B” had been sand-blasted to prepare its surface for the WC/Al-102 coatings. At a stand-off distance of 100 mm, the powder mixtures were plasma sprayed on the AA6082 surfaces to achieve an average coating thickness of 300 µm. The plasma spray set-up, at Thermaspray (Pty) Ltd, is shown in Figure 3.3.

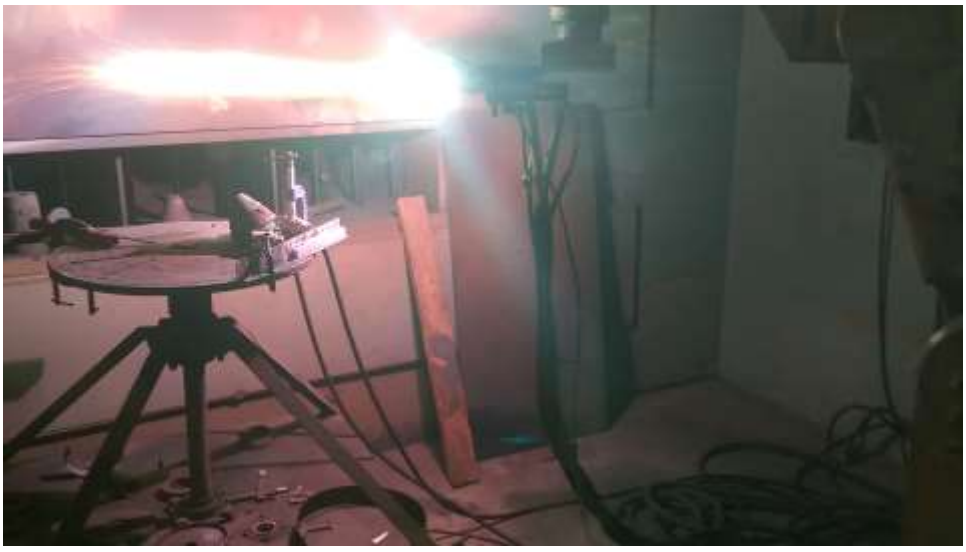

Figure 3.3: Plasma Spray Facility at ThermaSpray (Pty) Ltd South Africa.

To prepare the materials for mechanical testing and characterization, the sprayed sample strips were cut into smaller cuboids with uniform length of 18 mm, while their widths and thicknesses remained unchanged. Figure 3.4 shows the direction through which the samples were indented.

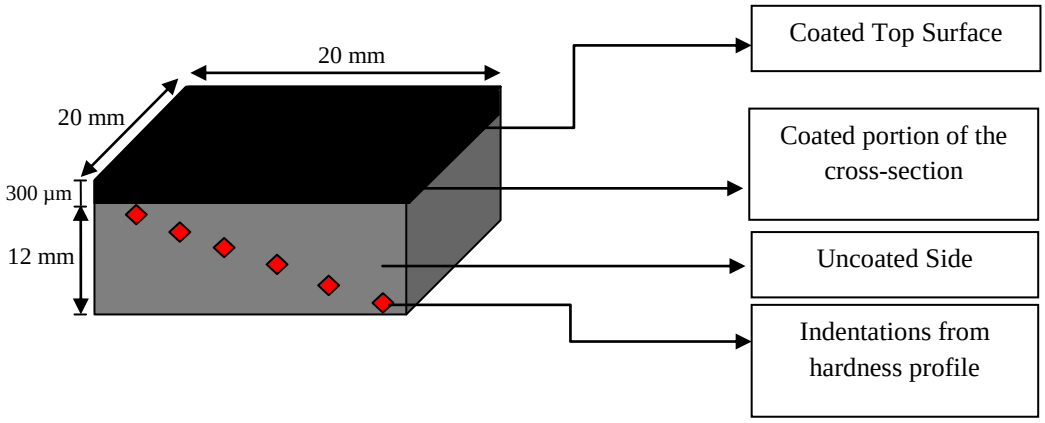

Figure 3.4: Schematic diagram showing how the coated samples were indented for micro-hardness profile test.

Vickers hardness tests were done on the coated surface and the uncoated cross section of each coated sample. Details of the Vickers hardness values from these are given in Appendix B. A micro-hardness profile was performed along the diagonal cross-section of the coated samples, using a load of 100 g. This was to check if, and to what extent, the hardness of the AA6082 substrate was altered by the heat input from plasma spray. Details of the cross-sectional micro-hardness profiles are shown in Appendix C. As shown in Figure 3.4, the indentations were made on the coating as well as the cross section of the AA6082 sample, close to the coating interface.

3.3 Sliding Wear

Following ASTM standard G133 – 05, sliding wear tests were performed on all samples.

3.3.1 Materials

All samples, coated and uncoated, are prepared to uniform dimension of 18 mm length, 18 mm width and 12 mm thickness. The lengths were cut longitudinally, while the widths were cut transversely. A hardened chrome steel (100Cr6) ball of 6 mm diameter, having hardness value between 58 – 63 HRC (690 – 810 HV), was used as the static partner positioned in the tribometer to abrade the sample surface.

3.3.2. Methods

Using an Anton Paar CSM pin-on-disk tribometer, sliding wear tests were performed on all coated surfaces, as well as the as-purchased metal surface for base reference. Using a 5 N load with a chrome ball, a sliding distance of 200 m was covered at a speed of 0.21 m/s.

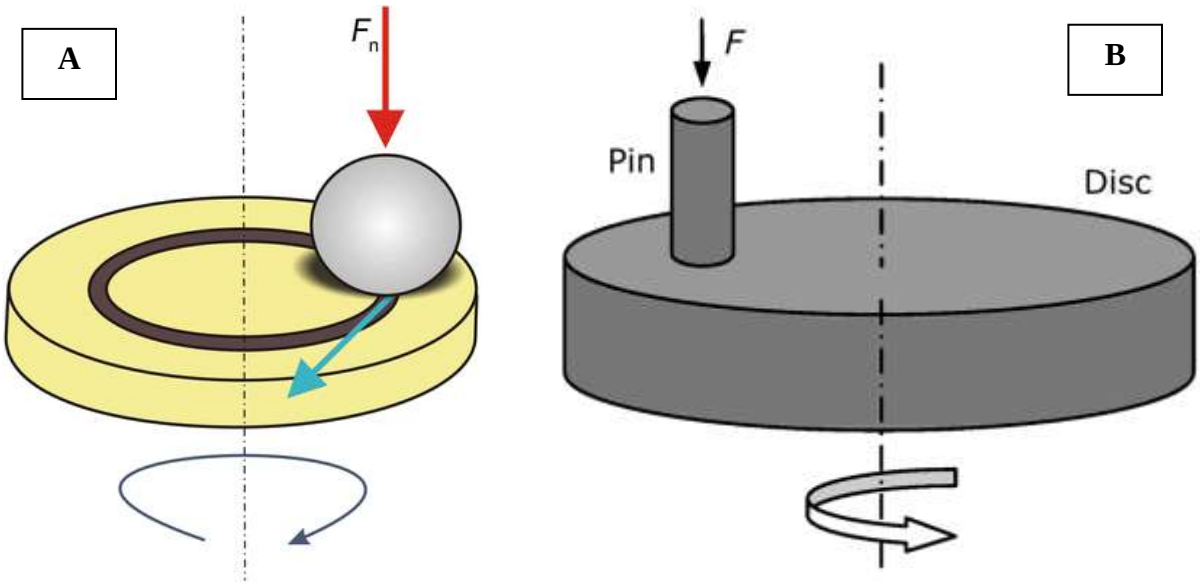

Figure 3.5: (a) Ball-on-flat by ASTM G133 – 05, and (b) Pin-on-disc by ASTM G99 – 95a.

Figure 3.5 (a) and (b) represent ASTM standards, namely G133 – 05 and G99 – 95a ball-on-disc and pin-on-disc procedures for sliding wear tests, respectively. For this study, the ball-on-disc was employed using 100 Cr6 ball. However, the formula used for pin-on-disc is applicable as the spherical end of a pin is likened to the ball itself.

3.3.3 Wear Rate

Using the ball on disk model in ASTM standard G99 – 05 (2000), the wear rates of the samples were calculated as shown in Equation 3.2:

$$W_R = 2\pi R\left[r^2 \sin^{-1}\left(d/2r\right) - \left(d/4\right)\left(4r^2 - d^2\right)^{1/2}\right] \qquad \text{Equation 3.2}$$

where:

W_R represents the wear rate as a function of disk (sample) volume loss

R = radius of the wear track

d = width of the wear track and

r = pin end radius.

3.4 Exposure Tests

Although the corrosion resistance of Al alloys are acceptable for use in transport applications (Miller et al., 2000; Gudić et al., 2010), the aim of the exposure tests was to determine whether the corrosion resistance of the coating was comparable with the substrate. All corrosion experiments were carried out in the de-aerated condition. By weight loss measurement, the volume of material lost due to corrosion was estimated in particular environments and under certain conditions. Based on the truck loading application of this study, the envisaged environment to which the materials will potentially be exposed is a neutral 3.5% NaCl solution. Yet, exposure to an acidic 3.5% NaCl environment was also examined.

3.4.1 Materials

From the as-received AA6082 strip, coupons were machined to 18×18×12 mm. The same dimensions were used for the uncoated coupons. A 3 mm diameter hole was drilled to suspend the coupons in solution. Surfaces of all coupons were ground and polished to a smooth finish. Measurements of the mass, length, width and thickness were recorded before immersion.

3.4.2 Methods

Three sets of solutions of 3.5 weight % of NaCl were prepared. The pH levels were adjusted to 2.03 and 11.35 with additions of sulphuric acid and sodium hydroxide respectively. The third solution, being neutral, was left unaltered with its pH at 7.45. Teflon tape was passed through the drilled holes to suspend all uncoated samples across the different solutions. No hole was drilled through the coated samples. Instead, each sample was covered in silicone rubber from the edges all round to the back, leaving only the sprayed 17.9×17.9 mm coated surface exposed to the solution. Teflon tape was strung into the dried silicone rubber and used to suspend the coated samples in solution. All solutions were then placed in a controlled water bath set at 25°C.

After 24 hours, the first series of duplicate coupons were withdrawn from the acidic, alkaline and neutral solutions. Samples were thoroughly cleaned and measurements of the mass, length, width and thickness were recorded. The same withdrawal, cleaning and measurement procedures were carried out exactly after 4, 7 and 14 days. For each of the samples immersed, the final mass was subtracted from the initial mass to obtain the loss in weight, due to corrosion. Weight losses were recorded for both uncoated and coated sets of coupons exposed to the corrosive environments.

In calculating the total surface area of the uncoated samples, the area of the 3 mm diameter hole drilled through the samples was taken into account. The area of the 3 mm circle was subtracted from both sides of the cuboid surface while the area of the walls of the cylindrical surface made by the perforated hole was added to the entire surface area.

$$Area = 2\left[\left(L \times W\right) - \left(\pi \frac{D^2}{4}\right)\right] + 2\left(L \times T\right) + 2\left(W \times T\right) + \left(\pi \times D \times T\right) \qquad \text{Equation 3.3}$$

where:

L = length of coupon (18 mm)

W = width of coupon (18 mm)

T = thickness of coupon (12 mm)

D = diameter of circle drilled into material surface (3 mm).

Corrosion rate is calculated using the equation in ASTM standard G31 – 72 and is given below:

$$CR = \left(K \times W\right) / \left(A \times T \times D\right) \qquad \text{Equation 3.4}$$

where:

CR = corrosion rate

K = 8.76×10^4 (the constant used to derive CR in mm/y)

W = mass loss (in g)

A = area of sample exposure (in cm^2)

T = time of exposure (in h)

D = density of material exposed to corrosive medium (in g/cm^3).

3.5 Electrochemical Tests

Linear polarization tests were performed on all samples using a potentiostat.

3.5.1 Materials

From the as-received AA6082 strip, another set of coupons were machined to 18×18×12 mm, resembling coated coupons examined in this same dimension. It was reasonable to use the same dimensions for uncoated coupons to set the base for this examination.

3.5.2 Methods

All coupons were subjected to grinding and polishing to a smooth finish. Using distilled water, a single batch electrolyte solution having 3.5 weight % of NaCl was prepared as for the immersion test (section 3.4). However, the pH value was kept at 5.80, similar to the work of Kartsonakis et al. (2016), and also at 2.03 for the acidic solution. Ag/AgCl was used as the reference electrode with graphite as the counter electrode in a solution controlled at 25°C. All uncoated and coated samples served as the working electrode for each test cycle. The experiments were conducted in a water bath, with beakers covered to keep the solution from evaporating. A scan rate of 0.167 mV/s was used for the test. The potential was scanned from –200 mV to 600 mV. Scans for the first sets of duplicate coupons were completed in the acidic, alkaline and neutral solutions.

Corrosion rates were calculated using the equations 3.5, 3.6 and 3.7:

$$CR = K_1 \frac{i_{corr}}{\rho} EW \qquad \text{Equation 3.5}$$

where:

$K_1 = 3.27 \times 10^{-3}$ (in mm g/μA cm y)

ρ = density of material exposed to corrosive media (in g/cm^3)

EW = equivalent weight of the element.

$$i_{corr} = \frac{B}{R_P} \text{ (corrosion current density, in } \mu A/cm^2) \qquad \text{Equation 3.6}$$

$$B = \frac{b_a \times b_c}{2.303(b_a + b_c)} \text{ (Stern-Geary constant, in V)} \qquad \text{Equation 3.7}$$

where:

b_a = slope of the anodic Tafel reaction (in V/decade)

b_c = slope of the cathodic Tafel reaction (in V/decade).

3.6 Characterization

Coated and uncoated samples were examined before and after exposure to the corrosive media.

3.6.1 Optical Microscopy

An Olympus BX63 optical microscope was used to measure four different sections of the circumference, to derive average values of the wear track widths for the uncoated and coated samples within the matrix. Also, it was used to view the cross-section of coated samples, to examine the coating-substrate interface. It was used to examine the worn surface of the 100Cr6 balls, to reveal the extent of the ball volume loss. The depths of penetration for the worn coated samples were derived by using an optical microscope to measure the differences between the top and the deepest points in the wear tracks of the coatings.

3.6.2 Stereo Microscopy

The stereo microscope was used for tested samples for both wear and corrosion. Wear track widths of uncoated and coated samples were also examined.

3.6.3 Scanning Electron Microscopy and Energy Dispersive Spectrometry

The morphology was studied of all uncoated and coated surfaces using a Carl Zeiss Field Emission Scanning Electron Microscope (FE-SEM) equipped with an Energy Dispersive X-ray Spectroscopy (EDS) detector. Weck's Reagent was used to etch the top view of the uncoated samples at different ageing temperatures, to reveal the size of precipitates within the matrix. SEM images were taken at different magnifications to derive the morphology of particles present

on the surface. The EDS was used to ascertain the chemical composition of the selected regions on the uncoated samples, as well as for the coating.

CHAPTER 4: RESULTS

This section highlights all the findings of the experiments carried out throughout the study. Prior to the wear and corrosion tests, it was important to determine the effect of heat treatment on the hardness values of the AA6082.

4.1 Effect of Heat Treatment on Hardness of Aluminium-6082 Alloy

The heat treatment of AA6082 was an important base line for the entire study. As-received samples of AA6082 T651 were tested in the uncoated state to confirm the mechanical properties before and after heat treatment shown in Table 4.1.

Table 4.1: Mechanical properties of the as-received alloy at room temperature.

Vickers hardness of top surface (HV)	106 ± 3.2
Vickers hardness of cross section, (HV)	106 ± 2.8
Yield Strength (MPa)	219 ± 0.6
Ultimate Tensile Strength (MPa)	337 ± 2.1

4.1.1 Hardness values for experiments A and B

The average hardness values after heat treatment experiments A and B are shown in Tables 4.2 and 4.3 respectively, and plotted in Figure 4.1. The measured Vickers hardness results of these hardness values are shown in Table C1 of Appendix C, while those for coated samples are shown in Tables C2, C3, C4, C5 and C6.

Table 4.2: Vickers hardness values of samples aged at 175°C for experiment A.

	Top of Sample		Cross-section of sample	
Time (h)	**Sample 1 Hardness (HV)**	**Sample 2 Hardness (HV)**	**Sample 1 Hardness (HV)**	**Sample 2 Hardness (HV)**
2	52 ± 0.6	54 ± 0.5	52 ± 0.8	55 ± 0.8
4	54 ± 0.5	47 ± 0.5	56 ± 0.8	48 ± 0.5
8	45 ± 0.7	49 ± 0.6	45 ± 1.0	51 ± 0.6
16	60 ± 0.4	50 ± 0.6	62 ± 0.9	51 ± 1.3
32	49 ± 0.7	57 ± 1.7	51 ± 1.6	58 ± 0.4

Table 4.3: Vickers hardness values of samples aged at 175°C for experiment B.

	TOP		SIDE	
Time (h)	**Sample 1 Hardness (HV)**	**Sample 2 Hardness (HV)**	**Sample 1 Hardness (HV)**	**Sample 2 Hardness (HV)**
2.5	69 ± 2.6	68 ± 2.6	64 ± 4.4	61 ± 4.4
5	77 ± 0.8	76 ± 3.2	70 ± 4.9	68 ± 2.5
10	81 ± 1.4	82 ± 1.7	66 ± 5.5	73 ± 7.6
20	102 ± 1.8	98 ± 2.9	101 ± 2.7	98 ± 2.3
40	82 ± 4.5	82 ± 1.9	75 ± 3.6	78 ± 3.3

The hardnesses shown in Tables 4.2 and 4.3 are plotted in Figure 4.1

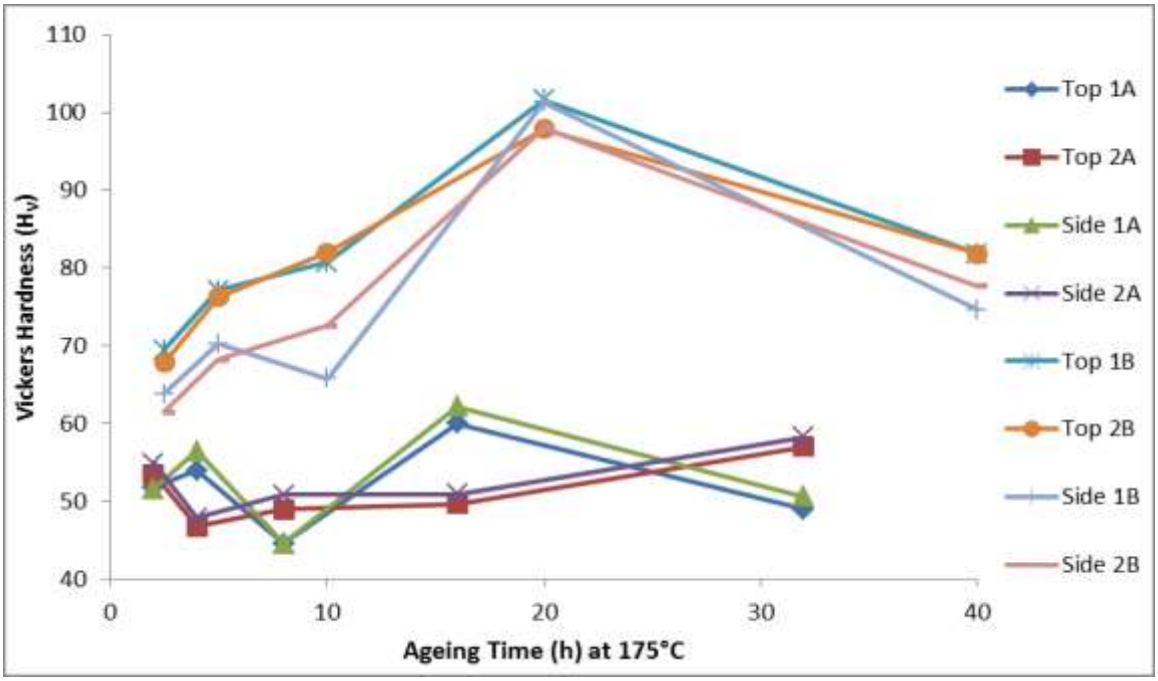

Figure 4.1: Average Vickers hardness results of samples aged at 175°C for experiments A and B.

For experiments A and B, two samples were heat treated for each experiment and the hardness of each sample was determined on the top surface and side (cross section). These were identified as Top 1A, 1B, 2A and 2B as well as Side 1A, 1B, 2A and 2B. The hardness measurements were determined for 2 h, 4 h 8 h, 16 h and 32 h ageing time for experiment A and 2.5 h, 5 h, 10 h, 20 h and 40 h for experiment B.

Due to the alteration in duration of solution treatment and post-quench storage temperature, the hardness values in Experiment B were significantly different from those of Experiment A. Variations in hardness values of samples were relatively large for all samples except that aged for 20 hours. The hardnesses of the 20 h aged sample, for both top surface and cross section, showed hardness values slightly lower than the as-received sample. It was observed that results in Experiment B yielded results that corresponded with expected results available in texts and is thus reliable base line for future experiments.

4.1.2 Tensile test results for experiments A and B

Tables 4.4, 4.5 and Figure 4.2 show the variations in yield strength (YS) and the ultimate tensile strength (UTS) against ageing time for both Experiments A and B.

Table 4.4: Tensile strength values of samples aged at 175°C for experiment A.

Time (h)	Yield Stress (MPa)	Ultimate Tensile Stress (MPa)
2	98 ± 1.5	211 ± 1.2
4	98 ± 1.5	217 ± 1.5
8	118 ± 1.6	257 ± 0.9
16	98 ± 1.0	200 ± 1.5
32	82 ± 1.5	196 ± 1.2

Table 4.5: Tensile strength values of samples aged at 175°C for experiment B.

Time (h)	Yield Stress (MPa)	Ultimate Tensile Stress (MPa)
2.5	125 ± 1.0	274 ± 0.6
5	165 ± 0.6	306 ± 0.6
10	191 ± 1.0	320 ± 1.0
20	221 ± 1.2	337 ± 1.0
40	175 ± 1.5	321 ± 1.2

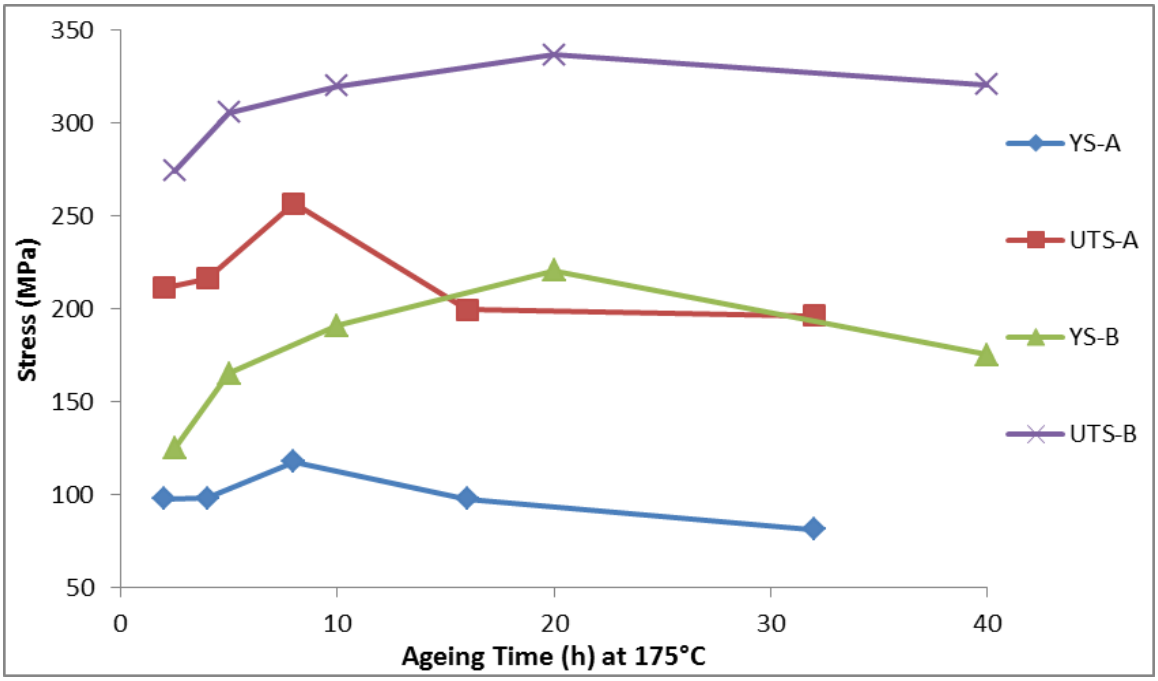

Figure 4.2: Average tensile strength result of samples aged at 175°C for experiment B.

From Figure 4.2, YS-A and UTS-A respectively represent the values yield strength and ultimate tensile strength for samples of experiment A. Likewise, YS-B and UTS-B represent the values yield strength and ultimate tensile strength for samples of experiment B respectively. The tensile test results indicated that the average values of yield strength and ultimate tensile strength showed a similar trend to the hardness values for experiment B. These results therefore confirmed that natural ageing decreased the strengthening of the samples of experiment A.

4.3 SEM for uncoated AA6082

A scanning electron microscope was used to view precipitates of the heat treated samples of AA6082 aged for different durations.

4.3.1 SEM and EDS Analyses

SEM images were taken at the polished and etched top surfaces, to evaluate the difference in precipitate sizes of samples aged for different lengths of time. Samples of Experiment B aged for 10 h, 20 h and 40 h were compared with the as-received sample.

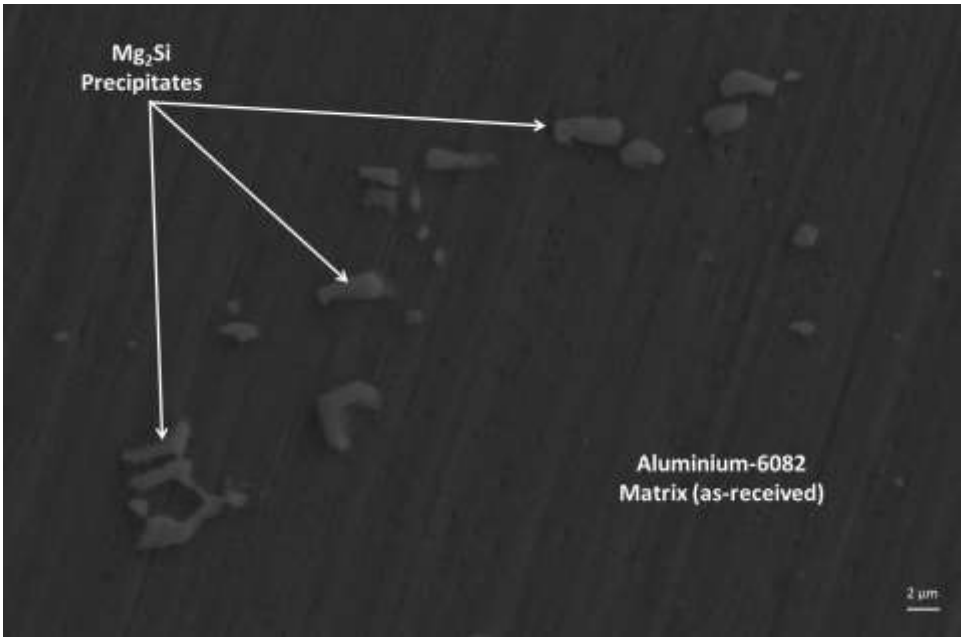

Figure 4.3: SEM (SE mode) image of the as-received AA6082 sample in T651 condition.

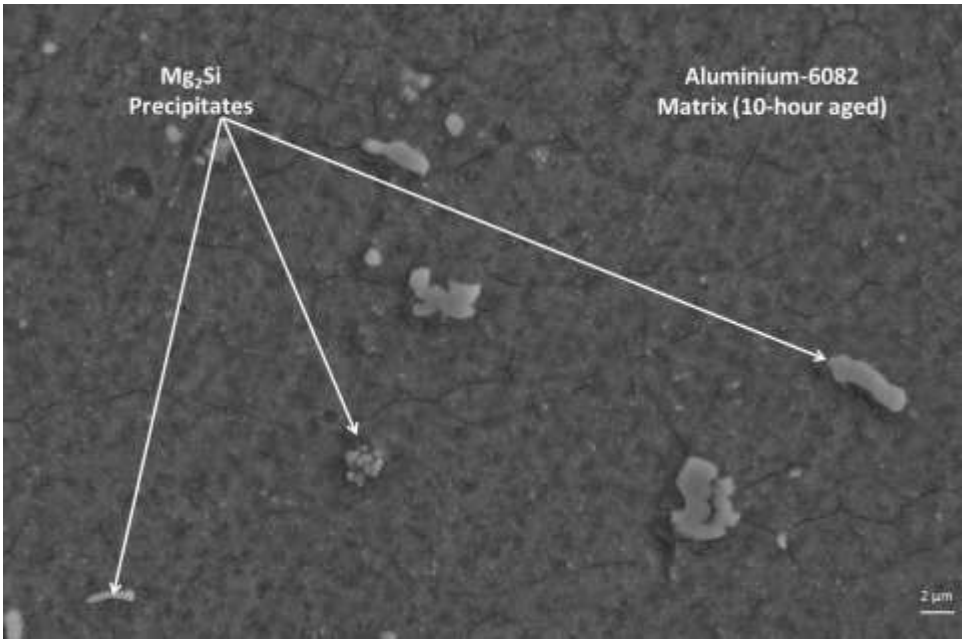

Figure 4.4: SEM (SE mode) image of the sample aged for 10 hours at 175°C.

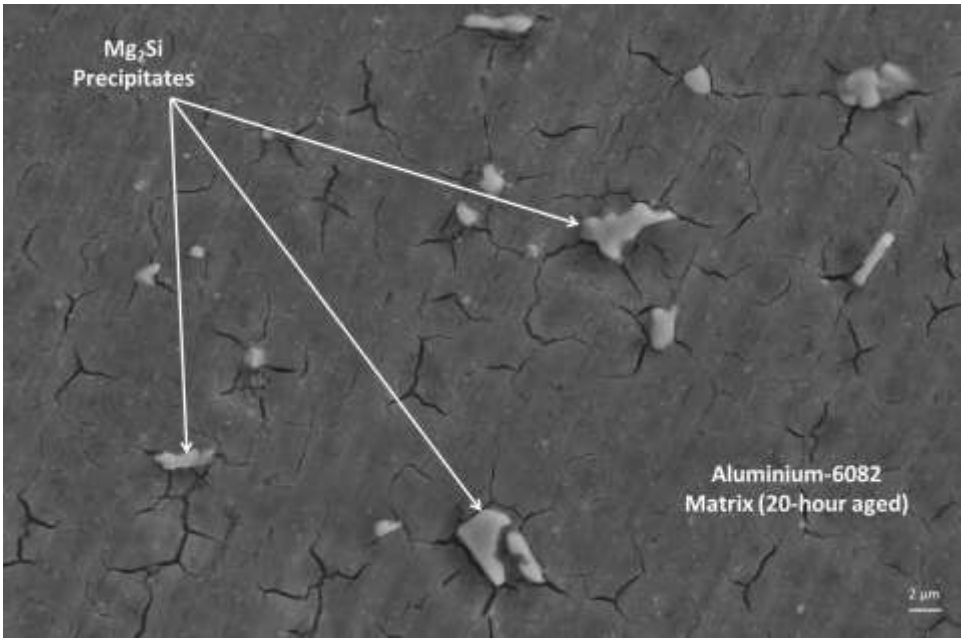

Figure 4.5: SEM (SE mode) image of the sample aged for 20 hours at 175°C.

Precipitates of the as-received and 20-hour aged samples were fairly identical in size, as shown in Figure A1 in Appendix A. This explains why their hardness values were similar.

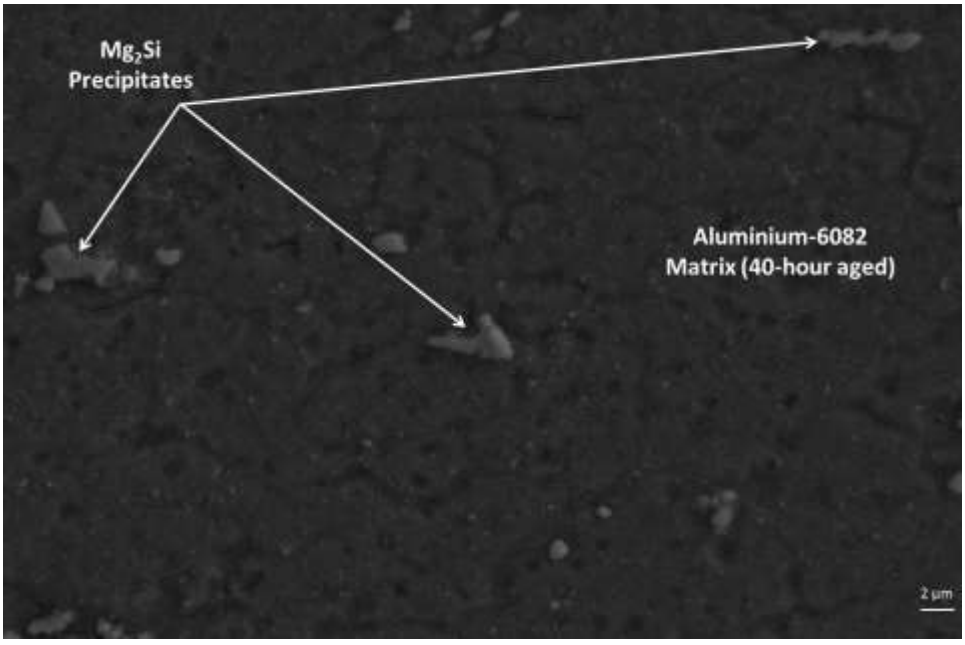

Figure 4.6: SEM (SE mode) image of the sample aged for 40 hours at 175°C.

Precipitates of the sample aged for 40 hours, in Figure 4.6, were smaller than those in the peak-aged 20-hour sample. Table 4.6 shows the elemental compositions of the largest precipitates shown in Figures 4.3, 4.4, 4.5 and 4.6.

Table 4.6: Elemental compositions of precipitates.

Element	As-received		10-hour aged		20-hour aged		40-hour aged	
	wt %	at. %	wt %	at. %	wt %	at. %	wt %	at. %
O	2.7	5.3	0.0	0.0	3.1	5.7	2.1	4.0
Al	60.8	69.7	60.7	68.5	59.7	64.2	59.3	68.3
Si	8.5	9.4	9.4	10.2	8.6	8.9	10.6	11.8
Mg	12.1	6.8	12.4	6.9	11.8	6.2	16.7	9.5
Cr	0.9	0.6	1.1	0.6	1.2	0.6	2.9	1.7
Fe	14.9	8.3	14.1	7.7	12.4	6.4	8.4	4.7

Figure 4.7 shows the elemental compositions of the precipitates in AA6082 after 10, 20 and 40 h of ageing, as well as in the as-received condition.

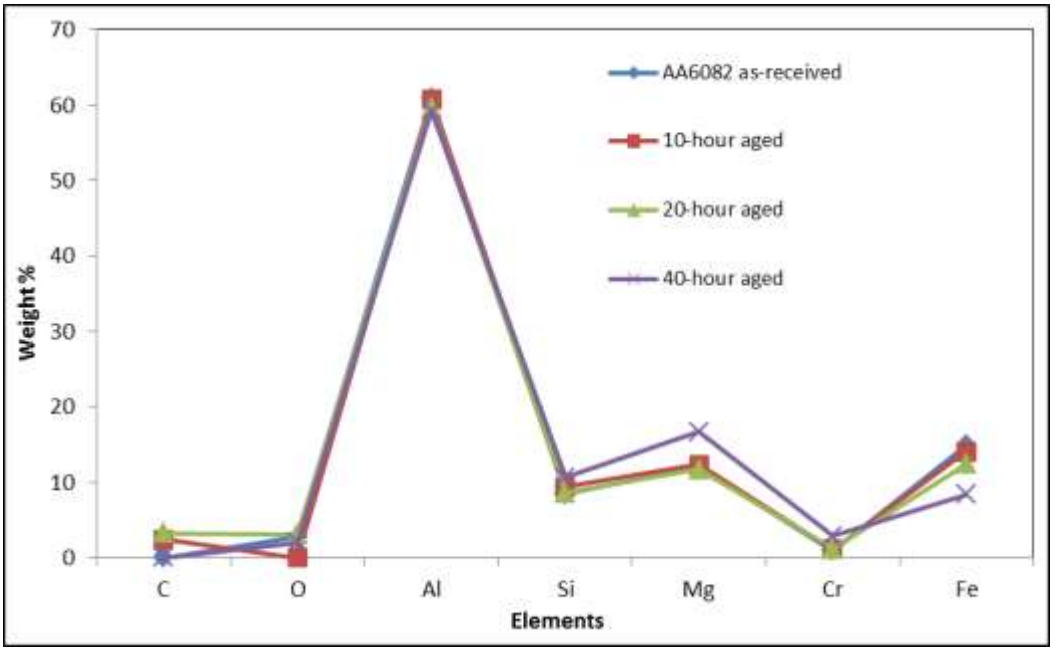

Figure 4.7: Weight % compositions of elements within precipitates.

4.4 Thermal Spray Coating

Figure 4.8 showed that the average particle size distribution for Al-102 powder was 77 µm.

d10 = 54.984µm *d50 = 76.588µm* *d90 = 106.462µm*

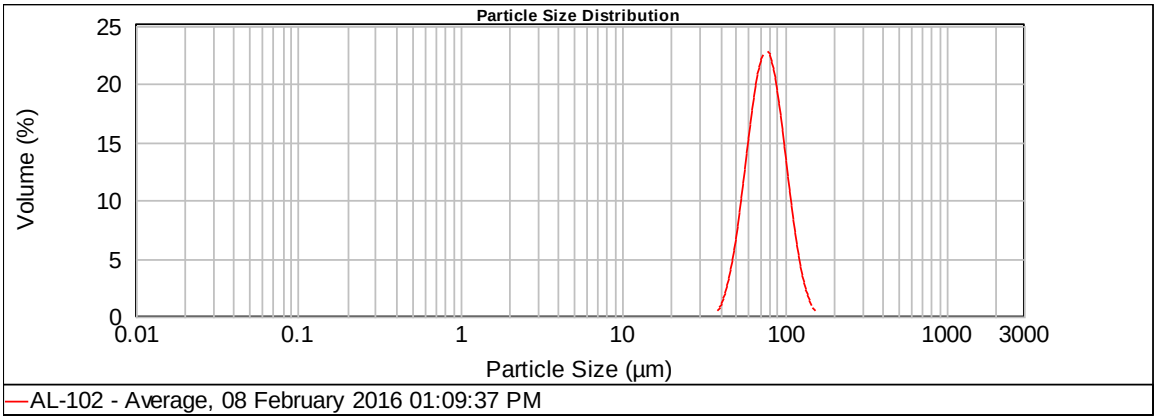

Figure 4.8: Particle size distribution of Al-102 powder as-purchased.

4.4.1 Hardness Tests on Thermally Spray-Coated Samples

Vickers hardness values were measured for the coated samples, as shown in Table 4.7 and plotted in Figure 4.9.

Table 4.7: Vickers hardness values of coated samples.

Powder Composition (vol. %)	Coated Surface (HV)	Cross Section (HV)
As-received	106 ± 3.2	106 ± 2.7
20%WC, 80%Al	130 ± 11.8	107 ± 11.7
40%WC, 60%Al	177 ± 12.7	109 ± 7.9
60%WC, 40%Al	228 ± 12.2	98 ± 11.4
80%WC, 20%Al	286 ± 22.3	110 ± 11.4
100%WC, 0% Al	285 ± 111.3	101 ± 11.3

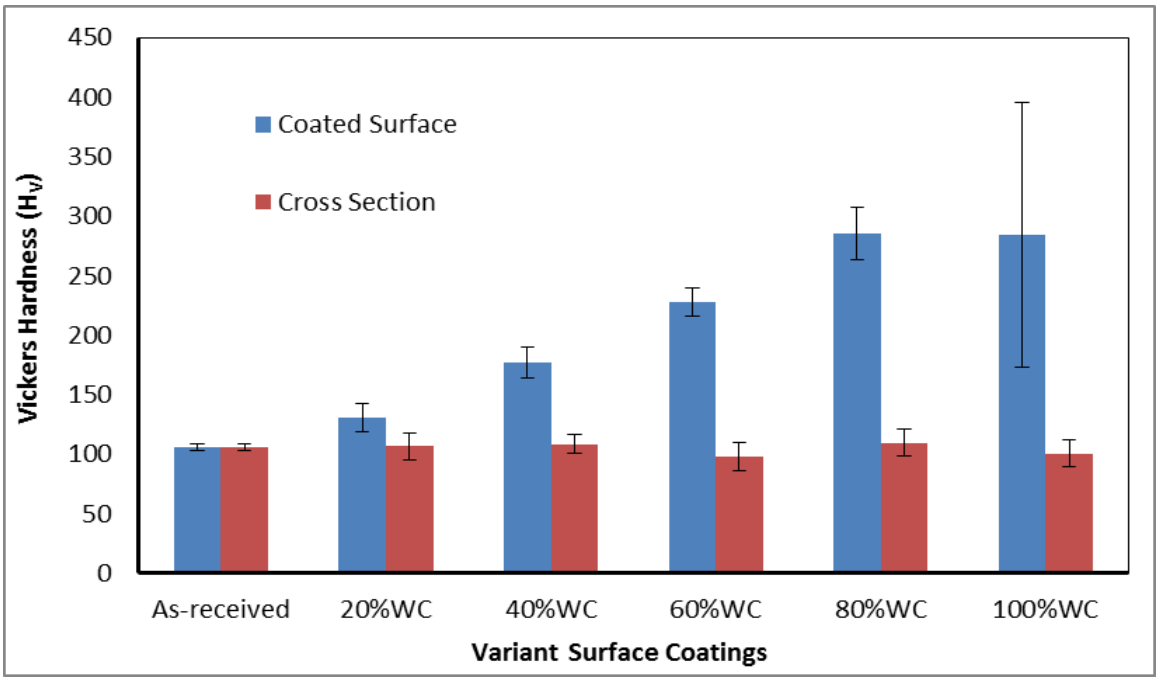

Figure 4.9: Vickers hardness of the coated surface and the cross-section of the samples.

These hardness values are an average of six points, taken along the diagonal of the uncoated and coated samples, details of which are shown in Appendix C. The hardness results of the cross section for all samples, coated and uncoated, were taken and shown in Figure 4.9. The uncoated sample, for which both the top surface and cross section were indented, had uniform hardness values across its area. For all the coated samples, the hardness values of the cross sections (substrate region below the coating interface) were similar to those of the uncoated sample. Also, the hardness values of the coated surfaces increased with an increase in WC content.

The error margin for the hardness results of the uncoated sample, both at the top surface and the cross section, were the smallest of all. Compared with these uncoated samples, the error margin was larger for the hardnesses of the coated samples. First, for all the coated surfaces, the error margin for their cross sections (substrate region) was similar and slightly larger than that of the uncoated sample. Second, the error margin of the coated surface was similar for the 20, 40 and 60 vol. % WC. The scatter of the hardness results on the 80 vol. % WC coating was slightly wider than the previous, while that of the 100 vol. % WC coating was the largest.

4.4.2 Micro-Hardness Profiles on Thermally Spray-Coated Samples

To ascertain the effect of heat on the substrate, hardnesses of the cross-sections were measured.

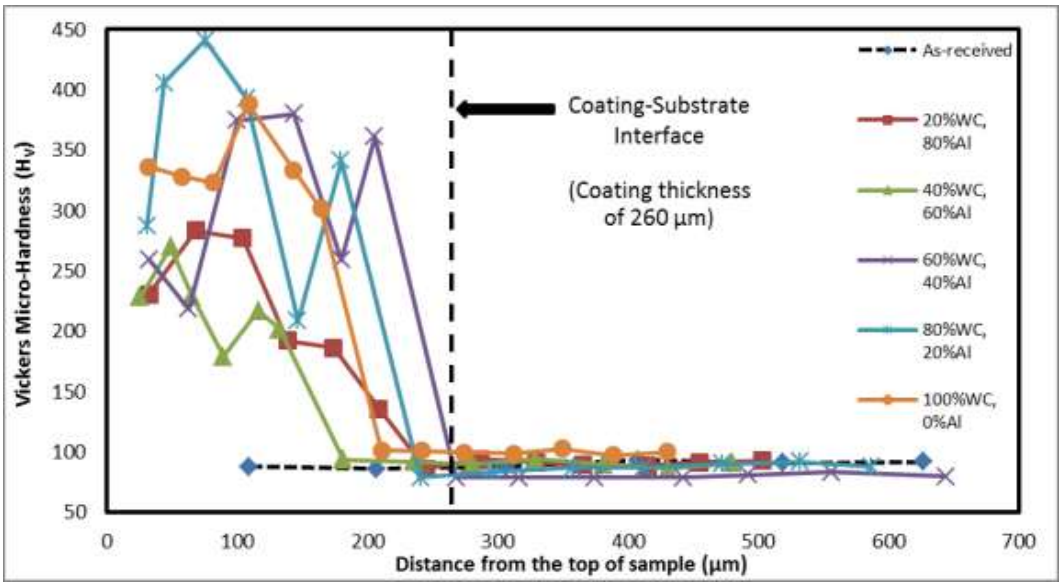

Figure 4.10: Micro-hardness profile of coated samples compared with uncoated one.

The hardnesses around the 300 µm thick coatings are significantly higher than those of the substrate region beneath the coating. The micro-hardness profiles in Figure 4.10 are the first of four readings taken on coated and uncoated samples, values of which are shown in Appendix C.

4.4.3 Optical Microscopy for Thermally Spray-Coated Samples

Optical microscopy images for the cross-sections of all the coated samples are shown in Figure 4.11.

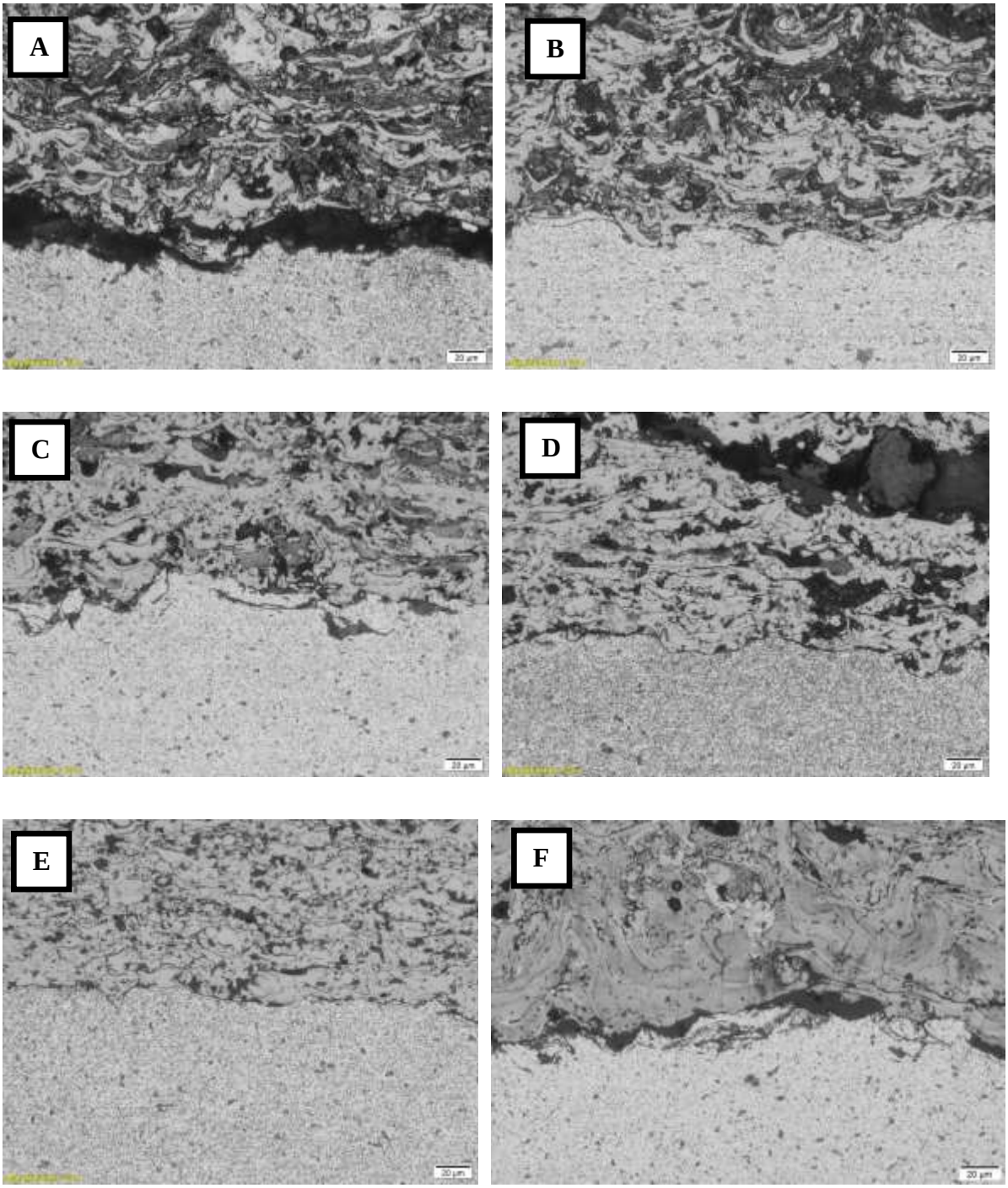

Figure 4.11: Optical images of the cross-section showing coating-substrate interface of (a) 20 (b) 40 (c) 60 (d) 80 (e) 100 vol. % WC and (f) 100 vol. % Al coatings.

Figures 4.11a, b, c, d, and e show the coating-substrate interfaces for the 20, 40, 60, 80 and 100 vol. % WC coating respectively, while Figure 4.11f shows the 100% Al-102 coating. The interfaces of the 40%, 60%, 80% and 100 vol. % WC coatings appeared to adhere sufficiently to the substrate. Similar to the 100% Al-102 coating as shown in Figure 4.11f, Figure 4.11a showed that the 20% WC coating might not have adhered sufficiently to the substrate.

The 20 vol. % WC coating had up to 80 vol. % Al-102 binder, which is very high. However, the WC concentration could still have been sufficient to create some interfacial bond with the substrate. Since the optical images were only the first step, further examination could reveal more details. It was thus important to examine the interfaces further, using the SEM.

4.4.4 SEM and EDS for Thermal Spray-Coated Samples

The cross-sectional SEM images for the interfaces of all coated samples are shown in Figures 4.12 to 4.16.

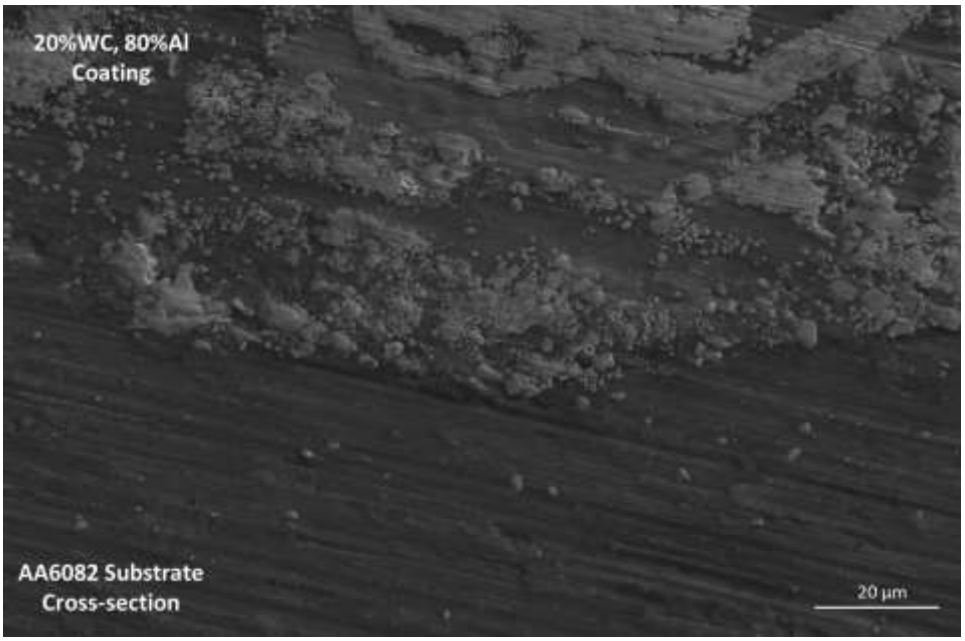

Figure 4.12: SEM (SE) image for the coating-substrate interface for the 20 vol. % WC sample.

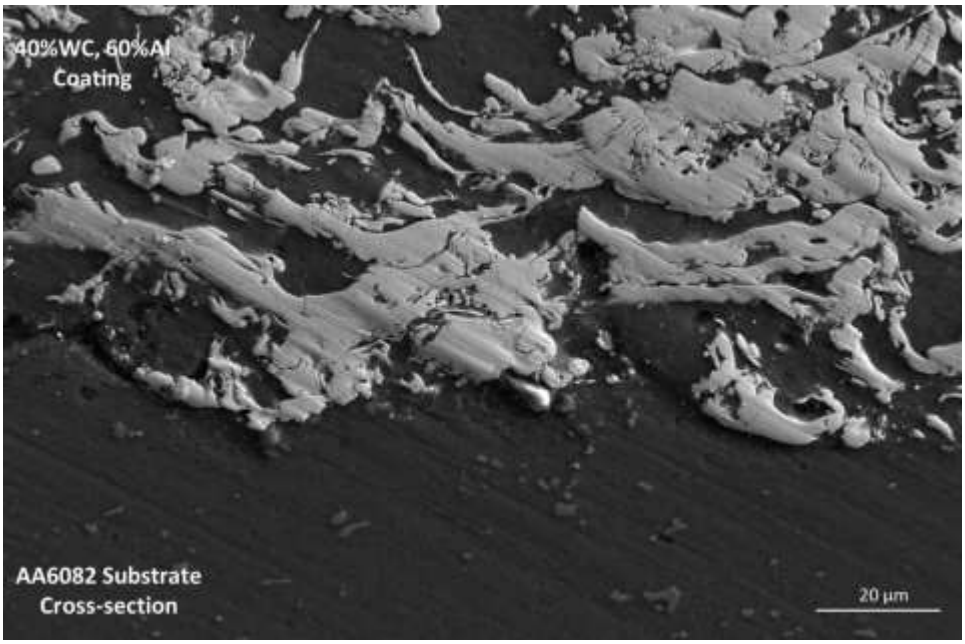

Figure 4.13: SEM (SE) image for the coating-substrate interface for the 40 vol. % WC sample.

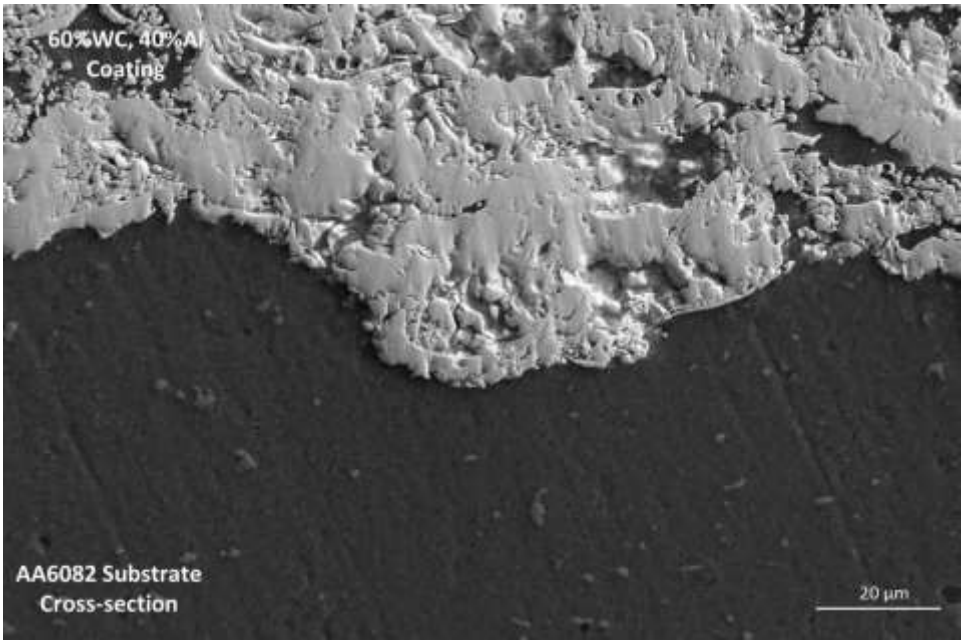

Figure 4.14: SEM (SE) image for the coating-substrate interface for the 60 vol. % WC sample.

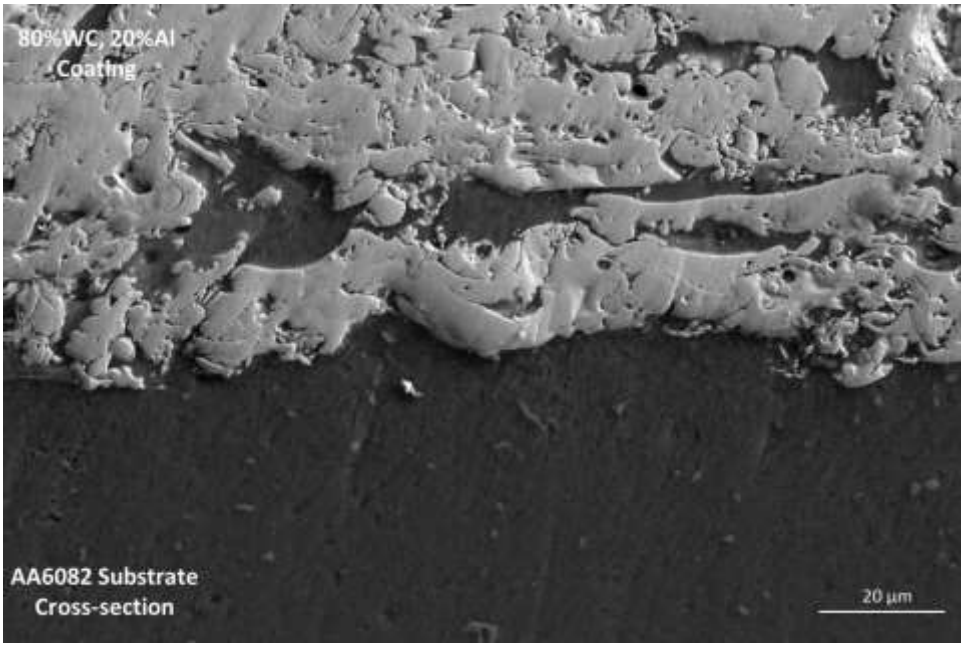

Figure 4.15: SEM (SE) image for the coating-substrate interface for the 80 vol. % WC sample.

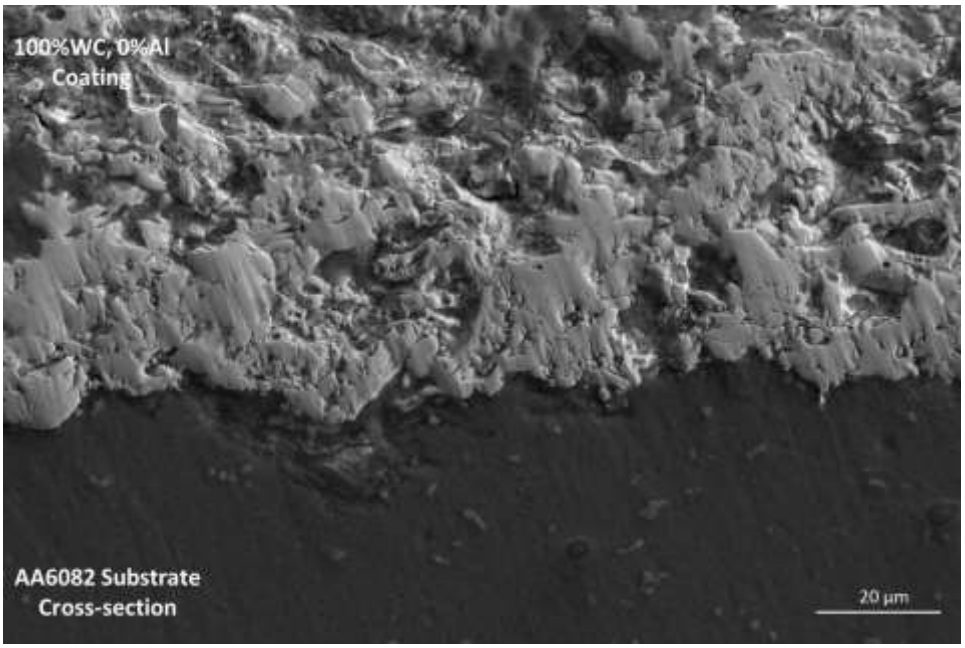

Figure 4.16: SEM (SE) image for the coating-substrate interface for the 100 vol. % WC sample.

These images showed that all the coatings bonded well with the substrate.

4.5 Sliding Wear

This section shows images, coefficients of friction and penetration depths.

4.5.1 Optical Microscopy images for wear tracks

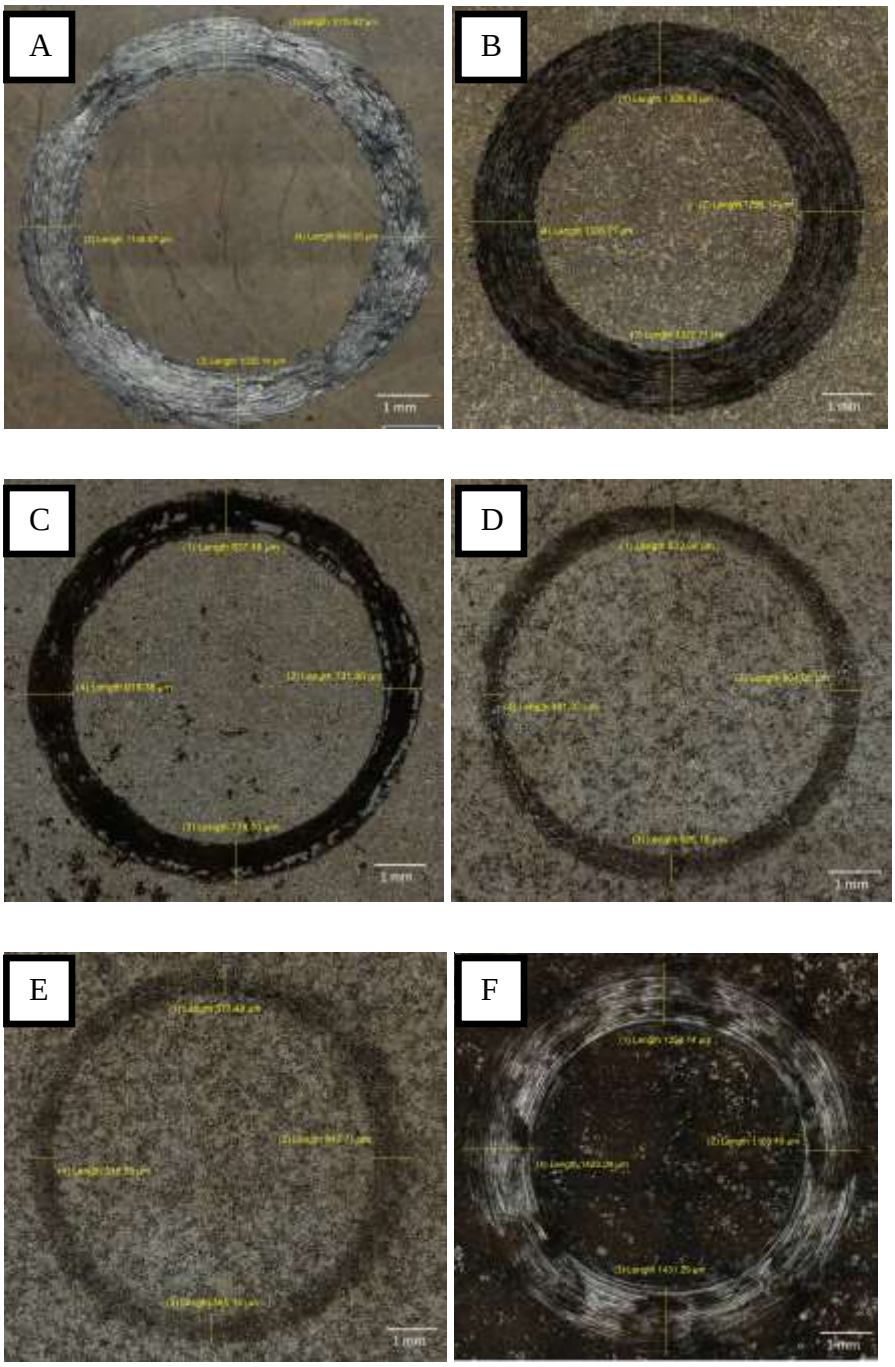

Figure 4.17: Optical images for the wear track of the (A) uncoated sample (B) 20 (C) 40 (D) 60 (E) 80 and (F) 100 vol. % WC coatings.

Widths measured were only similar for two of the four portions on the wear track of the uncoated (as-received) sample. The other two regions had different values, as shown in Figure 4.17A. The values of wear track widths, obtained from the optical microscope, are shown in Table 4.8 and plotted in Figure 4.18.

Table 4.8: Widths of sample wear tracks measured on the optical microscope.

Samples	**Widths on Optical Microscope (mm)**				
	A	B	C	D	Mean
0 vol. %WC	1.0	1.1	1.1	0.9	1.0 ± 0.1
20 vol. %WC	1.3	1.3	1.3	1.3	1.3 ± 0.0
40 vol. %WC	0.8	0.7	0.8	0.9	0.8 ± 0.1
60 vol. %WC	0.5	0.6	0.5	0.4	0.5 ± 0.1
80 vol. %WC	0.6	0.8	0.6	0.5	0.6 ± 0.2
100 vol. %WC	1.3	1.2	1.4	1.4	1.3 ± 0.1

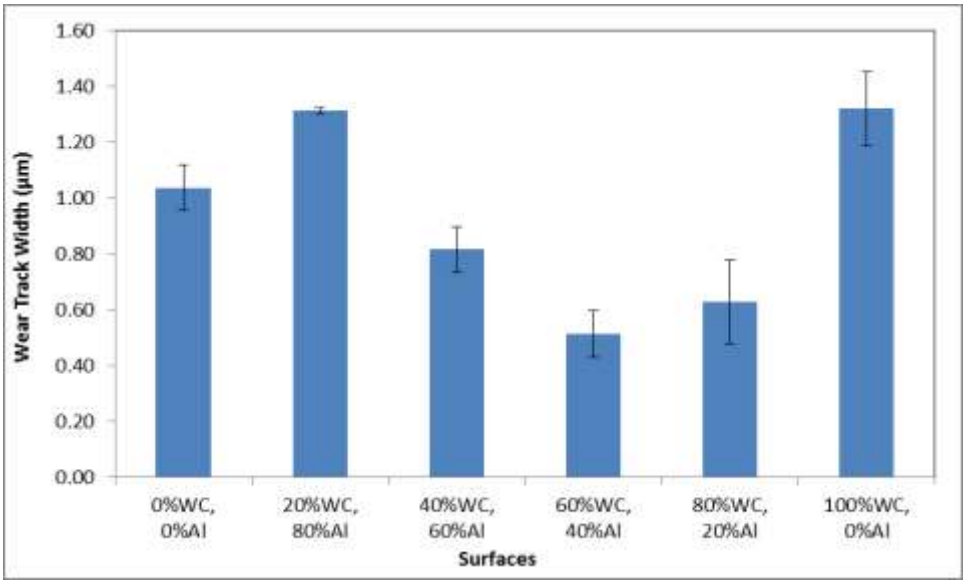

Figure 4.18: Widths of wear tracks obtained from optical microscope.

The coefficients of friction for all samples were measured during the sliding wear test and shown in Figure 4.19.

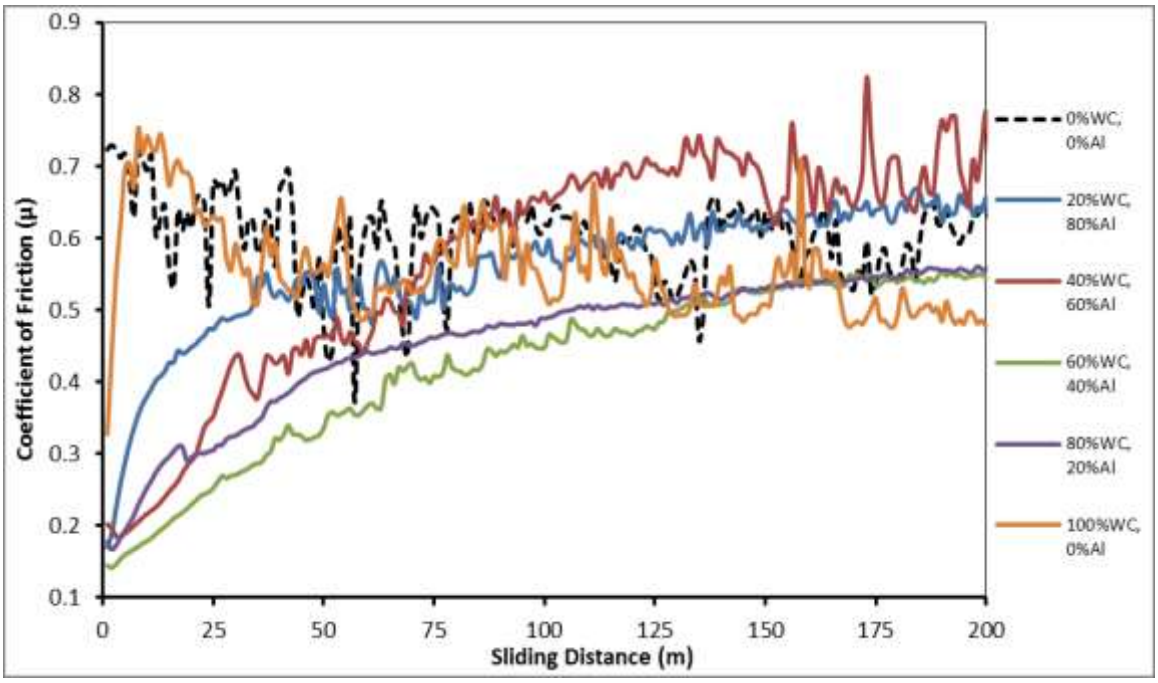

Figure 4.19: Coefficient of friction for uncoated and coated samples.

The coefficients of friction for the uncoated and the 100% WC coating samples both started out with relatively high coefficients of friction. The 20% WC, 40% WC, 60% WC and 80% WC coatings showed similar behaviour. Their CoFs started from relatively low values, increased gradually and then levelled out at 150 m sliding distance. From Figure 4.20, it is clear that the 60% WC and 80% WC coatings showed the highest resistance to penetration.

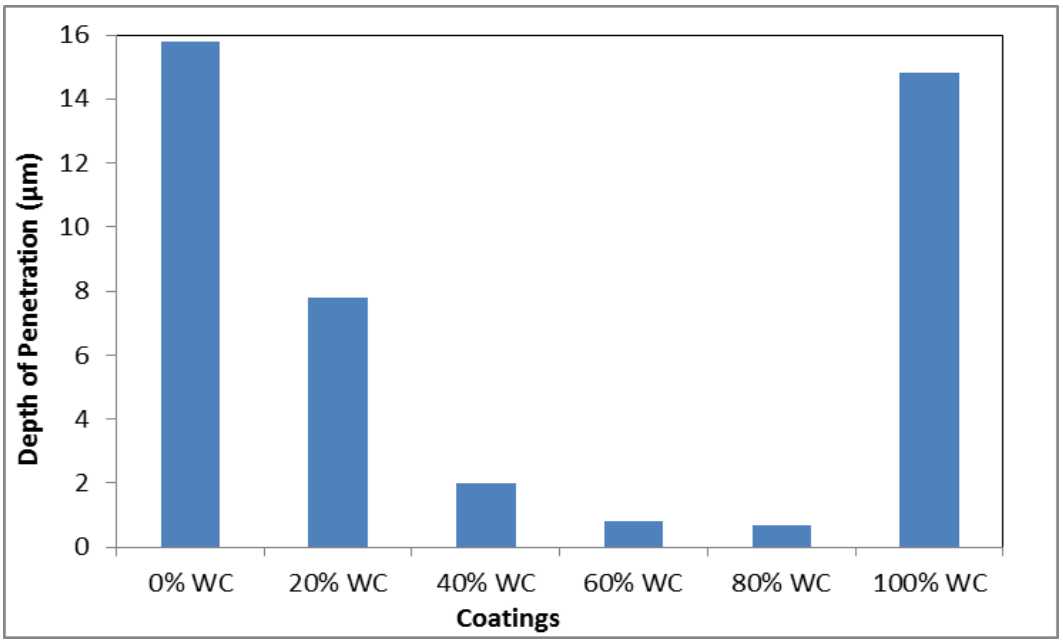

Figure 4.20: Depth of penetration from wear tests on uncoated and coated samples.

Using ASTM standard G 99, sample volume loss was calculated following equation 3.2 in Section 3.3.3. The results shown in Figure 4.21 have no errors as single inputs were calculated.

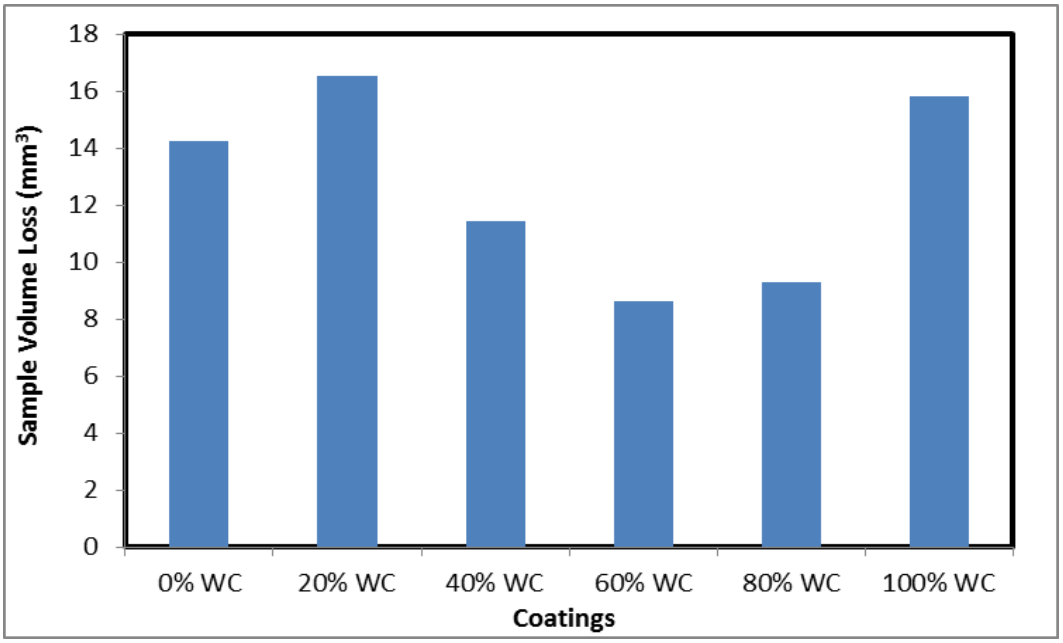

Figure 4.21: Wear rate as a function of sample volume loss of tested samples.

The optical images of the ball scars are shown at the same magnification in Figure 4.22.

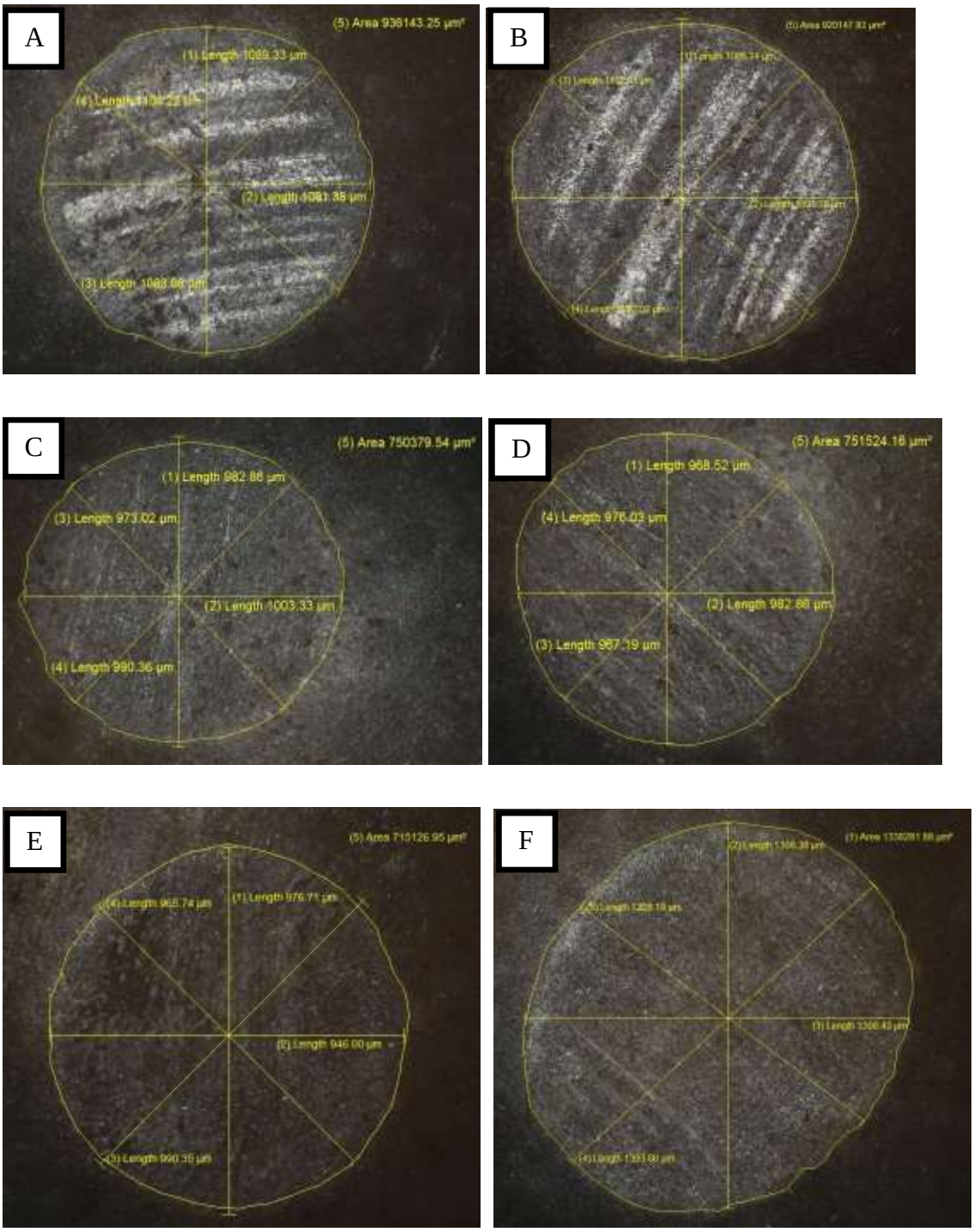

Figure 4.22: Optical images of wear scars on the 100 Cr6 steel balls from: (A) uncoated sample (B) 20 (C) 40 (D) 60 (E) 80 and (F) 100 vol. % WC.

The results of the ball scar diameters are shown in Table 4.9 reveal the extent of wear damage on the 100 Cr6 ball, due to the sliding wear process. These results are plotted in Figure 4.23.

Table 4.9: Total areas and widths of wear scars on 100 Cr6 balls as seen on optical microscope

Ball Scar	Area (μm^2)	1st (μm)	2nd (μm)	3rd (μm)	4th (μm)	Average (mm)
0%WC	936143	1089	1091	1083	1104	1.09 ± 0.01
20%WC	920148	1085	1091	1083	1122	1.10 ± 0.02
40%WC	750380	983	1003	990	973	0.99 ± 0.01
60%WC	751524	969	983	967	976	0.97 ± 0.01
80%WC	715127	977	946	990	966	0.97 ± 0.02
100%WC	1338282	1306	1308	1393	1208	1.30 ± 0.08

The average scar diameter for the ball used on 100% WC coating shows the largest scatter. No error bar is shown for the area of ball scar, as only one areal measurement was taken.

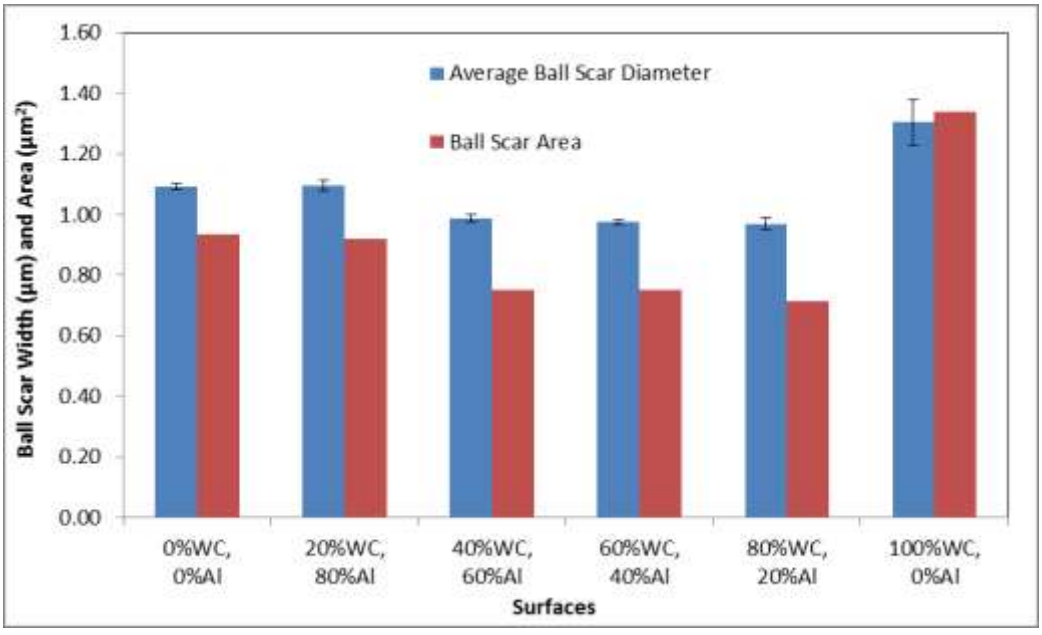

Figure 4.23: 100 Cr6 ball wear scar dimensions as a representation of wear track widths.

4.5.2 SEM and EDS Analyses for Wear Tracks

Wear tracks of uncoated and coated samples were examined to analyse the wear mechanisms.

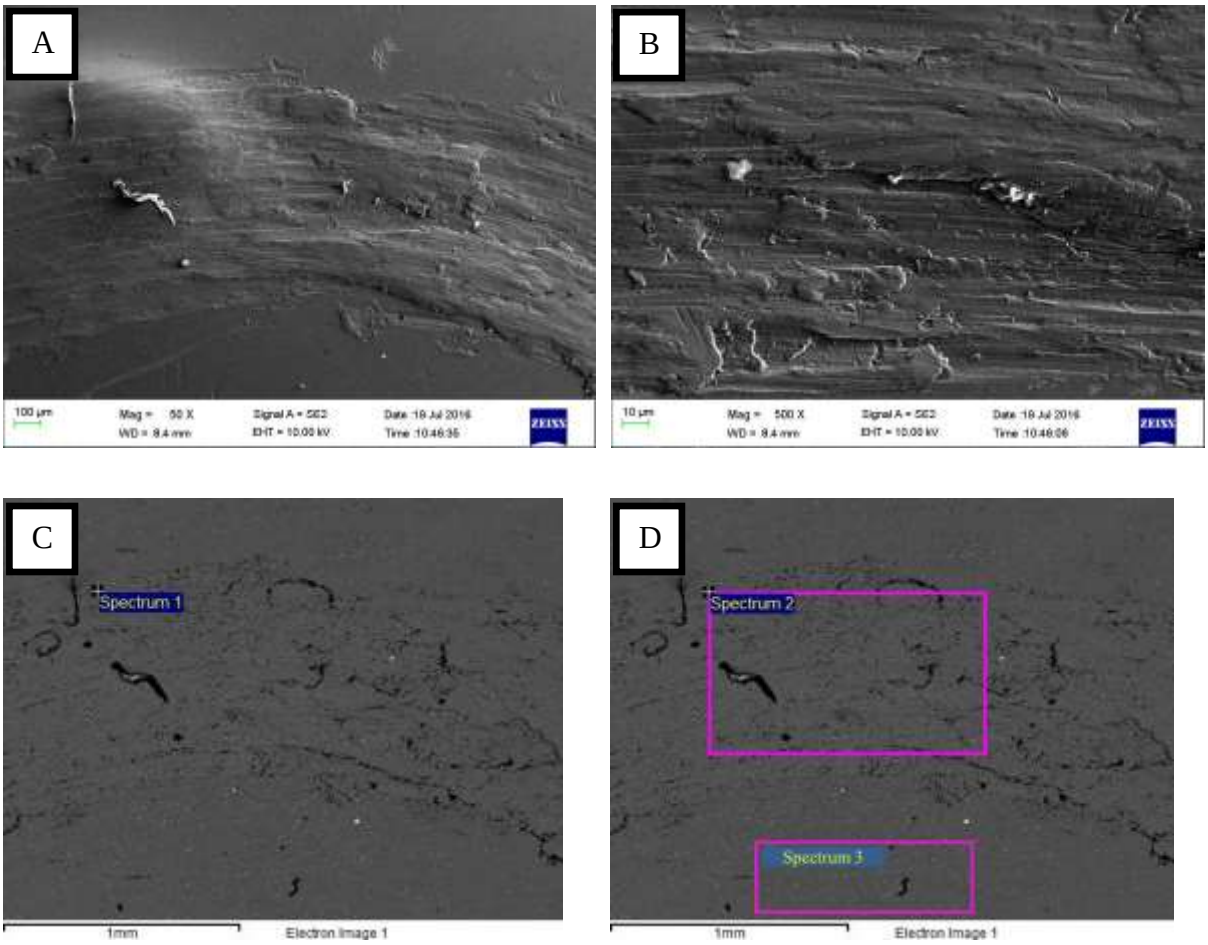

Figure 4.24: SEM (SE) images of the wear scars of the uncoated sample showing (A) Al build-up (B) severe smearing (C) EDS spot analysis in the wear track (D) EDS analysis of an area in the wear track and (E) EDS analysis of an area of the substrate outside the wear track.

The EDS analyses of the spot and areas shown in Figures 4.24 C and D show the main elements within and outside the wear track of the uncoated (as-received) sample. In Figure 4.24D, spectra 2 and 3, show the elements in and outside the wear track respectively. The concentration of the elements in spectra 1 to 3 are given in Table 4.10 and plotted in Figure 4.25.

Table 4.10: Elemental composition within and around the wear track of the as-received sample.

Elements	Spectrum 1 (wt %)	Spectrum 2 (wt %)	Spectrum 3 (wt %)
O	3.5	3.5	7.0
Mg	0.8	0.8	0.7
Al	94.6	94.7	91.3
Si	1.0	1.1	1.1

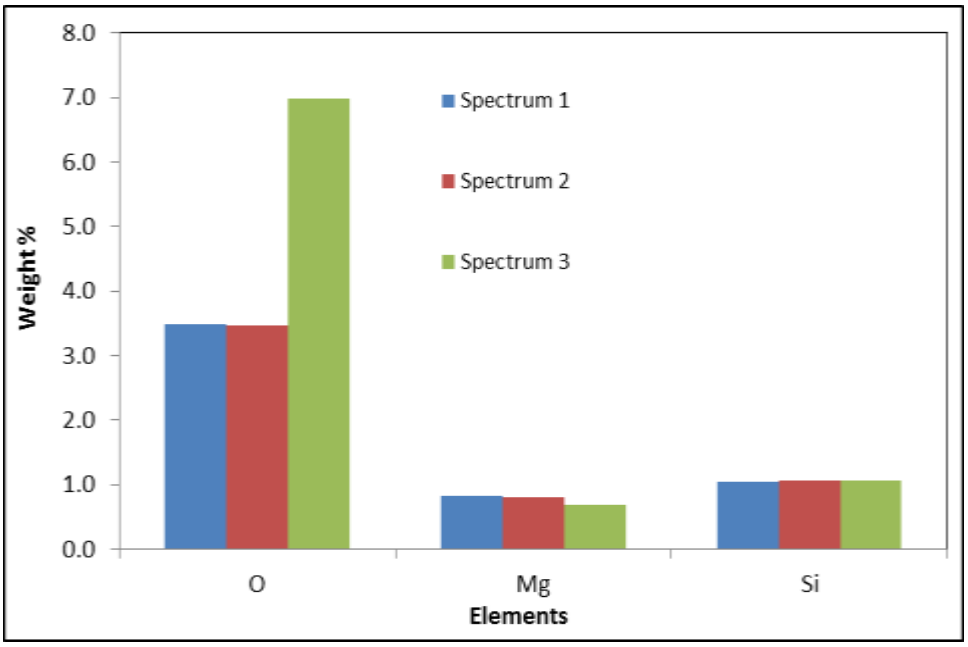

Figure 4.25: The elemental analyses are revealed by wt % of EDS spectra within and around wear track of uncoated sample made up of an Al matrix.

The elements shown in Figure 4.25 are percentage constituents for which AA6082 is the matrix. The amount of Mg and Si is similar both within and outside the wear track. However, there is a higher concentration of oxide layer outside the wear track than inside. This could be due to the significant damage of the protective oxide film during the sliding wear phenomenon.

The SEM images and EDS analyses of the wear tracks of the coated samples are shown in Figures 4.26 – 30.

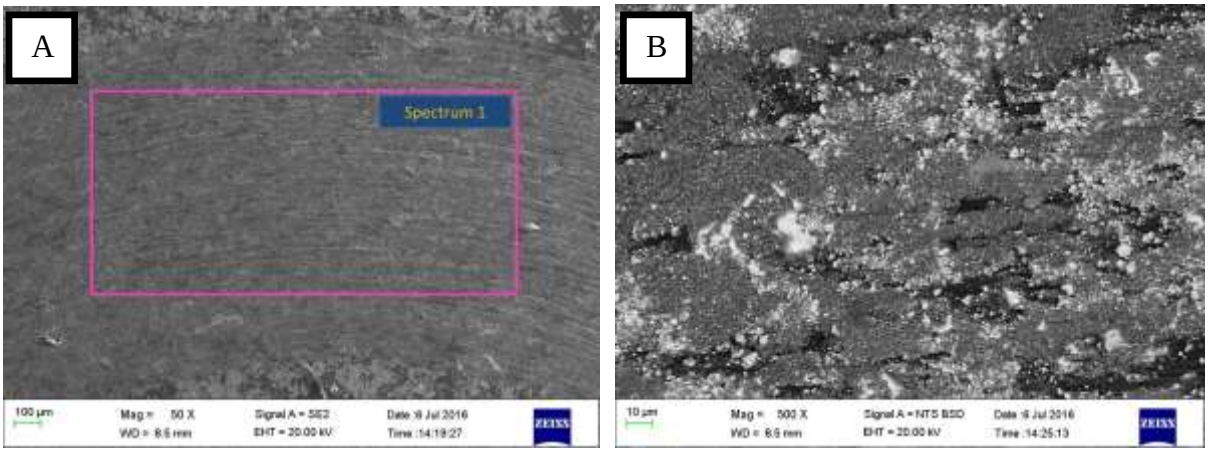

Figure 4.26: SEM (SE and BSE modes) images of the wear track on the 20 vol. % WC coating showing (A) lines along the wear track and the area that was analysed (B) carbide cracking, fragmentation and pull-out.

The absence of Cr within the wear track of the 20 vol. % WC coating is shown in Table 4.11, which is plotted in Figure 31.

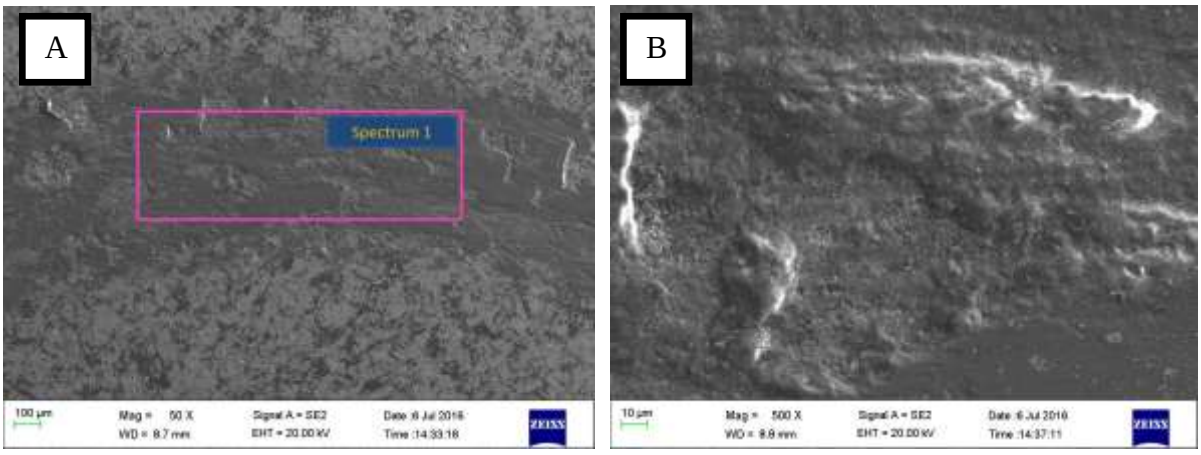

Figure 4.27: SEM (SE) images of the wear track on the 40 vol. % WC coating showing (A) smeared Cr from the 100Cr6 ball on wear track and the area that was analysed (B) carbide drag-out.

The presence of Cr within the wear track of the 40 vol. % WC coating is shown in Table 4.11, which is plotted in Figure 31.

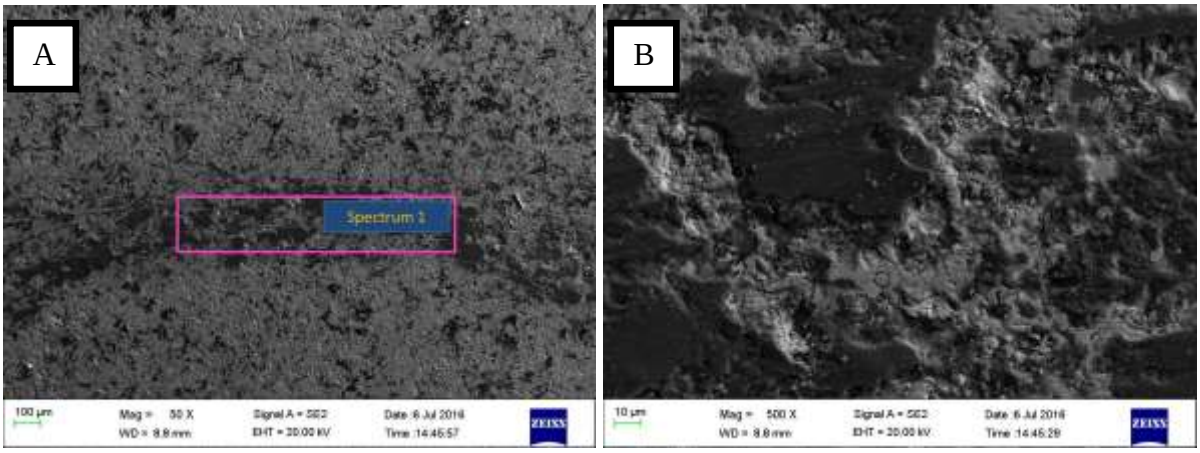

Figure 4.28: SEM (SE) images of the wear track on the 60% WC coating showing (A) wear track with less damage and the area that was analysed (B) carbide cracking, smeared Cr and Al on the wear track.

The presence of Cr within the wear track of the 60 vol. % WC coating is shown in Table 4.11, which is plotted in Figure 31.

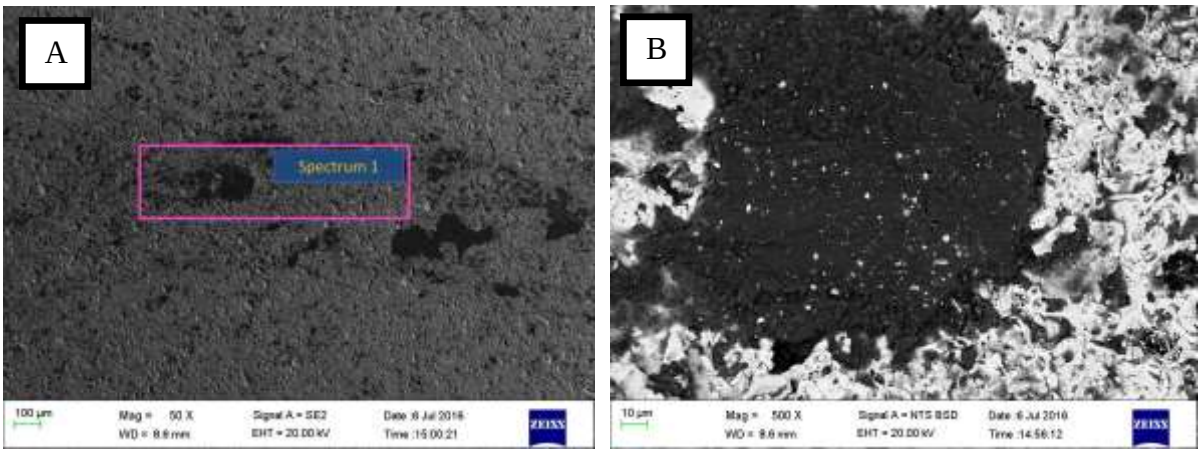

Figure 4.29: SEM (SE and BSE) images of the wear track on the 80% WC coating showing (A) minimal damage with Cr smeared on the wear track and area that was analysed (B) more severe smearing of Cr.

The presence of Cr within the wear track of the 80 vol. % WC coating is shown in Table 4.11, which is plotted in Figure 31.

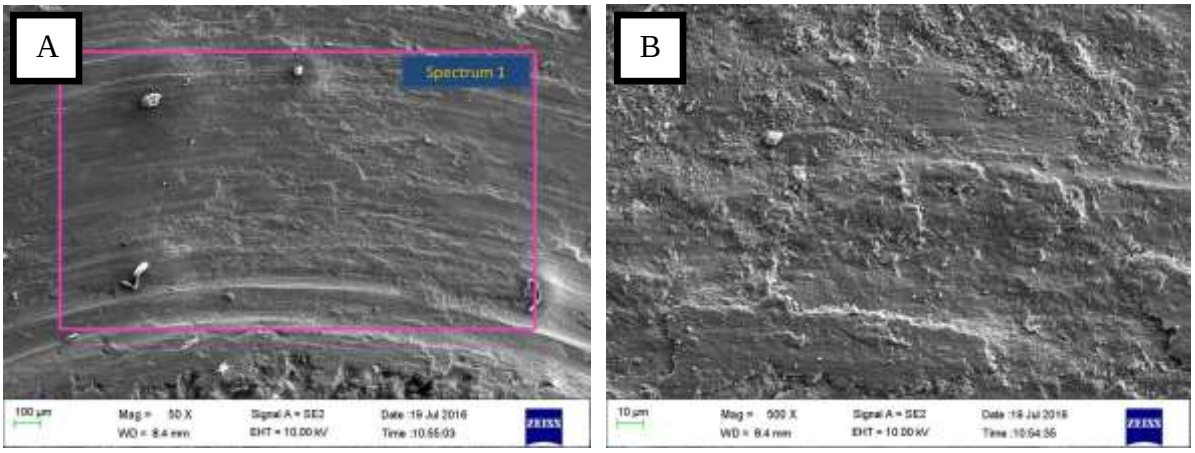

Figure 4.30: SEM (SE) images of the wear track on the 100% WC coating showing (A) lines and damage on wear track and the area that was analysed (B) severely damaged AA6082 wear track.

The absence of Cr particles within the wear track of the 100 vol. % WC coating is shown in Table 4.11, which is plotted in Figure 31.

Table 4.11 shows the elemental compositions of the wear tracks of the 20% WC, 40% WC, 60% WC, 80% WC and 100% WC coatings. These represent the EDS analyses of the wear tracks of the coated samples shown in Figures 4.26 – 30 A. The values are plotted in Figure 4.31.

Table 4.11: EDS analyses on the wear tracks for 20%, 40%, 60%, 80% and 100% WC coatings.

Elements	**20% WC**	**40% WC**	**60% WC**	**80% WC**	**100% WC**
O (wt %)	23.8	36.6	32.7	27.5	34.5
Al (wt %)	25.2	6.6	4.6	2.0	57.7
Cr (wt %)	0.0	0.5	0.5	0.3	0.0
Fe (wt %)	4.5	32.0	28.4	18.1	0.0
W (wt %)	44.2	24.3	33.8	52.2	0.0
Si (wt %)	2.4	0.0	0.0	0.0	7.8

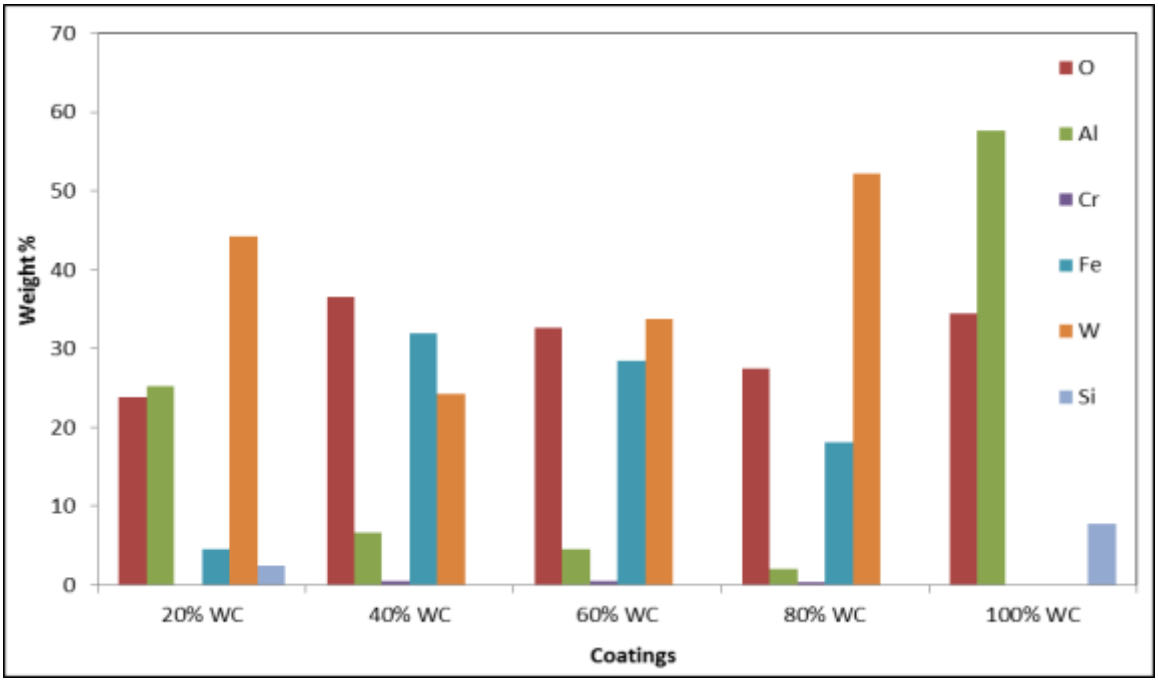

Figure 4.31: Elements in the wear track of coated samples, by wt %, derived by their EDS areal different spectra.

There is an incremental measure of W content progressing through the 40%WC, 60%WC and 80%WC coatings. The 20% WC coating had a higher wt % of W left on its wear track than both 40% WC and 60% WC coatings after sliding wear. The 100%WC coating has no W left on its wear track, as a lack of Al-102 binder caused all the coating to be worn off the substrate.

4.6 Immersion Tests

The immersion tests were performed in acidic (pH = 2.03), alkaline (pH = 11.35) and neutral (pH = 7.45) solution of 3.5% NaCl and the mass loss of the samples were determined. The differences in mass after immersion in the different solutions were used to calculate the corrosion rates as shown in Tables 4.12 – 4.14. Tables F1 and F2 in Appendix F show the length, width and thickness used to calculate the area of samples immersed in the different solutions during the exposure tests. Equation 3.4 was used to calculate corrosion rates of the uncoated samples and the average corrosion rates are shown in Table 4.12, and plotted in Figure 4.32.

Table 4.12: Average corrosion rates of as-received samples immersed in acidic (pH = 2.03), alkaline (pH = 11.35) and neutral (pH = 7.45) solutions.

Exposure Time (days)	CR in Acidic Solution (mm/y)	CR in Alkaline Solution (mm/y)	CR in Neutral Solution (mm/y)
1	5.07×10^{-1}	1.12×10^{0}	0.00
4	3.04×10^{-1}	1.56×10^{-1}	0.00
7	5.07×10^{-1}	4.68×10^{-2}	0.00
14	3.19×10^{-1}	1.79×10^{-2}	0.00

CR = corrosion rate (mm/y)

The corrosion rates for uncoated samples immersed in neutral solution could not be measured since the very thin layer of corrosion products was very tenacious and protective.

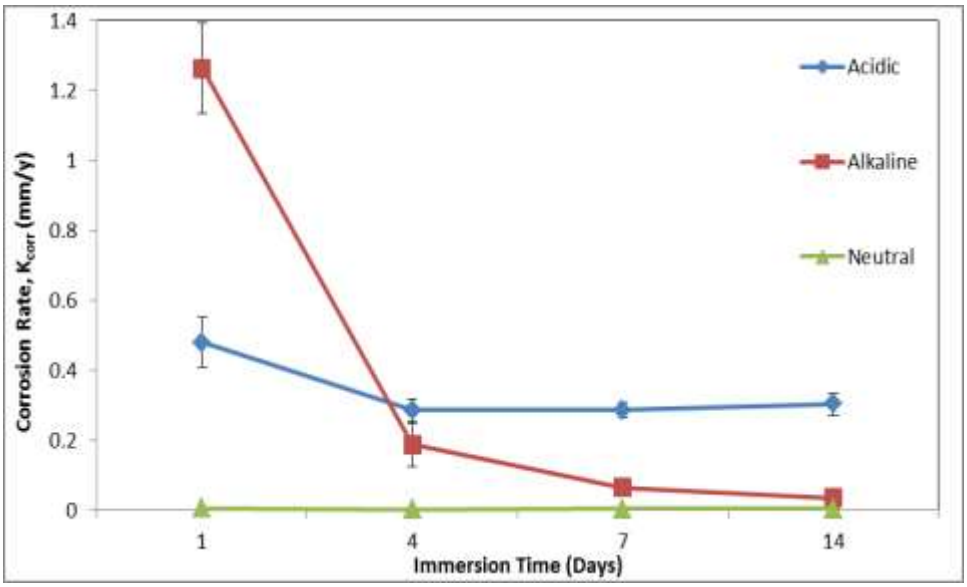

Figure 4.32: Corrosion rates of uncoated samples in acidic, alkaline and neutral media at 25°C.

The as-received sample exposed to the neutral solution gained some added mass due to the formation of corrosion products as shown in the images in Figures 4.33A and 4.33B.

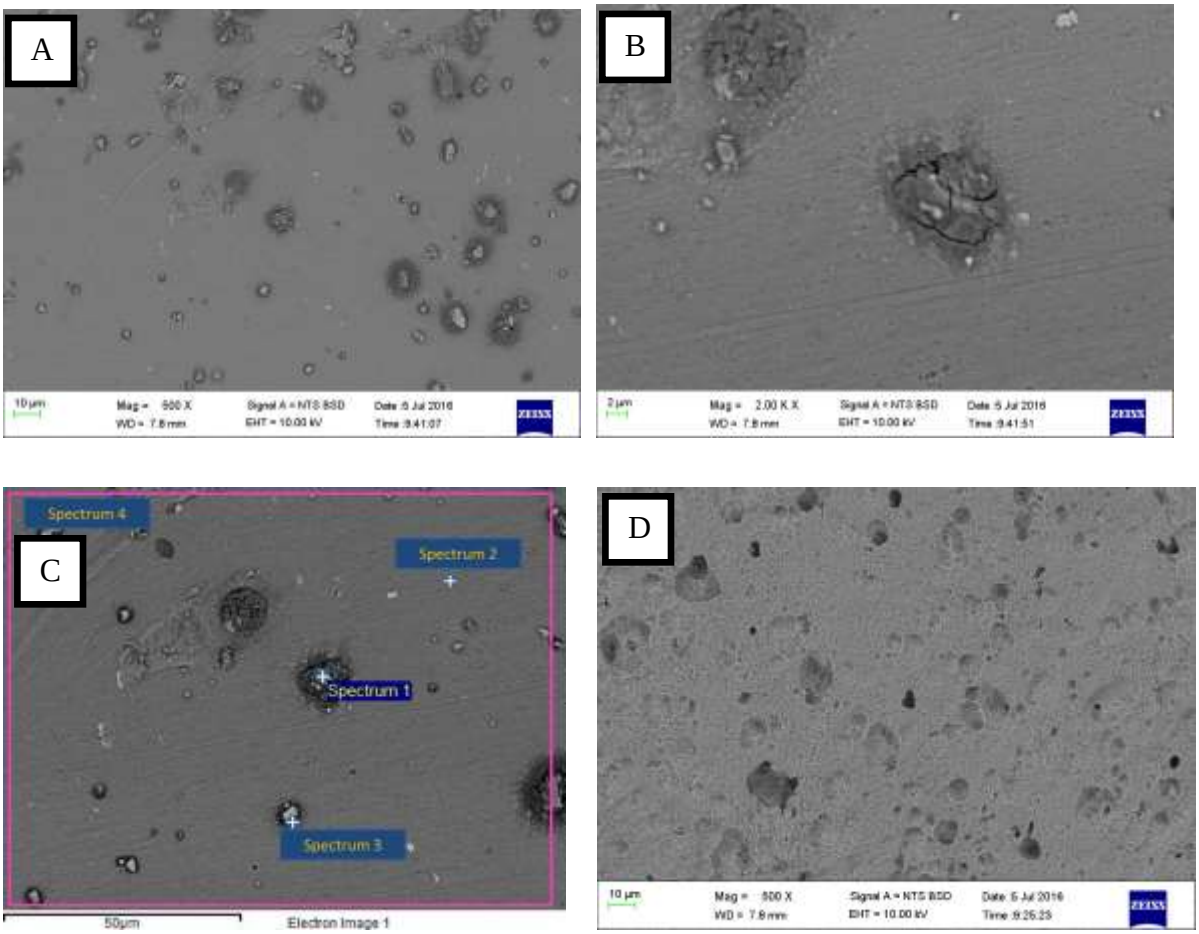

Figure 4.33: SEM (BSE) image showing (A) corrosion products, (B) Al_2O_3 formed on substrate, (C) EDS spot analyses of corrosion products and bare AA6082 as well as area analysed in neutral solution (D) as-received sample immersed for 14 days at 25°C in acidic solution.

Table 4.13 shows the amount of specific elements (wt %) found during EDS analyses, after the immersion tests. These values are plotted in Figure 4.34.

Table 4.13: Exposure of 0% WC (uncoated) sample in neutral solution.

Element	Spectrum 1	Spectrum 2	Spectrum 3	Spectrum 4
O (wt %)	31.5	3.8	13.1	7.4
Na (wt %)	1.8	0.0	0.5	0.0
Mg (wt %)	0.0	0.0	0.7	0.7
Al (wt %)	27.7	95.2	69.3	90.5
Si (wt %)	5.1	0.9	4.4	0.9
Cl (wt %)	3.9	0.2	3.5	0.5
Fe (wt %)	30.0	0.0	5.2	0.0
Mn (wt %)	0.0	0.0	3.3	0.0

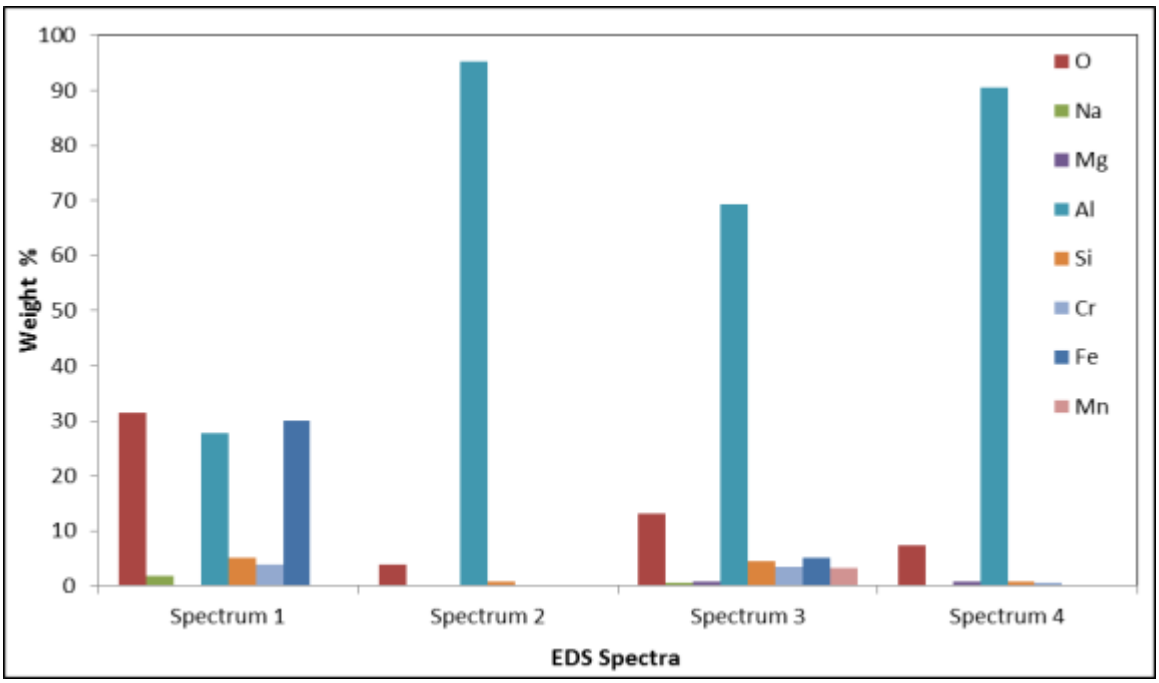

Figure 4.34: EDS results showing elemental composition by wt % of the as-received sample immersed into the neutral solution.

Table 4.13 and Figure 4.34 represent EDS results of the positions indicated on the surface of AA6082 immersed in the neutral solution (pH = 7.45). Spectra 1 and 3 both are spot analyses done on corrosion products. In spectrum 1, the concentration of O and Fe were higher than Al. However, the presence of Al is much higher in the other corrosion product shown in spectrum 3. Spectrum 2 is the spot analysis of the bare AA6082 with no corrosion product. Spectrum 4 is the analysis of the entire area selected, as shown in Figure 4.33.

Coated samples were also exposed to the acidic media (pH= 2.03). For these, a uniform surface area of 3.2 cm^2, smaller than those used for testing uncoated samples, was used. Table 4.14 shows the corrosion rates of uncoated and coated samples immersed into the acidic solution containing H_2SO_4 (pH = 2.03) for 14 days. The 100% WC coating appeared to have the lowest corrosion rate, followed by the 60% WC coating. The error margins for the corrosion rates for duplicate samples were minimal. These values are plotted in Figure 4.35.

Table 4.14: Corrosion rates of uncoated and coated samples immersed in acidic solution.

Coatings (g)	**M_I (g)**	**M_F (g)**	**ML (g)**	**CR (mm/y)**
Uncoated	10.5	10.4788	0.0063	$1.42 \pm 0.07 \times 10^{-1}$
20% WC	12.5	12.4855	0.0089	$1.10 \pm 0.04 \times 10^{-1}$
40% WC	12.7	12.7288	0.0126	$5.35 \pm 0.5 \times 10^{-2}$
60% WC	13.2	13.1859	0.0126	$2.11 \pm 0.3 \times 10^{-2}$
80% WC	13.0	13.0153	0.0004	$5.88 \pm 0.3 \times 10^{-2}$
100% WC	13.5	13.4919	0.0007	$1.95 \pm 0.3 \times 10^{-2}$

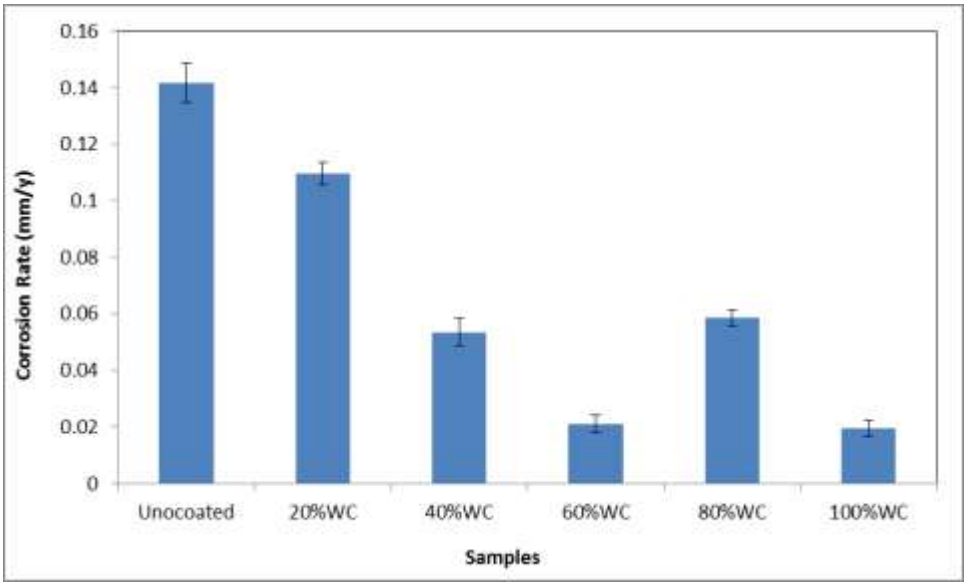

Figure 4.35: Corrosion rates of coated samples immersed for 14 days at 25°C, pH = 2.03.

In Figures 4.36 – 4.39, "Al" represents the Aluminium-102 powder constituent which is the dark region. On the other hand, the "WC" represents the tungsten carbide powder constituent, which is the light region within the coating matrix.

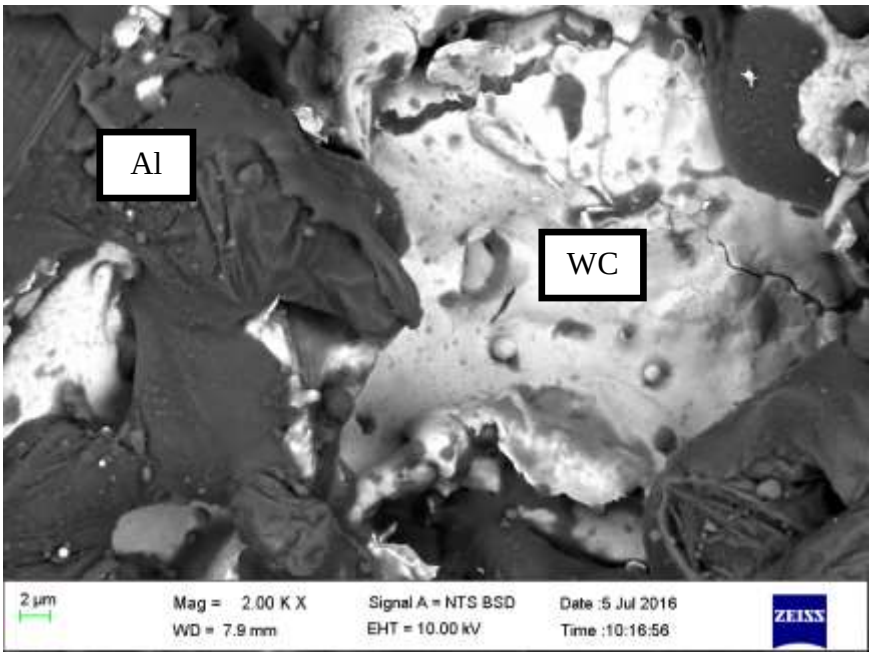

Figure 4.36: SEM (BSD) image showing 20%WC coating exposed to acidic solution.

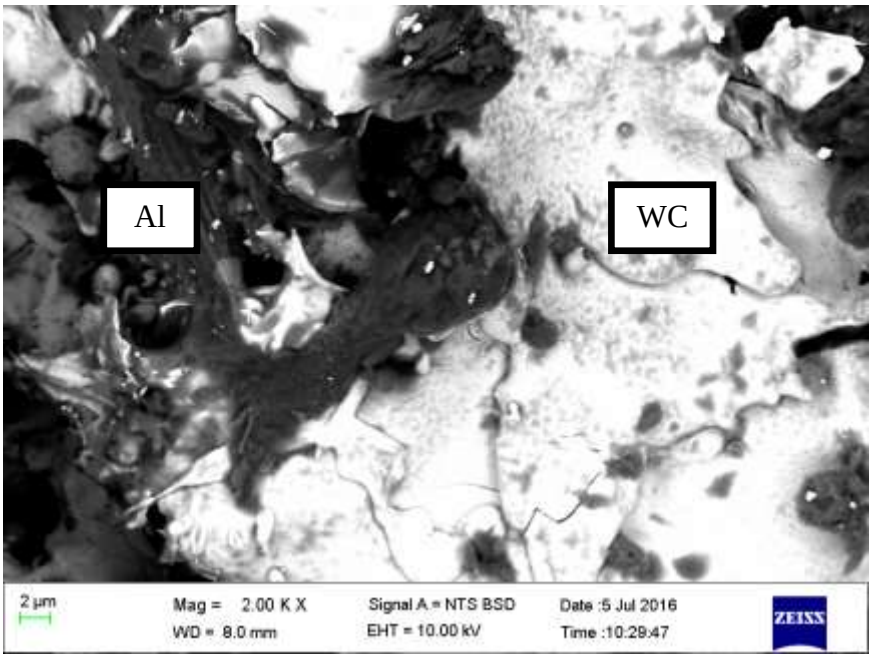

Figure 4.37: SEM (BSD) image showing 40%WC coating exposed to acidic solution.

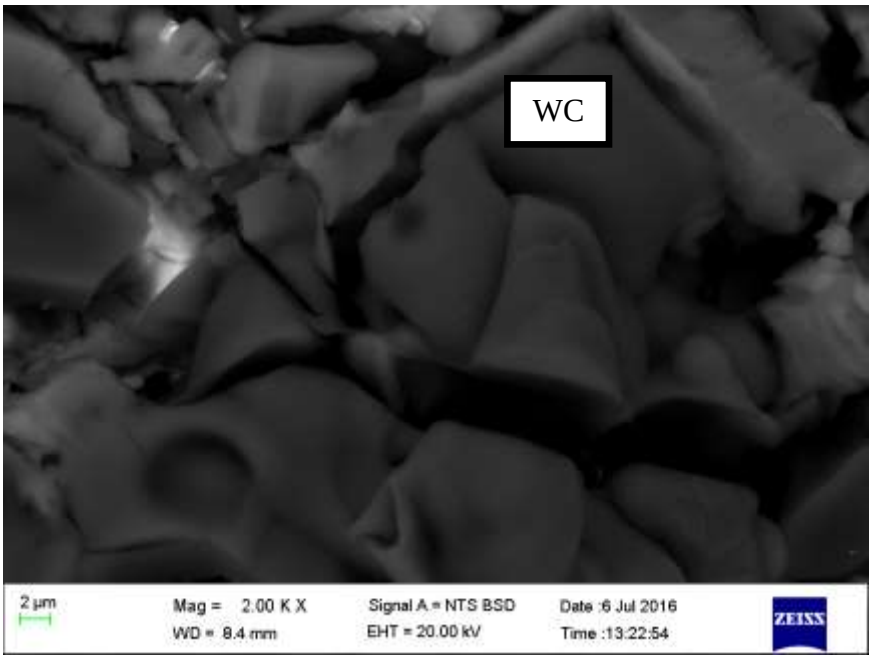

Figure 4.38: SEM (BSD) image showing 60%WC coating exposed to acidic solution.

The coatings appear more tenacious as WC content increases, except the 80% WC coating.

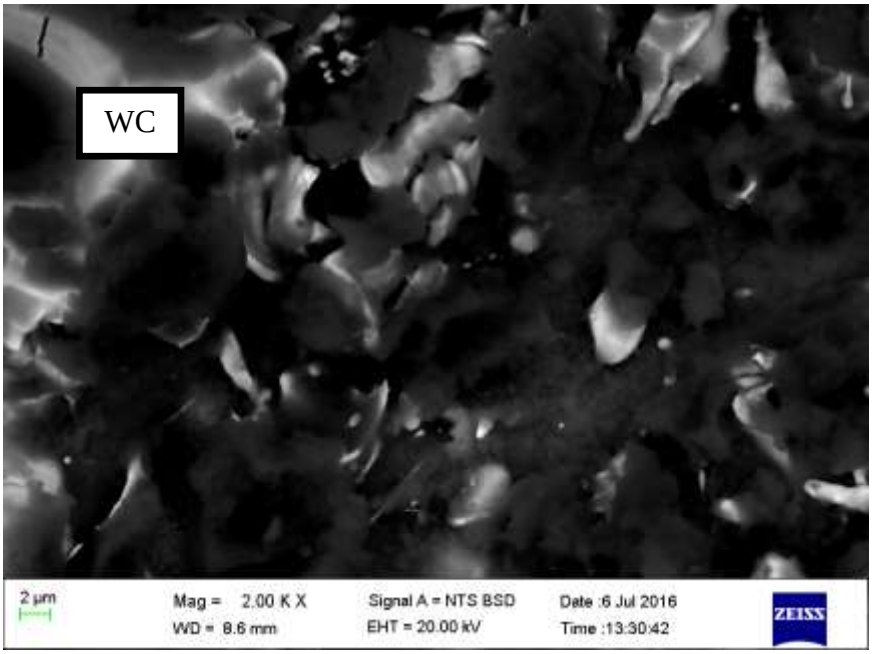

Figure 4.39: SEM (BSD) image showing 80%WC coating exposed to acidic solution.

4.7 Electrochemical Tests

The tests for samples in 3.5% NaCl neutral solution yielded results in the curves in Figure 4.40.

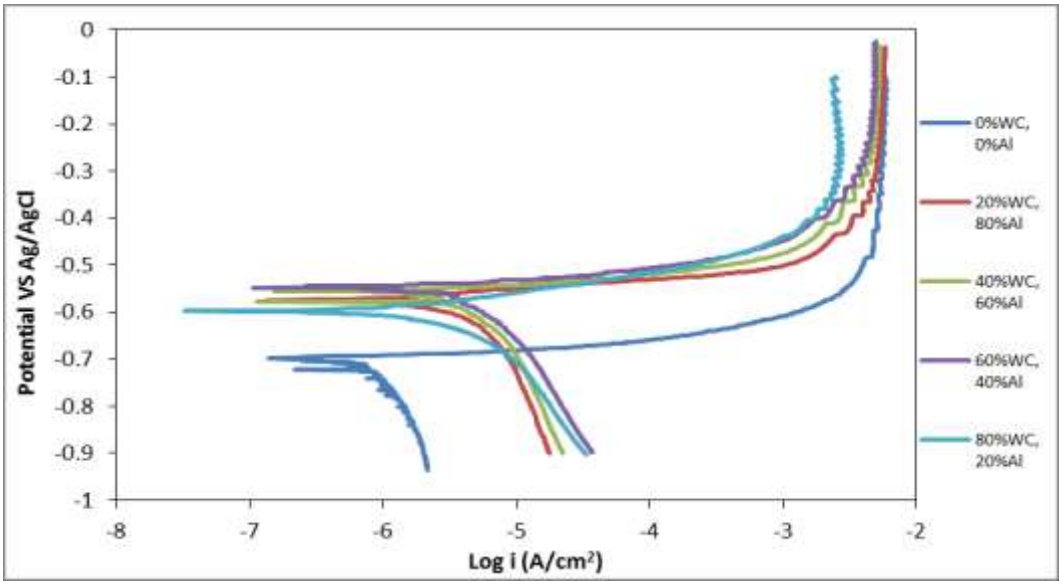

Figure 4.40: Linear polarization curves for samples tested at 25°C, pH = 5.80.

The electrochemical tests for coatings exposed to the acidic solution are shown in Figure 4.41.

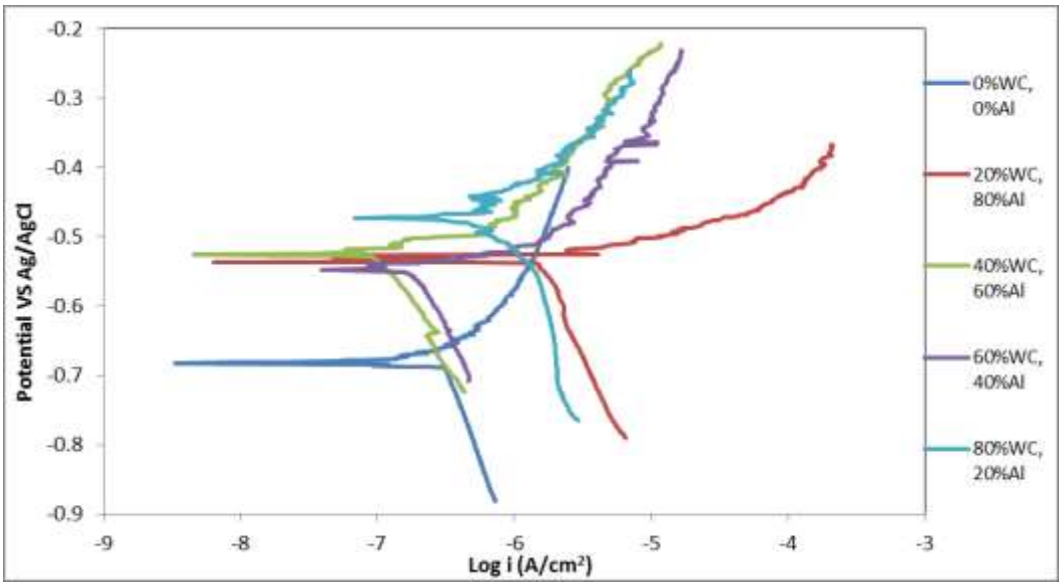

Figure 4.41: Linear polarization curves for samples tested in the acidic 3.5% NaCl solution at 25°C.

Table 4.15 shows polarization resistance data for corrosion rates, plotted in Figure 4.42.

Table 4.15: Corrosion data from the linear polarization resistance method for samples in the neutral and acidic 3.5% NaCl solution.

Coating & pH	ρ (g/cm^3)	E_{corr} (mV)	R_P	i_{corr} (μA/cm^2)	CR (mm/y)
0%WC pH = 2.03	2.70	-681	38838	13.78	1.50×10^{-1}
20%WC pH = 2.03	5.29	-492	97897	1.70	1.41×10^{-2}
40%WC pH = 2.03	7.87	-525	53168	7.90	5.95×10^{-2}
60%WC pH = 2.03	10.46	-548	29447	14.86	1.06×10^{-1}
80%WC pH = 2.03	13.04	-473	13126	20.51	1.42×10^{-1}
0%WC pH = 5.80	2.70	-699	7402	1.64	1.78×10^{-2}
20%WC pH = 5.80	5.29	-575	4704	2.36	1.96×10^{-2}
40%WC pH = 5.80	7.87	-556	2504	7.07	5.32×10^{-2}
60%WC pH = 5.80	10.46	-548	3107	4.20	3.00×10^{-2}
80%WC pH = 5.80	13.04	-598	9562	3.44	2.38×10^{-2}

E_{corr} = corrosion potential

I_{corr} = current density

R_P = polarisation resistance

ρ = density

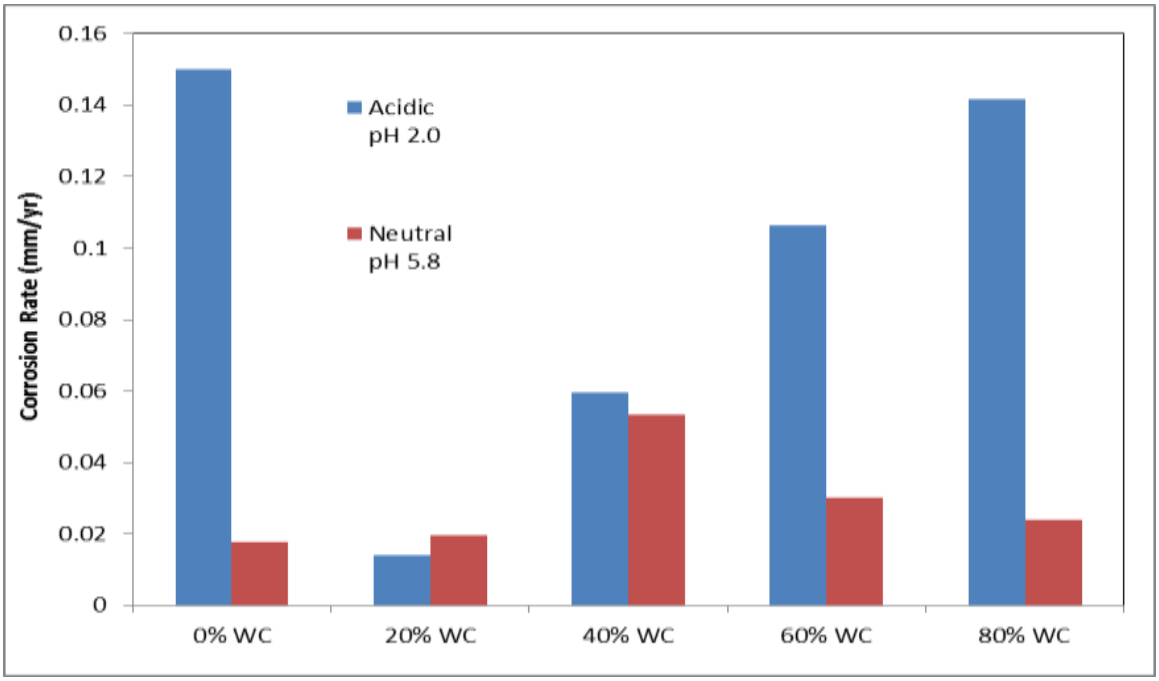

Figure 4.42: Corrosion rates by polarization resistance in acidic and neutral solutions at 25°C.

The corrosion potential in decreasing order from Figures 4.40 and 4.41 is:

60%WC > 40%WC > 20%WC > 80%WC > AA6082 uncoated [Neutral]

80%WC > 40%WC > 20%WC > 60%WC > AA6082 uncoated [Acidic]

Figure 4.42 shows the varying corrosion rates of samples exposed to both acidic and neutral 3.5% NaCl solutions during the linear polarisation tests, using the polarisation resistance technique. The uncoated sample had the highest corrosion rate in acidic solution, while the 40% WC coating had the highest in the neutral solution. However, the 20% WC coating had the lowest corrosion rate in the acidic solution, while the uncoated sample had the lowest in the neutral solution. The rank is:

40%WC > 60%WC > 80%WC > 20%WC > AA6082 uncoated [Neutral]

AA6082 uncoated > 80%WC > 60%WC > 40%WC > 20%WC [Acidic]

Using Tafel extrapolation method, corrosion rates were calculated as shown in Table 4.16 and plotted in Figure 4.43. The 40% WC coating had the lowest corrosion rate while the 20% WC

coating had the highest corrosion rate in acidic 3.5% NaCl solution. However, in the neutral 3.5% NaCl solution, the as-received AA6082 sample had the lowest corrosion rate while the 40% WC coating had the highest corrosion rate.

Table 4.16: Corrosion data from the Tafel extrapolation method for samples in the neutral and acidic 3.5% NaCl solution.

Coating and pH	**ρ (g/cm^3)**	**E_{corr} (mV)**	**i_{corr} (μA/cm^2)**	**Corrosion Rate (mm/y)**
0%WC pH = 2.03	2.70	-683	0.29	3.00×10^{-3}
20%WC pH = 2.03	5.29	-536	1.48	9.00×10^{-3}
40%WC pH = 2.03	7.87	-525	0.10	1.00×10^{-3}
60%WC pH = 2.03	10.46	-547	0.18	3.00×10^{-3}
80%WC pH = 2.03	13.04	-473	0.47	5.00×10^{-3}
0%WC pH = 5.80	2.70	-699	0.81	9.00×10^{-3}
20%WC pH = 5.80	5.29	-578	2.75	3.80×10^{-2}
40%WC pH = 5.80	7.87	-578	2.75	4.10×10^{-2}
60%WC pH = 5.80	10.46	-548	1.78	2.50×10^{-2}
80%WC pH = 5.80	13.04	-598	1.48	1.70×10^{-2}

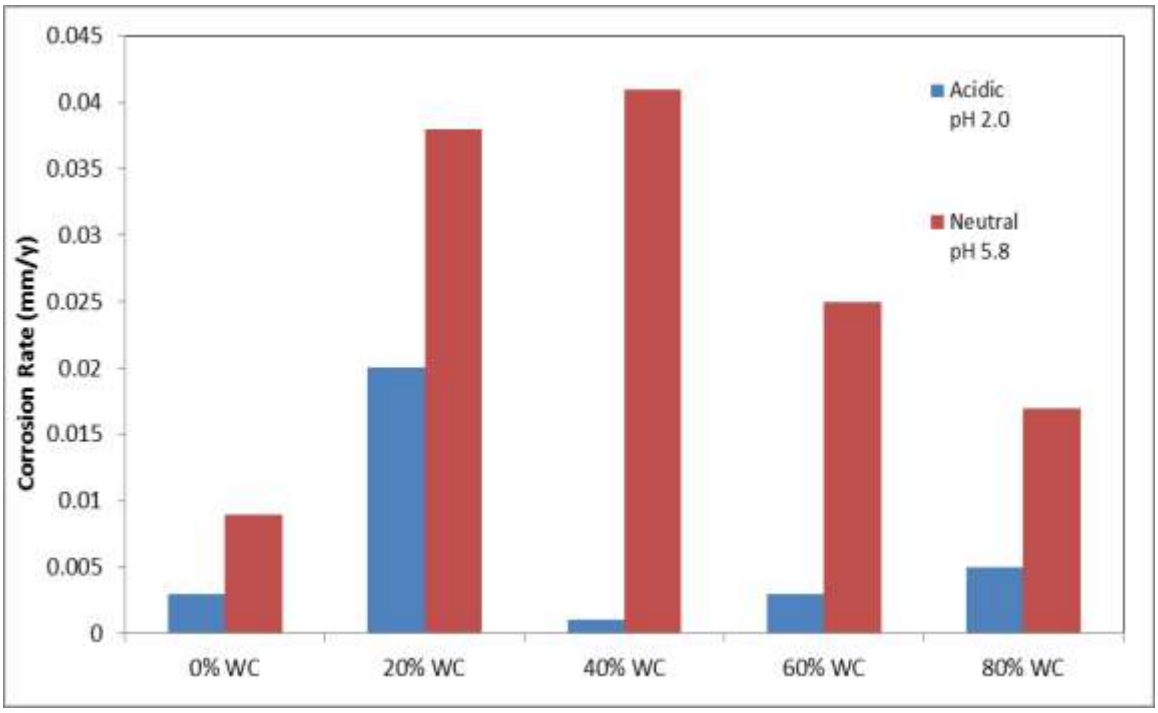

Figure 4.43: Corrosion rates by Tafel extrapolation in acidic and neutral solutions at 25°C.

The 100% WC coating was excluded from the electrochemical tests plotted in Figures 4.42 and 4.43 as it already failed the wear test due to the weak bond with the substrate. The uncoated AA6082 sample, which showed the lowest corrosion resistance in the neutral solution, performed best in the acidic solution. Although the 40% WC coating showed the highest corrosion resistance in the neutral solution, it was the second poorest in acidic solution after 20% WC.

By Tafel extrapolation shown in Figure 4.43, however, the rank of current densities is:

40%WC > 20%WC > 60%WC > 80%WC > AA6082 uncoated [Neutral]

20%WC > 80%WC > AA6082 uncoated > 60%WC > 40%WC [Acidic]

CHAPTER 5: DISCUSSION

This study has taken into account the effect of heat treatment on the AA6082 as-received in the T651 condition. Thereafter, plasma spraying was used to deposit wear resistant coatings on an AA6082 substrate. In order to ascertain how AA6082 substrate responded to heat from the plasma spray process, the coated substrate was subjected to mechanical tests. Afterwards, uncoated and coated samples were tested for hardness, wear and corrosion resistance.

5.1 Heat treatment on AA6082

Standard heat treatment procedures, promulgated by Paterson (2007a) for the Al industry in Southern Africa, show that the hardness and tensile strength of the heat treated samples reach a definite peak value in their T6 condition. This is similar to results obtained for experiment B in Figures 4.1 and 4.2 respectively. However, modifications such as solution treatment time and post-quench storage temperature resulted in a significant difference in the results from experiment A and B as shown in the previous chapter.

5.1.1 Heat treatment for experiment A

After quenching in water at room temperature, this study sought to establish the possibility of natural ageing occurring at the temperature higher than that used for storage. The samples were stored in a refrigerator at 0°C for 24 hours, during which some ageing occurred (Banhart et al., 2010; Strobel et al., 2016) as expected. From the hardness values in Figure 4.1, it was clear that there had been an alteration in the hardening mechanism of materials stored in the refrigerator at 0°C. Based on the industrial requirements to avoid solute clustering in post-quenched solution treated samples (Kovaćs et al., 1972), freezing the precipitates to avoid natural ageing is deemed effective only when the storage temperature is at or below –7°C (Paterson, 2007).

Natural ageing did occur at 0°C, although not as much as would have at room temperature. This is because 0°C was still not low enough to hinder the formation of precipitates in the supersaturated alloy. Therefore, natural pre-ageing, albeit for only 24 hours, lowered the effectiveness of the subsequent artificial ageing process (Pashley et al. 1967; Kleiner et al. 2001; Yamada et al. 2000; Ravi 2004). Experiment A has therefore confirmed the negative effect of natural pre-ageing in 6xxx series Al alloys.

5.1.2 Heat treatment for experiment B

Experiment B was carried out following recommended guidelines laid out by Paterson (2007) for heat treatment. After quenching in water at room temperature, all solution heat treated samples were stored at –17°C. This low temperature sufficiently cooled the samples to maintain the supersaturated solid solution and prevent natural ageing. The results of hardness and tensile strength yielded the expected definite peak values at T6.

The hardest region, being of peak (T6) strength for both top surface and cross-section of the samples tested, was obtained at 20 hours of artificial ageing, having its peak strength with hardness values of about 100±2 HV. This hardness value for the 20-hour aged sample shown in Table 4.3 was similar to that of the as-received sample shown in Table 4.1. This similarity between the as-received alloy in T651 condition and the peak-aged T6 makes experiment B the acceptable procedure.

From the time-temperature relationship shown in Figure 2.7, it is clear that a decreased ageing temperature requires an increased ageing time. For instance, in order to reach the peak aged T6 condition, more time is required for ageing at 150°C than at 190°C. An insufficient soaking time of 2 hours, prior to artificial ageing, was used in experiment A (Prabhukhot and Prasad, 2015); this, in addition to possible natural ageing at 0°C, rendered the entire heat treatment procedure ineffective. For the current study, maximum T6 hardness and strength was attained after 20 hours. Theoretically, this gives full control to factory workers who choose to work with particular temperatures which allow the full ageing cycle within certain durations for specific alloys. For this reason, the temperature that best corresponds with 8 to 10 hours work shift is mostly chosen in industry.

The tensile strength results for experiment B shown in Figure 4.2 agrees with that shown in Figure 2.7, as the curve representing 190°C lies within a range similar to the 175°C used in this study. Peak aged alloys have been found susceptible to stress corrosion cracking, intergranular corrosion and exfoliation corrosion (Wloka et al., 2007). To have an effective and efficient result in transport applications, up to 15% peak strength may be forfeited through over-ageing. This is so that more resilient alloys will not compromise the inherent properties considered during material selection (Chen et al., 2012; Knight et al., 2011, 2010; Yang et al., 2015).

Regardless of the volume fraction of particles, peak strength will occur at a given particle size, as the strengthening mechanisms have a square root relationship with the actual increase in strength (Gladman, 1999). Continued ageing for a longer period derives smaller incoherent particles with low strength, being the T7 temper at 40 hours and beyond (Kverneland et al., 2011; Peng et al., 2017). For example, increasing the coherency strain can enhance hardening in metals, thereby reducing the critical particle size required for maximum alloy strengthening. This is because critical particle size was attained at T6 condition, thus producing maximum strength at 20 hours, after which the mechanism is reversed and precipitation hardening reduces (Gladman, 1999).

The curve for 190°C lies within a range similar to the 175°C used in this study. Also, the peak aged T6 temper occurs at the one-day mark on the log curve which agrees with 20-hour range. This confirms that experiment B is the reliable base line for further study on AA6082. As Leo et al. (2016) concluded, heat treatment plays a major role precipitate growth and the microstructure of Al alloys. The microstructure of AA6082 used in this study was expected to change as it was solution treated for six hours at 520°C to achieve the supersaturated α solid solution, after which precipitation hardening takes place as the ageing time progressed from T4 up to and beyond the T6 temper conditions (Xu et al., 2017). From the microstructures shown in Figures 4.3 to 4.6, a progressive grain refinement process occurred up to the 40-hour ageing time, thus confirming the hypotheses made by Kumar et al. (2003) and Khan et al. (2008).

5.1.3 SEM and EDS for uncoated samples

Through an atomic model derived for GP-zones in a typical 6082 Al-Mg-Si system, Marioara et al. (2001) affirmed that the strength of the alloy, at any point during the peak ageing process, is determined by the volume fraction, structure and coherency of precipitates in relation to the bulk Al matrix. The research carried out by Myhr et al. (2001), regarding how age hardening causes controlled precipitation to harden alloys to maximum strength levels, holds in this study. The ultimate tensile strength and yield strength values of experiment B samples, shown in Figure 4.2, show the definite peak strength at T6 condition of AA6082. Tensile strength and other mechanical properties are improved as dislocation movements are slowed down through precipitation hardening (Gladman, 1999).

5.2 Mechanical Properties of Samples

The uncoated samples were 12 mm in thickness and, since AA6082 is a good conductor of heat, it was important to investigate the influence of the proposed thermal spray treatment on the structural strength and hardness of the AA6082. The plasma spray process melts the Al-102 powder which, having a much lower melting point than WC, then re-solidified to bind the WC particles onto the substrate.

5.2.1 Vickers Hardness and Micro-hardness Profile for Uncoated and Coated Samples

Vickers hardness readings were taken by directly indenting the top surface of the coating. Table 4.7 shows that these hardness values of the coating increased with increasing WC concentration. The 80% and 100% of WC coatings had similar hardness values which were the highest. However, the 100% WC coating was discarded for further use as it failed the wear test.

The cross sectional hardness measurements showed that maximum hardness at about 100 HV. The hardness of these substrate portions of the coated samples remained almost unchanged, similar to that of the as-received sample. Therefore, the thermal spray process did not have an adverse effect on bulk properties of the uncoated (as-received) AA6082.

Figure 4.10 represents the micro-hardness profile taken diagonally across the interface on the cross section of the sprayed samples. Certain particular points on the coated surface were harder than other points. This was due to inhomogeneous distribution of WC and Al-102 powder particles in the coating matrix during the plasma-spraying process shown in Figure 4.11.

5.2.2 SEM of coated samples

Figures 4.12 – 4.16 show SEM images of polished cross-sections of the coated samples, showing the various coating-substrate interfaces. A good adhesion of the 20% WC coating to the substrate is shown in Figure 4.12. Samples coated with 40% WC bonded adequately with the substrate as shown in Figure 4.13. From Figure 4.14, the 60% WC coating bonded well with the substrate, as the Al-102 binder was substantial. Samples coated with 80% WC in Figure 4.15 also bonded reasonably well with the substrate even though the Al-102 binder content was only 20%. Similar to the other coatings, the 100% WC coating also appeared to bond well with the substrate.

However, due to the absence of the Al-102 binder, the 100% WC coating delaminated during the grinding and polishing procedure, and much more during the sliding wear test.

5.3 Sliding Wear

Sliding wear is a common phenomenon in manufacturing where, due to machining and cutting, tools become degraded. The extent of damage depends on composition, microstructure, hardness, absence of a lubricant and the conditions under which the operation is taking place (Hutchings, 1992). For this study, WC was used as the wear resistant material with which the AA6082 substrate was coated. Unlike most existing research reported in literature on hard metals with Co binder, Al-12Si powder was used as the binder for this study. There was a significantly difference between the coefficients of friction and the wear rates of the different coatings and those of the uncoated sample.

5.3.1 Coefficients of friction (CoF)

All samples were tested for sliding wear. As the sliding experiment commenced, the uncoated AA6082 had the highest CoF, while samples with 20%, 40%, 60% and 80% WC all had similarly low CoF. The CoF of the uncoated sample slightly reduced with sliding distance, while others increased gradually, until all samples stabilized after a distance of 150 m. However, there were obvious differences in wear responses of all the samples. Samples with 20% and 40% WC were the most prone to losing much of their hard coatings as sliding wear commenced. However, those having 60% and 80% WC retained their hard coatings and, therefore, maintained relatively low CoFs. For the sample coated with 100% WC, all of its coating was immediately removed as there was no Al-102 binder. Therefore, it behaved as though it had no coating after a sliding distance of less than 10 m, as shown in Figure 4.19.

5.3.2 Penetration Depth and Wear Track Analysis

All samples showed different responses to sliding wear, as their surface compositions varied widely. Figure 4.20 shows the measured depth of penetration for all the samples. The uncoated sample had the deepest penetration and severe wear damage as seen in the optical microscopy images in Figure 4.17A. Large chunks of the AA6082 were dragged out and smeared over the

wear track, resulting in material build-up clearly shown in the SEM image. Figures 4.17B–F show the wear tracks of the other coated samples on which sliding wear was performed.

The 20%WC coating was almost as badly damaged as the uncoated sample. This is deduced by a wide wear track shown in Figure 4.17B. The 20% WC coating was seen to have been more deeply penetrated than 40% WC in Figure 4.17C. Although Al-102 powder was the binder, its higher concentration rendered the coating susceptible to erosion by the harder 100Cr6 ball used in CSM tribometer. Rather, an increase in WC concentration improved the wear resistance of the coated samples. However, 60% and 80% WC coatings had similar depths of penetration.

Table 4.8 and Figure 4.18 show that the 60% WC coating had the smallest wear track width and was the least worn coating. Figure 4.21 also shows that 60% WC had the least sample volume loss. Therefore, the 60% WC coating is the most preferred option as it is the most efficient of all the effective coatings. The 100% WC coating showed a similar penetration depth to the uncoated sample. Since the 100% WC coating delaminated from the substrate during the sliding experiment due to the complete absence of Al-102 binder which should assist the WC in adhering to the substrate. This weak adhesion was first observed during grinding and polishing of the samples. From effectiveness and economic points of view, the delamination of the 100% WC coating is a waste of material and energy. This 100% WC coating was therefore completely discarded as an option.

Figure 4.24A represents the SEM image of wear track for the uncoated AA6082, where due to the smearing of Al by the hard 100Cr6 ball in the CSM tribometer, a noticeable build-up of Al was observed. This severe smearing is shown, at higher magnification, by Figure 4.24B. The SEM image in figure 4.26A shows lines along the wear track of sample coated with 20% WC. A higher magnification of the same SEM view in Figure 4.26B confirmed that the lines were accompanied by cracking, fragmentation and drag-out of carbide particles from the matrix.

The 100 Cr6 ball was smeared more against the sample surface as the concentration of the harder WC increased. The Cr particles identified by EDS analysis in Table 4.11 and Figure 4.41 were mostly smeared against both surfaces while Al particles took the background binding role for the surface coating matrix. From Figure 4.30, the damage along the wear track of 100% WC coating

was as severe as that of the uncoated sample shown in Figure 4.24 because the WC was completely removed from the substrate just after sliding commenced.

Optical images of wear scars on the 100 Cr6 ball surface, used in the CSM tribometer to abrade the uncoated and coated samples, are shown in figures 4.23. The scars on the ball surfaces did not all take the shape of a regular circle. WC contents, which were not evenly distributed throughout the coating, made the ball wear differently at varying points of abrasive impact. The general ranking in diameters of ball scars shown in Table 4.9 and plotted in Figure 4.23 are similar to the ranking of sample wear track widths shown in Table 4.8 and plotted Figure 4.17.

5.4 Corrosion

The purpose for considering a WC-based coating was the advantage of high hardness and potential to improve the mechanical and wear properties of AA6082 surface. However, it was imperative to evaluate how the wear resistant coatings performed in different corrosive media. The choice of the most preferred coating would be a function of overall mechanical properties, material and process cost as well as resultant tare mass. It was established that heat from the plasma spray process employed to coat the substrate did not affect the mechanical properties of AA6082. The WC powder was 99.9% pure while the Al-102 powder used for this study contained 12% Si. The Si adds excellent flow characteristics. Al_2O_3 thus constitutes the dominant corrosion products expected in large amounts when exposed to corrosive media. Coupons were subjected to exposure and electrochemical tests.

5.4.1 Immersion Tests

Samples immersed in the neutral solution of 3.5% NaCl showed no mass loss. For samples exposed to the alkaline solution, the most severe corrosion rates occurred initially. Figure 4.32 shows that the corrosion rate dropped drastically and showed lower corrosion rates on the fourth day. By the seventh day, the corrosion rate was even lower and on the fourteenth day, the corrosion rate was insignificant. In the acidic solution, however, the corrosion rate was not as high after one day as recorded in alkaline solution, but dropped slightly and remained constant. The EDS results in Figure 4.34 show the elemental compositions of the corrosion products formed on the surface of the uncoated sample exposed to the neutral solution. Spectra 1 and 3 showed a wider range of constituent elements because they were corrosion products.

Of all the coated samples immersed in the acidic 3.5% NaCl solution, the 20% WC had the highest corrosion rate. Apart from the 100% WC which was discarded due to delamination, the 60% WC coating had the lowest corrosion rate of all samples immersed in the acidic solution for the exposure test, as shown in Figure 4.35. All the coated samples had lower corrosion rates than the uncoated sample.

5.4.2 Electrochemistry

The electrochemical characteristics of the uncoated and coated samples were reported. The uncoated coupons had the lowest corrosion potential in both neutral and acidic 3.5% NaCl media as shown in Figures 4.40 and 4.41 respectively. These results showed that the corrosion resistance of all coated surfaces were similar to the substrate. The 100%WC coating was not analysed because it failed the wear test. In this study, the corrosion rates were derived from the polarization resistance. These corrosion rates differed from the results of immersion tests. As seen from the immersion tests, the exposure time had a significant effect on the corrosion rates. For the immersion tests, the duration was varied over some days, while the electrochemical tests were performed immediately after exposure.

The binder content has been reported to affect the corrosion rate of WC-Co coatings (Kellner et al., 2009). Oh et al. (2016) justified the use of composite-based coatings, combining WC with Al_2O_3 which replaces the Co binder, as corrosion was seen to occur preferentially in the binder phase for a conventional WC-Co matrix. From a study carried out by Hochstrasser-Kurz et al. (2007), the amount of Co binder played a major role in the corrosion behaviour of the WC-Co matrix. Ghandehari (1980) found that W dissolves while Co passivates in an alkaline solution. Similarly, in this study, Al-102 in the acidic behaved differently than in the neutral solution.

In the neutral solution, the 40% WC coating had the highest corrosion rate while the uncoated sample had the lowest (from polarisation resistance). In the acidic solution, however, all coated samples had a lower corrosion rate than the uncoated sample, and corrosion rates of the coated samples decreased with lower WC contents. In the WC-Co matrix, the binder phase is known to dissolve preferentially in the acidic solution (Kamdi et al., 2014; Oh et al., 2016). In this study, the 20% WC coating had a higher concentration of the binder (80% Al-102) to keep it from

corroding rapidly. It follows that the 80% WC coating was rendered less effective in corrosion resistance, as its 20% Al-102 binder content was smaller.

Prior to this study, no work had been reported on the combination of WC and Al-102 powders as the coating matrix for any Al alloy substrate. Figures 4.36 – 4.39 show the SEM images of the surfaces of coatings, with 20 – 80% WC, exposed to the acidic 3.5% NaCl solution. Figure 4.36 shows the effect of the corrosive medium on the 20% WC coating. Its 80 vol. % Al-102 binder resulted in the formation of a larger volume of the tenacious layers in regions not fully protected by the smaller volume of corrosion-resistant WC. The acidic solution exhibited a slightly higher corrosion rate on the 40% WC coating as Figure 4.37 shows. The WC particles in both 60% and 80% WC were sufficiently resistant to the effect of the acidic solution.

The WC/Al-102 powder distribution in the 80% WC was less homogeneous than in 60% WC coating, as the light WC regions highly populated its surface. Also, the binder content in 80% WC was not sufficient to exhibit a corrosion resistance as reliable as 60% WC. Besides the superior corrosion resistance, the use of less WC material made 60% WC a preferred coating to 80% WC. The complete absence of Al-102 binder makes 100% WC coating delaminate from the AA6082 substrate so easily that it was rendered totally unreliable for any corrosive environment.

The ultimate determinant for profit in transport is the delivery of payload. Therefore, the ultimate goal in transport operations is to improve properties like structural strength as well as resistance to wear and corrosion. The as-received AA6082 had its highest hardness after 20 hours of artificial ageing. However, best wear resistance does not always correlate with highest hardness values, since ductility plays a role. Improved strength and wear resistance were observed in this study; these were achieved without compromising the intrinsic properties of AA6082.

The mechanical strength of the as-received AA6082 alloy was retained despite the heat input from plasma spray procedure by which the coatings were deposited on the alloy. Therefore, the plasma spray technique is a preferred spraying technique for AA6082. The varying mixtures of WC and Al-102 powders used to coat the substrate improved the hardness and wear resistance of the coatings, compared with the as-received AA6082. In terms of effectiveness and efficiency of coatings used for wear and corrosion resistance within the scope of this study, the 60% WC

coating performed best. Higher WC content, as in 60% and 80% WC coatings guarantee higher hardness, strength and wear resistance.

For the corrosion tests, coated samples showed optimal performance in neutral as well as acidic environment. Since the neutral environment is typical of most available worst case scenarios, the coated samples are preferred to uncoated AA6082. 100% WC failed the fundamental adhesion test and is thus found not useful in this study. Therefore, AA6082 slightly under-aged as T65 and plasma-sprayed with 60% WC coating has the best hardness and wear resistance in this study.

CHAPTER 6: CONCLUSION AND RECOMMENDATION

6.1 Conclusion

The following were major observations made during this study:

a) The mechanical properties of the as-received AA6082 T651 from the heat treatment in experiment B conformed to the expected behaviour of 6xxx Al alloys.

b) Natural pre-ageing in the as-received AA6082 T651 was found to be detrimental to the entire heat treatment process, as the subsequent artificial ageing process was significantly altered because the storage temperature was not low enough.

c) The hardness values of all coated samples, ranging from 20% to 100% WC, were found to be superior to the uncoated sample by as much as 170%.

d) The heat generated from the plasma spray process did not significantly compromise the hardness of the AA6082 substrate, as observed from the hardness profile. However, it could have done so on a thinner layer which could not be analysed.

e) All coated samples, except 100% WC, exhibited wear resistance significantly superior to the uncoated (as-received) sample.

f) In the acidic solution of 3.5% NaCl containing H_2SO_4, all coated samples showed superior corrosion resistance to the uncoated sample, with the 60% WC coating having the best corrosion resistance.

g) For electrochemical tests in the acidic solution, the coatings with higher concentration of the Al-102 binder had superior corrosion resistance than those with less.

6.2 Recommendation for Future Research

In this MSc work, WC and Al-102 powders were used to make the metal matrix composite sprayed in different volume compositions. The following recommendations are suggested:

a) To use WC powder at the sub-micron and nano-sized scales, as particle reinforcements at such scales are highly efficient (Gleiter, 1989, 1995; Jia and Fischer, 1996, 1997; Stewart et al., 1999; Dent et al., 2002; Hunt, 2004; Valiev et al., 2007; Newbery et al., 2008; Aravinth et al., 2012) and a significantly lower amount of the same material is required at the nano-scale than at the micro-scale (Wang et al., 2012).

b) To use the low pressure cold gas dynamic spraying (CGDS) technique as it results in neither oxidation nor degradation of the coating (Espallargas, 2015) and its spraying temperature range (200–600°C) conforms with the melting temperatures for both the AA6082 substrate [555–650°C] and the Al-102 binder [565–575°C] (Paterson, 2007).

REFERENCES

Agüero, A., Camón, F., García de Blas, J., del Hoyo, J.C., Muelas, R., Santaballa, A., Ulargui, S., Vallés, P., 2011. HVOF-Deposited WCCoCr as Replacement for Hard Cr in Landing Gear Actuators. J. Therm. Spray Technol. 20, 1292–1309. https://doi.org/10.1007/s11666-011-9686-1

Aguilera Luna, I., Mancha Molinar, H., Castro Román, M.J., Escobedo Bocardo, J.C., Herrera Trejo, M., 2013. Improvement of the tensile properties of an Al–Si–Cu–Mg aluminum industrial alloy by using multi stage solution heat treatments. Mater. Sci. Eng. A 561, 1–6. https://doi.org/10.1016/j.msea.2012.10.064

Ahn, S., Kang, S., 2001. Effect of various carbides on the dissolution behavior of Ti(C0.7N0.3) in a Ti(C0.7N0.3)–30Ni system. Int. J. Refract. Met. Hard Mater. 19, 539–545. https://doi.org/10.1016/S0263-4368(01)00044-0

Alam, M.E., Hamouda, A.M.S., Gupta, M., 2013. Microstructure, thermal and mechanical response of AZ51/Al2O3 nanocomposite with 2wt.% Ca addition. Mater. Des. 50, 1–6. https://doi.org/10.1016/j.matdes.2013.01.057

Alpas, A.T., Zhang, J., 1994. Effect of microstructure (particulate size and volume fraction) and counterface material on the sliding wear resistance of particulate-reinforced aluminum matrix composites. Metall. Mater. Trans. A 25, 969–983. https://doi.org/10.1007/BF02652272

Al-Qutub, A.M., Allam, I.M., Qureshi, T.W., 2006. Effect of sub-micron Al_2O_3 concentration on dry wear properties of 6061 aluminum based composite. J. Mater. Process. Technol. 172, 327–331. https://doi.org/10.1016/j.jmatprotec.2005.10.022

An, Y., Hou, G., Chen, J., Zhao, X., Liu, G., Zhou, H., Chen, J., 2014. Microstructure and tribological properties of iron-based metallic glass coatings prepared by atmospheric plasma spraying. Vacuum 107, 132–140. https://doi.org/10.1016/j.vacuum.2014.04.021

Aravinth, S., Sankar, B., Kamaraj, M., Chakravarthy, S.R., Sarathi, R., 2012. Synthesis and characterization of hexagonal nano tungsten carbide powder using multi walled carbon nanotubes. Int. J. Refract. Met. Hard Mater. 33, 53–57. https://doi.org/10.1016/j.ijrmhm.2012.02.010

Aruga, Y., Kozuka, M., Takaki, Y., Sato, T., 2014. Evaluation of Solute Clusters Associated with Bake-Hardening Response in Isothermal Aged Al-Mg-Si Alloys Using a Three-Dimensional Atom Probe. Metall. Mater. Trans. A 45, 5906–5913. https://doi.org/10.1007/s11661-014-2548-y

Asgari, H., Saha, G., Mohammadi, M., 2017. Tribological behavior of nanostructured high velocity oxy-fuel (HVOF) thermal sprayed WC-17NiCr coatings. Ceram. Int. 43, 2123–2135. https://doi.org/10.1016/j.ceramint.2016.10.193

Askeland, D.R., Pradeep, P.P., 2003. Dispersion Strengthening and Eutectic Phase Diagrams.

Balamurugan, G.M., Duraiselvam, M., Anandakrishnan, V., 2012. Comparison of high temperature wear behaviour of plasma sprayed WC–Co coated and hard chromium plated AISI 304 austenitic stainless steel. Mater. Des., New Rubber Materials, Test Methods and Processes 35, 640–646. https://doi.org/10.1016/j.matdes.2011.10.012

Ball, A., Smallman, R.., 1966. The deformation properties and electron microscopy studies of the intermetallic compound NiAl. Acta Metall. 14, 1349–1355. https://doi.org/10.1016/0001-6160(66)90251-3

Banhart, J., Lay, M.D.H., Chang, C.S.T., Hill, A.J., 2011. Kinetics of natural aging in Al-Mg-Si alloys studied by positron annihilation lifetime spectroscopy. Phys. Rev. B 83. https://doi.org/10.1103/PhysRevB.83.014101

Banhart, J., Liu, M., Yong, Y., Liang, Z., Chang, C.S.T., Elsayed, M., Lay, M.D.H., 2012. Study of ageing in Al–Mg–Si alloys by positron annihilation spectroscopy. Phys. B Condens. Matter 407, 2689–2696. https://doi.org/10.1016/j.physb.2012.03.028

Banhart, J., Sin, C., Chang, T., Liang, Z., Wanderka, N., Lay, M.D.H., Hill, A.J., 2010. Natural ageing in Al-Mg-Si alloys – a process of unexpected complexity, 559–571.

Basavarajappa, S., Chandramohan, G., Mahadevan, A., Thangavelu, M., Subramanian, R., Gopalakrishnan, P., 2007a. Influence of sliding speed on the dry sliding wear behaviour and the subsurface deformation on hybrid metal matrix composite. Wear 262, 1007–1012. https://doi.org/10.1016/j.wear.2006.10.016

Basavarajappa, S., Chandramohan, G., Paulo Davim, J., 2007b. Application of Taguchi techniques to study dry sliding wear behaviour of metal matrix composites. Mater. Des. 28, 1393–1398. https://doi.org/10.1016/j.matdes.2006.01.006

Beghini, M., Santus, C., 2013. An application of the weight function technique to inclined surface cracks under rolling contact fatigue, assessment and parametric analysis. Eng. Fract. Mech. 98, 153–168. https://doi.org/10.1016/j.engfracmech.2012.10.024

Berg, L.., Gjønnes, J., Hansen, V., Li, X.., Knutson-Wedel, M., Waterloo, G., Schryvers, D., Wallenberg, L.., 2001. GP-zones in Al–Zn–Mg alloys and their role in artificial aging. Acta Mater. 49, 3443–3451. https://doi.org/10.1016/S1359-6454(01)00251-8

Bernole, P.M., Graf, R., Guyot, P., 1973. Étude au microscope électronique et aux rayons X de la préprécipitation dans un alliage Al–10% Mg vieilli à la température ambiante. Philos. Mag. 28, 771–782. https://doi.org/10.1080/14786437308220982

Bielawski, M., 2004. Development of unbalanced magnetron sputtered Al–Mo coatings for cadmium replacement. Surf. Coat. Technol. 179, 10–17. https://doi.org/10.1016/S0257-8972(03)00796-5

Birol, Y., 2008. Thixoforging experiments with 6082 extrusion feedstock. J. Alloys Compd. 455, 178–185. https://doi.org/10.1016/j.jallcom.2007.01.053

Birol, Y., 2005. Pre-straining to improve the bake hardening response of a twin-roll cast Al–Mg–Si alloy. Scr. Mater. 52, 169–173. https://doi.org/10.1016/j.scriptamat.2004.10.001

Birol, Y., Karlik, M., 2006. The interaction of natural ageing with straining in a twin-roll cast AlMgSi automotive sheet. Scr. Mater. 55, 625–628. https://doi.org/10.1016/j.scriptamat.2006.06.009

Bist, A., Saini, J.S., Sharma, B., 2016. A review of tool wear prediction during friction stir welding of aluminium matrix composite. Trans. Nonferrous Met. Soc. China 26, 2003–2018. https://doi.org/10.1016/S1003-6326(16)64318-2

Blommedal, K., 2013. Corrosion Development in Welded AA6082 Alloys.

Bolelli, G., Berger, L.-M., Börner, T., Koivuluoto, H., Lusvarghi, L., Lyphout, C., Markocsan, N., Matikainen, V., Nylén, P., Sassatelli, P., Trache, R., Vuoristo, P., 2015. Tribology of HVOF- and HVAF-sprayed WC–10Co4Cr hardmetal coatings: A comparative assessment. Surf. Coat. Technol. 265, 125–144. https://doi.org/10.1016/j.surfcoat.2015.01.048

Bolelli, G., Cannillo, V., Lusvarghi, L., Riccò, S., 2006. Mechanical and tribological properties of electrolytic hard chrome and HVOF-sprayed coatings. Surf. Coat. Technol. 200, 2995–3009. https://doi.org/10.1016/j.surfcoat.2005.04.057

Bolelli, G., Cannillo, V., Lusvarghi, L., Rosa, R., Valarezo, A., Choi, W.B., Dey, R., Weyant, C., Sampath, S., 2012. Functionally graded WC–Co/NiAl HVOF coatings for damage tolerance, wear and corrosion protection. Surf. Coat. Technol. 206, 2585–2601. https://doi.org/10.1016/j.surfcoat.2011.11.018

Bonny, K., De Baets, P., Perez, Y., Vleugels, J., Lauwers, B., 2010. Friction and wear characteristics of WC–Co cemented carbides in dry reciprocating sliding contact. Wear 268, 1504–1517. https://doi.org/10.1016/j.wear.2010.02.029

Bonny, K., De Baets, P., Vleugels, J., Huang, S., Van der Biest, O., Lauwers, B., 2009. Impact of Cr3C2/VC addition on the dry sliding friction and wear response of WC–Co cemented carbides. Wear 267, 1642–1652. https://doi.org/10.1016/j.wear.2009.06.013

Borrelly, R., Merle, P., Adenis, D., 1989. Seebeck effect study of precipitation in 3004. Presented at the Light Metals: Proceedings of Sessions, AIME Annual Meeting (Warrendale, Pennsylvania), pp. 703–712.

Bouchear, M., Hamana, D., Laoui, T., 1996. GP zones and precipitate morphology in aged Al-Mg alloys. Philos. Mag. A 73, 1733–1740. https://doi.org/10.1080/01418619608243010

Bowman, R.R., Noebe, R.D., Raj, S.V., Locci, I.E., 1992. Correlation of deformation mechanisms with the tensile and compressive behavior of NiAl and NiAl(Zr) intermetallic alloys. Metall. Trans. A 23, 1493–1508. https://doi.org/10.1007/BF02647332

Bozzini, B., De Gaudenzi, G.P., Serra, M., Fanigliulo, A., Bogani, F., 2002. Corrosion behaviour of WC-Co based hardmetal in neutral chloride and acid sulphate media. Mater. Corros. 53, 328–334. https://doi.org/10.1002/1521-4176(200205)53:5<328::AID-MACO328>3.0.CO;2-G

Burnell-Gray, J.S., Datta, P.K., 1996. Surface Engineering Casebook. Woodhead Publishing.

Canales, A.A., Carrera, E., Silva, J.T., Valtierra, S., Colás, R., 2012. Mechanical properties in as-cast and heat treated Al-Si-Cu alloys. Int. J. Microstruct. Mater. Prop. 7, 281. https://doi.org/10.1504/IJMMP.2012.048518

Cao, L., Rometsch, P.A., Couper, M.J., 2013a. Effect of pre-ageing and natural ageing on the paint bake response of alloy AA6181A. Mater. Sci. Eng. A 571, 77–82. https://doi.org/10.1016/j.msea.2013.01.065

Cao, L., Rometsch, P.A., Couper, M.J., 2013b. Clustering behaviour in an Al–Mg–Si–Cu alloy during natural ageing and subsequent under-ageing. Mater. Sci. Eng. A 559, 257–261. https://doi.org/10.1016/j.msea.2012.08.093

Caporali, S., Fossati, A., Lavacchi, A., Perissi, I., Tolstogouzov, A., Bardi, U., 2008. Aluminium electroplated from ionic liquids as protective coating against steel corrosion. Corros. Sci. 50, 534–539. https://doi.org/10.1016/j.corsci.2007.08.001

Chakrabarti, D.., Laughlin, D.E., 2004. Phase relations and precipitation in Al–Mg–Si alloys with Cu additions. Prog. Mater. Sci. 49, 389–410. https://doi.org/10.1016/S0079-6425(03)00031-8

Chang, C.S.T., Banhart, J., 2011. Low-Temperature Differential Scanning Calorimetry of an Al-Mg-Si Alloy. Metall. Mater. Trans. A 42, 1960–1964. https://doi.org/10.1007/s11661-010-0596-5

Chang, C.S.T., Wieler, I., Wanderka, N., Banhart, J., 2009. Positive effect of natural pre-ageing on precipitation hardening in Al–0.44at% Mg–0.38at% Si alloy. Ultramicroscopy 109, 585–592. https://doi.org/10.1016/j.ultramic.2008.12.002

Chen, F., Chen, Z., Mao, F., Wang, T., Cao, Z., 2015a. TiB_2 reinforced aluminium based in situ composites fabricated by stir casting. Mater. Sci. Eng. A 625, 357–368. https://doi.org/10.1016/j.msea.2014.12.033

Chen, F., Wang, T., Chen, Z., Mao, F., Han, Q., Cao, Z., 2015b. Microstructure, mechanical properties and wear behaviour of Zn–Al–Cu–TiB_2 in situ composites. Trans. Nonferrous Met. Soc. China 25, 103–111. https://doi.org/10.1016/S1003-6326(15)63584-1

Chen, H., Gou, G., Tu, M., Liu, Y., 2010. Research on the Friction and Wear Behavior at Elevated Temperature of Plasma-Sprayed Nanostructured WC-Co Coatings. J. Mater. Eng. Perform. 19, 1–6. https://doi.org/10.1007/s11665-009-9411-0

Chen, H., Xu, C., Zhou, Q., Hutchings, I.M., Shipway, P.H., Liu, J., 2005. Micro-scale abrasive wear behaviour of HVOF sprayed and laser-remelted conventional and nanostructured WC–Co coatings. Wear 258, 333–338. https://doi.org/10.1016/j.wear.2004.09.044

Chen, J., Zhen, L., Yang, S., Shao, W., Dai, S., 2009. Investigation of precipitation behavior and related hardening in AA 7055 aluminum alloy. Mater. Sci. Eng. A 500, 34–42. https://doi.org/10.1016/j.msea.2008.09.065

Chen, M., Zhuang, Q., Lin, N., He, Y., 2017. Improvement in microstructure and mechanical properties of Ti(C,N)-Fe cermets with the carbon additions. J. Alloys Compd. 701, 408–415. https://doi.org/10.1016/j.jallcom.2017.01.119

Chen, S., Chen, K., Peng, G., Jia, L., Dong, P., 2012. Effect of heat treatment on strength, exfoliation corrosion and electrochemical behavior of 7085 aluminum alloy. Mater. Des. 35, 93–98. https://doi.org/10.1016/j.matdes.2011.09.033

Cheng, W.-J., Wang, C.-J., 2009. Growth of intermetallic layer in the aluminide mild steel during hot-dipping. Surf. Coat. Technol. 204, 824–828. https://doi.org/10.1016/j.surfcoat.2009.09.061

Chi, H., Jiang, L., Chen, G., Kang, P., Lin, X., Wu, G., 2015. Dry sliding friction and wear behavior of (TiB_2+h-BN)/2024Al composites. Mater. Des. 87, 960–968. https://doi.org/10.1016/j.matdes.2015.08.088

Cho, T.Y., Yoon, J.H., Kim, K.S., Song, K.O., Joo, Y.K., Fang, W., Zhang, S.H., Youn, S.J., Chun, H.G., Hwang, S.Y., 2008. A study on HVOF coatings of micron and nano WC–Co powders. Surf. Coat. Technol. 202, 5556–5559. https://doi.org/10.1016/j.surfcoat.2008.06.106

Clyne, T.W., Withers, P.J., 1995. An Introduction to Metal Matrix Composites. Cambridge University Press.

Creus, J., Idrissi, H., Mazille, H., Sanchette, F., Jacquot, P., 1999. Corrosion behaviour of Al/Ti coating elaborated by cathodic arc PVD process onto mild steel substrate. Thin Solid Films 346, 150–154. https://doi.org/10.1016/S0040-6090(98)01742-8

Cui, C.Y., Jin, T., Sun, X.F., 2011. Effects of heat treatments on the serrated flow in a Ni–Co–Cr-base superalloy. J. Mater. Sci. 46, 5546–5552. https://doi.org/10.1007/s10853-011-5501-0

Dauger, A., Boudili, E.., Roth, M., 1976. Structure interne des zones de guinier-preston dans l'aluminium - magnesium par diffraction des neutrons. Scr. Metall. 10, 1119–1124. https://doi.org/10.1016/0036-9748(76)90037-5

De Geuser, F., Lefebvre, W., Blavette, D., 2006. 3D atom probe study of solute atoms clustering during natural ageing and pre-ageing of an Al-Mg-Si alloy. Philos. Mag. Lett. 86, 227–234. https://doi.org/10.1080/09500830600643270

Dent, A.H., DePalo, S., Sampath, S., 2002. Examination of the wear properties of HVOF sprayed nanostructured and conventional WC-Co cermets with different binder phase contents. J. Therm. Spray Technol. 11, 551–558. https://doi.org/10.1361/105996302770348691
Detournay, E., Richard, T., Shepherd, M., 2008. Drilling response of drag bits: Theory and experiment. Int. J. Rock Mech. Min. Sci. 45, 1347–1360. https://doi.org/10.1016/j.ijrmms.2008.01.010
Di Girolamo, G., Brentari, A., Blasi, C., Serra, E., 2014. Microstructure and mechanical properties of plasma sprayed alumina-based coatings. Ceram. Int. 40, 12861–12867. https://doi.org/10.1016/j.ceramint.2014.04.143
Di Girolamo, G., Pilloni, L., Pulci, G., Marra, F., 2009. Tribological Characterization of WC-Co Plasma Sprayed Coatings. J. Am. Ceram. Soc. 92, 1118–1124. https://doi.org/10.1111/j.1551-2916.2009.03023.x
Ding, L., He, Y., Wen, Z., Zhao, P., Jia, Z., Liu, Q., 2015. Optimization of the pre-aging treatment for an AA6022 alloy at various temperatures and holding times. J. Alloys Compd. 647, 238–244. https://doi.org/10.1016/j.jallcom.2015.05.188
Directive, 2000a. Directive 2000/53/EC of the European Parliament and of the Council of Sep. 18, 2000 on End-of Life Vehicles. Off. J. Eur. Communities Artic. 7.
Directive, 2000b. The European Parliament and the Council of the European Union, Off. J. L 203, 1–8.
Donatus, U., Thompson, G.E., Omotoyinbo, J.A., Alaneme, K.K., Aribo, S., Agbabiaka, O.G., 2017. Corrosion pathways in aluminium alloys. Trans. Nonferrous Met. Soc. China 27, 55–62. https://doi.org/10.1016/S1003-6326(17)60006-2
Dumolt, S.D., Laughlin, D.E., Williams, J.C., 1984. Formation of a modified β′ phase in aluminum alloy 6061. Scr. Metall. 18, 1347–1350. https://doi.org/10.1016/0036-9748(84)90362-4
Dutta, I., Allen, S.M., 1991. A calorimetric study of precipitation in commercial aluminium alloy 6061. J. Mater. Sci. Lett. 10, 323–326. https://doi.org/10.1007/BF00719697
Edwards, G.A., Stiller, K., Dunlop, G.L., Couper, M.J., 1998. The precipitation sequence in Al–Mg–Si alloys. Acta Mater. 46, 3893–3904. https://doi.org/10.1016/S1359-6454(98)00059-7
Eichelberger, A.H., Teoh, E.R., McCartt, A.T., 2015. Vehicle choices for teenage drivers: A national survey of U.S. parents. J. Safety Res. 55, 1–5. https://doi.org/10.1016/j.jsr.2015.07.006
Eikum, A., Thomas, G., 1964. Precipitation and dislocation nucleation in quench-aged Al-Mg alloys. Acta Metall. 12, 537–545. https://doi.org/10.1016/0001-6160(64)90026-4
Ekaputra, I.M.W., Kim, W.-G., Park, J.-Y., Kim, S.-J., Kim, E.-S., 2016. Influence of Dynamic Strain Aging on Tensile Deformation Behavior of Alloy 617. Nucl. Eng. Technol. 48, 1387–1395. https://doi.org/10.1016/j.net.2016.06.013
El Mehtedi, M., Musharavati, F., Spigarelli, S., 2014. Modelling of the flow behaviour of wrought aluminium alloys at elevated temperatures by a new constitutive equation. Mater. Des. 1980-2015 54, 869–873. https://doi.org/10.1016/j.matdes.2013.09.013
Embury, J.., Nicholson, R.., 1963. Dislocation sources in an aluminium alloy. Acta Metall. 11, 347–354. https://doi.org/10.1016/0001-6160(63)90159-7
Engler, O., Schäfer, C., Myhr, O.R., 2015. Effect of natural ageing and pre-straining on strength and anisotropy in aluminium alloy AA 6016. Mater. Sci. Eng. A 639, 65–74. https://doi.org/10.1016/j.msea.2015.04.097

Engqvist, H., Beste, U., Axén, N., 2000a. The influence of pH on sliding wear of WC-based materials. Int. J. Refract. Met. Hard Mater. 18, 103–109. https://doi.org/10.1016/S0263-4368(00)00007-X

Engqvist, H., Högberg, H., Botton, G.., Ederyd, S., Axén, N., 2000b. Tribofilm formation on cemented carbides in dry sliding conformal contact. Wear 239, 219–228. https://doi.org/10.1016/S0043-1648(00)00315-X

Esmaeili, S., Vaumousse, D., Zandbergen, M.W., Poole, W.J., Cerezo, A., Lloyd, D.J., 2007. A study on the early-stage decomposition in the Al-Mg-Si-Cu alloy AA6111 by electrical resistivity and three-dimensional atom probe. Philos. Mag. 87, 3797–3816. https://doi.org/10.1080/14786430701408312

Esmaeili, S., Wang, X., Lloyd, D.J., Poole, W.J., 2003. On the precipitation-hardening behavior of the Al−Mg−Si−Cu alloy AA6111. Metall. Mater. Trans. A 34, 751–763. https://doi.org/10.1007/s11661-003-1003-2

Espallargas, N., 2015. Future Development of Thermal Spray Coatings. Woodhead Publishing. eBook ISBN: 9780857097743. 1–13.

Espallargas, N., Berget, J., Guilemany, J.M., Benedetti, A.V., Suegama, P.H., 2008. Cr3C2–NiCr and WC–Ni thermal spray coatings as alternatives to hard chromium for erosion–corrosion resistance. Surf. Coat. Technol. 202, 1405–1417. https://doi.org/10.1016/j.surfcoat.2007.06.048

Espinosa, L., Bonache, V., Salvador, M.D., 2011. Friction and wear behaviour of WC–Co–Cr3C2–VC cemented carbides obtained from nanocrystalline mixtures. Wear 272, 62–68. https://doi.org/10.1016/j.wear.2011.07.012

Ettmayer, P., Kolaska, H., Lengauer, W., Dreyer, K., 1995. Ti(C,N) cermets — Metallurgy and properties. Int. J. Refract. Met. Hard Mater. 13, 343–351. https://doi.org/10.1016/0263-4368(95)00027-G

Exner, H.E., 1979. Physical and chemical nature of cemented carbides. Int. Met. Rev. 24, 149–173. https://doi.org/10.1179/imtr.1979.24.1.149

Fernández, M.R., García, A., Cuetos, J.M., González, R., Noriega, A., Cadenas, M., 2015. Effect of actual WC content on the reciprocating wear of a laser cladding NiCrBSi alloy reinforced with WC. Wear 324–325, 80–89. https://doi.org/10.1016/j.wear.2014.12.021

Fransson, C., 2009. Accelerated Aging of Aluminium Alloys. Karlstads University.

Galos, J., Sutcliffe, M., Cebon, D., Piecyk, M., Greening, P., 2015. Reducing the energy consumption of heavy goods vehicles through the application of lightweight trailers: Fleet case studies. Transp. Res. Part Transp. Environ. 41, 40–49. https://doi.org/10.1016/j.trd.2015.09.010

Gant, A. J., Gee, M.G., Gohil, D.D., Jones, H.G., Orkney, L.P., 2013. Use of FIB/SEM to assess the tribo-corrosion of WC/Co hardmetals in model single point abrasion experiments. Tribol. Int. 68, 56–66. https://doi.org/10.1016/j.triboint.2012.11.008

Gao, L., Harada, Y., Kumai, S., 2015. Microstructural characterization of aluminum alloys using Weck's reagent, part I: Applications. Mater. Charact. 107, 426–433. https://doi.org/10.1016/j.matchar.2015.01.005

Gao, Q., Wu, S., Lü, S., Duan, X., An, P., 2016. Preparation of in-situ 5vol% TiB_2 particulate reinforced Al–4.5Cu alloy matrix composites assisted by improved mechanical stirring process. Mater. Des. 94, 79–86. https://doi.org/10.1016/j.matdes.2016.01.023

Gayler, M.L.V., Preston, G.D., 1929. The age-hardening of some aluminium alloys. J Inst Met 41, 191–247.

Gehin, A., Zwolinski, P., Brissaud, D., 2008. A tool to implement sustainable end-of-life strategies in the product development phase. J. Clean. Prod. 16, 566–576. https://doi.org/10.1016/j.jclepro.2007.02.012
Geng, Z., Duan, D., Hou, S., Li, S., 2016a. Tribological Behavior of WC-12Co Air Plasma–Sprayed Coating at Elevated Temperatures. Tribol. Trans. 59, 55–61. https://doi.org/10.1080/10402004.2015.1068423
Geng, Z., Hou, S., Shi, G., Duan, D., Li, S., 2016b. Tribological behaviour at various temperatures of WC-Co coatings prepared using different thermal spraying techniques. Tribol. Int. 104, 36–44. https://doi.org/10.1016/j.triboint.2016.08.025
Geng, Z., Li, S., Duan, D.L., Liu, Y., 2015. Wear behaviour of WC–Co HVOF coatings at different temperatures in air and argon. Wear, 20th Intenational Conference on Wear Materials 330–331, 348–353. https://doi.org/10.1016/j.wear.2015.01.035
Ghabchi, A., Sampath, S., Holmberg, K., Varis, T., 2014. Damage mechanisms and cracking behavior of thermal sprayed WC–CoCr coating under scratch testing. Wear 313, 97–105. https://doi.org/10.1016/j.wear.2014.02.017
Ghabchi, A., Varis, T., Turunen, E., Suhonen, T., Liu, X., Hannula, S.-P., 2010. Behavior of HVOF WC-10Co4Cr Coatings with Different Carbide Size in Fine and Coarse Particle Abrasion. J. Therm. Spray Technol. 19, 368–377. https://doi.org/10.1007/s11666-009-9433-z
Ghandehari, M.H., 1980. Anodic Behavior of Cemented WC-6% Co Alloy in Phosphoric Acid Solutions. J. Electrochem. Soc. 127, 2144. https://doi.org/10.1149/1.2129361
Gladman, T., 1999. Precipitation hardening in metals. Mater. Sci. Technol. 15, 30–36. https://doi.org/10.1179/026708399773002782
Glaeser, K.-P., 2010. Performance of articulated vehicles and road trains regarding road damage and load capacity. HVTT 11 - Int. Heavy Veh. Symp.
Gleiter, H., 1995. Nanostructured materials: state of the art and perspectives. Nanostructured Mater. 6, 3–14. https://doi.org/10.1016/0965-9773(95)00025-9
Gleiter, H., 1989. Nanocrystalline materials. Prog. Mater. Sci. 33, 223–315. https://doi.org/10.1016/0079-6425(89)90001-7
Gong, T., Yao, P., Zuo, X., Zhang, Z., Xiao, Y., Zhao, L., Zhou, H., Deng, M., Wang, Q., Zhong, A., 2016. Influence of WC carbide particle size on the microstructure and abrasive wear behavior of WC–10Co–4Cr coatings for aircraft landing gear. Wear 362–363, 135–145. https://doi.org/10.1016/j.wear.2016.05.022
Granta Material Intelligence, 2017. Age-hardening wrought Al-alloys.
Gudić, S., Smoljko, I., Kliškić, M., 2010. The effect of small addition of tin and indium on the corrosion behavior of aluminium in chloride solution. J. Alloys Compd. 505, 54–63. https://doi.org/10.1016/j.jallcom.2010.06.055
Guilemany, J.M., Dosta, S., Miguel, J.R., 2006. The enhancement of the properties of WC-Co HVOF coatings through the use of nanostructured and microstructured feedstock powders. Surf. Coat. Technol. 201, 1180–1190. https://doi.org/10.1016/j.surfcoat.2006.01.041
Guilemany, J.M., Nutting, J., Miguel, J.R., Dong, Z., 1995. Microstructure characterization of WC-Ni coatings obtained by HVOF thermal spraying. Scr. Metall. Mater. 33, 55–61. https://doi.org/10.1016/0956-716X(95)00045-W
Gul, F., Acilar, M., 2004. Effect of the reinforcement volume fraction on the dry sliding wear behaviour of Al–10Si/SiCp composites produced by vacuum infiltration technique.

Compos. Sci. Technol. 64, 1959–1970. https://doi.org/10.1016/j.compscitech.2004.02.013
Guo, X., Planche, M.-P., Chen, J., Liao, H., 2014. Relationships between in-flight particle characteristics and properties of HVOF sprayed WC-CoCr coatings. J. Mater. Process. Technol. 214, 456–461. https://doi.org/10.1016/j.jmatprotec.2013.09.029
Gupta, R.K., Fabijanic, D., Dorin, T., Qiu, Y., Wang, J.T., Birbilis, N., 2015. Simultaneous improvement in the strength and corrosion resistance of Al via high-energy ball milling and Cr alloying. Mater. Des. 84, 270–276. https://doi.org/10.1016/j.matdes.2015.06.120
Guyot, P., Cottignies, L., 1996. Precipitation kinetics, mechanical strength and electrical conductivity of AlZnMgCu alloys. Acta Mater. 44, 4161–4167. https://doi.org/10.1016/S1359-6454(96)00033-X
Hamana, D., Baziz, L., Bouchear, M., 2004. Kinetics and mechanism of formation and transformation of metastable β′-phase in Al–Mg alloys. Mater. Chem. Phys. 84, 112–119. https://doi.org/10.1016/j.matchemphys.2003.11.001
Hamana, D., Bouchear, M., Betrouche, M., Derafa, A., Rokhmanov, N.Y., 2001. Comparative study of formation and transformation of transition phases in Al–12 wt.% Mg alloy. J. Alloys Compd. 320, 93–102. https://doi.org/10.1016/S0925-8388(01)00923-9
Han, B.Q., Huang, J.Y., Zhu, Y.T., Lavernia, E.J., 2006. Effect of strain rate on the ductility of a nanostructured aluminum alloy. Scr. Mater. 54, 1175–1180. https://doi.org/10.1016/j.scriptamat.2005.11.035
Hashimoto, K., Fujimatsu, T., Tsunekage, N., Hiraoka, K., Kida, K., Santos, E.C., 2011. Study of rolling contact fatigue of bearing steels in relation to various oxide inclusions. Mater. Des. 32, 1605–1611. https://doi.org/10.1016/j.matdes.2010.08.052
Hihara, L.H., Latanision, R.M., 1992. Galvanic Corrosion of Aluminum-Matrix Composites. Corrosion 48, 546–552. https://doi.org/10.5006/1.3315972
Hirsch, J., 2014. Recent development in aluminium for automotive applications. Trans. Nonferrous Met. Soc. China 24, 1995–2002. https://doi.org/10.1016/S1003-6326(14)63305-7
Hochstrasser-Kurz, S., Mueller, Y., Latkoczy, C., Virtanen, S., Schmutz, P., 2007. Analytical characterization of the corrosion mechanisms of WC–Co by electrochemical methods and inductively coupled plasma mass spectroscopy. Corros. Sci. 49, 2002–2020. https://doi.org/10.1016/j.corsci.2006.08.022
Hong, S., Wu, Y., Wang, B., Zheng, Y., Gao, W., Li, G., 2014. High-velocity oxygen-fuel spray parameter optimization of nanostructured WC–10Co–4Cr coatings and sliding wear behavior of the optimized coating. Mater. Des. 55, 286–291. https://doi.org/10.1016/j.matdes.2013.10.002
Hossain, A., Kurny, A.S.W., 2013. Effect of Ageing Temperature on the Mechanical Properties of Al-6Si-0.5 Mg Cast Alloys with Cu Additions Treated by T6 Heat Treatment. Univers. J. Mater. Sci. 1, 1–5.
Hossain, M.N. Bin, Ahmed, T., Ehsan, M., Mahboob, M., Mamun, M., 2014. Performance Evaluation of a Light-weight Passenger Vehicle Using Regular Octane and Bio-fuel. Procedia Eng. 90, 605–610. https://doi.org/10.1016/j.proeng.2014.11.779
Houdková, Š., Zahálka, F., Kašparová, M., Berger, L.-M., 2011. Comparative study of thermally sprayed coatings under different types of wear conditions for hard chromium replacement. Tribol. Lett. 43, 139–154. https://doi.org/10.1007/s11249-011-9791-9

Huang, S.G., Li, L., Van der Biest, O., Vleugels, J., 2008. VC- and Cr3C2-doped WC–NbC–Co hardmetals. J. Alloys Compd. 464, 205–211. https://doi.org/10.1016/j.jallcom.2007.10.038

Human, A.M., Roebuck, B., Exner, H.E., 1998. Electrochemical polarisation and corrosion behaviour of cobalt and Co(W,C) alloys in 1 N sulphuric acid. Mater. Sci. Eng. A 241, 202–210. https://doi.org/10.1016/S0921-5093(97)00492-9

Human, A.M., Exner, H.E., 1996. Electrochemical behaviour of tungsten-carbide hardmetals. Mater. Sci. Eng. A 209, 180–191. https://doi.org/10.1016/0921-5093(95)10137-3

Hunt, W.H., 2004. Nanomaterials: Nomenclature, novelty, and necessity. JOM 56, 13–18. https://doi.org/10.1007/s11837-004-0281-5

Hussainova, I., Antonov, M., Voltsihhin, N., 2011. Assessment of zirconia doped hardmetals as tribomaterials. Wear 271, 1909–1915. https://doi.org/10.1016/j.wear.2010.11.034

Hutchings, I.M., 1992. Tribology: Friction and Wear of Engineering Materials. Edward Arnold Publishing. eBookISBN: 9780081009512.

Itoh, G., Cottereau, B., Kanno, M., 1990. Precipitation of the intermediate phase β′ in an Al-8%Mg alloy. Mater. Trans. JIM 31, 1041–1049.

Jacobs, L., Hyland, M.M., De Bonte, M., 1999. Study of the influence of microstructural properties on the sliding-wear behavior of HVOF and HVAF sprayed WC-cermet coatings. J. Therm. Spray Technol. 8, 125–132.

Jayalakshmi, S., Dezhi, Q., Sankaranarayanan, S., Gupta, M., 2013. Microstructure and mechanical properties of Mg-Al alloys with in situ Al<SUB align=“right”>4C<SUB align=“right”>3 phase synthesised by CO<SUB align=“right”>2 incorporation during liquid state processing. Int. J. Microstruct. Mater. Prop. 8, 283. https://doi.org/10.1504/IJMMP.2013.057066

Jia, K., Fischer, T.E., 1997. Sliding wear of conventional and nanostructured cemented carbides. Wear, 11th International Conference on Wear of Materials 203–204, 310–318. https://doi.org/10.1016/S0043-1648(96)07423-6

Jia, K., Fischer, T.E., 1996. Abrasion resistance of nanostructured and conventional cemented carbides. Wear 200, 206–214. https://doi.org/10.1016/S0043-1648(96)07277-8

Jiang, H., Zhang, Q., Chen, X., Chen, Z., Jiang, Z., Wu, X., Fan, J., 2007. Three types of Portevin–Le Chatelier effects: Experiment and modelling. Acta Mater. 55, 2219–2228. https://doi.org/10.1016/j.actamat.2006.10.029

Jin, G., Xu, B., Wang, H., Li, Q., Wei, S., 2007. Characterization of WC/Co coatings on metal substrates. Mater. Lett. 61, 2454–2456. https://doi.org/10.1016/j.matlet.2006.09.036

J.R. Davis & Associates, ASM International (Eds.), 2004. Handbook of thermal spray technology. ASM International, Materials Park, OH.

Kamali, R., Binesh, A.R., 2009. The importance of sensitive parameters effect on the combustion in a high velocity oxygen-fuel spray system. Int. Commun. Heat Mass Transf. 36, 978–983. https://doi.org/10.1016/j.icheatmasstransfer.2009.06.015

Kamdi, Z., Phang, C.Y., Ahmad, H., 2014. Corrosion behavior of WC-Co cermet coatings.

Karamış, M.B., Cerit, A.A., Selcuk, B., Nair, F., 2012. The effects of different ceramics size and volume fraction on wear behavior of Al matrix composites (for automobile cam material). wear 289, 73–81.

Karamış, M.B., Alper Cerit, A., Selçuk, B., Nair, F., 2012. The effects of different ceramics size and volume fraction on wear behavior of Al matrix composites (for automobile cam material). Wear 289, 73–81. https://doi.org/10.1016/j.wear.2012.04.012

Karimi, A., Verdon, C., Barbezat, G., 1993. Microstructure and hydroabrasive wear behaviour of high velocity oxy-fuel thermally sprayed WC-Co(Cr) coatings. Surf. Coat. Technol. 57, 81–89. https://doi.org/10.1016/0257-8972(93)90340-T

Kartsonakis, I.A., Dragatogiannis, D.A., Koumoulos, E.P., Karantonis, A., Charitidis, C.A., 2016. Corrosion behaviour of dissimilar friction stir welded aluminium alloys reinforced with nanoadditives. Mater. Des. 102, 56–67. https://doi.org/10.1016/j.matdes.2016.04.027

Kaygısız, Y., Maraşlı, N., 2015. Microstructural, mechanical and electrical characterization of directionally solidified Al–Si–Mg eutectic alloy. J. Alloys Compd. 618, 197–203. https://doi.org/10.1016/j.jallcom.2014.08.056

Kear, B., Skandan, G., Sadangi, R., 2001. Factors controlling decarburization in HVOF sprayed nano-WC/Co hardcoatings. Scr. Mater. 44, 1703–1707. https://doi.org/10.1016/S1359-6462(01)00867-3

Kellner, F.J.J., Hildebrand, H., Virtanen, S., 2009. Effect of WC grain size on the corrosion behavior of WC–Co based hardmetals in alkaline solutions. Int. J. Refract. Met. Hard Mater. 27, 806–812. https://doi.org/10.1016/j.ijrmhm.2009.02.004

Khaira, H.K., 2013. Precipitation Hardening.

Khan, A.S., Farrokh, B., Takacs, L., 2008. Effect of grain refinement on mechanical properties of ball-milled bulk aluminum. Mater. Sci. Eng. A 489, 77–84. https://doi.org/10.1016/j.msea.2008.01.045

Kim, Y., Buchheit, R.G., 2007. A characterization of the inhibiting effect of Cu on metastable pitting in dilute Al–Cu solid solution alloys. Electrochimica Acta 52, 2437–2446. https://doi.org/10.1016/j.electacta.2006.08.054

Kim, Y., Buchheit, R.G., Kotula, P.G., 2010. Effect of alloyed Cu on localized corrosion susceptibility of Al–Cu solid solution alloys—Surface characterization by XPS and STEM. Electrochimica Acta 55, 7367–7375. https://doi.org/10.1016/j.electacta.2010.06.069

Kimbrough, D.E., Cohen, Y., Winer, A.M., Creelman, L., Mabuni, C., 1999. A Critical Assessment of Chromium in the Environment. Crit. Rev. Environ. Sci. Technol. 29, 1–46. https://doi.org/10.1080/10643389991259164

Kimmari, E., Hussainova, I., Smirnov, A., Traksmaa, R., Preis, I., 2009. Processing and microstructural characterization of WC-based cermets doped by ZrO_2. Est. J. Eng. 15, 275. https://doi.org/10.3176/eng.2009.4.04

Kleiner, S., Henkel, C., Schulz, P., Uggowitzer, P.J., 2001. Paint bake response of aluminium alloy 6016. Aluminium 77, 185–189.

Knight, S.P., Birbilis, N., Muddle, B.C., Trueman, A.R., Lynch, S.P., 2010. Correlations between intergranular stress corrosion cracking, grain-boundary microchemistry, and grain-boundary electrochemistry for Al–Zn–Mg–Cu alloys. Corros. Sci. 52, 4073–4080. https://doi.org/10.1016/j.corsci.2010.08.024

Knight, S.P., Salagaras, M., Trueman, A.R., 2011. The study of intergranular corrosion in aircraft aluminium alloys using X-ray tomography. Corros. Sci. 53, 727–734.

Koc, R., Kodambaka, S.K., 2000. Tungsten carbide (WC) synthesis from novel precursors. J. Eur. Ceram. Soc. 20, 1859–1869. https://doi.org/10.1016/S0955-2219(00)00038-8

Kolar, M., Pedersen, K.O., Gulbrandsen-Dahl, S., Marthinsen, K., 2012. Combined effect of deformation and artificial aging on mechanical properties of Al–Mg–Si Alloy. Trans.

Nonferrous Met. Soc. China 22, 1824–1830. https://doi.org/10.1016/S1003-6326(11)61393-9
Konadu, D.S., Merwe, J. van der, Potgieter, J.H., Potgieter-Vermaak, S., Machio, C.N., 2010. The corrosion behaviour of WC-VC-Co hardmetals in acidic media. Corros. Sci. 52, 3118–3125. https://doi.org/10.1016/j.corsci.2010.05.033
Konyashin, I., Ries, B., Hlawatschek, D., Zhuk, Y., Mazilkin, A., Straumal, B., Dorn, F., Park, D., 2015. Wear-resistance and hardness: Are they directly related for nanostructured hard materials? Int. J. Refract. Met. Hard Mater. 49, 203–211. https://doi.org/10.1016/j.ijrmhm.2014.06.017
Konyashin, I., Ries, B., Lachmann, F., 2010. Near-nano WC–Co hardmetals: Will they substitute conventional coarse-grained mining grades? Int. J. Refract. Met. Hard Mater. 28, 489–497. https://doi.org/10.1016/j.ijrmhm.2010.02.001
Korchef, A., Champion, Y., Njah, N., 2007. X-ray diffraction analysis of aluminium containing Al8Fe2Si processed by equal channel angular pressing. J. Alloys Compd. 427, 176–182. https://doi.org/10.1016/j.jallcom.2006.03.010
Kovaćs, I., Lendvai, J., Nagy, E., 1972. The mechanism of clustering in supersaturated solid solutions of Al-Mg_2Si alloys. Acta Metall. 20, 975–983. https://doi.org/10.1016/0001-6160(72)90092-2
Krakhmalev, P.V., Sukumaran, J., Gåård, A., 2007. Effect of microstructure on edge wear mechanisms in WC–Co. Int. J. Refract. Met. Hard Mater. 25, 171–178. https://doi.org/10.1016/j.ijrmhm.2006.04.004
Kramer, D., Savage, M., Levine, L., 2005. AFM observations of slip band development in Al single crystals. Acta Mater. 53, 4655–4664. https://doi.org/10.1016/j.actamat.2005.06.019
Król, M., Tański, T., Matula, G., Snopiński, P., Tomiczek, A.E., 2015. Analysis of Crystallisation Process of Cast Magnesium Alloys Based on Thermal Derivative Analysis / Analiza Procesu Krystalizacji Odlewniczych Stopów Magnezu W Oparciu O Analizę Termicznoderywacyjną. Arch. Metall. Mater. 60. https://doi.org/10.1515/amm-2015-0478
Król, M., Tański, T., Snopiński, P., Tomiczek, B., 2017. Structure and properties of aluminium–magnesium casting alloys after heat treatment. J. Therm. Anal. Calorim. 127, 299–308. https://doi.org/10.1007/s10973-016-5845-4
Krupiński, M., Labisz, K., Tański, T., Krupińska, B., Król, M., Polok-Rubiniec, M., 2016. Influence of Mg Addition on Crystallisation Kinetics and Structure of the Zn-Al-Cu Alloy. Arch. Metall. Mater. 61. https://doi.org/10.1515/amm-2016-0132
Kumar, C.A.V., Rajadurai, J.S., 2016. Influence of rutile (TiO_2) content on wear and microhardness characteristics of aluminium-based hybrid composites synthesized by powder metallurgy. Trans. Nonferrous Met. Soc. China 26, 63–73. https://doi.org/10.1016/S1003-6326(16)64089-X
Kumar, K., Van Swygenhoven, H., Suresh, S., 2003. Mechanical behavior of nanocrystalline metals and alloys11The Golden Jubilee Issue—Selected topics in Materials Science and Engineering: Past, Present and Future, edited by S. Suresh. Acta Mater. 51, 5743–5774. https://doi.org/10.1016/j.actamat.2003.08.032

Kumar, S., Selvarajan, V., Padmanabhan, P.V. a, Sreekumar, K.P., 2006. Characterization and comparison between ball milled and plasma processed iron-aluminium thermal spray coatings. Surf. Coat. Technol. 201, 1267–1275. https://doi.org/10.1016/j.surfcoat.2006.01.051

Kumari, K., Anand, K., Bellacci, M., Giannozzi, M., 2010. Effect of microstructure on abrasive wear behavior of thermally sprayed WC–10Co–4Cr coatings. Wear 268, 1309–1319. https://doi.org/10.1016/j.wear.2010.02.001

Kverneland, A., Hansen, V., Thorkildsen, G., Larsen, H.B., Pattison, P., Li, X.Z., Gjønnes, J., 2011. Transformations and structures in the Al–Zn–Mg alloy system: A diffraction study using synchrotron radiation and electron precession. Mater. Sci. Eng. A 528, 880–887. https://doi.org/10.1016/j.msea.2010.10.001

Larsen-Basse, J., 1985. Binder extrusion in sliding wear of WC-Co alloys. Wear 105, 247–256. https://doi.org/10.1016/0043-1648(85)90071-7

Le Pochat, S., Bertoluci, G., Froelich, D., 2007. Integrating ecodesign by conducting changes in SMEs. J. Clean. Prod. 15, 671–680. https://doi.org/10.1016/j.jclepro.2006.01.004

Legg, K.O., Graham, M., Chang, P., Rastagar, F., Gonzales, A., Sartwell, B., 1996. The replacement of electroplating. Surf. Coat. Technol. 81, 99–105. https://doi.org/10.1016/0257-8972(95)02653-3

Lei, Y., Sun, J., Du, X., Zhai, Q., Hu, S., 2007. Properties and microstructure of VC/Cr_3C_2-doped WC/Co cemented carbides. Rare Met. 26, 584–590. https://doi.org/10.1016/S1001-0521(08)60011-X

Lekatou, A., Karantzalis, A., Evangelou, A., Gousia, V., Kaptay, G., Gácsi, Z., Baumli, P., Simon, A., 2015. Aluminium reinforced by WC and TiC nanoparticles (ex-situ) and aluminide particles (in-situ): Microstructure, wear and corrosion behaviour. Mater. Des. 65, 1121–1135. https://doi.org/10.1016/j.matdes.2014.08.040

Lekatou, A., Regoutas, E., Karantzalis, A.E., 2008. Corrosion behaviour of cermet-based coatings with a bond coat in 0.5M H2SO4. Corros. Sci. 50, 3389–3400. https://doi.org/10.1016/j.corsci.2008.09.020

Lekatou, A., Sioulas, D., Karantzalis, A.E., Grimanelis, D., 2015. A comparative study on the microstructure and surface property evaluation of coatings produced from nanostructured and conventional WC–Co powders HVOF-sprayed on Al7075. Surf. Coat. Technol. 276, 539–556. https://doi.org/10.1016/j.surfcoat.2015.06.017

Leo, P., D'Ostuni, S., Casalino, G., 2016. Hybrid welding of AA5754 annealed alloy: Role of post weld heat treatment on microstructure and mechanical properties. Mater. Des. 90, 777–786. https://doi.org/10.1016/j.matdes.2015.10.150

Lepper, K., James, M., Chashechkina, J., Rigney, D.A., 1997. Sliding behavior of selected aluminum alloys. Wear 203–204, 46–56. https://doi.org/10.1016/S0043-1648(96)07475-3

Li, X.Z., Hansen, V., GjØnnes, J., Wallenberg, L.R., 1999. HREM study and structure modeling of the η′ phase, the hardening precipitates in commercial Al–Zn–Mg alloys. Acta Mater. 47, 2651–2659. https://doi.org/10.1016/S1359-6454(99)00138-X

Li, Y., Zhao, Y.H., Ortalan, V., Liu, W., Zhang, Z.H., Vogt, R.G., Browning, N.D., Lavernia, E.J., Schoenung, J.M., 2009. Investigation of aluminum-based nanocomposites with ultra-high strength. Mater. Sci. Eng. A 527, 305–316. https://doi.org/10.1016/j.msea.2009.07.067

Li, Y.S., Tao, N.R., Lu, K., 2008. Microstructural evolution and nanostructure formation in copper during dynamic plastic deformation at cryogenic temperatures. Acta Mater. 56, 230–241. https://doi.org/10.1016/j.actamat.2007.09.020
Liao, H., Normand, B., Coddet, C., 2000. Influence of coating microstructure on the abrasive wear resistance of WC/Co cermet coatings. Surf. Coat. Technol. 124, 235–242. https://doi.org/10.1016/S0257-8972(99)00653-2
Liu, J.Z., Chen, J.H., Yang, X.B., Ren, S., Wu, C.L., Xu, H.Y., Zou, J., 2010. Revisiting the precipitation sequence in Al–Zn–Mg-based alloys by high-resolution transmission electron microscopy. Scr. Mater. 63, 1061–1064. https://doi.org/10.1016/j.scriptamat.2010.08.001
Liu, M., Banhart, J., 2016. Effect of Cu and Ge on solute clustering in Al–Mg–Si alloys. Mater. Sci. Eng. A 658, 238–245. https://doi.org/10.1016/j.msea.2016.01.095
Liu, M., Čížek, J., Chang, C.S.T., Banhart, J., 2015. Early stages of solute clustering in an Al–Mg–Si alloy. Acta Mater. 91, 355–364. https://doi.org/10.1016/j.actamat.2015.02.019
Liu, S., Sun, D., Fan, Z., Yu, H., Meng, H., 2008. The influence of HVAF powder feedstock characteristics on the sliding wear behaviour of WC–NiCr coatings. Surf. Coat. Technol. 202, 4893–4900. https://doi.org/10.1016/j.surfcoat.2008.03.014
Liu, S., Zheng, X., Geng, G., 2010. Dry sliding wear behavior and corrosion resistance of NiCrBSi coating deposited by activated combustion-high velocity air fuel spray process. Mater. Des. 31, 913–917. https://doi.org/10.1016/j.matdes.2009.07.034
Liu, X., Liang, L., Xu, X., Li, X., Li, Y., 2014. Reciprocating wear behavior of WC–10Ni3Al cermet in contact with Ti6Al4V. Wear 321, 16–24. https://doi.org/10.1016/j.wear.2014.09.009
Lloyd, D.J., 1994. Particle reinforced aluminium and magnesium matrix composites. Int. Mater. Rev. 39, 1–23. https://doi.org/10.1179/imr.1994.39.1.1
Lohne, O., Dons, A.L., 1983. Quench sensitivity in AlMgSi alloys containing Mn or Cr. Scand. J. Metall. 12, 34–36.
Lovelock, H.L. de V., 1998. Powder/Processing/Structure Relationships in WC-Co Thermal Spray Coatings: A Review of the Published Literature. J. Therm. Spray Technol. 7, 357–373. https://doi.org/10.1361/105996398770350846
Lynch, J.P., Brown, L.M., Jacobs, M.H., 1982. Microanalysis of age-hardening precipitates in aluminium alloys. Acta Metall. 30, 1389–1395. https://doi.org/10.1016/0001-6160(82)90159-6
Ma, W., Wang, B., Fu, lei, Zhou, J., Huang, M., 2015. Influence of process parameters on deep drawing of AA6111 aluminum alloy at elevated temperatures. J. Cent. South Univ. 22, 1167–1174. https://doi.org/10.1007/s11771-015-2630-7
Mahmoodan, M., Aliakbarzadeh, H., Gholamipour, R., 2009. Microstructural and mechanical characterization of high energy ball milled and sintered WC–10 wt%Co–xTaC nano powders. Int. J. Refract. Met. Hard Mater. 27, 801–805. https://doi.org/10.1016/j.ijrmhm.2009.02.001
Mahmud, T.A.B., Saha, G.C., Khan, T.I., 2014. Mechanical property changes in HVOF sprayed nano-structured WC-17wt.%Ni(80/20)Cr coating with varying substrate roughness. IOP Conf. Ser. Mater. Sci. Eng. 60, 12007. https://doi.org/10.1088/1757-899X/60/1/012007
Maiti, A.K., Mukhopadhyay, N., Raman, R., 2007. Effect of adding WC powder to the feedstock of WC–Co–Cr based HVOF coating and its impact on erosion and abrasion resistance. Surf. Coat. Technol. 201, 7781–7788. https://doi.org/10.1016/j.surfcoat.2007.03.014

Mao, S., Yang, H., Li, J., Huang, F., Song, Z., 2011. Corrosion properties of aluminium coatings deposited on sintered NdFeB by ion-beam-assisted deposition. Appl. Surf. Sci. 257, 5581–5585. https://doi.org/10.1016/j.apsusc.2011.01.049

Marioara, C.D., Andersen, S.J., Jansen, J., Zandbergen, H.W., 2001. Atomic model for GP-zones in a 6082 Al–Mg–Si system. Acta Mater. 49, 321–328. https://doi.org/10.1016/S1359-6454(00)00302-5

Masuda, T., Takaki, Y., Sakurai, T., Hirosawa, S., 2010. Combined Effect of Pre-Straining and Pre-Aging on Bake-Hardening Behavior of an Al-0.6 mass%Mg-1.0 mass%Si Alloy. Mater. Trans. 51, 325–332. https://doi.org/10.2320/matertrans.L-M2009831

Mateen, A., Saha, G.C., Khan, T.I., Khalid, F.A., 2011. Tribological behaviour of HVOF sprayed near-nanostructured and microstructured WC-17wt.%Co coatings. Surf. Coat. Technol. 206, 1077–1084. https://doi.org/10.1016/j.surfcoat.2011.07.075

Matthews, S., James, B., 2010. Review of Thermal Spray Coating Applications in the Steel Industry: Part 1—Hardware in Steel Making to the Continuous Annealing Process. J. Therm. Spray Technol. 19, 1267–1276. https://doi.org/10.1007/s11666-010-9518-8

Mazahery, A., Shabani, M.O., 2012. Tribological behaviour of semisolid–semisolid compocast Al–Si matrix composites reinforced with TiB_2 coated B_4C particulates. Ceram. Int. 38, 1887–1895. https://doi.org/10.1016/j.ceramint.2011.10.016

Mazzer, E.M., Afonso, C.R.M., Galano, M., Kiminami, C.S., Bolfarini, C., 2013. Microstructure evolution and mechanical properties of Al–Zn–Mg–Cu alloy reprocessed by spray-forming and heat treated at peak aged condition. J. Alloys Compd. 579, 169–173. https://doi.org/10.1016/j.jallcom.2013.06.055

Miao, W.., Laughlin, D.., 1999. Precipitation hardening in aluminum alloy 6022. Scr. Mater. 40, 873–878. https://doi.org/10.1016/S1359-6462(99)00046-9

Mikhaylovskaya, A.V., Kotov, A.D., Pozdniakov, A.V., Portnoy, V.K., 2014. A high-strength aluminium-based alloy with advanced superplasticity. J. Alloys Compd. 599, 139–144. https://doi.org/10.1016/j.jallcom.2014.02.061

Milkereit, B., Schick, C., Kessler, O., 2010. Continuous cooling precipitation diagrams depending on the composition of aluminum-magnesium-silicon alloys. 12th Int. Conf. Alum. Alloys 407–412.

Miller, W.S., Zhuang, L., Bottema, J., Wittebrood, A., De Smet, P., Haszler, A., Vieregge, A., 2000. Recent development in aluminium alloys for the automotive industry. Mater. Sci. Eng. A 280, 37–49.

Mohamed, M.S., Foster, A.D., Lin, J., Balint, D.S., Dean, T.A., 2012. Investigation of deformation and failure features in hot stamping of AA6082: Experimentation and modelling. Int. J. Mach. Tools Manuf. 53, 27–38. https://doi.org/10.1016/j.ijmachtools.2011.07.005

Monticelli, C., Frignani, a., Zucchi, F., 2004. Investigation on the corrosion process of carbon steel coated by HVOF WC/Co cermets in neutral solution. Corros. Sci. 46, 1225–1237. https://doi.org/10.1016/j.corsci.2003.09.013

Mori, G., Zitter, H., Lackner, A., Schretter, M., 2001. Influencing the corrosion resistance of cemented carbides by addition of Cr_3C_2, TiC and TaC. Proc 15th Int Plansee Semin. 2, 222–236.

Morks, M.F., Gao, Y., Fahim, N.F., Yingqing, F.U., Shoeib, M.A., 2005. Influence of binder materials on the properties of low power plasma sprayed cermet coatings. Surf. Coat. Technol. 199, 66–71. https://doi.org/10.1016/j.surfcoat.2005.02.159

Mraied, H., Cai, W., Sagüés, A.A., 2016. Corrosion resistance of Al and Al–Mn thin films. Thin Solid Films 615, 391–401. https://doi.org/10.1016/j.tsf.2016.07.057
Murayama, M., Hono, K., 1999. Pre-precipitate clusters and precipitation processes in Al–Mg–Si alloys. Acta Mater. 47, 1537–1548. https://doi.org/10.1016/S1359-6454(99)00033-6
Murthy, J.K.N., Venkataraman, B., 2006. Abrasive wear behaviour of WC–CoCr and Cr_3C_2–20(NiCr) deposited by HVOF and detonation spray processes. Surf. Coat. Technol. 200, 2642–2652. https://doi.org/10.1016/j.surfcoat.2004.10.136
Myalska, H., Michalska, J.K., Moskal, G., Szymański, K., 2017. Effect of nano-sized TiC powder on microstructure and the corrosion resistance of WC-Co thermal spray coatings. Surf. Coat. Technol. 318, 270–278. https://doi.org/10.1016/j.surfcoat.2017.01.078
Myhr, O., 2001. Modelling of the age hardening behaviour of Al–Mg–Si alloys. Acta Mater. 49, 65–75. https://doi.org/10.1016/S1359-6454(00)00301-3
Naerheim, Y., Coddet, C., Droit, P., 1995. Effect of thermal spray process selection on tribological performance of WC–Co and Al_2O_3–TiO_2 coatings. Surf. Eng. 11, 66–70. https://doi.org/10.1179/sur.1995.11.1.66
Naga Krishna, N., Akash, A.K., Sivaprasad, K., Narayanasamy, R., 2010. Studies on void coalescence analysis of nanocrystalline cryorolled commercially pure aluminium formed under different stress conditions. Mater. Des. 31, 3578–3584. https://doi.org/10.1016/j.matdes.2010.01.056
Natishan, P.., Lawrence, S.., Foster, R.., Lewis, J., Sartwell, B.., 2000. Salt fog corrosion behavior of high-velocity oxygen-fuel thermal spray coatings compared to electrodeposited hard chromium. Surf. Coat. Technol. 130, 218–223. https://doi.org/10.1016/S0257-8972(00)00671-X
Nebti, S., Hamana, D., Cizeron, G., 1995. Calorimetric study of pre-precipitation and precipitation in Al-Mg alloy. Acta Metall. Mater. 43, 3583–3588. https://doi.org/10.1016/0956-7151(95)00023-O
Newbery, A.P., Ahn, B., Topping, T.D., Pao, P.S., Nutt, S.R., Lavernia, E.J., 2008. Large UFG Al alloy plates from cryomilling. J. Mater. Process. Technol. 203, 37–45. https://doi.org/10.1016/j.jmatprotec.2007.09.078
Nicholson, G.L., Davis, C.L., 2012. Modelling of the response of an ACFM sensor to rail and rail wheel RCF cracks. NDT E Int. 46, 107–114. https://doi.org/10.1016/j.ndteint.2011.11.010
Nieminen, R., Vuoristo, P., Niemi, K., Mäntylä, T., Barbezat, G., 1997. Rolling contact fatigue failure mechanisms in plasma and HVOF sprayed WC-Co coatings. Wear 212, 66–77. https://doi.org/10.1016/S0043-1648(97)00138-5
Nozato, R., Ishihara, S., 1980. Calorimetric study of precipitation process in Al-Mg alloys. Trans. Jpn. Inst. Met. 21, 580–588.
Oh, S.-J., Kim, B.-S., Yoon, J.-K., Hong, K.-T., Shon, I.-J., 2016. Enhanced mechanical properties and consolidation of the ultra-fine WC–Al_2O_3 composites using pulsed current activated heating. Ceram. Int. 42, 9304–9310. https://doi.org/10.1016/j.ceramint.2016.02.113
Osamura, K., Ogura, T., 1984. Metastable phases in the early stage of precipitation in Al-Mg alloys. Metall. Trans. Phys. Metall. Mater. Sci. 15 A, 835–842.
Ostermann, F., 1995. TALAT - a training programme for aluminium application technologies in Europe. Mater. Sci. Eng. A 199, 73–77. https://doi.org/10.1016/0921-5093(95)09911-5

Ozturk, F., Pekel, H., Halkaci, H.S., 2011. The effect of strain-rate sensitivity on formability of AA 5754-O at cold and warm temperatures. J. Mater. Eng. Perform. 20, 77–81. https://doi.org/10.1007/s11665-010-9652-y

Palanivel, R., Dinaharan, I., Laubscher, R.F., Davim, J.P., 2016. Influence of boron nitride nanoparticles on microstructure and wear behavior of AA6082/TiB_2 hybrid aluminium composites synthesized by friction stir processing. Mater. Des. 106, 195–204. https://doi.org/10.1016/j.matdes.2016.05.127

Pan, Y., Li, D.Y., Zhang, H., 2011. Enhancing the wear resistance of sintered WC–Co composite by adding pseudo-elastic TiNi constituent. Wear 271, 1916–1921. https://doi.org/10.1016/j.wear.2011.01.052

Pardo, A., Casajús, P., Mohedano, M., Coy, A.E., Viejo, F., Torres, B., Matykina, E., 2009. Corrosion protection of Mg/Al alloys by thermal sprayed aluminium coatings. Appl. Surf. Sci. 255, 6968–6977. https://doi.org/10.1016/j.apsusc.2009.03.022

Parliament, E.U., Council, E.U., 2003. Directive 2002/95/EC on the restriction of the use of certain hazardous substances in electrical and electronic equipment. J Eur Union 46, 19–23.

Pashley, D.W., Jacobs, M.H., Vietz, J.T., 1967. The basic processes affecting two-step ageing in an Al-Mg-Si alloy. Philos. Mag. 16, 51–76. https://doi.org/10.1080/14786436708229257

Pashley, D.W., Rhodes, J.W., Sendorek, A., 1966. Delayed aging in Al-Mg-Si alloys: effect on structure and mechanical properties. J Inst Met 94, 41–49.

Paterson, A.E., 2007. Introduction to Aluminium, Third Edition. Aluminium Federation of Southern Africa.

Pawlowski, L., 2008. The Science and Engineering of Thermal Spray Coatings. John Wiley & Sons, Ltd, Chichester, UK.

Peng, X., Guo, Q., Liang, X., Deng, Y., Gu, Y., Xu, G., Yin, Z., 2017. Mechanical properties, corrosion behavior and microstructures of a non-isothermal ageing treated Al-Zn-Mg-Cu alloy. Mater. Sci. Eng. A 688, 146–154. https://doi.org/10.1016/j.msea.2017.01.086

Perry, J.M., Hodgkiess, T., Neville, A., 2002. A comparison of the corrosion behavior of WC-Co-Cr and WC-Co HVOF thermally sprayed coatings by in situ atomic force microscopy (AFM). J. Therm. Spray Technol. 11, 536–541. https://doi.org/10.1361/105996302770348673

Perry, J.M., Neville, A., Wilson, V.A., Hodgkiess, T., 2001. Assessment of the corrosion rates and mechanisms of a WC–Co–Cr HVOF coating in static and liquid–solid impingement saline environments. Surf. Coat. Technol. 137, 43–51. https://doi.org/10.1016/S0257-8972(00)01062-8

Picas, J.A., Forn, A., Matthäus, G., 2006. HVOF coatings as an alternative to hard chrome for pistons and valves. Wear 261, 477–484. https://doi.org/10.1016/j.wear.2005.12.005

Picas, J.A., Punset, M., Teresa Baile, M., Martín, E., Forn, A., 2011. Tribological evaluation of HVOF thermal-spray coatings as a hard chrome replacement. Surf. Interface Anal. 43, 1346–1353. https://doi.org/10.1002/sia.3721

Picas, J.A., Xiong, Y., Punset, M., Ajdelsztajn, L., Forn, A., Schoenung, J.M., 2009. Microstructure and wear resistance of WC–Co by three consolidation processing techniques. Int. J. Refract. Met. Hard Mater., International Conference on the Science of Hard Materials - 9 27, 344–349. https://doi.org/10.1016/j.ijrmhm.2008.07.002

Pirso, J., Viljus, M., Letunovitš, S., 2006. Friction and dry sliding wear behaviour of cermets. Wear 260, 815–824. https://doi.org/10.1016/j.wear.2005.04.006

Pogatscher, S., Antrekowitsch, H., Leitner, H., Ebner, T., Uggowitzer, P.J., 2011. Mechanisms controlling the artificial aging of Al–Mg–Si Alloys. Acta Mater. 59, 3352–3363. https://doi.org/10.1016/j.actamat.2011.02.010

Prabhu, B., Suryanarayana, C., An, L., Vaidyanathan, R., 2006. Synthesis and characterization of high volume fraction Al–Al_2O_3 nanocomposite powders by high-energy milling. Mater. Sci. Eng. A 425, 192–200. https://doi.org/10.1016/j.msea.2006.03.066

Prabhukhot, A., Prasad, K., 2015. Effect of heat treatment on hardness of 6082-T6 aluminium alloy. Int. J. Sci. Eng. Res. 6.

Pramod, S.L., Bakshi, S.R., Murty, B.S., 2015. Aluminum-Based Cast In Situ Composites: A Review. J. Mater. Eng. Perform. 24, 2185–2207. https://doi.org/10.1007/s11665-015-1424-2

Pramod, S.L., Prasada Rao, A.K., Murty, B.S., Bakshi, S.R., 2015. Effect of Sc addition on the microstructure and wear properties of A356 alloy and A356–TiB_2 in situ composite. Mater. Des. 78, 85–94. https://doi.org/10.1016/j.matdes.2015.04.026

Qiao, Y., Fischer, T.E., Dent, A., 2003. The effects of fuel chemistry and feedstock powder structure on the mechanical and tribological properties of HVOF thermal-sprayed WC–Co coatings with very fine structures. Surf. Coat. Technol. 172, 24–41. https://doi.org/10.1016/S0257-8972(03)00242-1

Qiao, Y., Liu, Y., Fischer, T.E., 2001. Sliding and Abrasive Wear Resistance of Thermal-Sprayed WC-Co Coatings. J. Therm. Spray Technol. 10, 118–125. https://doi.org/10.1361/105996301770349583

Qin, X., Sun, D., Xie, L., Wu, Q., 2014. Hardening mechanism of Cr5 backup roll material induced by rolling contact fatigue. Mater. Sci. Eng. A 600, 195–199. https://doi.org/10.1016/j.msea.2014.01.100

Ramesh, C.S., Pramod, S., Keshavamurthy, R., 2011. A study on microstructure and mechanical properties of Al 6061–TiB_2 in-situ composites. Mater. Sci. Eng. A 528, 4125–4132. https://doi.org/10.1016/j.msea.2011.02.024

Rastegar, F., Richardson, D.E., 1997. Alternative to chrome: HVOF cermet coatings for high horse power diesel engines. Surf. Coat. Technol. 90, 156–163. https://doi.org/10.1016/S0257-8972(96)03112-X

Ravi, C., 2004. First-principles study of crystal structure and stability of $Al_xMg_ySi_z$(Cu) precipitates. Acta Mater. 52, 4213–4227. https://doi.org/10.1016/j.actamat.2004.05.037

Registration, Evaluation, Authorisation and Restriction of Chemicals, 2017. Wikipedia.

Reis, L., Li, B., de Freitas, M., 2014. A multiaxial fatigue approach to Rolling Contact Fatigue in railways. Int. J. Fatigue 67, 191–202. https://doi.org/10.1016/j.ijfatigue.2014.02.001

Rhys-Jones, T.N., 1990. The use of thermally sprayed coatings for compressor and turbine applications in aero engines. Surf. Coat. Technol. 42, 1–11. https://doi.org/10.1016/0257-8972(90)90109-P

Rometsch, P.A., Cao, L.F., Xiong, X.Y., Muddle, B.C., 2011. Atom probe analysis of early-stage strengthening behaviour in an Al–Mg–Si–Cu alloy. Ultramicroscopy 111, 690–694. https://doi.org/10.1016/j.ultramic.2010.11.009

Roven, H.J., 1992. A model for fracture toughness predictions in aluminium alloys exhibiting the slip band decohesion mechanism. Scr. Metall. Mater. 26, 1383–1388. https://doi.org/10.1016/0956-716X(92)90653-V

Røyset, J., Stene, T., Saeter, J.A., Reiso, O., 2006. The effect of intermediate storage temperature and time on the age hardening response of Al-Mg-Si alloys. Mater. Sci. Forum 519–521, 239–244.
Russell, K.C., Aaronson, H.I., 1975. Sequences of precipitate nucleation. J. Mater. Sci. 10, 1991–1999. https://doi.org/10.1007/BF00754490
Sahin, Y., 2007. Tribological behaviour of metal matrix and its composite. Mater. Des. 28, 1348–1352. https://doi.org/10.1016/j.matdes.2006.01.032
Saito, H., Iwabuchi, A., Shimizu, T., 2006. Effects of Co content and WC grain size on wear of WC cemented carbide. Wear 261, 126–132. https://doi.org/10.1016/j.wear.2005.09.034
Sajjadi, S.A., Ezatpour, H.R., Torabi Parizi, M., 2012. Comparison of microstructure and mechanical properties of A356 aluminum alloy/Al_2O_3 composites fabricated by stir and compo-casting processes. Mater. Des. 34, 106–111. https://doi.org/10.1016/j.matdes.2011.07.037
Sanchette, F., Ducros, C., Billard, A., Rébéré, C., Berziou, C., Reffass, M., Creus, J., 2009. Nanostructured aluminium based coatings deposited by electron-beam evaporative PVD. Thin Solid Films 518, 1575–1580. https://doi.org/10.1016/j.tsf.2009.09.057
Sartwell, B.D., Natishan, P.M., Singer, I.L., Legg, K.O., Schell, J.D., Sauer, J.P., 1998. Replacement of chromium electroplating using HVOF thermal spray coatings, in: AESF Plating Forum.
Sato, T., Kojima, Y., Takahashi, T., 1982. Modulated structures and GP zones in Al-Mg alloys. Metall. Trans. Phys. Metall. Mater. Sci. 13 A, 1373–1378.
Satyanarayana, K.G., Pillai, R.M., Pai, B.C., 2002. Recent developments and prospects in cast aluminium matrix composites. Trans. Indian Inst. Met. 55, 115–130.
Scholl, H., Hofman, B., Rauscher, A., 1992. Anodic polarization of cemented carbides of the type [(WC,M): M = Fe, Ni or Co] in sulphuric acid solution. Electrochimica Acta 37, 447–452. https://doi.org/10.1016/0013-4686(92)87034-W
Schwartzkopf, P., Keiffer, R., 1953. Refractory Hard Metals Borides, Carbides, Nitrides and Silicides. The MacMillan Company, New York.
Serizawa, A., Hirosawa, S., Sato, T., 2008. Three-Dimensional Atom Probe Characterization of Nanoclusters Responsible for Multistep Aging Behavior of an Al-Mg-Si Alloy. Metall. Mater. Trans. A 39, 243–251. https://doi.org/10.1007/s11661-007-9438-5
Serres, N., Hlawka, F., Costil, S., Langlade, C., Machi, F., 2010. Microstructures and environmental assessment of metallic NiCrBSi coatings manufactured via hybrid plasma spray process. Surf. Coat. Technol. 205, 1039–1046. https://doi.org/10.1016/j.surfcoat.2010.03.048
Sevim, I., Eryurek, I.B., 2006. Effect of fracture toughness on abrasive wear resistance of steels. Mater. Des. 27, 911–919. https://doi.org/10.1016/j.matdes.2005.03.009
Shatov, A.V., Ponomarev, S.S., Firstov, S.A., 2009. Modeling the effect of flatter shape of WC crystals on the hardness of WC-Ni cemented carbides. Int. J. Refract. Met. Hard Mater. 27, 198–212. https://doi.org/10.1016/j.ijrmhm.2008.07.008
Shatov, A.V., Ponomarev, S.S., Firstov, S.A., 2008. Fracture of WC–Ni cemented carbides with different shape of WC crystals. Int. J. Refract. Met. Hard Mater. 26, 68–76. https://doi.org/10.1016/j.ijrmhm.2007.03.002
Shi, L., Yang, H., Guo, L.G., Zhang, J., 2014. Constitutive modeling of deformation in high temperature of a forging 6005A aluminum alloy. Mater. Des. 1980-2015 54, 576–581. https://doi.org/10.1016/j.matdes.2013.08.037

Shokuhfar, A., Nejadseyfi, O., 2014. A comparison of the effects of severe plastic deformation and heat treatment on the tensile properties and impact toughness of aluminum alloy 6061. Mater. Sci. Eng. A 594, 140–148. https://doi.org/10.1016/j.msea.2013.11.067

Smith, W.F., 1973. The effect of reversion treatments on precipitation mechanisms in an Al-1.35 at. pct Mg_2Si alloy. Metall. Trans. 4, 2435–2440. https://doi.org/10.1007/BF02669387

Sobolev, V.V., Guilemany, J.M., Miguel, J.R., Calero, J.A., 1996a. Influence of thermal processes on coating formation during high velocity oxy-fuel (HVOF) spraying of WC-Ni powder particles. Surf. Coat. Technol. 82, 121–129. https://doi.org/10.1016/0257-8972(95)02657-6

Sobolev, V.V., Guilemany, J.M., Miguel, J.R., Calero, J.A., 1996b. Investigation of the development of coating structure during high velocity oxy-fuel (HVOF) spraying of WC-Ni powder particles. Surf. Coat. Technol. 82, 114–120. https://doi.org/10.1016/0257-8972(95)02656-8

Song, M., 2009. Effects of volume fraction of SiC particles on mechanical properties of SiC/Al composites. Trans. Nonferrous Met. Soc. China 19, 1400–1404.

Song, R.G., Wang, C., Jiang, Y., Li, H., Lu, G., Wang, Z.X., 2012. Microstructure and properties of Al_2O_3/TiO_2 nanostructured ceramic composite coatings prepared by plasma spraying. J. Alloys Compd. 544, 13–18. https://doi.org/10.1016/j.jallcom.2012.07.032

Souza, V.A.D., Neville, A., 2007. Aspects of microstructure on the synergy and overall material loss of thermal spray coatings in erosion–corrosion environments. Wear, 16th International Conference on Wear of Materials 263, 339–346. https://doi.org/10.1016/j.wear.2007.01.071

Spriggs, G.E., 1995. A history of fine grained hardmetal. Int. J. Refract. Met. Hard Mater., Special Issue on Fine Grained Hardmetals 13, 241–255. https://doi.org/10.1016/0263-4368(95)92671-6

Stack, M.M., Abd El-Badia, T.M., 2008. Some comments on mapping the combined effects of slurry concentration, impact velocity and electrochemical potential on the erosion–corrosion of WC/Co–Cr coatings. Wear 264, 826–837. https://doi.org/10.1016/j.wear.2007.02.025

Starink, M.J., Zahra, A.-M., 1998. β′ and β precipitation in an Al–Mg alloy studied by DSC and TEM. Acta Mater. 46, 3381–3397. https://doi.org/10.1016/S1359-6454(98)00053-6

Stewart, D.A., Shipway, P.H., McCartney, D.G., 2000. Microstructural evolution in thermally sprayed WC–Co coatings: comparison between nanocomposite and conventional starting powders. Acta Mater. 48, 1593–1604. https://doi.org/10.1016/S1359-6454(99)00440-1

Stewart, D.A., Shipway, P.H., McCartney, D.G., 1999. Abrasive wear behaviour of conventional and nanocomposite HVOF-sprayed WC–Co coatings. Wear 225–229, Part 2, 789–798. https://doi.org/10.1016/S0043-1648(99)00032-0

Stiller, K., Warren, P.., Hansen, V., Angenete, J., Gjønnes, J., 1999. Investigation of precipitation in an Al–Zn–Mg alloy after two-step ageing treatment at 100° and 150°C. Mater. Sci. Eng. A 270, 55–63. https://doi.org/10.1016/S0921-5093(99)00231-2

Stokes, J., Looney, L., 2001. HVOF system definition to maximise the thickness of formed components. Surf. Coat. Technol. 148, 18–24. https://doi.org/10.1016/S0257-8972(01)01272-5

Strobel, K., Easton, M.A., Sweet, L., Couper, M.J., Nie, J.-F., 2011. Relating quench sensitivity to microstructure in 6000 series aluminium alloys. Mater. Trans. 52, 914–919. https://doi.org/10.2320/matertrans.L-MZ201111

Strobel, K., Lay, M.D.H., Easton, M.A., Sweet, L., Zhu, S., Parson, N.C., Hill, A.J., 2016. Effects of quench rate and natural ageing on the age hardening behaviour of aluminium alloy AA6060. Mater. Charact. 111, 43–52. https://doi.org/10.1016/j.matchar.2015.11.009

Subrahmanyam, J., Srivastava, M.P., Sivakumar, R., 1986. Characterization of plasma-sprayed WC-Co coatings. Mater. Sci. Eng. 84, 209–214. https://doi.org/10.1016/0025-5416(86)90240-5

Suresh, S., Shenbaga Vinayaga Moorthi, N., Vettivel, S.C., Selvakumar, N., 2014a. Mechanical behavior and wear prediction of stir cast Al–TiB_2 composites using response surface methodology. Mater. Des. 59, 383–396. https://doi.org/10.1016/j.matdes.2014.02.053

Suresh, S., Shenbaga Vinayaga Moorthi, N., Vettivel, S.C., Selvakumar, N., Jinu, G.R., 2014b. Effect of graphite addition on mechanical behavior of Al6061/TiB_2 hybrid composite using acoustic emission. Mater. Sci. Eng. A 612, 16–27. https://doi.org/10.1016/j.msea.2014.06.024

Sutthiruangwong, S., Mori, G., 2003. Corrosion properties of Co-based cemented carbides in acidic solutions. Int. J. Refract. Met. Hard Mater. 21, 135–145. https://doi.org/10.1016/S0263-4368(03)00027-1

Sutthiruangwong, S., Mori, G., Kösters, R., 2005. Passivity and pseudopassivity of cemented carbides. Int. J. Refract. Met. Hard Mater. 23, 129–136. https://doi.org/10.1016/j.ijrmhm.2004.11.006

Szklarska-Smialowska, Z., 1999. Pitting corrosion of aluminum. Corros. Sci. 41, 1743–1767. https://doi.org/10.1016/S0010-938X(99)00012-8

Szymański, K., Hernas, A., Moskal, G., Myalska, H., 2015. Thermally sprayed coatings resistant to erosion and corrosion for power plant boilers - A review. Surf. Coat. Technol. 268, 153–164. https://doi.org/10.1016/j.surfcoat.2014.10.046

Thakur, L., Arora, N., Jayaganthan, R., Sood, R., 2011. An investigation on erosion behavior of HVOF sprayed WC–CoCr coatings. Appl. Surf. Sci. 258, 1225–1234. https://doi.org/10.1016/j.apsusc.2011.09.079

Tomlinson, W.J., Linzell, C.R., 1988. Anodic polarization and corrosion of cemented carbides with cobalt and nickel binders. J. Mater. Sci. 23, 914–918. https://doi.org/10.1007/BF01153988

Torsæter, M., Lefebvre, W., Marioara, C.D., Andersen, S.J., Walmsley, J.C., Holmestad, R., 2011. Study of intergrown L and Q′ precipitates in Al–Mg–Si–Cu alloys. Scr. Mater. 64, 817–820. https://doi.org/10.1016/j.scriptamat.2011.01.008

Total Materia, 2013. Precipitation Hardening of Aluminum Alloys, Key To Metals.

Trdan, U., Grum, J., 2012. Evaluation of corrosion resistance of AA6082-T651 aluminium alloy after laser shock peening by means of cyclic polarisation and ElS methods. Corros. Sci. 59, 324–333. https://doi.org/10.1016/j.corsci.2012.03.019

Upadhyay, R.K., Kumaraswamidhas, L.A., Azam, M.S., 2013. Rolling element bearing failure analysis: A case study. Case Stud. Eng. Fail. Anal. 1, 15–17. https://doi.org/10.1016/j.csefa.2012.11.003

Upadhyaya, G.S., 2001. Materials science of cemented carbides — an overview. Mater. Des., 1.Selected Papers from the 3rd International Conference on Cast Metal Matrix Composites & 2. Advances in Cemented Carbides 22, 483–489. https://doi.org/10.1016/S0261-3069(01)00007-3

Ureña, A., Rams, J., Campo, M., Sánchez, M., 2009. Effect of reinforcement coatings on the dry sliding wear behaviour of aluminium/SiC particles/carbon fibres hybrid composites. Wear 266, 1128–1136. https://doi.org/10.1016/j.wear.2009.03.016

Valiev, R.Z., Zehetbauer, M.J., Estrin, Y., Höppel, H.W., Ivanisenko, Y., Hahn, H., Wilde, G., Roven, H.J., Sauvage, X., Langdon, T.G., 2007. The Innovation Potential of Bulk Nanostructured Materials. Adv. Eng. Mater. 9, 527–533. https://doi.org/10.1002/adem.200700078

Van, R., Sinte, M., Mittemeijer, E.J., 1988. Precipitation of Guinier-Preston zones in aluminum-magnesium; a calorimetric analysis of liquid-quenched and solid-quenched alloys. Metall. Trans. Phys. Metall. Mater. Sci. 19 A, 2433–2443.

van der Merwe, R., Sacks, N., 2013. Effect of TaC and TiC on the friction and dry sliding wear of WC–6 wt.% Co cemented carbides against steel counterfaces. Int. J. Refract. Met. Hard Mater. 41, 94–102. https://doi.org/10.1016/j.ijrmhm.2013.02.009

van Huis, M.A., Chen, J.H., Sluiter, M.H.F., Zandbergen, H.W., 2007. Phase stability and structural features of matrix-embedded hardening precipitates in Al–Mg–Si alloys in the early stages of evolution. Acta Mater. 55, 2183–2199. https://doi.org/10.1016/j.actamat.2006.11.019

van Huis, M.A., Sluiter, M.H.F., Chen, J.H., Zandbergen, H.W., 2007. Concurrent substitutional and displacive phase transformations in Al-Mg-Si nanoclusters. Phys. Rev. B 76. https://doi.org/10.1103/PhysRevB.76.174113

Vargel, C., 2004. Chapter A.2 - Physical Properties of Aluminium, in: Corrosion of Aluminium. Elsevier, Amsterdam, pp. 19–20.

Veeresh Kumar, G.B., Rao, C.S.P., Selvaraj, N., 2012. Studies on mechanical and dry sliding wear of Al6061–SiC composites. Compos. Part B Eng. 43, 1185–1191. https://doi.org/10.1016/j.compositesb.2011.08.046

Venkatachalam, P., Ravisankar, B., Kumaran, S., 2010. Microstructure and mechanical properties of 2014 Al alloy processed by equal channel angular pressing (ECAP). Int. J. Microstruct. Mater. Prop. 5, 88. https://doi.org/10.1504/IJMMP.2010.032504

Venkataraman, B., Sundararajan, G., 1996. The sliding wear behaviour of Al-SiC particulate composites—I. Macrobehaviour. Acta Mater. 44, 451–460. https://doi.org/10.1016/1359-6454(95)00217-0

Venkateswara Rao, K.T., Hayashigatani, H.F., Yu, W., Ritchie, R.O., 1988. On the fracture toughness of aluminum-lithium alloy 2090-T8E41 at ambient and cryogenic temperatures. Scr. Metall. 22, 93–98. https://doi.org/10.1016/S0036-9748(88)80312-0

Verdon, C., Karimi, A., Martin, J.-L., 1998. A study of high velocity oxy-fuel thermally sprayed tungsten carbide based coatings. Part 1: Microstructures. Mater. Sci. Eng. A 246, 11–24. https://doi.org/10.1016/S0921-5093(97)00759-4

Vernhes, L., Lee, D.A., Poirier, D., Li, D., Klemberg-Sapieha, J.E., 2013. HVOF Coating case study for power plant process control ball valve application. J. Therm. Spray Technol. 22, 1184–1192. https://doi.org/10.1007/s11666-013-9978-8

Vijayarangan, S., Rajamanickam, N., Sivananth, V., 2013. Evaluation of metal matrix composite to replace spheroidal graphite iron for a critical component, steering knuckle. Mater. Des. 43, 532–541. https://doi.org/10.1016/j.matdes.2012.07.007

Villalobos-Gutiérrez, C.J., Gedler-Chacón, G.E., La Barbera-Sosa, J.G., Piñeiro, A., Staia, M.H., Lesage, J., Chicot, D., Mesmacque, G., Puchi-Cabrera, E.S., 2008. Fatigue and corrosion fatigue behavior of an AA6063-T6 aluminum alloy coated with a WC–10Co–4Cr alloy

deposited by HVOF thermal spraying. Surf. Coat. Technol. 202, 4572–4577. https://doi.org/10.1016/j.surfcoat.2008.04.044
Vlok, F., Stumpf, W., Pistorius, C., 2007. Understanding metals across the spectrum. University of Pretoria.
Vorhauer, A., Pippan, R., 2004. On the homogeneity of deformation by high pressure torsion. Scr. Mater. 51, 921–925. https://doi.org/10.1016/j.scriptamat.2004.04.025
Wan, L., Huang, Y., Lv, Z., Lv, S., Feng, J., 2014. Effect of self-support friction stir welding on microstructure and microhardness of 6082-T6 aluminum alloy joint. Mater. Des. 55, 197–203. https://doi.org/10.1016/j.matdes.2013.09.073
Wang, G., Gu, K., Huang, Z., Ding, P., 2016. Improving the wear resistance of as-sprayed WC coating by deep cryogenic treatment. Mater. Lett. 185, 363–365. https://doi.org/10.1016/j.matlet.2016.09.032
Wang, Q., Li, L., Yang, G., Zhao, X., Ding, Z., 2012. Influence of heat treatment on the microstructure and performance of high-velocity oxy-fuel sprayed WC–12Co coatings. Surf. Coat. Technol. 206, 4000–4010. https://doi.org/10.1016/j.surfcoat.2012.03.080
Wang, T., Zheng, Y., Chen, Z., Zhao, Y., Kang, H., 2014. Effects of Sr on the microstructure and mechanical properties of in situ TiB_2 reinforced A356 composite. Mater. Des. 64, 185–193. https://doi.org/10.1016/j.matdes.2014.07.040
Wang, X., Poole, W.J., Esmaeili, S., Lloyd, D.J., Embury, J.D., 2003. Precipitation strengthening of the aluminum alloy AA6111. Metall. Mater. Trans. Phys. Metall. Mater. Sci. 34, 2913–2924.
Wang, Y., Song, J., 2010. Dry sliding wear behavior of Al_2O_3 fiber and SiC particle reinforced aluminium based MMCs fabricated by squeeze casting method. Chin. J. Nonferrous Met. 21, 1441–1448.
Ward, L.P., Pilkington, A., 2014. The Dry Sliding Wear Behavior of HVOF-Sprayed WC: Metal Composite Coatings. J. Mater. Eng. Perform. 23, 3266–3278. https://doi.org/10.1007/s11665-014-1122-5
Wayne, S.F., Sampath, S., 1992. Structure/property relationships in sintered and thermally sprayed WC-Co. J. Therm. Spray Technol. 1, 307–315. https://doi.org/10.1007/BF02647158
Weidow, J., Andrén, H.-O., 2011. Grain and phase boundary segregation in WC–Co with TiC, ZrC, NbC or TaC additions. Int. J. Refract. Met. Hard Mater. 29, 38–43. https://doi.org/10.1016/j.ijrmhm.2010.06.010
Wenner, S., Marioara, C.D., Andersen, S.J., Holmestad, R., 2012. Effect of room temperature storage time on precipitation in Al–Mg–Si(–Cu) alloys with different Mg/Si ratios. Int. J. Mater. Res. 103, 948–954. https://doi.org/10.3139/146.110795
Wesmann, J.A.R., Espallargas, N., 2016. Effect of atmosphere, temperature and carbide size on the sliding friction of self-mated HVOF WC–CoCr contacts. Tribol. Int. 101, 301–313. https://doi.org/10.1016/j.triboint.2016.04.032
Wiley: Magnesium, Magnesium Alloys, and Magnesium Composites - Manoj Gupta, Nai Mui Ling Sharon [WWW Document], n.d. URL http://eu.wiley.com/WileyCDA/WileyTitle/productCd-0470494174.html (accessed 10.26.16).
Wloka, J., Hack, T., Virtanen, S., 2007. Influence of temper and surface condition on the exfoliation behaviour of high strength Al–Zn–Mg–Cu alloys. Corros. Sci. 49, 1437–1449. https://doi.org/10.1016/j.corsci.2006.06.033

Wood, R.J.K., 2010. Tribology of thermal sprayed WC–Co coatings. Int. J. Refract. Met. Hard Mater., Tribology of Hard Coatings 28, 82–94. https://doi.org/10.1016/j.ijrmhm.2009.07.011

Wu, G., Zeng, X., Yuan, G., 2008. Growth and corrosion of aluminum PVD-coating on AZ31 magnesium alloy. Mater. Lett. 62, 4325–4327. https://doi.org/10.1016/j.matlet.2008.07.014

Xu, J.-S., Zhang, X.-C., Xuan, F.-Z., Wang, Z.-D., Tu, S.-T., 2014. Rolling contact fatigue behavior of laser cladded WC/Ni composite coating. Surf. Coat. Technol. 239, 7–15. https://doi.org/10.1016/j.surfcoat.2013.11.005

Xu, Z., Liu, M., Jia, Z., Roven, H.J., 2017a. Effect of cryorolling on microstructure and mechanical properties of a peak-aged AA6082 extrusion. J. Alloys Compd. 695, 827–840. https://doi.org/10.1016/j.jallcom.2016.10.135

Xu, Z., Roven, H.J., Jia, Z., 2017b. Effects of cryogenic temperature and pre-stretching on mechanical properties and deformation characteristics of a peak-aged AA6082 extrusion. Mater. Sci. Eng. A 679, 379–390. https://doi.org/10.1016/j.msea.2016.10.049

Xue, J., Wang, J., Han, Y., Li, P., Sun, B., 2011. Effects of CeO_2 additive on the microstructure and mechanical properties of in situ TiB_2/Al composite. J. Alloys Compd. 509, 1573–1578. https://doi.org/10.1016/j.jallcom.2010.10.152

Yadav, D., Bauri, R., 2015. Friction Stir Processing of Al-TiB_2 In Situ Composite: Effect on Particle Distribution, Microstructure and Properties. J. Mater. Eng. Perform. 24, 1116–1124. https://doi.org/10.1007/s11665-015-1404-6

Yadav, D., Bauri, R., 2011. Processing, microstructure and mechanical properties of nickel particles embedded aluminium matrix composite. Mater. Sci. Eng. A 528, 1326–1333. https://doi.org/10.1016/j.msea.2010.10.035

Yamada, K., Sato, T., Kamio, A., 2000. Effects of Quenching Conditions on Two-Step Aging Behavior of Al-Mg-Si Alloys. Mater. Sci. Forum 331–337, 669–674. https://doi.org/10.4028/www.scientific.net/MSF.331-337.669

Yan, Y., Liang, Z.Q., Banhart, J., 2014. Influence of Pre-Straining and Pre-Ageing on the Age-Hardening Response of Al-Mg-Si Alloys. Mater. Sci. Forum 794–796, 903–908. https://doi.org/10.4028/www.scientific.net/MSF.794-796.903

Yan, S. qing, Li, X. fu, 2014. The effect of Si morphology on the microstructure and wear property of ZA48 alloy. Int. J. Microstruct. Mater. Prop. 9, 88. https://doi.org/10.1504/IJMMP.2014.061055

Yang, Q., Senda, T., Hirose, A., 2006. Sliding wear behavior of WC–12% Co coatings at elevated temperatures. Surf. Coat. Technol. 200, 4208–4212. https://doi.org/10.1016/j.surfcoat.2004.12.032

Yang, Q., Senda, T., Ohmori, A., 2003. Effect of carbide grain size on microstructure and sliding wear behavior of HVOF-sprayed WC–12% Co coatings. Wear 254, 23–34.

Yang, W., Ji, S., Wang, M., Li, Z., 2014. Precipitation behaviour of Al–Zn–Mg–Cu alloy and diffraction analysis from η′ precipitates in four variants. J. Alloys Compd. 610, 623–629. https://doi.org/10.1016/j.jallcom.2014.05.061

Yang, W., Ji, S., Zhang, Q., Wang, M., 2015. Investigation of mechanical and corrosion properties of an Al–Zn–Mg–Cu alloy under various ageing conditions and interface analysis of η′ precipitate. Mater. Des. 85, 752–761. https://doi.org/10.1016/j.matdes.2015.06.183

Yassar, R.S., Field, D.P., Weiland, H., 2005. The effect of cold deformation on the kinetics of the β″ precipitates in an Al-Mg-Si alloy. Metall. Mater. Trans. Phys. Metall. Mater. Sci. 36, 2059–2065.

Yi, C., Fan, H., Xiong, J., Guo, Z., Dong, G., Wan, W., Chen, H., 2013. Effect of WC content on the microstructures and corrosion behavior of Ti(C, N)-based cermets. Ceram. Int. 39, 503–509. https://doi.org/10.1016/j.ceramint.2012.06.055

Yin, B., Zhou, H.D., Yi, D.L., Chen, J.M., Yan, F.Y., 2010. Microsliding wear behaviour of HVOF sprayed conventional and nanostructured WC–12Co coatings at elevated temperatures. Surf. Eng. 26, 469–477. https://doi.org/10.1179/026708410X12506870724352

Yu, S.Y., Ishii, H., Tohgo, K., Cho, Y.T., Diao, D., 1997. Temperature dependence of sliding wear behavior in SiC whisker or SiC particulate reinforced 6061 aluminum alloy composite. Wear 213, 21–28. https://doi.org/10.1016/S0043-1648(97)00207-X

Yukawa, H., Murata, Y., Morinaga, M., Takahashi, Y., Yoshida, H., 1995. Heterogeneous distributions of Magnesium atoms near the precipitate in Al-Mg based alloys. Acta Metall. Mater. 43, 681–688. https://doi.org/10.1016/0956-7151(94)00266-K

Yun, J.-H., Rhee, S.-W., 1998. Effect of carrier gas on metal-organic chemical vapour deposition of aluminium from dimethylethylamine alane. J. Mater. Sci. Mater. Electron. 9, 1–4.

Žagar, S., Grum, J., 2013. Residual stress, fatigue and electrical conductivity analysis after shot peening of aluminium alloy AlZn5.5MgCu. Int. J. Microstruct. Mater. Prop. 8, 447. https://doi.org/10.1504/IJMMP.2013.059480

Zeng, D., Lu, L., Li, Z., Zhang, J., Jin, X., Zhu, M., 2014. Influence of laser dispersed treatment on rolling contact wear and fatigue behavior of railway wheel steel. Mater. Des. 1980-2015 54, 137–143. https://doi.org/10.1016/j.matdes.2013.08.041

Zhang, X.C., Xu, B.S., Xuan, F.Z., Tu, S.T., Wang, H.D., Wu, Y.X., 2008. Rolling contact fatigue behavior of plasma-sprayed CrC–NiCr cermet coatings. Wear 265, 1875–1883. https://doi.org/10.1016/j.wear.2008.04.048

Zhang, X.C., Xu, B.S., Xuan, F.Z., Wang, Z.D., Tu, S.T., 2011. Failure mode and fatigue mechanism of laser-remelted plasma-sprayed Ni alloy coatings in rolling contact. Surf. Coat. Technol. 205, 3119–3127. https://doi.org/10.1016/j.surfcoat.2010.08.122

Zhang, Z., Qin, H., Zhu, W., Lim, A., 2012. The single vehicle routing problem with toll-by-weight scheme: A branch-and-bound approach. Eur. J. Oper. Res. 220, 295–304. https://doi.org/10.1016/j.ejor.2012.01.035

Zhang, Z., Wang, H., Xu, B.-S., Zhang, G., 2015. Investigation on influence of WC–Ni addition on rolling contact fatigue behavior of plasma sprayed Ni-based alloy coating. Tribol. Int. 90, 509–518. https://doi.org/10.1016/j.triboint.2015.05.021

Zhao, X.-Q., Zhou, H.-D., Chen, J.-M., 2006. Comparative study of the friction and wear behavior of plasma sprayed conventional and nanostructured WC–12%Co coatings on stainless steel. Mater. Sci. Eng. A 431, 290–297. https://doi.org/10.1016/j.msea.2006.06.009

Zhao, Y., Zheng, Y., Zhou, W., Lv, X., 2014. Characterization of functionally gradient Ti(C, N)-based cermets fabricated by vacuum liquid phase sintering and nitriding treatment during cooling. Int. J. Refract. Met. Hard Mater. 46, 20–23. https://doi.org/10.1016/j.ijrmhm.2014.05.003

Zhen, L., Kang, S.B., 1997. The effect of pre-aging on microstructure and tensile properties of Al-Mg-Si alloys. Scr. Mater. 36, 1089–1094. https://doi.org/10.1016/S1359-6462(96)00487-3

Zheng, Y., Liu, W., Yuan, Q., Wen, L., Xiong, W., 2005. Effect of grain growth inhibitor on the microstructure and mechanical properties of Ti(C,N)-based cermet. Key Eng. Mater. 280–283, 1413–1416.

Zheng, Y., You, M., Xiong, W., Liu, W., Wang, S., 2003. Valence-electron structure and properties of main phases in Ti(C, N)-based cermets. Mater. Chem. Phys. 82, 877–881. https://doi.org/10.1016/j.matchemphys.2003.07.008

Zhong, H., Rometsch, P.A., Zhu, Q., Cao, L., Estrin, Y., 2017. Effect of pre-ageing on dynamic strain ageing in Al-Mg-Si alloys. Mater. Sci. Eng. A 687, 323–331. https://doi.org/10.1016/j.msea.2017.01.051

Zhou, S., Zhao, W., Xiong, W., 2009. Microstructure and properties of the cermets based on Ti(C,N). Int. J. Refract. Met. Hard Mater. 27, 26–32. https://doi.org/10.1016/j.ijrmhm.2008.01.011

APPENDICES

This section contains the source data from values in the results and other chapters were derived.

Appendix A: Mechanical Tests after Heat Treatment

Below are the results of mechanical tests performed on the heat treated AA6082 before any surface treatment was performed. In Table A1, “top” refers to the Vickers hardness (HV) value of the coated surface of the material, while “side” refers to the cross section of the coating.

Table A1: Hardness values in experiment A artificially aged for 2 hours.

Order	Top – Sample 1	Top – Sample 2	Side – Sample 1	Side – Sample 2
1	51.6	53.6	52.7	53.9
2	50.9	54.1	50.6	55.6
3	51.6	52.8	51.1	54.3
4	52.3	53.3	52.0	54.4
5	52.3	53.8	52.3	56.1
6			51.0	55.0

Table A2: Hardness values in experiment A artificially aged for 4 hours.

Order	Top – Sample 1	Top – Sample 2	Side – Sample 1	Side – Sample 2
1	54.7	46.4	57.2	48.3
2	53.8	47.2	56.3	48.2
3	53.6	46.7	56.7	47.6
4	53.4	46.1	57.3	47.2
5	54.2	47.4	55.9	47.6
6			55.2	48.3

Table A3: Hardness values in experiment A artificially aged for 8 hours.

Order	Top – Sample 1	Top – Sample 2	Side – Sample 1	Side – Sample 2
1	44.5	48.7	46.3	49.7
2	45.3	48.9	44.0	51.5
3	44.6	49.1	43.5	50.8
4	43.3	48.3	44.1	50.8
5	44.9	49.8	44.6	51.1
6			45.0	51.2

Table A4: Hardness values in experiment A artificially aged for 16 hours.

Order	Top – Sample 1	Top – Sample 2	Side – Sample 1	Side – Sample 2
1	60.5	49.1	63.8	50.9
2	59.9	48.9	62.5	51.0
3	59.5	50.1	61.3	51.5
4	59.8	49.8	61.9	51.5
5	60.0	50.3	62.3	48.4
6			61.4	52.2

Table A5: Hardness values in experiment A artificially aged for 32 hours.

Order	Top – Sample 1	Top – Sample 2	Side – Sample 1	Side – Sample 2
1	49.6	59.7	48.2	58.2
2	48.4	57.1	49.9	58.3
3	49.6	55.1	51.1	58.6
4	48.2	56.5	50.0	58.3
5	48.9	56.6	51.4	57.5
6			53.0	58.6

Table A6: Hardness values in experiment B artificially aged for 2.5 hours.

Order	Top – Sample 1	Top – Sample 2	Side – Sample 1	Side – Sample 2
1	71.8	68.0	64.4	57.6
2	72.5	65.9	62.5	59.3
3	67.4	65.5	56.7	63.2
4	68.7	67.5	62.7	57.2
5	66.7	72.0	67.6	62.8
6			69.0	68.8

Table A7: Hardness values in experiment B artificially aged for 5 hours.

Order	Top – Sample 1	Top – Sample 2	Side – Sample 1	Side – Sample 2
1	77.5	76.5	64.9	66.3
2	76.8	76.5	65.1	68.0
3	78.2	80.8	71.6	69.9
4	76.0	75.8	68.4	72.4
5	77.2	71.8	76.3	67.1
6			75.1	65.7

Table A8: Hardness values in experiment B artificially aged for 10 hours.

Order	Top – Sample 1	Top – Sample 2	Side – Sample 1	Side – Sample 2
1	81.7	81.8	68.8	73.8
2	79.2	84.8	65.8	84.2
3	80.3	80.6	62.1	77.4
4	79.7	82.1	75.2	68.0
5	82.7	80.5	60.6	63.0
6			62.1	69.0

Table A9: Hardness values in experiment B artificially aged for 20 hours.

Order	Top – Sample 1	Top – Sample 2	Side – Sample 1	Side – Sample 2
1	100.0	96.4	98.8	97.0
2	102.2	94.7	101.9	99.5
3	100.1	101.0	102.3	99.8
4	101.4	101.0	97.8	100.4
5	104.5	96.4	105.5	96.9
6			101.6	94.4

Table A10: Hardness values in experiment B artificially aged for 40 hours.

Order	Top – Sample 1	Top – Sample 2	Side – Sample 1	Side – Sample 2
1	77.4	81.4	76.5	77.3
2	87.3	84.4	75.6	79.7
3	82.7	83.1	80.3	78.1
4	84.7	80.9	71.1	73.3
5	77.0	79.4	72.9	75.0
6			71.1	82.5

Table A11: Differences in precipitate sizes for heat treated samples of experiment B.

As-received	**5-hour Aged**	**10-hour Aged**	**20-hour Aged**
0.97	1.63	0.70	1.83
1.42	1.34	0.56	1.83
1.37	1.43	1.15	1.79
1.45	1.58	1.44	1.39
0.80	1.71	1.43	1.76
2.37	1.24	1.11	1.52
2.26	0.92	0.48	1.82

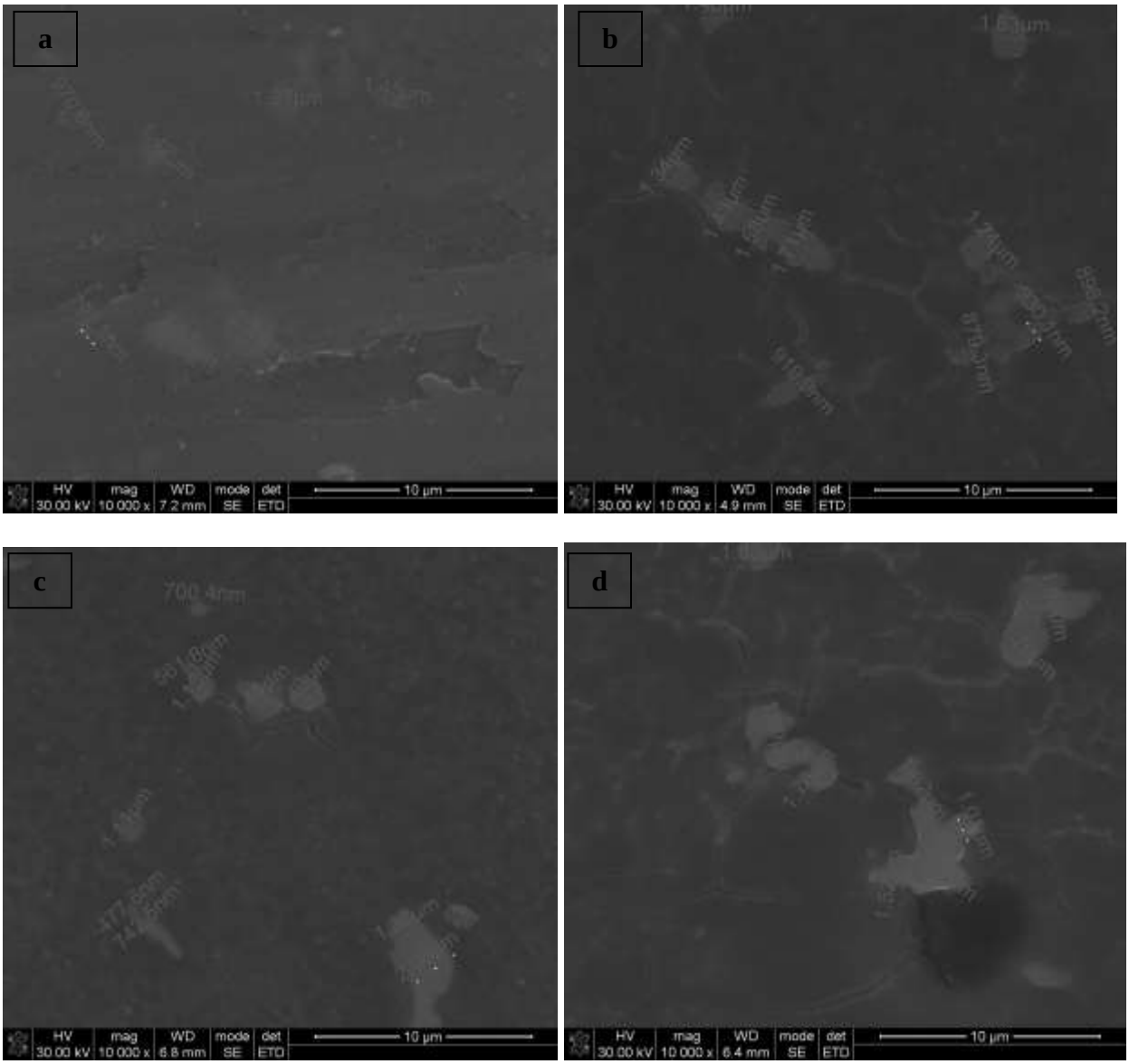

Figure A1: Precipitate size for (a) as-received (b) 5-hour aged (c) 10-hour aged and (d) 20-hour aged sample.

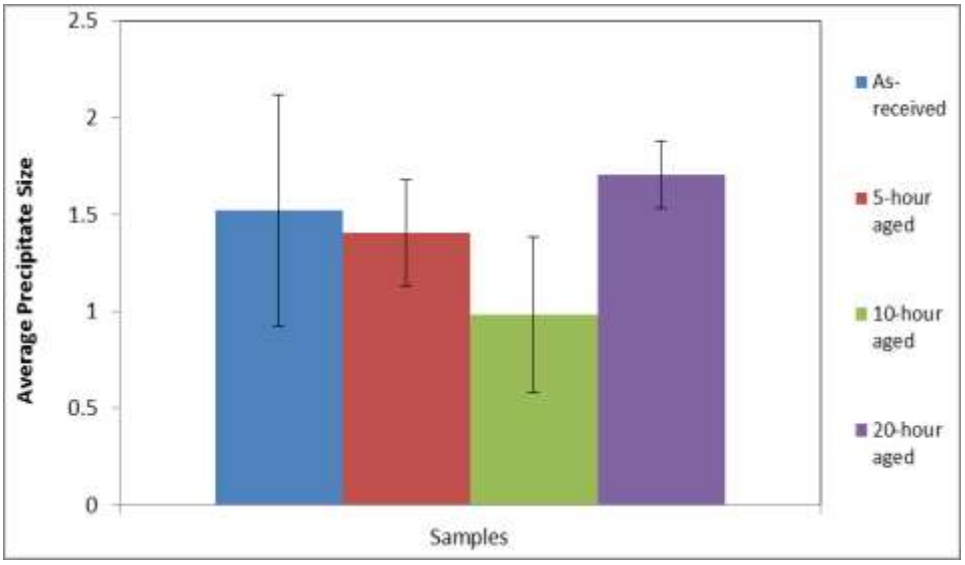

Figure A2: Average precipitate size for samples in Experiment B.

Appendix B: Hardness Values for Uncoated and Coated Samples

Table B1: Hardness values for uncoated (as-received) sample.

Order	Top Surface	Cross-section
1	106.0	105.4
2	105.8	105.9
3	101.1	102.6
4	104.3	104.4
5	109.1	108.7
6	109.8	110.1

Table B2: Hardness values for 20% WC coating.

Order	Top Surface	Cross-section
1	139.2	100.3
2	127.4	123.5
3	108.7	108.0
4	138.1	109.0
5	139.3	109.9
6	128.9	88.1

Table B3: Hardness values for 40% WC coating.

Order	Top Surface	Cross-section
1	193.9	106.4
2	191.6	122.9
3	163.9	105.6
4	175.7	110.2
5	167.6	107.2
6	170.4	99.3

Table B4: Hardness values for 60% WC coating.

Order	Top Surface	Cross-section
1	215.1	107.2
2	232.3	87.7
3	246.1	104.9
4	233.6	72.1
5	227.1	104.5
6	213.7	111.2

Table B5: Hardness values for 80% WC coating.

Order	Top Surface	Cross-section
1	309.8	111.4
2	309.4	110.9
3	275.8	106.4
4	293.5	94.2
5	270.3	105.4
6	255.1	129.1

Table B6: Hardness values for 100% WC coating.

Order	Top Surface	Cross-section
1	306.8	110.6
2	411.0	81.2
3	303.5	108.9
4	383.2	96.3
5	147.3	108.6
6	156.2	97.9

Appendix C: Micro-hardness Profile of Uncoated and Coated Samples

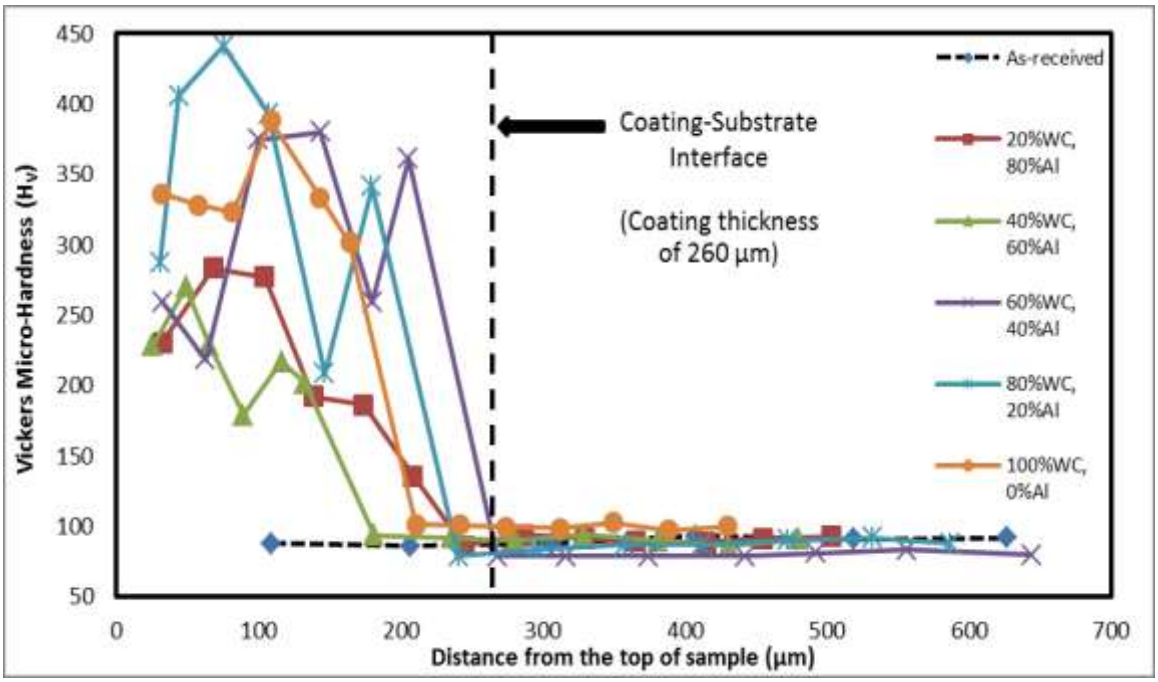

Figure C1: First micro-hardness profile.

			217.4					
	D1	**D2**	**HV**	**HD**	**VD**	**∑ VD**	**DD**	**∑ DD**
20% WC 80% Al (coat)	30.15	30.15	230.5		32.33	32.33	32.33	32.33
	27.56	23.62	283.2	74.12	35.92	68.25	82.37	114.7
	26.93	26.93	277	72.56	35.88	104.1	80.95	195.6
	31.49	30.62	192.3	71.51	34.26	138.4	79.29	274.9
	31.68	31.68	186.1	70.62	35.48	173.9	79.03	354
	36.01	37.98	135.5	65.92	34.95	**208.8**	74.61	**428.6**
Substrate	46.27	46.59	86	50	35.73	244.6	61.45	490
	43.92	44.94	93.9	93.8	41.79	286.3	102.7	592.7
	46.22	43.93	91.3	93.33	43.02	329.4	102.8	695.5
	44.86	46.32	89.2	94.97	35.51	364.9	101.4	796.9
	47.18	44.35	88.5	91.15	50.02	414.9	104	900.9
	43.53	46.65	91.2	86.91	39.55	454.4	95.49	996.3
	45.3	44.11	92.8	103.3	48.2	**502.6**	114	**1110**
			90.41					

			220.7					
40% WC 60% Al (coat)	26.52	30.48	228.3		25.48	25.48	25.48	25.48
	26.4	26.04	269.7	38.96	23.42	48.9	45.46	70.94
	30.85	26.1	228.7	129.7	16.33	65.23	130.7	201.6
	29.5	34.88	179	64.33	24.02	89.25	68.67	270.3
	28.61	28.61	217	100.1	27	116.3	103.7	374
	27.21	33.47	201.5	78.49	16.2	**132.5**	80.14	**454.1**
Substrate	47.34	47.34	93.8	50	48.84	181.3	69.9	524
	48.46	41.47	91.7	102.8	54.63	235.9	116.4	640.4
	42.21	48.46	90.2	103.6	44.69	280.6	112.8	753.3
	47.72	41.14	93.9	114.6	48.07	328.7	124.3	877.5
	42.46	42.26	89.7	122.8	51.94	380.6	133.4	1011
	46.48	46.48	85.7	112.6	50.14	430.8	123.3	1134
	41.95	41.95	90.9	100.8	49.17	**479.9**	112.2	**1246**
			90.84					

			308.8					
60% WC 40% Al (coat)	26.31	26.31	259.3		32.42	32.42	32.42	32.42
	25.78	25.78	218.2	82.16	30.32	62.74	87.58	120
	21.06	23.42	374.9	76.49	37.43	100.2	85.16	205.2
	18.83	25.34	380.2	82.16	43.22	143.4	92.83	298
	25.22	28.3	259	74.71	36.59	180	83.19	381.2
	19.12	26.21	361	91.67	25.3	**205.3**	95.1	**476.3**
Substrate	51.87	51.87	78.8	50	62.53	267.8	80.06	556.3
	51.85	45.22	78.7	105.8	48.12	315.9	116.2	672.6
	45.17	51.83	78.8	147.9	58.51	374.4	159.1	831.6
	44.94	44.94	78.9	110.7	67.63	442.1	129.7	961.4
	45.12	50.54	81.1	113.4	50.14	492.2	124	1085
	49.09	45.22	83.4	81.38	63.81	556	103.4	1189
	44.95	51.52	79.7	114.6	87.73	**643.8**	144.3	**1333**
			79.91					

			346.2					
80% WC 20% Al (coat)	26.67	24.15	287.2		30.57	30.57	30.57	30.57
	24.09	24.09	405.9	82.85	13.48	44.05	83.94	114.5
	20.78	20.22	441.3	76.45	31.56	75.61	82.71	197.2
	20.57	20.57	393.3	79.14	31.44	107.1	85.16	282.4
	26.03	33.66	208.2	81.05	39.56	146.6	90.19	372.6
	20.9	20.9	341.1	151.1	32.89	**179.5**	154.6	**527.2**
Substrate	45.2	51.95	78.6	50	61.14	240.6	78.98	606.2
	50.03	44.18	83.6	90.05	54.86	295.5	105.4	711.6
	43.43	49.08	86.7	87.48	61.78	357.3	107.1	818.7
	47.99	47.99	86.7	92.85	54.62	411.9	107.7	926.4
	47.24	43.66	89.8	82.97	59.83	471.7	102.3	1029
	46.97	42.89	91.9	93.39	60.17	531.9	111.1	1140
	44.15	47.74	87.8	101.8	54.51	**586.4**	115.5	**1255**
			86.44					

			335.2					
100% WC 0% Al (coat)	23.46	23.52	336.1		31.49	31.49	31.49	31.49
	21.01	26.52	328.3	77.79	26.17	57.66	82.07	113.6
	23.19	24.71	323.3	79.53	24.22	81.88	83.14	196.7
	24.12	19.59	388.2	75.34	26.63	108.5	79.91	276.6
	24.28	22.87	333.7	99.16	34.59	143.1	105	381.6
	20.8	20.8	301.3	125	21.14	**164.2**	126.8	**508.4**
Substrate	40.83	44.83	101.1	50	46.31	210.6	68.15	576.6
	44.06	41.7	100.9	84.72	31.16	241.7	90.27	666.8
	44.76	41.58	99.5	85.29	32.53	274.2	91.28	758.1
	42.14	44.64	98.5	89.05	37.61	311.9	96.67	854.8
	43.25	41.76	102.6	86.66	37.9	349.8	94.59	949.4
	41.82	45.5	97.3	88.32	38.37	388.1	96.29	1046
	44.17	41.95	100	83.86	41.87	**430**	93.73	**1139**
			99.99					

			91.48				VD	
As-received	44.41	47.46	87.9				108.9	108.9
	44.94	44.94	86.1				98.19	207.1
	44.44	47.65	87.5				99.14	306.2
	45.59	43.68	93.1				100.8	407.1
	43.46	46.84	91				111.6	518.6
	43.07	43.07	91.6				107.7	626.3
	43.09	46.06	93.3				103	729.2
	44.64	43.86	94.7				87.98	817.2
	44.07	46.67	90.1				97.31	914.5
	45.63	44.39	91.5				96.47	1011
	44.9	45.74	90.3				95.02	1106
	45.18	42.38	96.8				115.9	1222
	43.18	45.02	95.4				111.8	1334

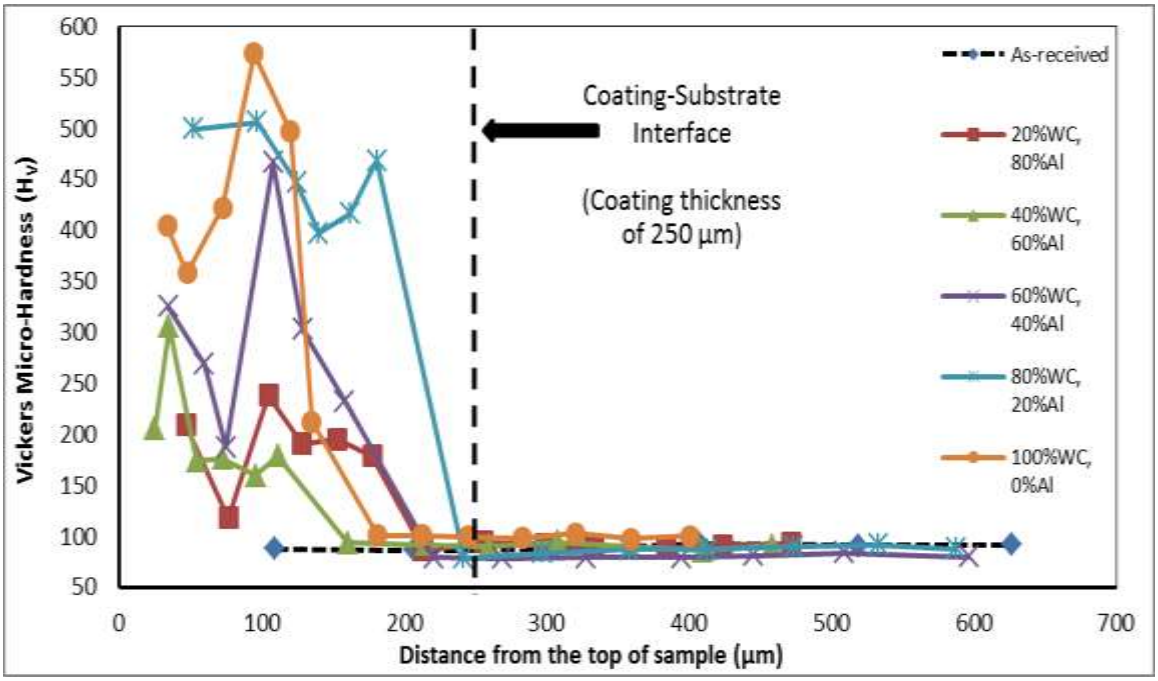

Figure C2: Second reading for micro-hardness profile.

			188.5					
	D1	**D2**	**HV**	**HD**	**VD**	**∑ VD**	**DD**	**∑ DD**
20% WC 80% Al (coat)	28.06	31.52	209		46.67	46.67	46.67	46.67
	38.87	40.37	118.1	95.92	29.94	76.61	100.5	147.2
	26.42	29.36	238.4	85.87	27.96	104.6	90.31	237.5
	32.39	30.04	190.9	71.51	23.59	128.2	75.3	312.8
	32.75	32.75	195.5	70.78	24.66	152.8	74.95	387.7
	33.3	31.09	178.9	62.71	24.96	**177.8**	67.49	**455.2**
Substrate	46.27	46.59	86	50	35.73	213.5	61.45	516.7
	43.92	44.94	93.9	93.8	41.79	255.3	102.7	619.4
	46.22	43.93	91.3	93.33	43.02	298.3	102.8	722.1
	44.86	46.32	89.2	94.97	35.51	333.8	101.4	823.5
	47.18	44.35	88.5	91.15	50.02	383.9	104	927.5
	43.53	46.65	91.2	86.91	39.55	423.4	95.49	1023
	45.3	44.11	92.8	103.3	48.2	**471.6**	114	**1137**
			90.41					

			199.9					
40% WC 60% Al (coat)	27.69	32.39	205.5		24.85	24.85	24.85	24.85
	23.41	23.41	305.3	40.68	10.09	34.94	41.91	66.76
	32.83	32.83	174.3	72.44	19.3	54.24	74.97	141.7
	32.77	32.12	176.2	80.06	18.09	72.33	82.08	223.8
	30.62	37.55	159.6	73.34	23.44	95.77	76.99	300.8
	32.63	32.63	178.5	85.04	15.53	**111.3**	86.45	**387.2**
Substrate	47.34	47.34	93.8	50	48.84	160.1	69.9	457.1
	48.46	41.47	91.7	102.8	54.63	214.8	116.4	573.5
	42.21	48.46	90.2	103.6	44.69	259.5	112.8	686.4
	47.72	41.14	93.9	114.6	48.07	307.5	124.3	810.7
	42.46	42.26	89.7	122.8	51.94	359.5	133.4	944
	46.48	46.48	85.7	112.6	50.14	409.6	123.3	1067
	41.95	41.95	90.9	100.8	49.17	**458.8**	112.2	**1179**
			90.84					

			297.4					
60% WC 40% Al (coat)	23.22	24.51	325.6		34.22	34.22	34.22	34.22
	24.41	28.12	268.8	68.78	25.55	59.77	73.37	107.6
	31.32	31.58	187.5	62.17	15.1	74.87	63.98	171.6
	20.38	19.49	466.6	78.17	33.06	107.9	84.87	256.4
	24.49	24.49	303.1	79.57	20.97	128.9	82.29	338.7
	27.09	29.39	232.5	68.92	29.31	**158.2**	74.89	**413.6**
Substrate	51.87	51.87	78.8	50	62.53	220.7	80.06	493.7
	51.85	45.22	78.7	105.8	48.12	268.9	116.2	609.9
	45.17	51.83	78.8	147.9	58.51	327.4	159.1	769
	44.94	44.94	78.9	110.7	67.63	395	129.7	898.7
	45.12	50.54	81.1	113.4	50.14	445.1	124	1023
	49.09	45.22	83.4	81.38	63.81	509	103.4	1126
	44.95	51.52	79.7	114.6	87.73	**596.7**	144.3	**1270**
			79.91					

			455.8					
80% WC 20% Al (coat)	17.97	20.57	499.4		52.1	52.1	52.1	52.1
	19.1	19.19	505.9	78.31	44.95	97.05	90.29	142.4
	20.19	20.54	447.1	54.14	27.71	124.8	60.82	203.2
	21.41	21.41	397.3	51.79	15.08	139.8	53.94	257.2
	21.15	21.05	416.5	44.62	22.21	162.1	49.84	307
	20.38	19.41	468.5	43.69	18.7	**180.8**	47.52	**354.5**
Substrate	45.2	51.95	78.6	50	61.14	241.9	78.98	433.5
	50.03	44.18	83.6	90.05	54.86	296.8	105.4	538.9
	43.43	49.08	86.7	87.48	61.78	358.5	107.1	646
	47.99	47.99	86.7	92.85	54.62	413.2	107.7	753.8
	47.24	43.66	89.8	82.97	59.83	473	102.3	856.1
	46.97	42.89	91.9	93.39	60.17	533.2	111.1	967.2
	44.15	47.74	87.8	101.8	54.51	**587.7**	115.5	**1083**
			86.44					

			411.4					
100% WC 0% Al (coat)	21.68	21.15	404.4		33.37	33.37	33.37	33.37
	21.36	24.12	358.6	78.19	14.29	47.66	79.49	112.9
	21.81	20.11	422.1	70.89	24.89	72.55	75.13	188
	15.85	20.11	573.6	66.12	21.64	94.19	69.57	257.6
	21.37	21.37	497.3	60.77	25.84	120	66.04	323.6
	29.03	30.04	212.6	73.91	14.98	**135**	75.41	**399**
Substrate	40.83	44.83	101.1	50	46.31	181.3	68.15	467.2
	44.06	41.7	100.9	84.72	31.16	212.5	90.27	557.4
	44.76	41.58	99.5	85.29	32.53	245	91.28	648.7
	42.14	44.64	98.5	89.05	37.61	282.6	96.67	745.4
	43.25	41.76	102.6	86.66	37.9	320.5	94.59	840
	41.82	45.5	97.3	88.32	38.37	358.9	96.29	936.3
	44.17	41.95	100	83.86	41.87	**400.8**	93.73	**1030**
			99.99					

			91.48				VD	
As-received	44.41	47.46	87.9				108.9	108.9
	44.94	44.94	86.1				98.19	207.1
	44.44	47.65	87.5				99.14	306.2
	45.59	43.68	93.1				100.8	407.1
	43.46	46.84	91				111.6	518.6
	43.07	43.07	91.6				107.7	626.3
	43.09	46.06	93.3				103	729.2
	44.64	43.86	94.7				87.98	817.2
	44.07	46.67	90.1				97.31	914.5
	45.63	44.39	91.5				96.47	1011
	44.9	45.74	90.3				95.02	1106
	45.18	42.38	96.8				115.9	1222
	43.18	45.02	95.4				111.8	1334

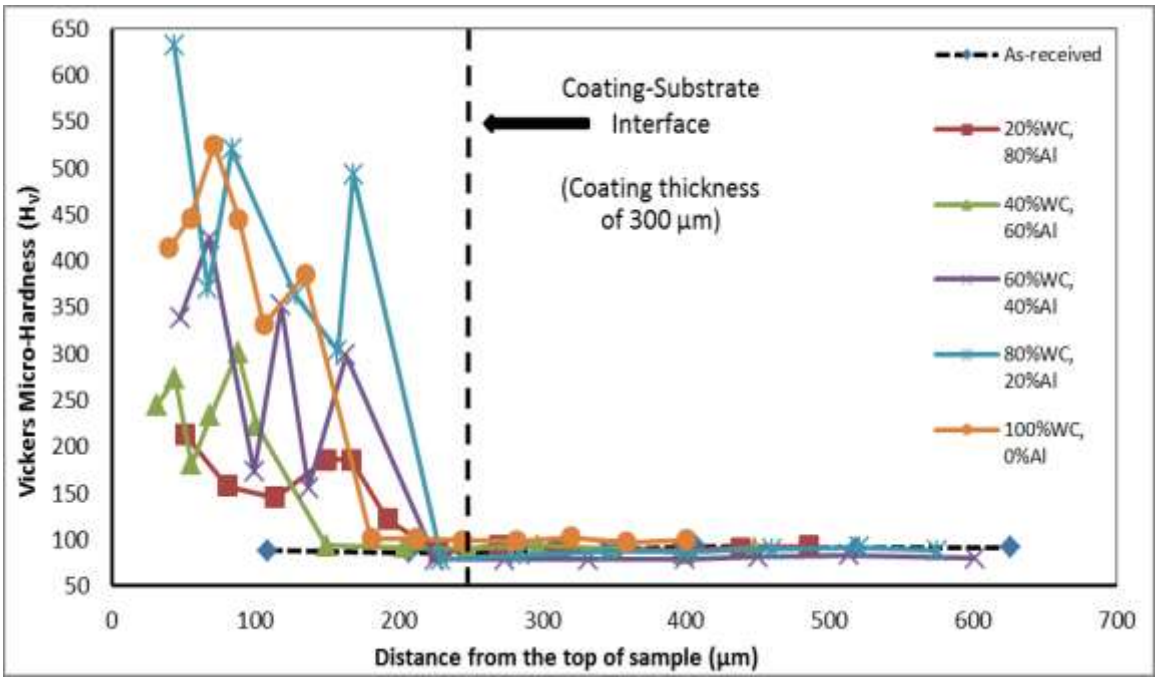

Figure C3: Third reading for micro-hardness profile.

			168.4					
	D1	**D2**	**HV**	**HD**	**VD**	**∑ VD**	**DD**	**∑ DD**
20% WC 80% Al (coat)	29.88	29.06	213.5		50.98	50.98	50.98	50.98
	36.78	31.84	157.5	83.58	29.57	80.55	88.66	139.6
	37.73	37.73	145.3	78.15	33.21	113.8	84.91	224.6
	30.89	32.31	185.7	70.47	35.81	149.6	79.05	303.6
	33.62	33.58	186.1	56.13	17.05	166.6	58.66	362.3
	39.22	38.72	122.1	75.48	25.6	**192.2**	79.7	**442**
Substrate	46.27	46.59	86	50	35.73	228	61.45	503.4
	43.92	44.94	93.9	93.8	41.79	269.7	102.7	606.1
	46.22	43.93	91.3	93.33	43.02	312.8	102.8	708.9
	44.86	46.32	89.2	94.97	35.51	348.3	101.4	810.3
	47.18	44.35	88.5	91.15	50.02	398.3	104	914.2
	43.53	46.65	91.2	86.91	39.55	437.8	95.49	1010
	45.3	44.11	92.8	103.3	48.2	**486**	114	**1124**
			90.41					

			243					
40% WC 60% Al (coat)	29.23	29.23	244.5		31.13	31.13	31.13	31.13
	26.72	25.33	273.8	69.56	12.63	43.76	70.7	101.8
	29.24	34.76	181.1	77.71	11.77	55.53	78.6	180.4
	23.15	33.19	233.7	77.75	13.23	68.76	78.87	259.3
	25.44	25.44	301.9	75.08	19.31	88.07	77.52	336.8
	30.27	30.27	223	76.04	12.43	**100.5**	77.05	**413.9**
Substrate	47.34	47.34	93.8	50	48.84	149.3	69.9	483.8
	48.46	41.47	91.7	102.8	54.63	204	116.4	600.2
	42.21	48.46	90.2	103.6	44.69	248.7	112.8	713
	47.72	41.14	93.9	114.6	48.07	296.7	124.3	837.3
	42.46	42.26	89.7	122.8	51.94	348.7	133.4	970.6
	46.48	46.48	85.7	112.6	50.14	398.8	123.3	1094
	41.95	41.95	90.9	100.8	49.17	**448**	112.2	**1206**
			90.84					

			290.3					
60% WC 40% Al (coat)	19.97	26.85	338.4		47.85	47.85	47.85	47.85
	21.73	20.08	424.3	68.78	20.35	68.2	71.73	119.6
	33.27	32.22	172.9	55.06	31.15	99.35	63.26	182.8
	20.78	25.12	352.1	80.53	18.59	117.9	82.65	265.5
	34.91	34.06	155.9	66.96	19.42	137.4	69.72	335.2
	24.88	25.01	298	79.87	25.69	**163.1**	83.9	**419.1**
Substrate	51.87	51.87	78.8	50	62.53	225.6	80.06	499.2
	51.85	45.22	78.7	105.8	48.12	273.7	116.2	615.4
	45.17	51.83	78.8	147.9	58.51	332.2	159.1	774.5
	44.94	44.94	78.9	110.7	67.63	399.8	129.7	904.2
	45.12	50.54	81.1	113.4	50.14	450	124	1028
	49.09	45.22	83.4	81.38	63.81	513.8	103.4	1132
	44.95	51.52	79.7	114.6	87.73	**601.5**	144.3	**1276**
			79.91					

			446.9					
80% WC 20% Al (coat)	17.26	16.98	632.7		43.42	43.42	43.42	43.42
	24.38	24.38	369.7	61.75	23.67	67.09	66.13	109.6
	16.79	16.79	520	52.92	16.74	83.83	55.5	165.1
	20.73	24.46	363.2	49.16	44.49	128.3	66.3	231.4
	24.98	24.51	302.9	44.04	29.05	157.4	52.76	284.1
	20.15	18.64	493	71.3	11.02	**168.4**	72.15	**356.3**
Substrate	45.2	51.95	78.6	50	61.14	229.5	78.98	435.2
	50.03	44.18	83.6	90.05	54.86	284.4	105.4	540.7
	43.43	49.08	86.7	87.48	61.78	346.2	107.1	647.8
	47.99	47.99	86.7	92.85	54.62	400.8	107.7	755.5
	47.24	43.66	89.8	82.97	59.83	460.6	102.3	857.8
	46.97	42.89	91.9	93.39	60.17	520.8	111.1	968.9
	44.15	47.74	87.8	101.8	54.51	**575.3**	115.5	**1084**
			86.44					

			424.6					
100% WC 0% Al (coat)	21.13	21.13	414.4		39.66	39.66	39.66	39.66
	20.25	20.25	446.5	67.85	15.36	55.02	69.57	109.2
	18.05	19.54	525	56.62	15.96	70.98	58.83	168.1
	19.35	21.48	444.9	62.23	17.2	88.18	64.56	232.6
	24.44	22.87	331.4	71.75	17.88	106.1	73.94	306.6
	21.47	22.42	385.1	83.3	28.49	**134.6**	88.04	**394.6**
Substrate	40.83	44.83	101.1	50	46.31	180.9	68.15	462.7
	44.06	41.7	100.9	84.72	31.16	212	90.27	553
	44.76	41.58	99.5	85.29	32.53	244.6	91.28	644.3
	42.14	44.64	98.5	89.05	37.61	282.2	96.67	741
	43.25	41.76	102.6	86.66	37.9	320.1	94.59	835.6
	41.82	45.5	97.3	88.32	38.37	358.4	96.29	931.8
	44.17	41.95	100	83.86	41.87	**400.3**	93.73	**1026**
			99.99					

			91.48				VD	
As-received	44.41	47.46	87.9				108.9	108.9
	44.94	44.94	86.1				98.19	207.1
	44.44	47.65	87.5				99.14	306.2
	45.59	43.68	93.1				100.8	407.1
	43.46	46.84	91				111.6	518.6
	43.07	43.07	91.6				107.7	626.3
	43.09	46.06	93.3				103	729.2
	44.64	43.86	94.7				87.98	817.2
	44.07	46.67	90.1				97.31	914.5
	45.63	44.39	91.5				96.47	1011
	44.9	45.74	90.3				95.02	1106
	45.18	42.38	96.8				115.9	1222
	43.18	45.02	95.4				111.8	1334

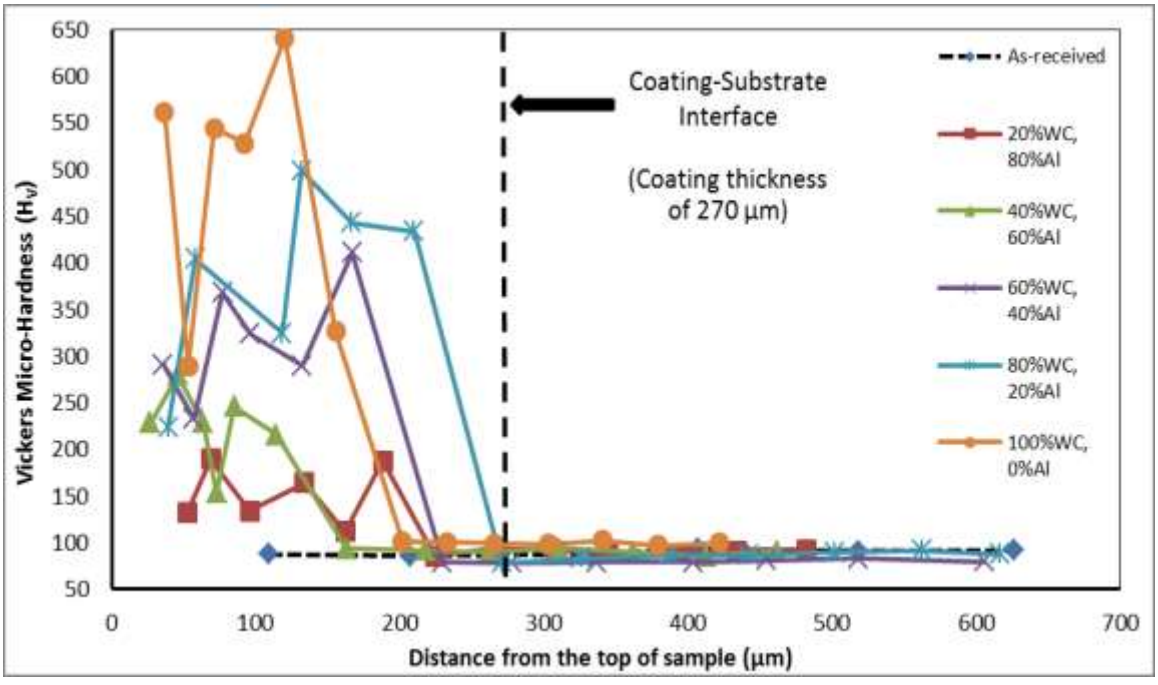

Figure C4: Fourth reading for micro-hardness profile.

			153.2					
	D1	**D2**	**HV**	**HD**	**VD**	**∑ VD**	**DD**	**∑ DD**
20% WC 80% Al (coat)	37.44	37.44	131.9		52.38	52.38	52.38	52.38
	31.06	31.51	189.5	80.72	16.59	68.97	82.41	134.8
	35.56	38.87	133.9	69.01	26.99	95.96	74.1	208.9
	31.93	35.29	164.2	89.06	38.18	134.1	96.9	305.8
	38.16	43.33	111.7	73.71	28.06	162.2	78.87	384.7
	30.63	32.24	187.7	80.14	26.33	**188.5**	84.35	**469**
Substrate	46.27	46.59	86	50	35.73	224.3	61.45	530.5
	43.92	44.94	93.9	93.8	41.79	266.1	102.7	633.2
	46.22	43.93	91.3	93.33	43.02	309.1	102.8	735.9
	44.86	46.32	89.2	94.97	35.51	344.6	101.4	837.3
	47.18	44.35	88.5	91.15	50.02	394.6	104	941.3
	43.53	46.65	91.2	86.91	39.55	434.2	95.49	1037
	45.3	44.11	92.8	103.3	48.2	**482.4**	114	**1151**
			90.41					

			225.5					
40% WC 60% Al (coat)	31.11	25.81	228.9		26.62	26.62	26.62	26.62
	26.02	25.46	279.9	68.27	19.2	45.82	70.92	97.54
	31.33	25.62	228.7	76.35	17.89	63.71	78.42	176
	39.03	39.03	153.4	87.69	9.4	73.11	88.19	264.1
	29.4	25.52	245.9	91.44	12.23	85.34	92.25	356.4
	30.93	27.64	216.2	84.06	28.88	**114.2**	88.88	**445.3**
Substrate	47.34	47.34	93.8	50	48.84	163.1	69.9	515.2
	48.46	41.47	91.7	102.8	54.63	217.7	116.4	631.6
	42.21	48.46	90.2	103.6	44.69	262.4	112.8	744.4
	47.72	41.14	93.9	114.6	48.07	310.5	124.3	868.7
	42.46	42.26	89.7	122.8	51.94	362.4	133.4	1002
	46.48	46.48	85.7	112.6	50.14	412.5	123.3	1125
	41.95	41.95	90.9	100.8	49.17	**461.7**	112.2	**1237**
			90.84					

			319.5					
60% WC 40% Al (coat)	25.64	24.86	290.9		35.71	35.71	35.71	35.71
	25.67	25.67	232.9	55.74	21.49	57.2	59.74	95.45
	22.94	21.92	368.6	66.85	19.9	77.1	69.75	165.2
	23.8	23.8	323.7	59.16	19.36	96.46	62.25	227.4
	27.67	27.67	289.8	49.12	35.69	132.2	60.72	288.2
	20.27	22.21	411	44.97	35.02	**167.2**	57	**345.2**
Substrate	51.87	51.87	78.8	50	62.53	229.7	80.06	425.2
	51.85	45.22	78.7	105.8	48.12	277.8	116.2	541.5
	45.17	51.83	78.8	147.9	58.51	336.3	159.1	700.5
	44.94	44.94	78.9	110.7	67.63	404	129.7	830.2
	45.12	50.54	81.1	113.4	50.14	454.1	124	954.3
	49.09	45.22	83.4	81.38	63.81	517.9	103.4	1058
	44.95	51.52	79.7	114.6	87.73	**605.6**	144.3	**1202**
			79.91					

			388.2					
80% WC 20% Al (coat)	27.85	29.72	223.8		39.63	39.63	39.63	39.63
	23.1	19.74	404.2	67.32	18.6	58.23	69.84	109.5
	23.67	24.13	324.6	63.68	60.05	118.3	87.53	197
	21.04	21.04	498.9	61.02	13.8	132.1	62.56	259.6
	20.77	20.13	443.4	46	34.75	166.8	57.65	317.2
	20.98	20.36	434	72.83	43.06	**209.9**	84.61	**401.8**
Substrate	45.2	51.95	78.6	50	61.14	271	78.98	480.8
	50.03	44.18	83.6	90.05	54.86	325.9	105.4	586.2
	43.43	49.08	86.7	87.48	61.78	387.7	107.1	693.3
	47.99	47.99	86.7	92.85	54.62	442.3	107.7	801.1
	47.24	43.66	89.8	82.97	59.83	502.1	102.3	903.4
	46.97	42.89	91.9	93.39	60.17	562.3	111.1	1014
	44.15	47.74	87.8	101.8	54.51	**616.8**	115.5	**1130**
			86.44					

			482.1					
100% WC 0% Al (coat)	19.19	19.19	562		36.61	36.61	36.61	36.61
	29.72	20.9	289.5	65.04	16.59	53.2	67.12	103.7
	18.21	18.21	544.5	58.64	18.33	71.53	61.44	165.2
	18.55	18.55	528.3	80.52	20.63	92.16	83.12	248.3
	17.05	16.96	641.3	60.34	27.86	120	66.46	314.8
	23.51	23.51	327	67.78	35.6	**155.6**	76.56	**391.3**
Substrate	40.83	44.83	101.1	50	46.31	201.9	68.15	459.5
	44.06	41.7	100.9	84.72	31.16	233.1	90.27	549.7
	44.76	41.58	99.5	85.29	32.53	265.6	91.28	641
	42.14	44.64	98.5	89.05	37.61	303.2	96.67	737.7
	43.25	41.76	102.6	86.66	37.9	341.1	94.59	832.3
	41.82	45.5	97.3	88.32	38.37	379.5	96.29	928.6
	44.17	41.95	100	83.86	41.87	**421.4**	93.73	**1022**
			99.99					

			91.48				VD	
As-received	44.41	47.46	87.9				108.9	108.9
	44.94	44.94	86.1				98.19	207.1
	44.44	47.65	87.5				99.14	306.2
	45.59	43.68	93.1				100.8	407.1
	43.46	46.84	91				111.6	518.6
	43.07	43.07	91.6				107.7	626.3
	43.09	46.06	93.3				103	729.2
	44.64	43.86	94.7				87.98	817.2
	44.07	46.67	90.1				97.31	914.5
	45.63	44.39	91.5				96.47	1011
	44.9	45.74	90.3				95.02	1106
	45.18	42.38	96.8				115.9	1222
	43.18	45.02	95.4				111.8	1334

Appendix D: SEM – EDS Results for Heat Treatment

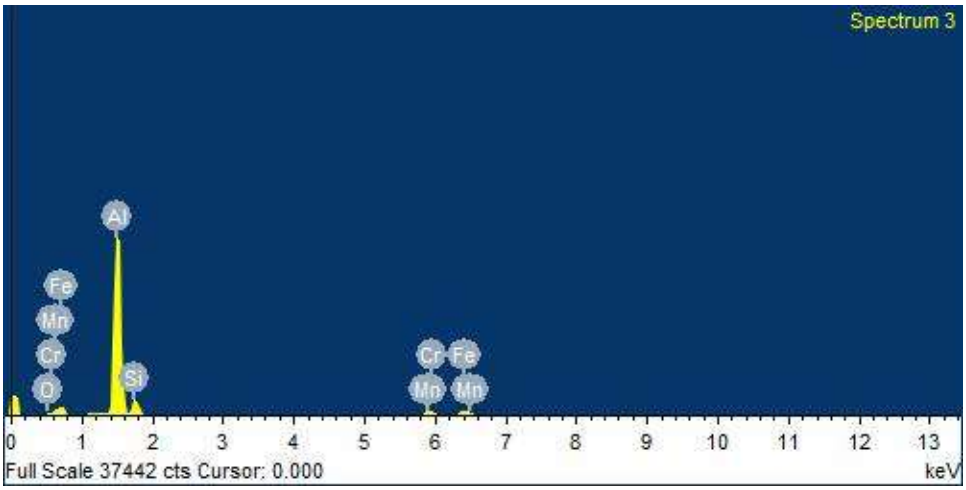

Figure D1: EDS spectrum for precipitates of the as-received AA6082 (Fig. 4.3).

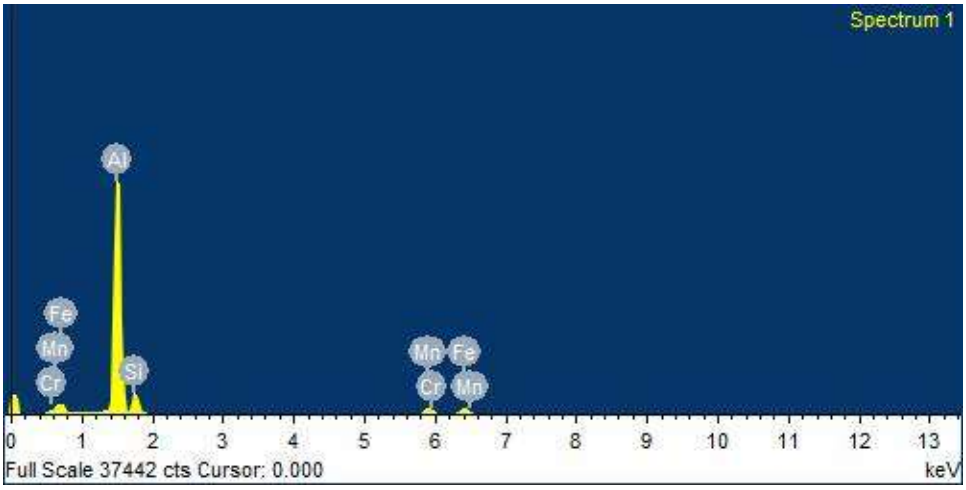

Figure D2: EDS spectrum for precipitates of the sample aged for 10 hours (Fig. 4.4).

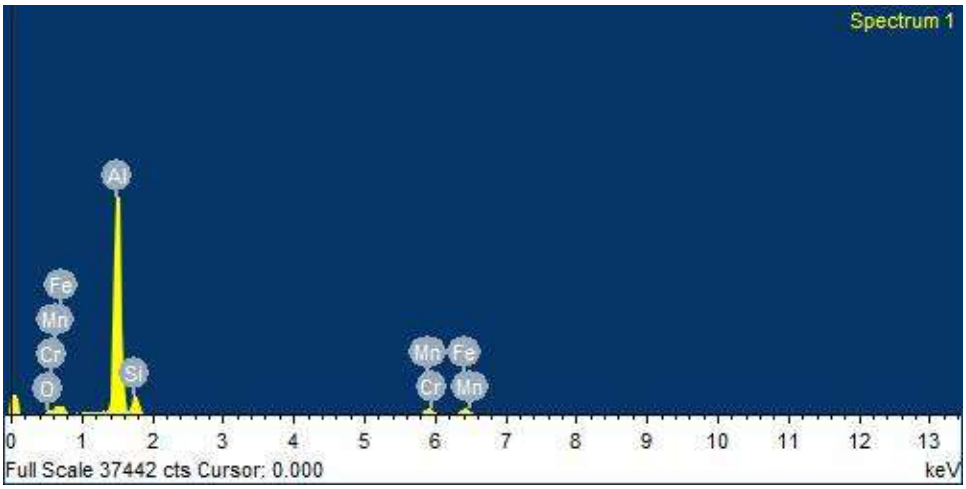

Figure D3: EDS spectrum for precipitates of the sample aged for 20 hours (Fig. 4.5).

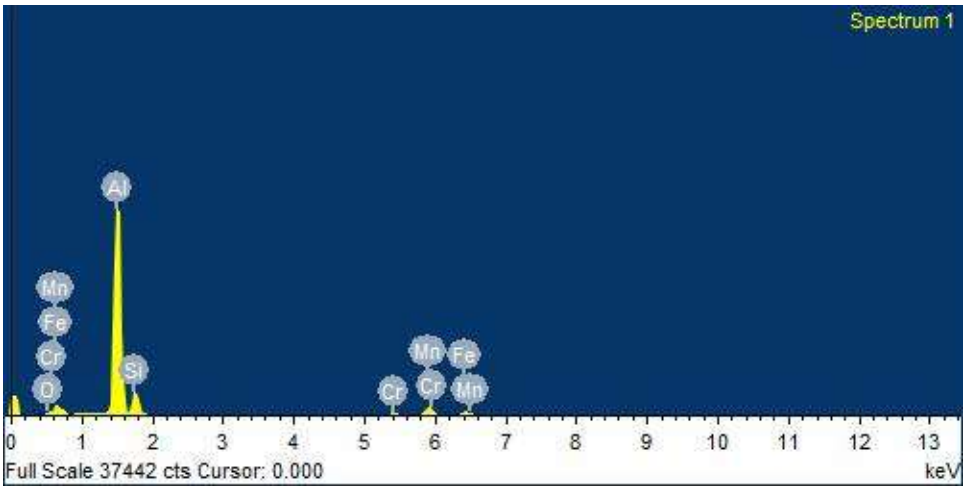

Figure D4: EDS spectrum for precipitates of the sample aged for 40 hours (Fig. 4.6).

Appendix E1: SEM and EDS Analyses for Wear Results

Weight percentage is represented by wt %. The analyses derived from both the scanning electron microscopy (SEM) and energy dispersive spectrometry (EDS) spectra are given as raw data.

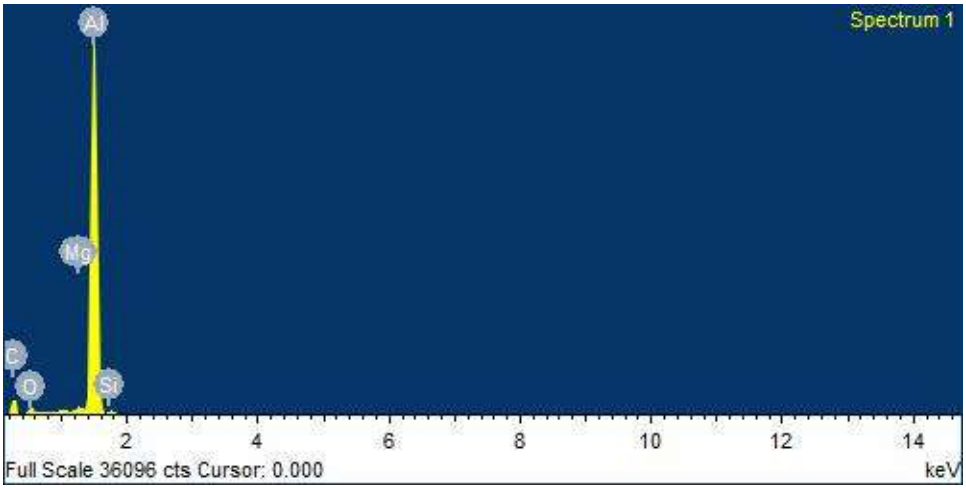

Figure E1: EDS spectrum 1 for wear track of uncoated sample (Fig. 4.34C).

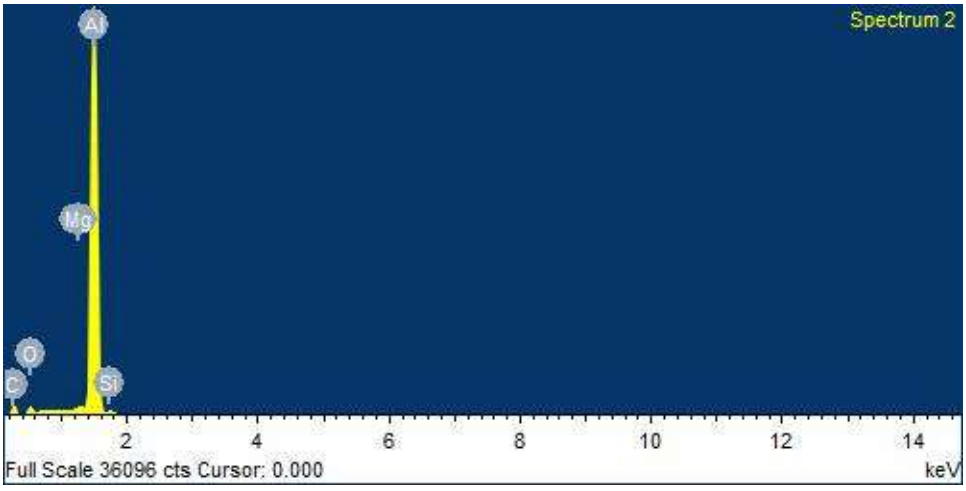

Figure E2: EDS spectrum 2 for wear track of uncoated sample (Fig. 4.34D).

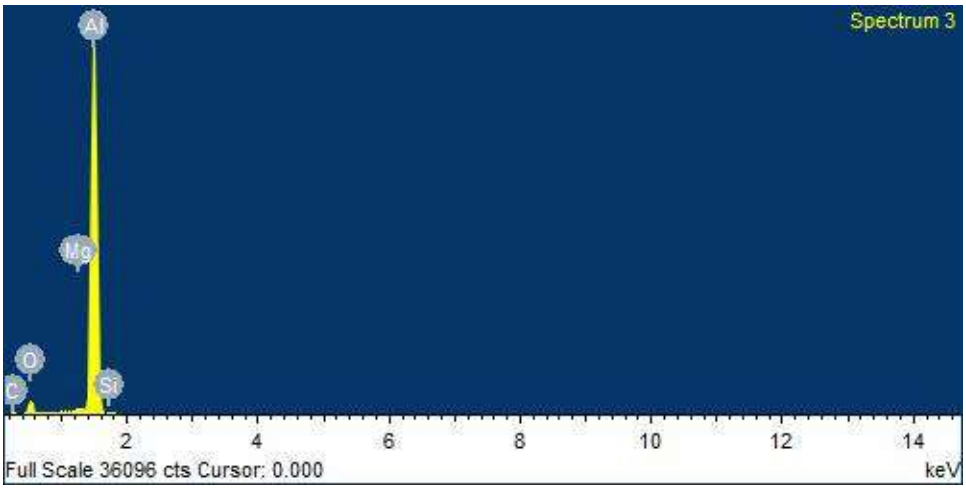

Figure E3: EDS spectrum 3 outside the wear track of uncoated sample (Fig. 4.34E).

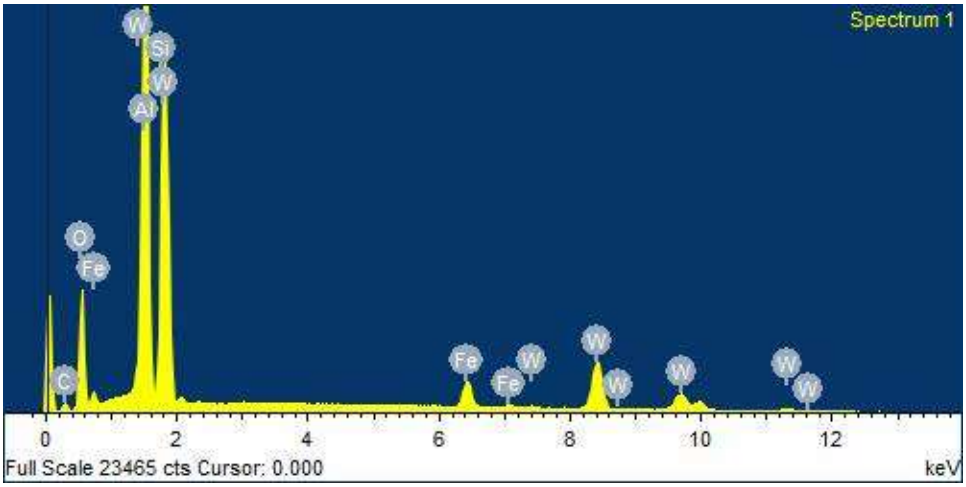

Figure E4: EDS spectrum for wear track of 20%WC coating (Fig. 4.36C).

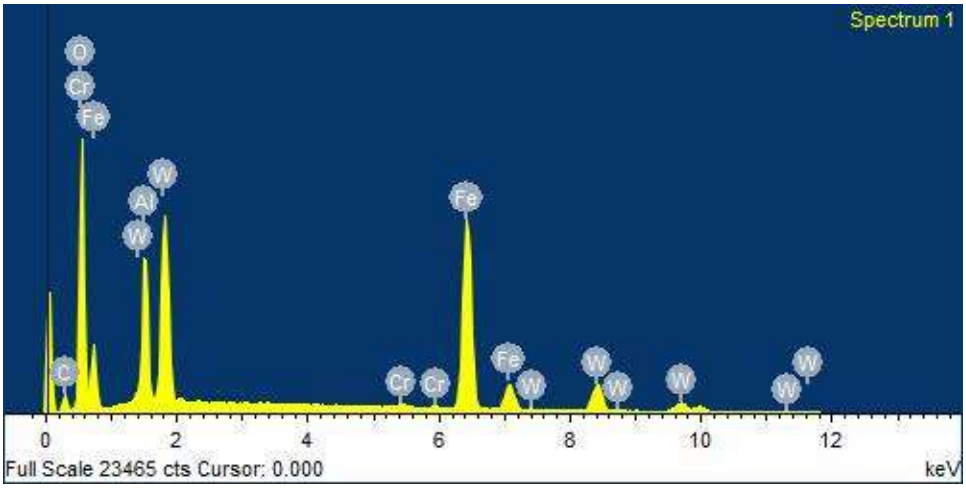

Figure E5: EDS showing presence of Cr and other elements on wear track of 40%WC coating (Fig. 4.37C).

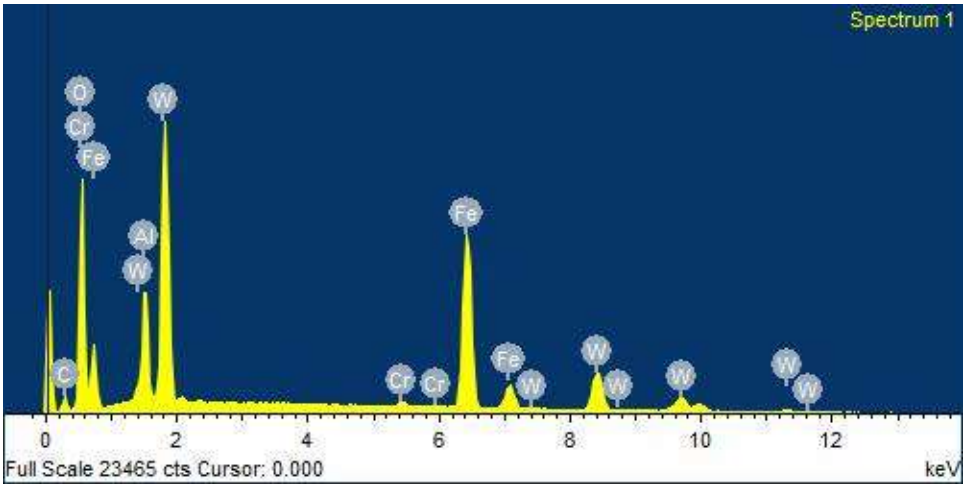

Figure E6: EDS spectrum still showing Cr on wear track of 60%WC coating (Fig. 4.38C).

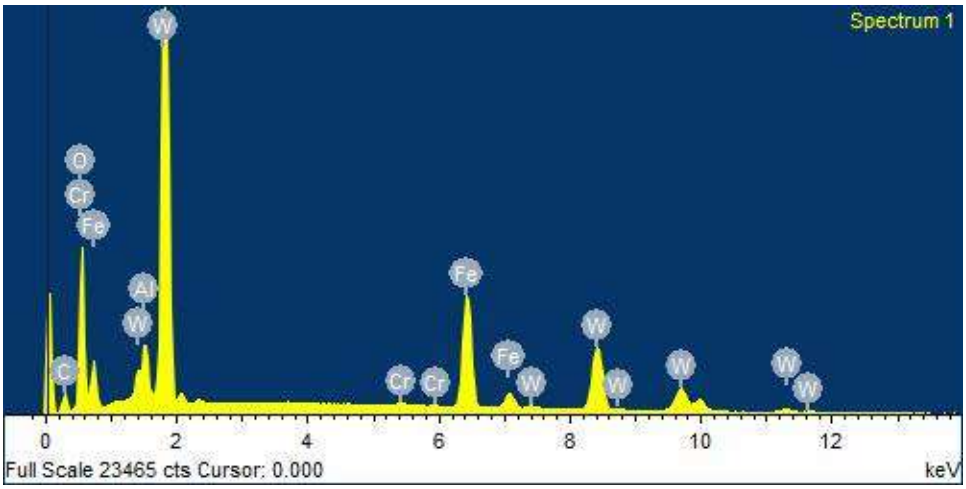

Figure E7: EDS spectrum still showing Cr on wear track of 80%WC coating (Fig. 4.39C).

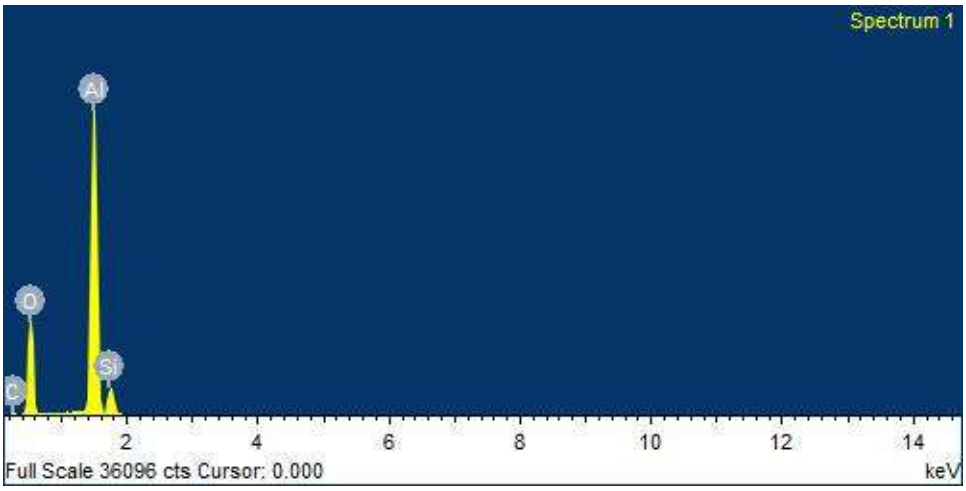

Figure E8: EDS spectrum showing neither W nor Cr on wear track of 100%WC coating (Fig. 4.40C).

Appendix E2: SEM and EDS Analyses for Corrosion Results

Weight percentage is represented by wt %. The analyses derived from the scanning electron microscopy (SEM) and energy dispersive spectrometry (EDS) spectra are given as raw data.

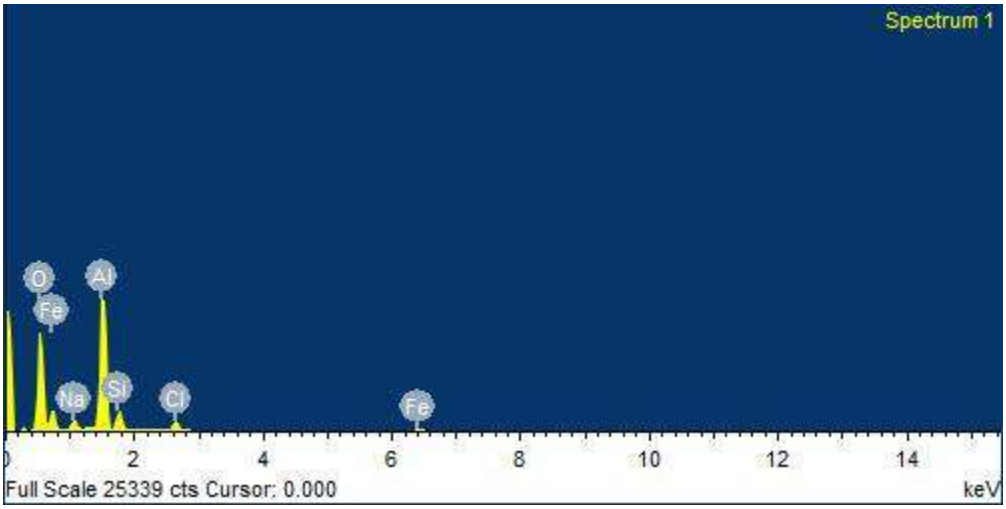

Figure E9: EDS spectrum showing corrosion products which result in mass gain in neutral solution (fig. 4.43C).

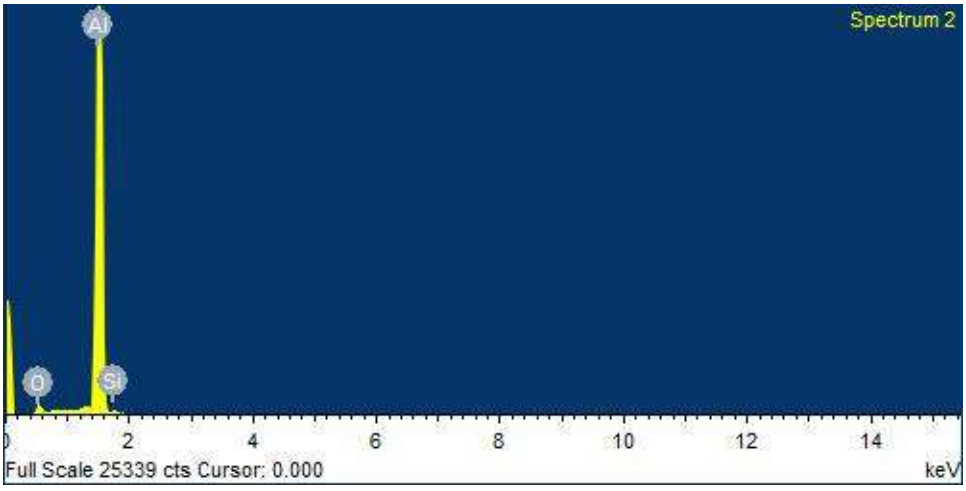

Figure E10: EDS spectrum showing bare substrate in neutral solution (fig. 4.43D).

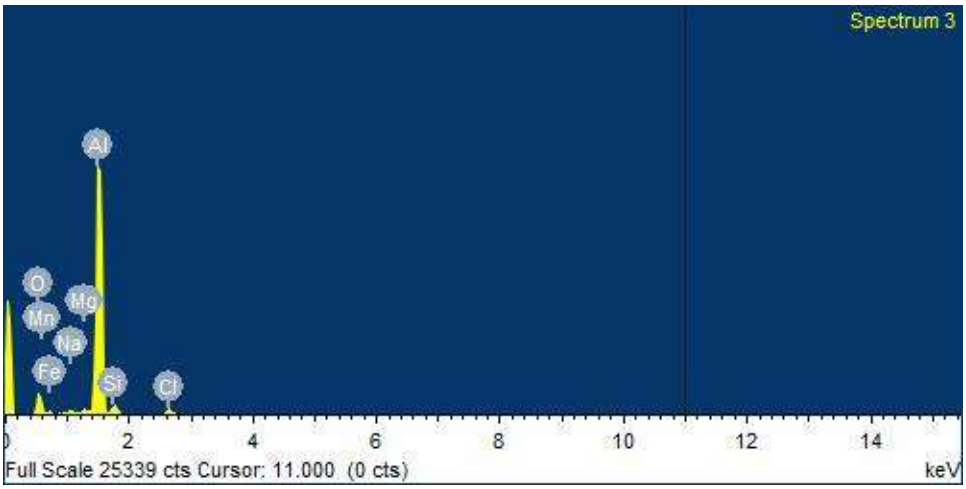

Figure E11: EDS spectrum showing corrosion products which result in mass gain in neutral solution (fig. 4.43E).

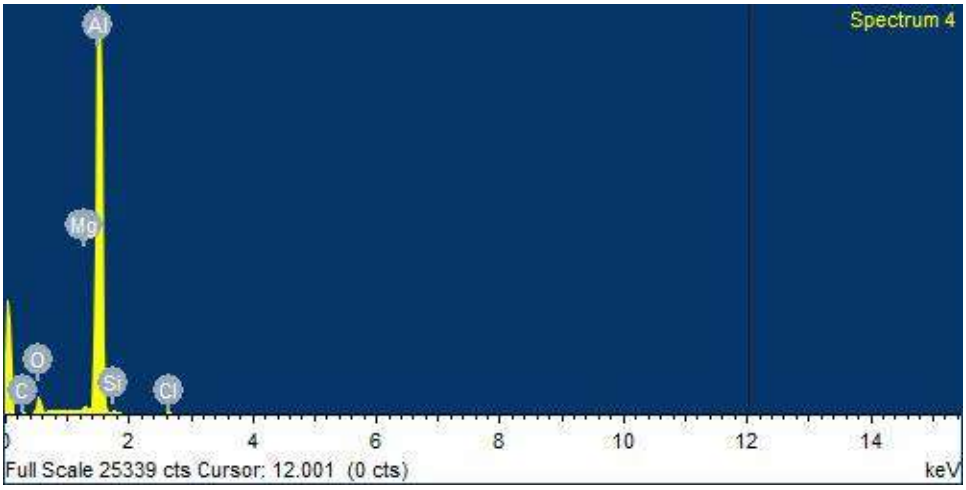

Figure E12: EDS areal spectrum showing bare substrate in neutral solution (fig. 4.43F).

Table E1: Data showing dimensions for first set of uncoated samples used for exposure test.

Acidic Solution			Alkaline Solution			Neutral Solution		
L (mm)	W (mm)	T (mm)	L (mm)	W (mm)	T (mm)	L (mm)	W (mm)	T (mm)
17.8	17.8	12	17.5	18.4	12	18.4	17.7	12
18.1	18.3	12	17.8	18.4	12	17.5	17.8	12
17.8	17.9	12	17.5	17.8	12	18.2	17.5	12
17.9	17.1	12	18.4	17.8	12	18.4	17.5	12

Table E2: Data showing dimensions for second set of uncoated samples used for exposure test.

Acidic Solution			Alkaline Solution			Neutral Solution		
L (mm)	W (mm)	T (mm)	L (mm)	W (mm)	T (mm)	L (mm)	W (mm)	T (mm)
18.2	18.2	11.9	18.2	18.3	11.9	18	17.6	11.9
18	17.9	11.9	17.5	17.3	11.6	18	17.6	11.8
18	17.8	12	17.5	17.4	11.9	17.4	17.8	12
18.2	17.8	12	17.3	17.7	11.9	17	18.8	11.9

L = length of sample (in mm)

W = width of sample (in mm)

T = thickness of sample (in mm)

T_E = time of exposure (days)

M_I = initial mass of sample (g)

M_F = final mass of sample (g)

ML = mass loss of sample after exposure (g)

A = area of sample (cm^2)

Table E3: Corrosion rates for first set of uncoated sample immersed in acidic solution.

T_E (days)	A (cm^2)	M_I (g)	M_F (g)	ML (g)	CR (mm/y)
1	16.3	10.2484	10.2423	0.0061	5.07×10^{-1}
4	16.0	9.7525	9.7388	0.0137	2.90×10^{-1}
7	16.0	9.8997	9.8741	0.0256	3.09×10^{-1}
14	15.5	9.4123	9.3611	0.0512	3.19×10^{-1}

Table E4: Corrosion rates for second set of uncoated sample immersed in acidic solution.

T_E (days)	A (cm^2)	M_I (g)	M_F (g)	ML (g)	CR (mm/y)
1	15.9	9.7412	9.7361	0.0051	4.34×10^{-1}
4	16.4	9.6658	9.6511	0.0147	3.04×10^{-1}
7	15.9	9.9001	9.8758	0.0243	2.95×10^{-1}
14	16.2	9.8641	9.3611	0.0447	2.68×10^{-1}

Table E5: Corrosion rates for first set of uncoated sample immersed in alkaline solution.

T_E (days)	A (cm^2)	M_I (g)	M_F (g)	ML (g)	CR (mm/y)
1	16.3	10.1704	10.1537	0.0167	1.38×10^{0}
4	15.1	9.1335	9.1245	0.0090	2.02×10^{-1}
7	15.4	9.4012	9.3945	0.0067	8.42×10^{-2}
14	15.4	9.3277	9.3238	0.0039	2.44×10^{-2}

Table E6: Corrosion rates for second set of uncoated sample immersed in alkaline solution.

T_E (days)	A (cm^2)	M_I (g)	M_F (g)	ML (g)	CR (mm/y)
1	16.0	9.6216	9.6083	0.0133	1.12×10^{0}
4	1.62	9.9617	9.9542	0.0075	1.56×10^{-1}
7	15.7	9.6428	9.6390	0.0038	4.68×10^{-2}
14	16.2	10.0499	10.0469	0.0030	1.79×10^{-2}

Table E7: Corrosion rates for first set of uncoated sample immersed in neutral solution.

T_E (days)	A (cm^2)	M_I (g)	M_F (g)	ML (g)	CR (mm/y)
1	16.2	10.1514	10.1512	0.0002	0.00
4	15.7	9.7153	9.7152	0.0001	0.00
7	15.9	9.5954	9.5953	0.0001	0.00
14	15.9	9.8902	9.8901	0.0001	0.00

Table E8: Corrosion rates for second set of uncoated sample immersed in neutral solution.

T_E (days)	A (cm^2)	M_I (g)	M_F (g)	ML (g)	CR (mm/y)
1	15.9	9.8633	9.8631	0.0002	0.00
4	16.0	9.9416	9.9415	0.0001	0.00
7	15.8	9.6971	9.6969	0.0002	0.00
14	15.7	9.6213	9.6211	0.0002	0.00

PUBLICATIONS AND PRESENTATIONS

Several communications have proceeded from this research project and are listed as follows:

Journal Article

Evaluating the mechanical and corrosion properties of aluminium-6082, with and without plasma-sprayed WC coatings. *Manuscript Submitted, 2017.*

Presentations

1. **O. S. MacGregor**, J. W. van der Merwe, M. O. Daramola. Improving Erosion-Corrosion Resistance of Aluminium-6061 Alloy Using Metal Spray Coating Consisting of Nano-Structured Tungsten Carbide Powder. **Oral Presentation.** 3rd African Materials Science and Engineering Network (AMSEN) Workshop hosted by the University of the Witwatersrand, Johannesburg, South Africa. 26 – 29 May 2015. Page 291.

2. **O. S. MacGregor**, J. W. van der Merwe, M. O. Daramola, O. T. Johnson, A. E. Paterson. The Effect of Heat Treatment on the Mechanical Properties of Aluminium-6082 Alloy. **Oral Presentation.** 8th International Conference of the African Materials Research Society (AMRS), University of Ghana, Legon, Accra, Ghana. 6 – 11 December 2015.

3. **O. S. MacGregor**, J. W. van der Merwe, M. O. Daramola, O. T. Johnson, A. E. Paterson. Using Surface Treatment to Improve the Wear Resistance of Aluminium-6082 Alloy for Transport Applications. **Oral Presentation.** Aluminium Federation of Southern Africa (AFSA) International Conference at Cape Town, in 15 – 18 March 2016.